March 2024

TolTEC: A New Multichroic Imaging Polarimeter for the Large Millimeter Telescope

Nat S. DeNigris
University of Massachusetts Amherst

TOLTEC: A NEW MULTICHROIC IMAGING POLARIMETER FOR THE LARGE MILLIMETER TELESCOPE

A Dissertation Presented

by

NAT S. DENIGRIS

Submitted to the Graduate School of the
University of Massachusetts Amherst in partial fulfillment
of the requirements for the degree of

DOCTOR OF PHILOSOPHY

February 2024

Astronomy

TOLTEC: A NEW MULTICHROIC IMAGING POLARIMETER FOR THE LARGE MILLIMETER TELESCOPE

A Dissertation Presented

by

NAT S. DENIGRIS

Approved as to style and content by:

Grant W. Wilson, Chair

Alexandra Pope, Member

Katherine E. Whitaker, Member

Andrea Pocar, Member

Daniela Calzetti, Department Chair
Astronomy

DEDICATION

To the future scientist pondering the night sky, to the innate stargazer in us all.

ACKNOWLEDGEMENTS

It is surreal to be at a point in my life where I can write the acknowledgements for my PhD dissertation. There were many people who helped me get to this point, so please forgive me for how long this section will be...

First, my most heartfelt thanks to my advisor Grant Wilson. Thank you for your mentorship and patience over the years. You are my template for what it means to be both a passionate scientist and a compassionate leader. Thank you for taking a chance on me and inviting me along on the TolTEC journey. It has been an amazing six(!) years and I wouldn't be the scientist I am today without you.

A massive thank you to my mom Mina and grandma Kimiko. I have cherished every phone call, visit home, and video chat over the years. Thank you Grandma for telling me stories of your cousin Charlie Asawa (he worked on the first ruby laser!) and for inspiring me to strive for something in my life beyond "good enough". I hope this humble collection of pages makes you proud.

Next, thank you to my lovely found family at UMass Amherst: Daria, Emily, Nick, Dan, Brendan, Kody, and Becca. Thank you for the years of adventures and the many more to come. To Mel and Casey: I don't have the right words to explain how instrumental you were in this process...so I'll stick with something silly and say that the plans for Craft Haüs V on Mars are in the mail.

To Jed and Sarah, the best cohort ever: you have not only been huge sources of inspiration but also dear friends. I will always remember the times spent puzzling over assignments, catching silly coding errors, and celebrating each others successes, both personal and professional. Thank you for accepting this former physicist into your ranks and turning them into an avid astronomer.

Of course I can't forget my home away from home, the Moan and Dove. Thank you Dicap, Nate, Janell, Dan, Sophia, Nick, Rick, Steve, and the rest for providing me ungodly amounts of beer and company; both were instrumental in the completion of this document.

It should go without saying but an infinite amount appreciation for the TolTEC team. I can't possibly list all of you (though I will in our upcoming paper), but a small shout-out to the former and current members: Miranda, Amy, Selah, Reid, Emily M., Caleigh, Steve, Tom, Zhiyuan, Michael, Min, Emily L., Phil, Dennis, Giles, Joey, Sam, Itziar, and Marcial. Goodness, I would not be here today without you and all of the support you offered throughout the years.

I want to also express my deepest appreciation for my fellow TolTEC collaborator and informal mentor Sara Simon. You were the person who first put me on the path to study galaxy clusters and I couldn't be more grateful to be here. Thank you for taking me under your wing, checking in on me throughout the thesis process, and being a wonderful mentor and friend.

A super special thanks to my friends across the pond at Cardiff: Tom, Sam, and Carole. Thank you for coming through in the eleventh hour with that spare 300 K filter. I owe you many a pint next time we cross paths.

To my NASA GSFC family, especially Jay and Rachel, thank you for waiting this long for me. I'm incredibly excited to come home.

Last, but never least, many hugs for my cat Sméagol for enduring multiple moves around Maryland and Massachusetts, seeing me through three degrees, and being a constant in the midst of the chaos.

Again, thank you all for believing in me and supporting me this far. This thesis was completed thanks to you.

ABSTRACT

TOLTEC: A NEW MULTICHROIC IMAGING POLARIMETER FOR THE LARGE MILLIMETER TELESCOPE

FEBRUARY 2024

NAT S. DENIGRIS

B.Sc., UNIVERSITY OF MARYLAND, BALTIMORE COUNTY

M.Sc., UNIVERSITY OF MASSACHUSETTS, AMHERST

Ph.D., UNIVERSITY OF MASSACHUSETTS AMHERST

Directed by: Professor Grant W. Wilson

The TolTEC camera is a new millimeter-wave imaging polarimeter designed to fill the focal plane of the 50-m diameter Large Millimeter Telescope (LMT). Combined with the LMT, TolTEC offers high angular resolution (5″, 6.3″, 9.5″) for simultaneous, polarization-sensitive observations in its three wavelength bands: 1.1, 1.4, and 2.0 mm. Additionally, TolTEC is designed to reach groundbreaking mapping speeds in excess of 1 deg^2/mJy2/hr, which will enable the completion of deep surveys of large-scale structure, galaxy evolution, and star formation that are currently limited when considering practical observation times for other ground-based observatories.

This thesis covers the design as well as the in-lab and LMT characterization of the instrument. The chapter on the design overview (§2) describes each subsystem (cryogenics, optics, detectors, and detector readout), then the in-lab characterization chapter (§3) examines the performance of each subsystem prior to installation at the

LMT. In particular, this chapter provides the instrument's responsivity, efficiency, beam response, and readout noise while testing at UMass Amherst. The following chapter (§4) covers the initial results from commissioning at the LMT between December 2022 and April 2023. Based on the in-lab testing and LMT commissioning, I provide a number of procedures for operating/repairing the instrument in the appendices (§**??**).

I conclude (§5) with the development of a new pilot study to leverage TolTEC's high resolution and sensitivity with the goal of exploring galaxy cluster thermodynamics across cosmic time. While TolTEC observations of galaxy clusters were not available for this thesis, I describe the analysis pipeline I developed to perform a power spectrum analysis on intracluster medium (ICM) pressure fluctuations. The result of this pipeline is a power spectrum that can be analyzed to extract information on the thermodynamic state of the ICM. This type of study has only been performed on two clusters as of 2023, thus with TolTEC's mapping speed and sensitivity we will be able to expand this study and create the largest sample of its kind.

TABLE OF CONTENTS

Page

ACKNOWLEDGEMENTS ..... **v**

ABSTRACT ..... **vii**

LIST OF TABLES ..... **xiii**

LIST OF FIGURES ..... **xiv**

CHAPTER

1. INTRODUCTION **1**

1.1 A historical prelude 1
1.2 X-ray studies of clusters 3
1.3 The Sunyaev-Zel'dovich Effect 7
1.4 A new look at the mm-wave sky 10

2. OVERVIEW OF THE TOLTEC CAMERA **13**

2.1 Cryogenics 14

2.1.1 Design Overview 15
2.1.2 Thermal Stages 16
2.1.3 Cryocoolers 17

2.2 Optics 18

2.2.1 Warm Optics 18
2.2.2 Cold Optics 20

2.2.2.1 Filters at 300 and 45 K 20
2.2.2.2 Lyot Stop, 1 K Baffle, and Other Radiation Absorption Tactics 20
2.2.2.3 Beyond the baffle, the path to the focal planes 23

2.3 Detectors 25

2.3.1 Motivation for using LEKIDs in TolTEC . . . 26
2.3.2 LEKID Physics . . . 28
2.3.3 What type of LEKIDs does TolTEC use? . . . 30
2.3.4 Sources of detector noise . . . 32

2.4 Detector Readout . . . 33

2.4.1 Design Overview . . . 34

2.4.1.1 Cabling, attenuators, and DC blocks . . . 34
2.4.1.2 Low Noise Amplifiers . . . 35
2.4.1.3 ROACH2 and IF slices . . . 38

2.4.2 Reading out a single detector . . . 38
2.4.3 Reading out multiple detectors . . . 41

3. LABORATORY TESTING . . . 45

3.1 Timeline for lab testing at UMass . . . 45
3.2 Cryogenics . . . 46

3.2.1 Modeling TolTEC cryogenic performance . . . 46
3.2.2 Utilizing the model to build the 1 and 0.1 K Stages . . . 49
3.2.3 Cryogenic Performance . . . 55

3.2.3.1 Cryocoolers . . . 55
3.2.3.2 Custom Copper Thermal Straps . . . 56
3.2.3.3 Detector Array Temperatures . . . 57

3.3 Detectors . . . 59

3.3.1 Bandpass . . . 59
3.3.2 Responsivity . . . 61
3.3.3 Efficiency . . . 67
3.3.4 Detector Noise . . . 71

3.4 Optics . . . 72

3.4.1 1 K Baffle . . . 72
3.4.2 Beam Response . . . 74

3.5 Detector Readout . . . 79

3.5.1 Cold electronics transmission . . . 80
3.5.2 Noise with minimal optical loading . . . 82
3.5.3 Relative noise contributions . . . 86

4. COMMISSIONING AT THE LMT 90

4.1 Introduction 91
4.2 Instrument overview 92

4.2.1 Cryogenics 92
4.2.2 Optics 95
4.2.3 Half-Wave Plate and Rotator 96
4.2.4 Detectors and Readout Electronics 97

4.3 Installation and Hardware Performance 98

4.3.1 Overview 98
4.3.2 Optical Alignment 98
4.3.3 Cryogenics Performance 100
4.3.4 Bandpasses 101
4.3.5 Efficiency 102

4.4 Measurement and Scanning Strategies 103

4.4.1 Readout Method 103

4.4.1.1 Detector Identification Sweeps 103
4.4.1.2 Tune Procedure 104
4.4.1.3 DriveFit 107

4.4.2 Observing Modes 110

4.4.2.1 Raster 111
4.4.2.2 Lissajous 111
4.4.2.3 Additional modes 112

4.5 Data Reduction and Management 113

4.5.1 Mapmaking 113

4.5.1.1 Citlali 113
4.5.1.2 Minkasi 116

4.5.2 Data Archive 118

4.6 Calibration 118

4.6.1 Focus and Astigmatism 118
4.6.2 Beammaps 119
4.6.3 Flux Calibration 121
4.6.4 Pointing 122

4.7 Performance 124
4.7.1 Polarization 125
4.7.2 Noise 126
4.7.2.1 Detector readout noise 126
4.7.2.2 BLIP predictions 128
4.7.2.3 Vibrational noise 130
4.7.3 Sensitivity and Mapping Speed 135
4.8 Conclusions 138
5. A NOVEL SZ STUDY WITH TOLTEC 141
5.1 Pressure Fluctuations in the Intracluster Medium 141
5.1.1 Physics with Fluctuations 141
5.1.2 High Resolution Studies of ICM Fluctuations 144
5.2 Setting the Stage 145
5.2.1 The Proposed Cluster Sample 145
5.2.2 Status of Cluster Observations 146
5.3 The Analysis Pipeline 147
5.3.1 Methodology 147
5.3.2 Power spectrum calculation 150
5.3.3 Caveats 152
5.4 Results from Simulations 153
5.4.1 A Toy Model 154
5.4.2 A Spherically Symmetric Cluster 157
5.4.3 Extending the Analysis to A Dynamically Active Cluster 161
5.4.4 Next Steps in Development 163
5.5 Conclusions 164
6. CONCLUSION 167
7. APPENDIX 171
BIBLIOGRAPHY 204

LIST OF TABLES

Table **Page**

2.1 TolTEC **design** specifications reproduced from Bryan et. al. (2018). 15

2.2 TolTEC's 4 K cold optics elements following the Lyot stop. 21

2.3 Summary of TolTEC's detector array specifications. 26

3.1 Table of modeled heat loading and estimated cooling power. 49

3.2 Effect of changing the thickness of the central busbar on the temperature along the bar. 51

3.3 Table of average base temperatures reached by each cryocoolers' stages. 56

3.4 Modeled versus measured temperatures at the 1 K thermal shielding and 0.1 K array. 58

4.1 An accounting of the resonators in the three TolTEC arrays by design, automatically identified at lab, and automatically identified at the site. 105

4.2 Measured polarization fractions (p) and polarization angles ($\varphi_{\rm sky}$) for 3C 286 in two different configurations with literature values at similar wavelengths. 125

4.3 Mean values and uncertainty of NEFD and mapping speed for each TolTEC band at zero opacity and with the telescope observing at the zenith. 138

5.1 Sample of clusters for proposed pilot study. 146

7.1 Table detailing how to troubleshoot the dilution refrigerator's TolTEC specific issues. 188

LIST OF FIGURES

Figure **Page**

1.1 Comparison of different observations of the Coma cluster. 2

1.2 A comparison of X-ray mission flux sensitivities. 6

1.3 A comparison of mm-wave instrument sensitivities to the SZ. 9

1.4 Plot of tSZ surface brightness with the TolTEC, ACT, and Planck bandpasses overlaid. 11

2.1 Photos of TolTEC and the LMT. 14

2.2 TolTEC's thermal stages. 15

2.3 In-lab photo of the 1 and 0.1 K thermal busbars and the 4 K custom flexible copper straps below the optics bench. 17

2.4 CAD model of the LMT receiver cabin including the ASU designed and fabricated TolTEC warm coupling optics. Image credit: E. Castillo. 19

2.5 TolTEC's 1 K baffle. 20

2.6 CAD model of TolTEC's 4 K optics bench and three bands. 24

2.7 An image of a single lumped element kinetic inductance detector (LEKID) pixel from Austermann et. al. (2018). 27

2.8 A schematic of the radio frequency (RF) signal chain for a single detector network. 34

2.9 Stainless steel cables and their bending jig. 36

2.10 The three oxygen-free high-conductivity copper (OFHC Cu) clamps for the low noise amplifiers (LNAs). 37

2.11 A cartoon of how a single detector's transmission (S_{21}) response changes with increasing optical loading. 40

3.1 TolTEC's development timeline. 47

3.2 CAD model of the 1 and 0.1 K busbars. 54

3.3 3/4 view of TolTEC CAD model highlighting the four thermal stages. 55

3.4 The Cryogenic Device Laboratory's Fourier Transform Spectrometer at UMass Amherst. 60

3.5 A white light fringe example from an FTS measurement. 61

3.6 TolTEC's bandpasses as measured in the laboratory. 62

3.7 The cryogenic blackbody installed on the optics bench in front of the 1.1 mm array prior to closing the cyrostat. 64

3.8 An example of derivatives taken of S_{21} with respect to frequency for five temperature settings of the cryogenic blackbody. 65

3.9 Histogram of laboratory responsivity values. 66

3.10 Histograms of the TolTEC efficiencies for each detector array. 70

3.11 1 K baffle and 4 K awning installed in 4 K optical volume. 74

3.12 The XY robot arm Wyatt being tested in the UMass Amherst laboratory prior to a cooldown. 75

3.13 Examples of beammaps taken in 2019 and 2021. 76

3.14 Graphic detailing the dichroic filter compression issue. 77

3.15 The loopback gain through TolTEC's cryostat in the cooldown prior to shipment to the LMT. 81

3.16 An example of a typical PSD for a **single network** under minimal optical loading. 85

3.17 Simplified graphic of a single readout network showing the common point used for comparing noise measurements for different elements in the network. 86

4.1 A photo of the TolTEC camera inside the receiver cabin at the Large Millimeter Telescope (LMT). 93

4.2 A CAD model of a top-down, cross-section view of TolTEC's cryostat. 94

4.3 A CAD model showing the warm optics (M4, M5, and M6) inside of the receiver cabin. 95

4.4 Timestreams for one of the central 1.1 mm array detectors. 99

4.5 TolTEC's array temperatures measured at the warmest point in the 1 and 0.1 K thermal chains (e.g., at the entry of the busbars to the array package). 101

4.6 The network sweep showing the full 500 MHz bandwidth of the readout of detector network 0. Neighbouring readout channels are plotted in alternating color. 104

4.9 Two 270 GHz coverage maps from the December 2022 commissioning run. 110

4.10 A example of results from a TolTEC beammap observation of radio galaxy J1159+292. 121

4.11 Examples of pointing observations for radio galaxy J0112+227. 123

4.12 Median fractional frequency noise S_{xx} as a function of drive attenuation for several networks. 128

4.13 Predicted background-limited infrared performance (BLIP) for varying factors of detector noise (detector NEP/BLIP) for the TolTEC 1.1 mm, 1.4 mm, and 2.0 mm arrays for varying factors of detector noise. 129

4.14 TolTEC's vibrational noise performance. 132

4.15 Power spectra density of the TolTEC timestreams of a beammap-type observation of those networks where the dark detectors are identified: 0, 1, and 4. 133

4.16 Flux density uncertainty vs. integration time of each of the A_i regions for each coadded map in each one of the TolTEC bands. 137

5.1 An example of a 10 minute TolTEC Lissajous scan over Abell 1835 (background image from the SDSS catalog) generated with the TolTEC Observation Planner. 147

5.2 Coadded map of the two 30 minute TolTEC observations over MACS J0717.5+3725. 148

5.3 A visual showing the analysis pipeline used to calculate the pressure fluctuation power spectrum for a galaxy cluster observed by TolTEC. 149

5.4 Reproductions of window functions and their Fourier Transforms from Khatri & Gaspari (2016). 151

5.5 Three examples of randomly generated 2D $1/f$ spectra used as a toy model. 156

5.6 An example of a randomly generated 1/f spectrum and the result of continuing the power spectrum analysis shown in Fig. 5.5 to calculate A_{2D}. 157

5.7 Simulated intensity maps in the three TolTEC bands used for the analysis in §5.4.2. 158

5.8 Maps from different steps in the analysis procedure. The first map is the median Compton-y map generated from running the `hie_bayes` code on the simulated TolTEC maps shown in Figure 5.7. 159

5.9 The resulting power spectrum for the smooth, symmetric cluster simulation with no contamination from instrument noise, atmospheric noise, or DSFGs. 160

5.10 An example of a simulated Compton-y map from the Galaxy Cluster Merger Catalog being run through the initial analysis steps. 162

5.11 An example of the analysis pipeline output for the average pressure fluctuation power spectrum using a simulated Compton-y map from the Galaxy Cluster Merger Catalog. 162

7.1 Phase diagram for dilution refrigerator helium mixture and simplified schematic. 172

7.2 Cross sectional view of the dilution refrigerator. 173

7.3 Custom made copper straps. 177

7.4 TolTEC's main cryostat valve closed with a metal vacuum hose connected to a pump out of frame. 182

7.5 TolTEC's Cryomech compressors are located on the 29m level in the receiver cabin. 185

7.6 Example of a VNA sweep showing that the LNA for the network is on and the readout electronics are performing correctly. 196

7.7 LNA bias board circuit diagram and photo. 200

7.8 Photos of the laser alignment plate installed on TolTEC. 202

CHAPTER 1

INTRODUCTION

"The only way to learn is by playing, the only way to win is by learning, and the only way to begin is by beginning."

Sam Reich, *Game Changer*

1.1 A historical prelude

Our Universe contains a wide variety of matter, encompassing different scales, phases, and particle types. At the smallest scales, we ponder the interactions between different particles, the composition of the Universe, and how these materials influence its evolution. Conversely, at the largest scales we confront the clustering of matter in the form of galaxy groups, clusters, and superclusters interconnected by the cosmic web: a result of initial perturbations in the density field of the 'small stuff'. It is here, on the scale of galaxy clusters, that we can delve into the study of the thermodynamics and formation history, as well as gain insights into cosmology and the enigmatic nature of dark matter and dark energy.

Galaxy clusters were first referenced in literature by Charles Messier in the late 1700s, at the time described as concentrations of "nebulae" [1]. F.W. Herschel followed up on Messier's observations with a study of the Coma cluster (see Fig. 1.1 for observations of the Coma cluster in different wavelengths), remarking that there were "many hundreds of nebulae which are to be seen in what I have called the nebulous stratum of Coma Berenices" [2]. It would be well over a century before this vision of clusters took on a new form, with the discussion shifting towards a debate

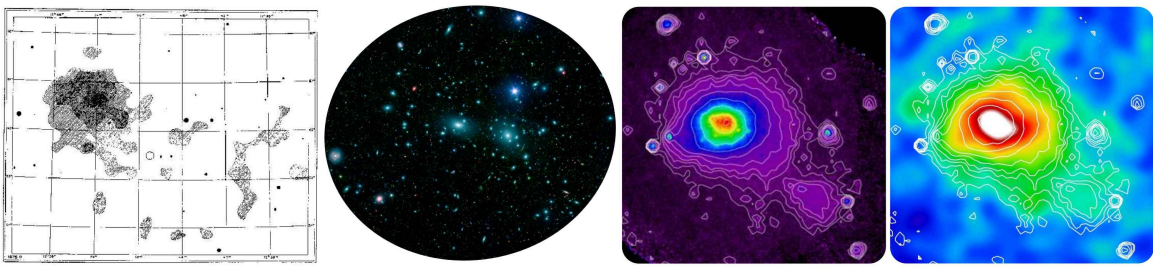

Figure 1.1: Comparison of different observations of the Coma cluster. Each offers a unique insight into cluster physics. *Left*: Density map of the Coma cluster from Max Wolf's 1902 paper created from optical telescope observations [3]. *Left, center*: Infrared observations from Spitzer (3.6, 4.5, 8.0 μm) and optical observations from SDSS of the Coma cluster. Image credit: NASA.*Right, center*: X-ray observation of the bremmstrahlung effect in the Coma cluster using ROSAT. Image credit: NASA/ESA. *Right*: mm-wave observation of the Sunyaev-Zel'dovich Effect in the Coma cluster using Planck. Image credit: NASA/ESA.

on whether the observed "nebulae" were extra- or intragalactic. In the 1930s, Edwin Hubble established that the "nebulae" were indeed galaxies external to the Milky Way. Additionally, in 1933, Fritz Zwicky opened the door to a detailed understanding of galaxy cluster mass when his study of galactic motion in the Coma cluster hinted towards the existence of dark matter and its role as galaxy clusters' largest mass component.

By the mid-20th century, George Abell published his first catalog on the distribution of clusters of galaxies[1] using the 48-inch Schmidt telescope at the Palomar Observatory to produce images with resolutions as high as $2''$ [2] [4]. Subsequently, the study of galaxy clusters became firmly rooted in optical observations[3] for the next

[1] Coincidentally enough, also a PhD thesis!

[2] Modern ground-based optical telescopes have diameters larger than 3 meters (120 inches) and can achieve resolutions below $1''$. To increase the effective area of the telescope, and thus achievable resolution, newer telescopes have segmented mirrors coupled with adaptive optics.

[3] Optical wavelengths for astronomy are typically considered to be between 400 and 900 nm, or 750 to 333 THz, respectively.

two decades. Using surveys of optically observed galaxies, one could describe the cluster richness[4] and concentration to perform statistical studies on clusters. Then, in the 1960s and 1970s, came a push for multi-wavelength cluster studies with the introduction of large-scale radio and X-ray observations.

Felten et. al. (1966) reported unexpected X-ray emission from the Coma cluster, citing thermal bremmstrahlung radiation due to a volume-filling hot gas as the most likely cause [5]. In the same paper, they incorrectly suggested another possibility for the X-ray radiation: inverse Compton (IC) scattering of cosmic microwave background (CMB) photons off of hot electrons. Gurskey et. al. (1972) followed up on this observation with the *Uhuru* observatory, building up a catalog of X-ray selected galaxy clusters and drawing similar conclusions. These and other contemporary studies became a major stepping stone for subsequent groups hoping to explain the origin of X-ray emission from clusters. This was one of the motivations for Sunyaev and Zel'dovich's 1972 paper on the IC scattering of cosmic background radiation (CMB) by the hot intracluster medium. However, they established that IC scattering through the hot electron gas would not generate X-rays, rather it would generate a characteristic spectral distortion on the CMB that would come to be known as the Sunyaev-Zel'dovich Effect (SZ) [6]. It would be over a decade before the first SZ detection was made by Birkinshaw, Gull, and Hardebeck using the 40-m radio telescope at Owens Valley Radio Observatory[5] [7].

1.2 X-ray studies of clusters

In the current paradigm, we theorize that galaxy clusters are dominated by dark matter (DM) with a hot ($T_e > 10^7$ K $\simeq 1$ keV), highly-ionized, low-density gas known

[4]Richness refers to the number of galaxies associated with a cluster.

[5]The detection itself being at 20.3 GHz (14.8 mm) was well into the decrement of the SZ spectrum.

as the intracluster medium (ICM) embedded within the DM halo ($M \geq 10^{14}$ $M_{\odot}$) [8]. By studying the ICM we can estimate cluster mass and temperature as well as examine the role of feedback[6] in cluster formation/evolution.

One mechanism through which we can observe the ICM is through X-ray radiation as the gas primarily emits via bremsstrahlung radiation plus emission lines from heavy elements. Using their sub-arcsecond resolution instruments, X-ray studies have revealed a number of key details about the structure of galaxy clusters and their (thermo)dynamics. For instance, *Chandra* found the temperature and entropy profiles of clusters decrease toward their cores, but typically flatten out at a temperature around 1 keV on 10-100 kpc scales [9]. This could imply that the ICM in the core (within 100 kpc of the center) either cools non-radiatively or that some other mechanism heats the gas, injecting energy and suppressing cooling [10, 11]. Proposed heating mechanisms from simulation include AGN feedback, shock heating from infalling gas, and gas sloshing from mergers or infalling gas [12, 13]. X-ray observations have also demonstrated substantial ICM heating from member galaxies through AGN and starbursts [9, 11, 14–18]. These analyses, coupled with lensing observations that trace the dark matter potential well, have allowed us to develop a more complete census of the energy budget of the ICM.

However, X-ray observations feature two major limitations when it comes to studying galaxy clusters. Firstly, X-ray flux decreases as the gas density squared and so observations will have decreased sensitivity to the lowest density regions of the ICM on the cluster outskirts. The cluster outskirts are where the accretion of gas and smaller halos introduce non-thermal contributions[7] to the energy budget.

---

[6]Asking an astronomer what they mean by feedback can quickly become complicated. In this context, I am specifically referring to the injection of energy into the surrounding intracluster medium from non-gravitational sources, such as active galactic nuclei and supernovae.

[7]Non-thermal contributions refers to sources of pressure (e.g., energy per volume) that have not had their energy thermalized/virialized on the cluster's dynamical timescale (for a 10^{14} $M_{\odot}$ cluster

Assuming the simplest model for the electron gas density, the spherically symmetric isothermal β profile [19], the density of the cluster goes as

$$n_e(r) = n_0\left(1 + \left(\frac{r}{r_c}\right)^2\right)^{-3\beta/2}, \tag{1.1}$$

where n_0 is the density at the center, r is distance from the cluster center, r_c is the cluster core size, and β is the slope of the density profile outside of the core[8]. This model was first proposed by Cavaliere and Fusco-Femiano (1976), with the assumption that both the cluster's gas and its galaxies are in hydrostatic equilibrium with the gravitational potential of the DM halo [20]. The surface brightness from X-ray emission is given by

$$I_x(r) = \frac{1}{(1+z)^4}\int \epsilon(T) n_e^2(r) dl, \tag{1.2}$$

where ϵ is the X-ray emissivity and so, assuming the density profile above, the X-ray surface brightness can fall off as approximately $-3\beta + \frac{1}{2}$ (typical values place $\beta \sim 2/3 - 1$)[9]. Thus X-ray telescopes can quickly lose sensitivity to the ICM on scales $\gtrsim$500 kpc [21] (see Fig. 1.2). There have been studies to extend the sensitivity of existing observations through stacking archival data or combining data from different instruments; however, this relies on accumulating tens to hundreds hours of integration time to make significant improvements [22].

Secondly, as seen in the prior equation, X-ray surface brightness undergoes cosmological dimming and thus observations will have lower sensitivity to high redshift

---

t_{dyn} ~1 Gyr). Sources include turbulence, bulk motion, magnetic fields, and cosmic rays. Compare this to the pressure acting against gravity when under an assumption of hydrostatic equilibrium.

[8] β itself is defined as $\mu m_p \sigma_r^2 / k_B T$ where $\mu = < m > / m_p$ is the mean molecular mass of the ISM [20]. For a fully ionized hydrogen gas, $\mu = 0.5$.

[9] The relationship between X-ray surface brightness and β becomes apparent after taking the following integral over the density from Eqn. 1.1: $\int_{b^2}^{\infty} dx\,(1 + x/r_c^2)^{-3\beta}/\sqrt{x - b^2}$ where $x = r^2$.

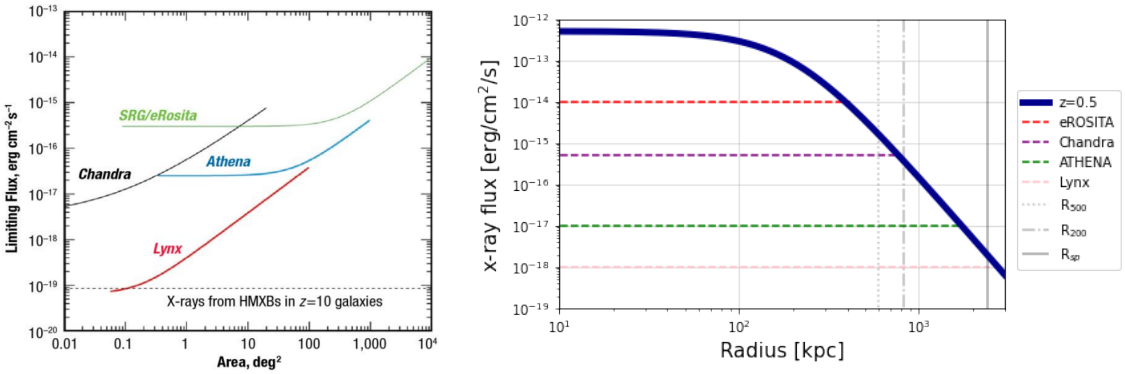

Figure 1.2: *Left*: Figure from [25] comparing the point-source sensitivities between *Chandra* and three upcoming X-ray missions during for 15 Ms ($\sim$ 4167 hours) of integration time. The limits reached in this plot are indicative of the survey coverage offered by the different instruments, highlighting in particular Lynx's offer of low flux limits across a wide area regime. *Right*: Model of X-ray instrument sensitivity to an isothermal β profile assuming a 10^{14} $M_\odot$ galaxy cluster with $L_x = 1e44$ erg/s at $z = 0.5$. The horizontal lines show the lowest recorded or predicted limiting flux of each instrument for an observation (as compared to a survey). The vertical dashed lines represent the location of characteristic radii R_{500} and R_{200} plus the theoretical R_{sp} (the splashback radius). To probe the outskirts of the cluster requires sensitivity to regions well-beyond R_{200} [26].

sources. Due to their earlier stages in formation, high redshift clusters experience heightened accretion rates of material as well as greater AGN and starburst activity making them a rich area for testing the interactions between formation and feedback [11]. Since the surface brightness is $\propto (1+z)^{-4}$, X-ray studies of higher redshift clusters may be increasingly challenging without the jump in sensitivity from upcoming (2030s and beyond) X-ray space telescopes such as ATHENA and Lynx (see Fig. 1.2 for a plot comparing X-ray instrument sensitivities) [23, 24].

Thus, despite the great strides in understanding the inner regions clusters through *Chandra* and *XMM-Newton* observations, we are still missing key observational constraints on physical processes connected to structure formation [8, 26]. Many fundamental questions about the physics of clusters and their use as cosmological probes remain, such as:

1. What is the role of non-thermal pressure support on the formation and evolution of large scale structure across cosmic time?

2. What is the role of mergers and large scale accretion in the energy distribution of clusters?

3. Which combination of observables places the best overall constraint on cluster mass with the fewest systematic effects?

To address these questions requires high resolution, high sensitivity studies of clusters using an observable, such as the Sunyaev-Zel'dovich Effect, in tandem with X-ray observations.

1.3 The Sunyaev-Zel'dovich Effect

As shown below, the SZ's surface brightness, unlike X-ray observations, is directly proportional to the gas density and is redshift-independent. As such, the SZ may be used as a convenient observable to trace the ICM out to cluster radii beyond 500 kpc and higher redshifts than current X-ray missions (see Fig. 1.3).

The largest component of the SZ signal from the ICM is the thermal SZ effect (tSZ), which is a function of ICM gas temperature and density, thus making the tSZ a measure of pressure along the line of sight (LOS). In the non-relativistic limit of electron temperatures, a good approximation for galaxy clusters with $T_e \leq 15$ keV ($\sim 1.7 \times 10^8$ K), the tSZ can be characterized by a change in CMB surface brightness[10] given by

$$\Delta I_{tSZ} = I_0 \, g(x) y, \tag{1.3}$$

[10]Throughout this document, you may see 'surface brightness' used interchangeably with 'intensity'. In astronomy, these have the same units of specific flux per solid angle, or Jy/sr (or even W/m^2/Hz/sr, if you prefer SI units).

where $I_0 = 2(k_B T_{CMB})^3/(hc)^2$ (units of MJy/sr), $x \equiv h\nu/k_B T_{CMB}$ (unitless), and g(x) is the unitless spectral shape of the effect given by

$$g(x) = \frac{x^4 e^x}{(e^x - 1)^2}\Big(x\frac{e^x + 1}{e^x - 1} - 4\Big)(1 + \delta_{SZE}(x, T_e)), \tag{1.4}$$

where δ_{SZE} handles relativistic effects imparted to the spectrum by high energy ICM electrons, and y is the unitless Compton-y parameter equal to

$$y = \frac{\sigma_T}{m_e c^2}\int_{LOS} n_e k_B T_e dl, \tag{1.5}$$

which is the integral of $P_e = n_e k_B T_e$ along the LOS, containing the SZ's dependence on the density profile of the cluster [27, 28]. As such, the SZ surface brightness is directly proportional to the integral of the gas density n_e rather than its square. Assuming the isothermal β model above and taking the integral with respect to the LOS l, the Compton-y profile goes as

$$y(\theta) \propto \left(1 + \left(\frac{\theta}{\theta_c}\right)^2\right)^{1/2 - 3\beta/2}. \tag{1.6}$$

For ease of integration, it is worth performing a variable substitution such that the profile is a function of θ, the physical distance from the cluster center in the plane of the sky ($\theta^2 = r^2 - l^2$). This will be the variable convention we use in Chapter 5.

It is important to emphasize that the isothermal β model depends on major assumptions that are not observed experimentally (i.e., the temperature profile of the cluster is not spatially independent). Despite this, the model can be used to approximate a smooth underlying ICM profile in both X-ray and SZ observations [20].

Another important feature of the tSZ is its redshift-independence. The SZ is not an emission mechanism of its own, it simply imparts a characteristic distortion onto the CMB. This distortion appears with three dominant features in the surface

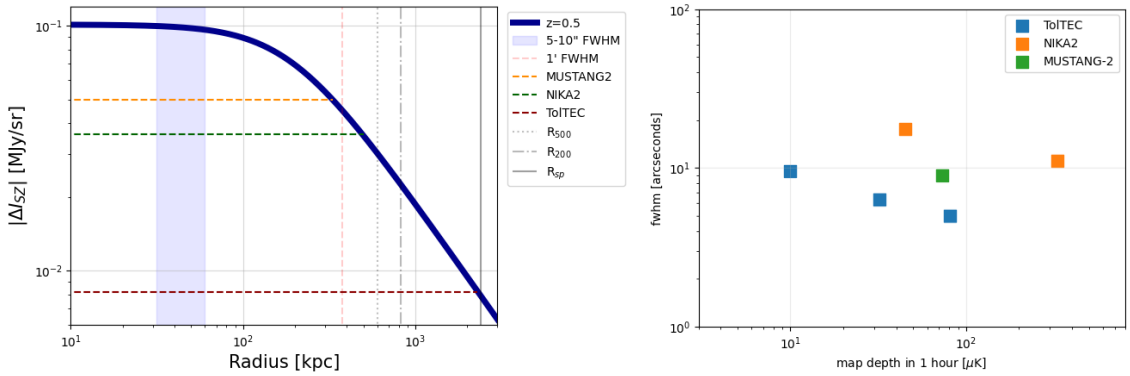

Figure 1.3: *Left*: Illustration of different mm-wave instruments' sensitivity to an isothermal β profile assuming a 10^{14} $M_\odot$ galaxy cluster at $z = 0.5$. Note, this figure shows absolute value of the surface brightness using a detection frequency of 150 GHz (2.0 mm). This figure is merely meant as a rough estimate of the radii that each instrument can probe in a single observation. The vertical band represents the scale coverage at this redshift assuming 5 to 10″ beams. The grey vertical lines are the same characteristic radii as shown in Figure 1.2. Using SZ observations of clusters, we can explore the fainter outskirts where newer material accumulates. *Right*: A plot comparing the map depths achieved by different facilities in an hour based on their reported sensitivities. In the figure, down and to the left is better performance, showing that TolTEC offers higher sensitivity and resolution across its three bands.

brightness spectrum: (1) below $\sim$ 220 GHz (1.4 mm), we observe a 'cold' spot, or decrement, compared to the background at the location of the cluster; (2) above this frequency, a map would see a 'hot' spot, or increment; and (3) when centered at $\sim$ 220 GHz, or the null, there is no apparent change from the background. At the null frequency another form of the SZ, the kinetic SZ effect (kSZ), has its maximum intensity.

This secondary component of the SZ effect, the kinetic SZ effect (kSZ), is the result of a Doppler shift imparted onto the primary CMB by the bulk motion of the ICM. Typically, this effect is quoted as a decrease in the temperature of the CMB

$$\Delta T_{kSZ} = -T_{CMB,0}\,\tau_e \frac{v_z}{c} \tag{1.7}$$

where τ_e is the optical depth of the electrons along the line of sight to the CMB photons, v_z is the peculiar velocity of the cluster[11], and c is the speed of light [27]. The kSZ may be positive if the bulk motion is in the direction of the observer, or negative if moving in the opposite direction. The peak of the effect is approximately an order of magnitude weaker than the tSZ, making it significantly more challenging to observe [28]. Observations of the kSZ measure the mass-weighted gas velocity along the LOS, which has been used to constrain the population of 'missing baryons' in the ICM's diffuse 'warm-hot' ($10^5 - 10^7$ K) phase as the effect is insensitive to electron temperature and, to first order, only depends on the electron density and cluster velocity along the LOS [29, 30].

It is important to note that as a mm-wave observable, there is the possibility of confusion between the SZ and other sources such as dusty star-forming galaxies (DSFGs) and lensing of the cosmic infrared background (CIB). To make progress in cluster studies, it is then vital to resolve this population of galaxies along the line of sight to, and behind, the cluster and to be able to measure the background contribution of high redshift DSFGs.

1.4 A new look at the mm-wave sky

The Astro2010 Decadal Survey's call for a fast, mm/sub-mm wavelength camera to conduct large-scale, high-resolution surveys has been largely unanswered. To meet this demand, our collaboration developed TolTEC[12]: a new multichroic imaging polarimeter with simultaneous imaging at 1.1, 1.4, and 2.0 mm. TolTEC is the newest facility instrument installed at the 50-m single dish Large Millimeter Telescope

[11] A typical value for v_z is 1000 km/s.

[12] Note that TolTEC is not an acronym. I've had to argue with a non-zero number of reviewers about this fact. The mix of cases are meant to evoke AzTEC, TolTEC's forerunner, as well as distinguish the camera from the Toltec civilization. The name for AzTEC was originally an acronym; while the acronym did not stick, the spelling convention did.

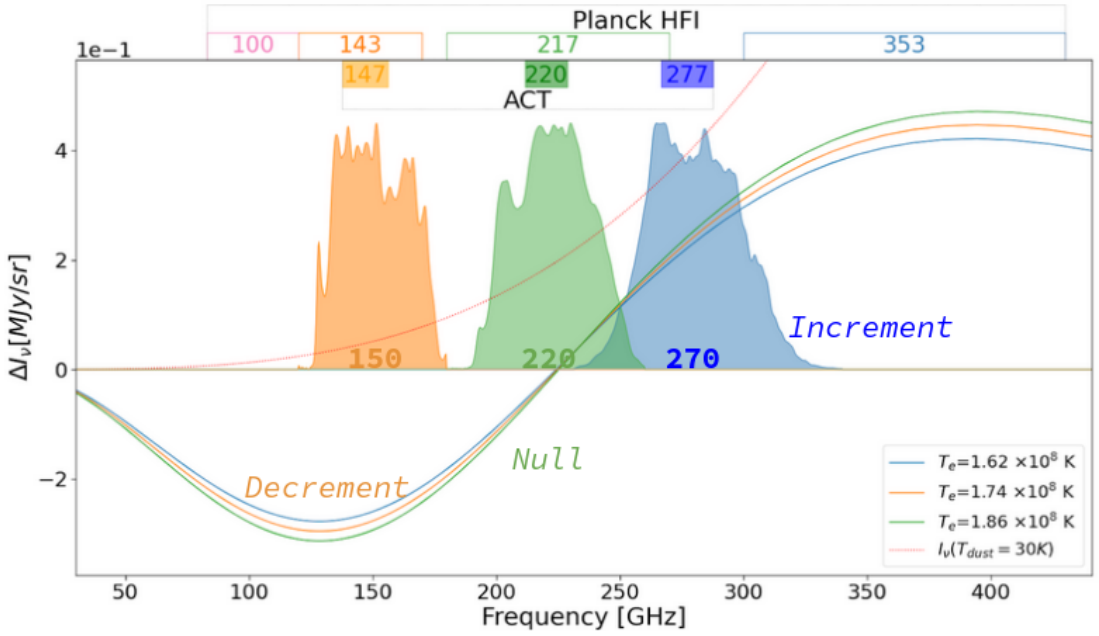

Figure 1.4: Plot of tSZ surface brightness with the TolTEC, ACT, and Planck bandpasses overlaid. The TolTEC bandpasses (150 GHz/2.0 mm in orange, 220 GHz/1.4 mm in green, and 270 GHz/1.1 mm in blue) shown were measured at UMass Amherst in Summer 2020 (see §3 for further details). TolTEC overlaps well with ACT and *Planck* for high resolution follow-up observations. *Herschel*, not pictured here, can provide constraints on the high frequency tail of the tSZ, thus putting upper limits on the temperature of the ICM. The curves showing the effect of varying T_e were adapted by Zhiyuan Ma from the software *SZpack* [31, 32]. The selected T_e values were chosen based on gas temperature estimates for the most massive clusters. The dotted line above the tSZ curves models the signal expected for a dusty galaxy ($S_{1.1\,\mathrm{mm}} = 1$ mJy for a 5″ beam) assuming a dust temperature of 30 K. This curve has been scaled to fit on the plot with the tSZ curves.

(LMT). Importantly, for studies of galaxy clusters, TolTEC offers coverage over three mm-wavelengths spanning the SZ's decrement, null, and increment, which can also be used to better disentangle contaminants with differing spectral behavior, such as DSFGs (see Fig. 1.4).

TolTEC's combination of three bands, thousands of detectors, and a 50 m diameter telescope makes it a potential keystone for studies of galaxy clusters through the

SZ. Lower resolution[13] facilities, such as AdvACT and SPT3G, have incredible mapping speeds and are ideal for building up cluster catalogs, but their $\gtrsim 1'$ resolution precludes a detailed investigation of cluster substructure in all but the most local cluster samples [33, 34]. Higher resolution facilities are often missing one or more of the features offered by TolTEC. For instance, the NIKA2 instrument on IRAM-30m utilizes a similar detector technology to TolTEC but with fewer detectors, less frequency coverage, and at a lower altitude site [35]. MUSTANG-2, another high resolution camera, on the Green Bank Telescope (GBT) has the same resolution as TolTEC's 150 GHz (2.0 mm) array but only a single band, 90 GHz (3 mm)[36]. Additionally, ultra-high resolution facilities, such as ALMA, require a prohibitive amount of integration time in order to map an entire cluster. But ultimately, while TolTEC does fill this important niche, the most detailed studies of clusters will come from combining observations from these facilities and TolTEC in order to reach a level of an unprecedented sensitivity, resolution, and frequency coverage.

In this thesis, I describe the TolTEC camera's design, in-lab characterization, and on-sky testing along with a plan for a pilot project to systematically study TolTEC's ability to measure thermodynamic and evolutionary traits of galaxy clusters over cosmic time.

My thesis is organized as follows: §2 provides an overview of the design of the TolTEC camera. §3 covers the laboratory characterization that occurred between 2018 and 2021 at UMass Amherst. §4 explores the instrument deployment and initial performance at the Large Millimeter Telescope. §5 reviews the Sunyaev-Zel'dovich Effect in galaxy clusters and discusses a proposed study using TolTEC. §6 is a conclusion chapter that summarizes results from the thesis.

[13]When I mention the resolution of mm-wave instruments I will use the following descriptions: (1) low resolution, $\theta_{FWHM} \geq 60''$; (2) high resolution, $1'' < \theta_{FWHM} < 60''$; and (3) ultra-high resolution, $\theta_{FWHM} \leq 1''$.

CHAPTER 2

OVERVIEW OF THE TOLTEC CAMERA

"You're going to be amazing."

Griffin McElroy, *The Adventure Zone: Balance*

This section provides solely an overview of the instrument design. Please refer to §3 for laboratory testing results and to §4 for instrument performance after installation at the Large Millimeter Telescope.

TolTEC is a facility instrument for the 50-m diameter Large Millimeter Telescope (LMT), which resides atop the dormant volcano Sierra Negra[1] in Mexico. The camera features simultaneous imaging plus polarimetry at 1.1, 1.4, and 2.0 mm (or 270, 220, and 150 GHz, respectively). TolTEC contains 7716 superconducting Lumped Element Kinetic Inductance Detectors (LEKIDs) across its three focal planes [37–40]. Table 2.1 provides the designed full-width half-maximum (FWHM) of the beams and mapping speeds for each band. When coupled with the LMT, TolTEC features a $4'$ field of view (FoV) which, with its $\leq 10''$ beams on the sky, will allow us to create high-resolution, large-scale maps of both nearby and extragalactic systems.

TolTEC's mapping speeds have critical implications for the science that can be achieved using the instrument[2]. As seen in Table 2.1, TolTEC was designed to have

[1]Sierra Negra has an elevation of approximately 15,000 feet (4600 meters) making the road to visit the LMT one of the highest in North America.

[2]Note that the range shown in Table 2.1 for the mapping speed is to provide conservative estimates based on TolTEC's forerunner, AzTEC. It has been empirically shown that the atmosphere increased

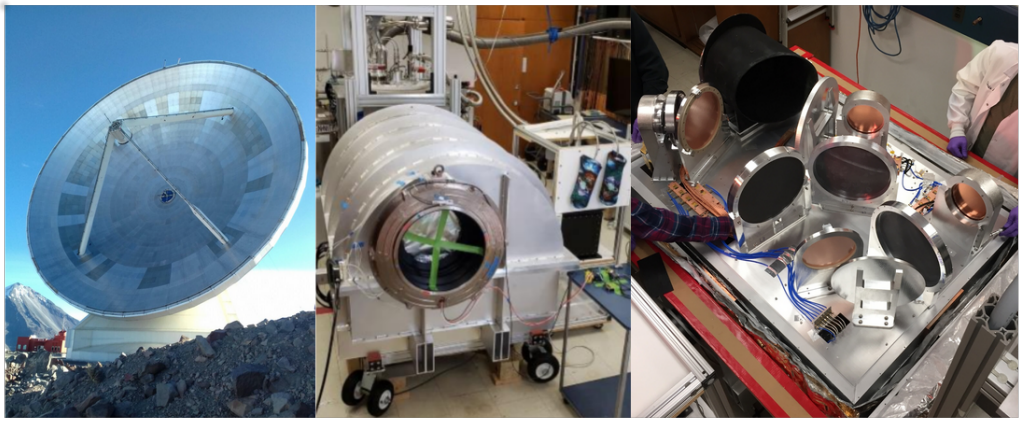

Figure 2.1: *Left*: The Large Millimeter Telescope (LMT) is a 50-m diameter Cassegrain telescope on the Sierra Negra mountain. It has recently been upgraded to its full capability after operating with 32-m since opening in 2011. Image source: INAOE/LMT. *Center*: The TolTEC camera in the UMass Amherst Cryogenic Devices Lab. Image taken during a fit check for the half-wave plate rotator. *Right*: TolTEC's optics bench. TolTEC features three focal plane arrays that can be used to simultaneously image a source in three colours.

mapping speeds between 1.9 to 74.4 $\mathrm{deg}^2/\mathrm{mJy}^2/\mathrm{hour}$. Maximizing the mapping speed not only allows an observer to build up a larger survey by covering larger areas of the sky, but it also minimizes a map's noise, or "depth", level [41]

$$\sigma = \sqrt{\frac{\text{Map Area}}{(\text{Mapping Speed}) \times (\text{Survey Time})}}, \tag{2.1}$$

which is reported in units of mJy. For a given area and integration time, a larger mapping speed will allow one to image fainter targets than before.

2.1 Cryogenics

This section provides overview for the design of TolTEC's cryogenics. For information on cryogenic performance in the laboratory, please refer to §3.2.

---

the white noise in AzTEC's 280 GHz band by $\sqrt{7}$, thus decreasing the mapping speed by a factor of 7 [41]. The larger number in the range is our most optimistic mapping speed without this degradation while the lower value includes the full factor of 7.

Table 2.1: Table reproduced from [41]. TolTEC **design** specifications for the number of detectors, predicted angular resolution, and predicted mapping speed for each of the three bands.

	1.1 mm	1.4 mm	2.0 mm	Units
Number of detectors	4012	2532	1172	
FWHM	5	6.3	9.5	arcsec
Mapping Speed	1.9 – 13.4	3.1 – 22.0	10.5 – 74.4	$\mathrm{deg}^2/\mathrm{mJy}^2/\mathrm{hr}$

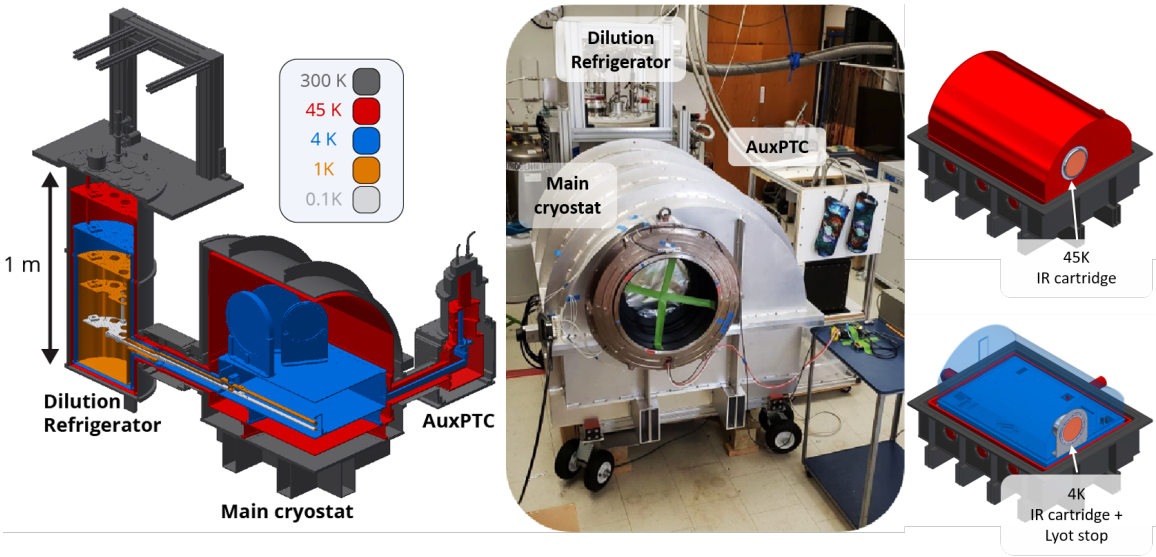

Figure 2.2: *Left*: CAD model of TolTEC and its thermal stages. The two coolest stages reside below the optics bench in the 4 K volume, forming thermal links to the three detector focal planes. *Right*: Photo below the 4 K optics bench showing the thermal busbar paths to the three detector array packages.

2.1.1 Design Overview

TolTEC's design, and large size, was driven by the 30-cm diameter window and the area of the 4 K optics bench (1.3 m x 1.0 m) required to fit the detector arrays plus the optics to create the three bands. These features presented a unique challenge in developing a cryogenic system to handle cooling on the physical scales required. We utilized a nested shell design (see Fig. 2.2) to facilitate modifications and repairs to the system by separating not only the cryogenics into separate parts, but also the

electronic and optical subsystems. Thus, while each subsystem works in tandem, they reside in relative isolation for ease of debugging and making potential modifications.

2.1.2 Thermal Stages

As shown in the left panel of Fig. 2.2, TolTEC is comprised of three cryogenic modules: the main cryostat and two separate cryocoolers. Interior to the room temperature outer vacuum shell (OVS), the camera features four thermal stages established by the cryocoolers: 45 K, 4 K, 1 K, and 0.1 K. The four thermal stages are mechanically constrained by low thermal conductivity links formed from G10 and carbon fiber tubes. The 45 K stage serves to shield the colder stages from the 300 K vacuum shell's radiative loading and to thermalize cables entering and leaving the cryostat. The 4 K stage contains the optics bench and cables traveling from the 45 K stage to the low noise amplifiers and detectors. Lastly, the coldest two stages 1 K and 0.1 K, host the detector shielding, supports, and focal planes.

It is important to note that both the 300 K and 45 K shells are sources of IR photons that can heat the stages interior to them. Therefore, we lower their IR emissivities by polishing them. Polished aluminum can have a room temperature IR emissivity $\lesssim 6\%$; both the 300 K shell interior, the dominant source of IR photons in the system, and the 45 K shell exterior were polished using Atlas Techonologies' proprietary 'Emissivac' process to have a surface roughness $< 0.2\mu m$ [42]. The polished 45 K shell is also surround by 20 layers of multi-layer insulation (MLI) to provide radiative shielding to the inner stage. The relationship between the effective emissivity and the number of MLI layers, n_{MLI}, is given by $\epsilon_{eff} \approx \epsilon_0/n_{MLI}$ where ϵ_0 is the emissivity of the material without MLI.

While the 4 K shell's exterior is not polished, it does feature 10 layers of MLI that scatter any IR photons not absorbed by the shell. Conversely, we selected a blackened interior for the 4 K stage to absorb scattered IR photons that do enter

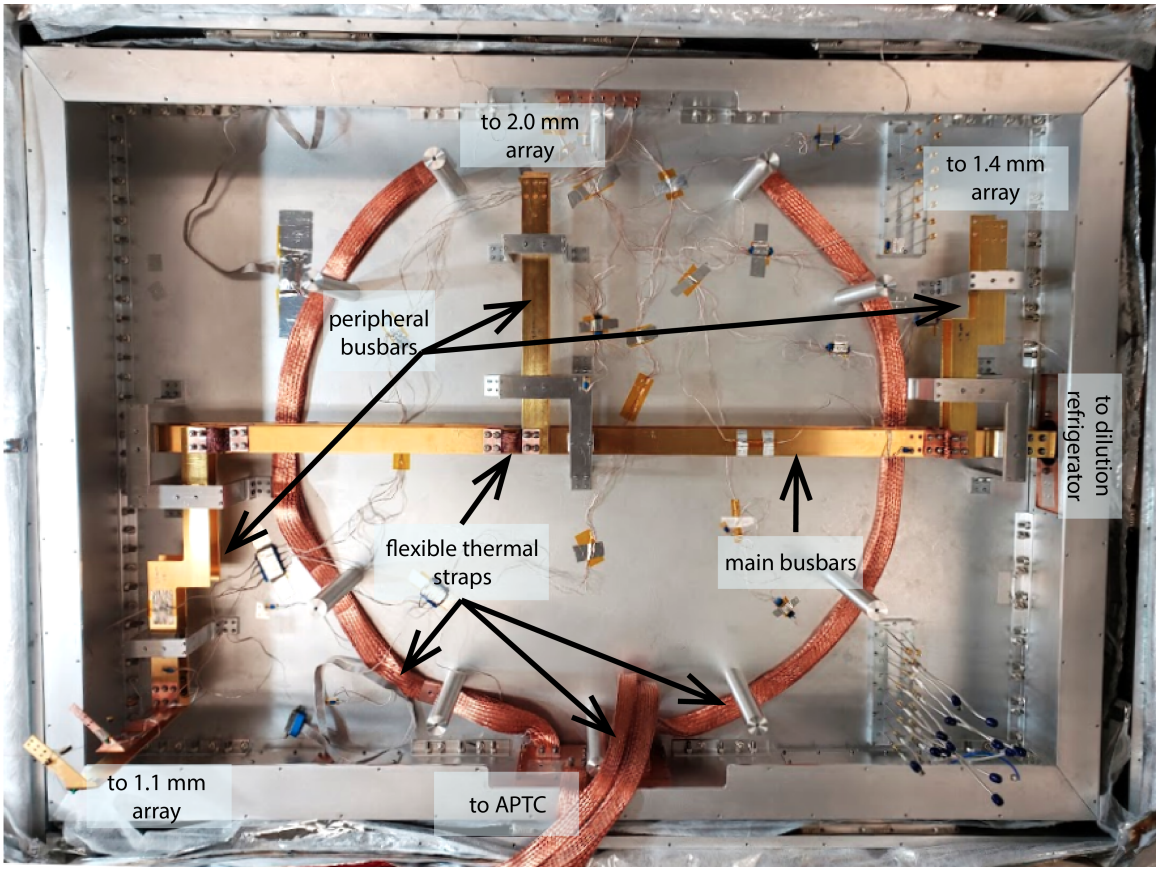

Figure 2.3: In-lab photo of the 1 and 0.1 K thermal busbars and the 4 K custom flexible copper straps below the optics bench. The busbars attach to the back of the detector assemblies above the optics bench. The flexible copper straps below the optics bench reduce thermal gradients across the base of the 4 K stage by providing a more direct thermal path to the APTC. We also attached flexible copper straps to the DF and APTC 4 K plates that connect to locations on the optics bench in order to reduce thermal gradients and offer further cooling for the low noise amplifiers.

the optical volume in order to reduce background optical loading on the detectors. The blackening method we selected was a combination of carbon charcoal cloth and baffling, which we discuss below.

2.1.3 Cryocoolers

We establish the four different stages outlined above through the integration of two separate cryocooler systems. The first is a Cryomech 415 Pulse Tube Cooler, henceforth called the Auxiliary Pulse Tube Cooler (APTC), which is used to cool the

45 and 4 K stages only (also known as Stages 1 and 2). Assisting the APTC in cooling these two stages is an Oxford Triton 2016 Dilution Refrigerator (DR); however, the DR alone provides the heat lift for the two coldest stages (also known as Stages 3 and 4). For information on the operating principles behind the APTC and the DR, please refer to the appendices (§**??**) below.

The two warmer stages, 45 and 4 K, are established with bolted connections between oxygen-free high conductivity copper (OFHC Cu) plates in the main cryostat shells to annealed OFHC Cu cylinders that connect to cold heads/plates in the APTC and DR. The two cooler stages, 1 and 0.1 K, are comprised of parallel sets of annealed, gold-plated OFHC Cu busbars traveling from the detector assemblies (see Fig. 2.3) to the proper cold plates in the DR. Additionally, throughout all four thermal stages, we utilize custom-made copper straps to maintain high thermal conductance across joints while allowing for flexibility of joints during thermal contractions and vibration isolation from the cryocoolers.

2.2 Optics

TolTEC's optics are split into two sections, the warm optics external to the main cryostat and the cold optics internal to it. The warm optics were not utilized for testing until we installed TolTEC at the LMT.

2.2.1 Warm Optics

Coupling the radiation from the sky into TolTEC requires a series of ∼300 K optics. The LMT is a bent Cassegrain telescope and features a 50-m parabolic primary dish (M1), comprised of 180 electroformed nickel panels with a rhodium coating plus actuators to correct the dish shape, and a 2-m hyperbolic secondary mirror (M2) attached to a movable hexapod that allows for focus optimization [43, 44]. Radiation reflected from the secondary will reach a tertiary mirror (M3) stationed just before

the telescope's Cassegrain focus. M3 can be pointed to either side of the receiver cabin to reflect incoming light to different instruments' coupling optics. Additionally, the mirror is attached to a motor that allows it to track the telescope elevation in order to reflect the beam correctly. When pointed towards TolTEC's warm coupling optics, M3 reflects radiation to M4, a parabolic mirror, M5, a flat, and M6, another parabolic mirror [45]. The three mirrors comprising the warm coupling optics were designed at Arizona State University (ASU). All three mirrors are solid aluminum with a polished finish resulting in an emissivity around 1% [41]. The main design principle behind having three separate mirrors was to be able to have multiple degrees of freedom to correct TolTEC's alignment to M2 as well as to condense the optical path within the limited receiver cabin space.

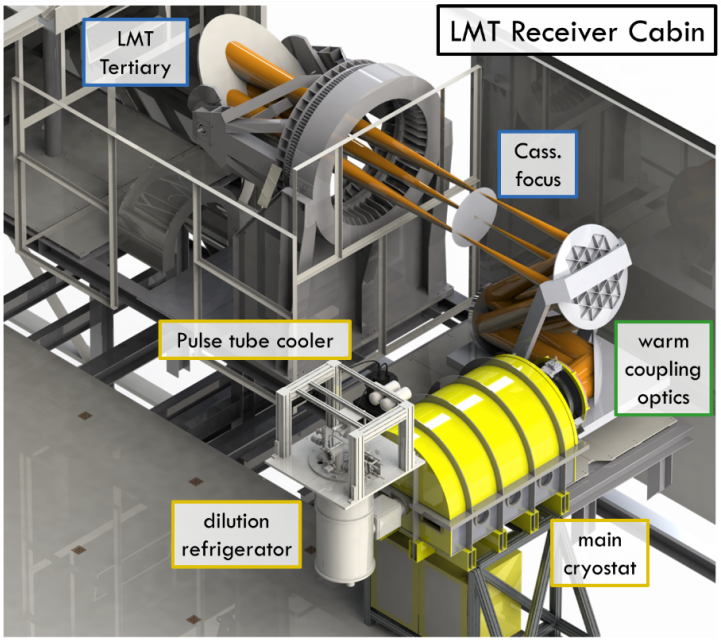

Figure 2.4: CAD model of the LMT receiver cabin including the ASU designed and fabricated TolTEC warm coupling optics. Image credit: E. Castillo.

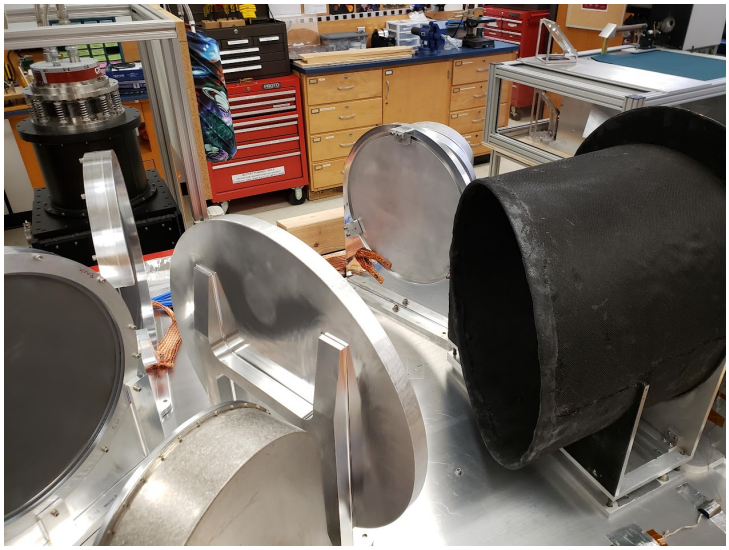

Figure 2.5: The 1 K baffle installed in the main cryostat while testing at the UMass laboratory. The baffle is blackened using a combination of charcoal-imbued cloth and Stycast. Radiation entering the window will be reflected/scattered by aluminum surfaces. In particular, undesired infrared radiation that enters the optical volume shown here will be preferentially absorbed by the baffle's blackened surface.

2.2.2 Cold Optics

2.2.2.1 Filters at 300 and 45 K

The main cryostat features a 30 cm diameter, 3.2 mm thick window made of ultra high molecular weight polyethylene (UHMW PE). Just behind the window is an IR scattering filter from Cardiff University that reflects 95% of any incoming infrared (IR) radiation. Following the 300 K elements is a 45 K filter cassette which acts as a "shader" to further reflect IR radiation from reaching the 4 K volume.

2.2.2.2 Lyot Stop, 1 K Baffle, and Other Radiation Absorption Tactics

The next step in the optics chain is the start of 4 K optics. The first element at this stage is the Lyot stop, which is composed of a four filter cartridge plus an aluminum mount. The four filters include 2 IR blocking filters angled at 20° followed by a pair

Table 2.2: A list of the optics internal to TolTEC's 4 K volume after the Lyot stop with their focal lengths, where applicable, and a description of the element. Under the description, the silicon lenses have their thicknesses provided. DF refers to a dichroic filter and LPE refers to a lowpass edge filter.

Temperature	Element	Focal Length [mm]	Description
1.1 mm path			
4 K	M7	812.10	Elliptical mirror
	DF1	-	Transmit 1.1 mm
	L1	235.27	Convex, d = 220 mm
	L2	-203.30	Concave, d = 160 mm
1 K	LPE	-	Lowpass ν filter, 10.3 cm^{-1}
0.1 K	Feedhorns	-	Beam shaping
	Waveguides	-	Highpass ν filter
1.4 mm path			
4 K	M7	812.10	Elliptical mirror
	DF1	-	Reflect 1.4 and 2.0 mm
	L3	375.15	Convex, d = 320 mm
	DF2	-	Transmit 1.4 mm
	Flat	-	Folding flat
	L4	273.51	Convex, d = 320 mm
1 K	LPE	-	Lowpass ν filter, 8.70 cm^{-1}
0.1 K	Feedhorns	-	Beam shaping
	Waveguides	-	Highpass ν filter
2.0 mm path			
4 K	M7	812.10	Elliptical mirror
	DF1	-	Reflect 1.4 and 2.0 mm
	L3	375.15	Convex, d = 320 mm
	DF2	-	Reflect 2.0 mm
	L5	273.51	Convex, d = 320 mm
1 K	LPE	-	Lowpass ν filter, 5.75 cm^{-1}
0.1 K	Feedhorns	-	Beam shaping
	Waveguides	-	Highpass ν filter

of low-pass filters with cutoffs of 16 cm^{-1} (480 GHz) and 12 cm^{-1} (360 GHz)[3]. The Lyot stop is located at the entrance to the 4 K shell, placing it at an image of the primary mirror.

During in-lab testing, we found that we had sufficient cooling overhead at 1 K to provide additional radiation shielding around the Lyot stop. We added a 28.5 cm long blackened copper baffle on the 1 K stage in order to absorb stray light entering from the window. The Lyot stop baffle was built out of a rolled sheet of copper, then blackened using LOCTITE® Stycast-2850 to attach charcoal-infused cloth to the surface[4]. It is offset from the 4 K optics bench through carbon fiber standoffs to allow for a thermal connection to the 1 K stage. By placing a baffle around the Lyot stop, we provide a large surface area for stray, scattered light to be absorbed long before reaching the detector arrays as well as a lower background loading on the Lyot stop compared to the surrounding 4 K aluminum lid.

In addition to the Lyot stop baffle, we provided more shielding within the detector assemblies. Surrounding the detectors is a 1 K copper support that was initially open on three sides; this design minimized mass, but it allowed scattered light to reach the detectors. By adding a front wall to the copper support, plus a blackened aluminum baffle that surrounds the detector feedhorns, we significantly reduced the background loading on the detector arrays.

The top of the 4 K volume also features a blackened 4 K awning. It is offset from the lid of the 4 K shell by a set of nylon rods, but directly attached to the 4 K copper plate connecting to the DF using a custom-made OFHC copper strap. Since the awning is blackened and approximately the same area as the 4 K shell lid, it provides a large surface area to preferentially absorb scattered light. Using a similar

[3]As a note, filters cutoffs are often reported in wavenumber units of inverse centimeters rather than frequency units of GHz. A rough conversion factor between the two units is 1 cm^{-1} ∼30 GHz.

[4]For cases where we mention that we "blackened" the surface assume that this was done using LOCTITE® Stycast-2850 plus charcoal-infused cloth, unless stated otherwise.

strategy, we added a layer of charcoal-infused cloth over the optics bench to reduce the number of reflective surfaces in the 4 K volume.

2.2.2.3 Beyond the baffle, the path to the focal planes

Following the Lyot stop and baffle is a 4 K elliptical mirror, M7, that directs the light towards the first dichroic filter (DF1) and the 1.1 mm array. DF1 is a high pass filter that reflects only the incoming 1.4 and 2.0 mm radiation allowing the rest through to the 1.1 mm array (see Fig. 2.6).

Splitting off to the 1.1 mm array path, there are two field flattening silicon lenses: the first lens, L1, is a single convex lens and the second lens, L2, is a single concave lens. The 1.4 and 2.0 mm radiation reflected from DF1 then passes through a single convex lens, L3, then is is split by DF2 to form the 1.4 mm and 2.0 mm bands. The 1.4 mm band's optical path has a folding flat in addition to a single convex lens that is identical to that in the 2.0 mm band's optical path. This last lens focuses the radiation onto the detector array, similar to the combined action of L1 and L2 for the 1.1 mm optical path. Each of the five lenses in the system have anti-reflection (AR) coating mechanically etched into the silicon [46]. This is necessary as the silicon lenses have a high index of refraction (n = 3.41), which causes substantial reflections at the surface without the coating present [47]. The design of the mirrors and lenses was handled by ASU and, after fabrication of the lenses by an external company, University of Michigan provided the AR coating on the lenses; the filters, Lyot stop, and dichroics were all provided by Cardiff University [48, 49]. It is important to note that the AR coating varies between the lenses such that L1 and L2 were optimized for the 1.1 mm array, L4 for the 1.4 mm array, and L5 for the 2.0 mm array. L3, tasked with transmitting two bands, has a combined AR coating that handles both the 1.4 and 2.0 mm bands.

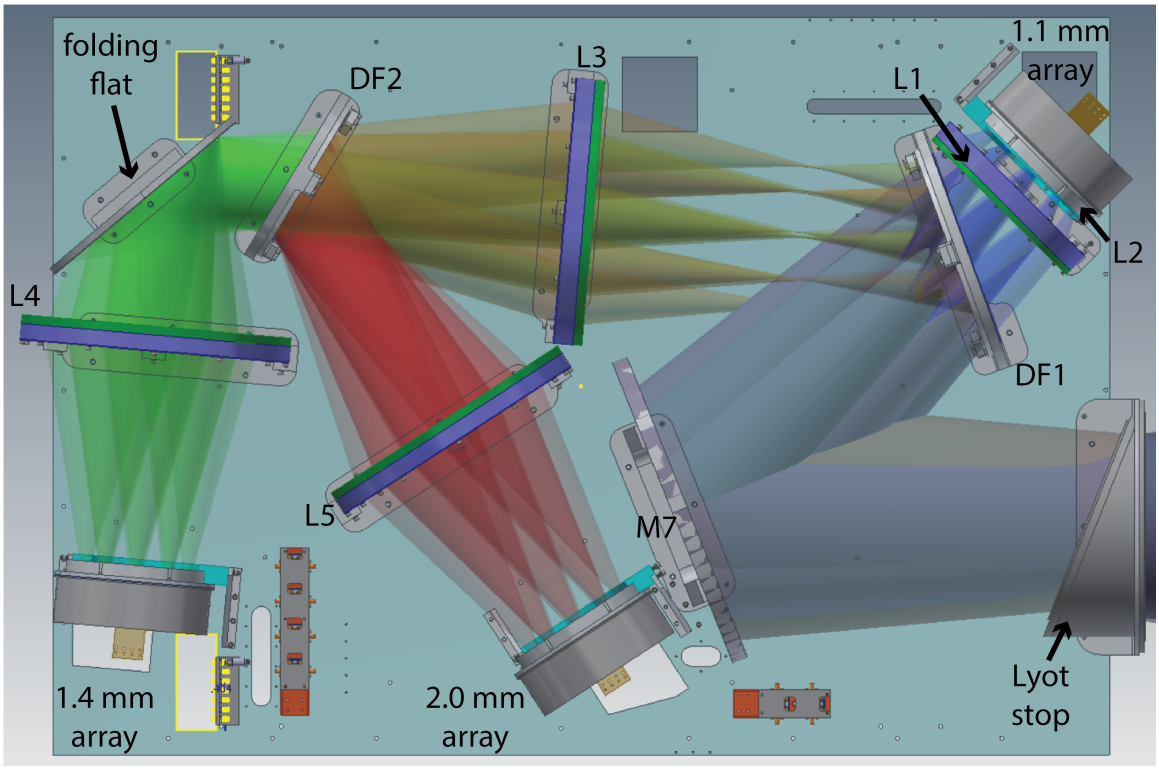

Figure 2.6: CAD model of TolTEC's 4 K optics bench and optical elements, highlighting the path differences between the three bands. The beams shown are from a Zemax model provided by Phil Mauskopf and Emily Lunde at ASU. The beams are separated into their corresponding band where blue is 270 GHz, green is 220 GHz, and red is 150 GHz.

After their respective lenses, at each detector assembly the light must pass through a 1 K lowpass filter (LPE) to arrive at the corrugated feedhorn (FH) array. Each feedhorn array is made of a stack of between 20 to 40 150 mm silicon wafers that have been aligned then coated in copper and gold [39]. Our feedhorns' profiles were designed by Sara Simon and the arrays were fabricated by Jay Austermann's group at NIST [39, 50]. The feedhorn arrays were fabricated from the more expensive silicon rather than aluminum in order to better match the thermal contractions of the feedhorns to the detector array. Other experiments have seen damage to the

detectors due to mismatched contractions bringing the two arrays into contact[5]. A single FH sits above a single detector array pixel, which is a pair of detectors sensitive to orthogonal, linear polarization states (either 0 and 90 degrees or 45 and 135 degrees; see Figure 2.7). Corrugated FHs reduce coupling of undesired Gaussian modes in the incoming light to the detector arrays such that TolTEC couples only to the fundamental Gaussian mode [53, 54], which is characterized by symmetric beams with optical intensity given by [55]

$$I(r, z) = I_0 e^{-2\frac{r^2}{w(z)^2}} \tag{2.2}$$

where r is the distance perpendicular to the beam transmission, z is the distance along the beam's path, and $w(z)$ is the beam radius (distance where the intensity drops to $1/e^2$ of I_0). Between the feedhorns and the detectors is a waveguide array that acts as a highpass frequency filter. In other words, the waveguide array will cutoff around wavelengths larger than the diameter of the waveguide, thus defining the low frequency edge of an array's bandpass.

In §3.3, we further describe the effect of the filters in defining TolTEC's bandpasses using laboratory measurements.

2.3 Detectors

TolTEC hosts three separate superconducting detector arrays, each with their own focal plane. Each array, designed and fabricated at NIST-Boulder, is comprised of Lumped Element Kinetic Inductance Detectors (LEKIDs) which are superconducting thin-film microresonators where the resonator acts as the device's absorber [37–39, 56].

[5]A handy mnemonic to remember which metals contract the most during a cooldown is "Always remember your ABCs" [51]. Going in order from largest contraction to smallest: A for aluminum, B for brass, C for copper, and S for stainless steel. Silicon contracts even less than stainless steel below 120 K, but its coefficient of thermal expansion is positive until that point [52].

As of 2023, TolTEC is one of four ground-based mm-wave cameras[6] to feature LEKID arrays, making it one of the earliest adopters of this technology [35, 57, 58].

Table 2.3: Summary of TolTEC's detector array specifications. A single pixel in TolTEC is two orthogonal detectors with a frequency spacing greater than the median to avoid cross-talk. The NEP at the array reported here is derived from a model assuming a median atmosphere for the LMT at 70° elevation [41]. The responsivity was measured at UMass for the 1.1 and 2.0 mm arrays while the designed 1.4 mm array value is reported here (see §3.3 for details).

Parameters	**Units**	**1.1 mm**	**1.4 mm**	**2.0 mm**
# of networks		7	4	2
Pixel count		2006	1266	586
Pixel spacing	mm	2.75	3.364	4.90
Median frequency spacing	kHz	90	158	390
NEP at the array	$aW/\sqrt{Hz}$	50	70	95
Responsivity	1/pW	0.65e-4	1.17e-4	1.85e-4
Quality factor Q_r	1e3	20	15	15

2.3.1 Motivation for using LEKIDs in TolTEC

For use in mm-wavelength astronomy applications, LEKIDs are a cost-effective, high-yield option. TolTEC selected LEKIDs rather than other detector technologies, such as transition edge sensors (TESes), for three primary reasons. First, LEKIDs are easily multiplexed in the frequency domain. TolTEC's arrays are divided into networks with hundreds of LEKIDs capacitively coupled to a single superconducting transmission line. Each array has a multiplex factor of between 510 to 684 detectors per network read out in a 500 MHz band. Based on design values provided by NIST-Boulder, the designed resonance frequency spacing is on order of $\lesssim 0.5$ MHz (see Table 2.3) [59]. It is worth noting that during fabrication, resonance frequency collisions can occur where resonator dips overlap. NIST-Boulder has demonstrated that these collisions can be reduced through post-process 'editing' of individual detectors [39, 60].

[6]The other three being NIKA, NIKA2, and MUSCAT.

TolTEC did not make these edits and, as a result, has observed resonator frequency collisions on the order of $\sim 5\%$; however, this is an avenue for a future upgrade to the camera. Secondly, LEKIDs are relatively easy to fabricate requiring fewer lithography processing steps (depositions, layer etchings) when compared to TESes (tens of steps including depositions, etches, backetches). Combining their ease of fabrication and multiplexibility, LEKID arrays are straightforward to test and integrate, or 'plug-and-play', when baselining a new instrument. Lastly, the readout circuit for a LEKID array involves minimal cryogenic electronic components compared to TESs. Since each LEKID network has a single transmission line, there are only 13 readout circuits in TolTEC's entire system. Additionally, components in the readout chain, aside from the low noise amplifiers (LNAs), were developed using proven technologies and commercially available products which minimized the amount of new development for the readout electronics subsystem.

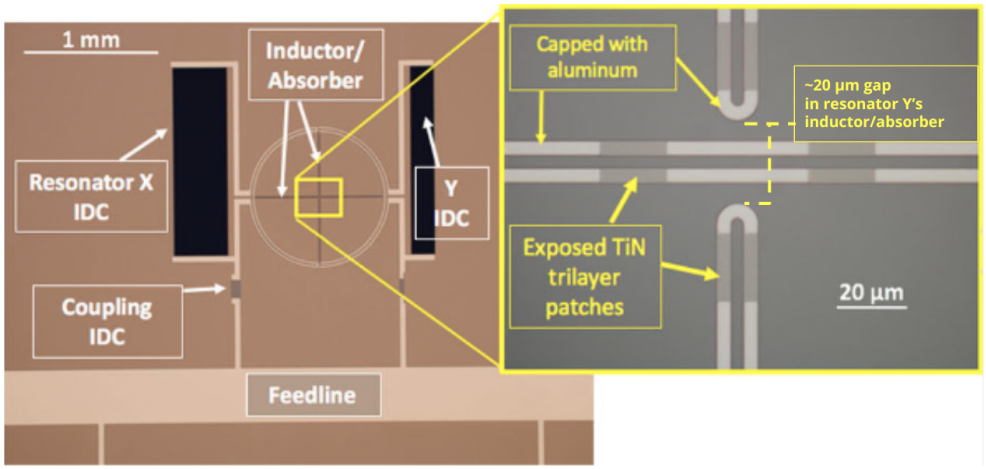

Figure 2.7: Figure reproduced from Austermann et. al. (2018) with additional label to highlight the gap in the LEKID absorber. An image of a single lumped element kinetic inductance detector (LEKID) pixel showing two detectors X and Y with different polarization sensitivities. On the right is a magnification of the center of the absorbing elements. The two detectors do not touch in the center; however, the detector that is split in the middle still performs as a 'lumped' element due to the size of the mm-wave photons ($\geq$ 1.1 mm) compared to the size of the gap ($\sim 20\mu m$).

2.3.2 LEKID Physics

To understand the principles behind LEKID operation, first consider an LC resonator circuit. When an inductor (L) and capacitor (C) are placed in parallel, they form a circuit which will dissipate power with a characteristic resonance frequency ω_0

$$\omega_0 = 2\pi f_0 = \frac{1}{\sqrt{LC}} \tag{2.3}$$

This relationship can be exploited as an astronomical tool by designing a device where changes in optical power predictably affect the device's resonance frequency. Thus if one were to use a superconductor (SC) as both a photon absorber and inductor, one could measure Cooper pair breaking events in response to varying levels of optical power as a change in the inductance, and thus, the circuit's resonance frequency.

According to the Bardeen-Cooper-Schrieffer (BCS) theory of superconducting materials, the ground state of a superconductor at $T < T_C$, where T_C is the superconducting transition temperature, is given by the formation of electron pairs known as Cooper pairs [61]. Once created, Cooper pairs can travel in the superconductor's atomic lattice with no impedance due to their macroscopic wavefunction, thus experiencing no resistance; however, they are not the only charge carriers in a superconducting material. Charge may also be carried by quasiparticles, which are free electrons not bound into Cooper pairs [38, 40]. As the temperature decreases below T_C, so does the number of quasiparticles in the system due to the formation of Cooper pairs.

The main operational principle behind a LEKID is its change in kinetic inductance, and thus complex impedance, as it absorbs photons, breaking Cooper pairs and generating quasiparticles [62]. Kinetic inductance, as compared to geometric inductance, refers to how charge carriers (e.g., Cooper pairs, quasiparticles) will resist changes in current due to their momentum, or stored kinetic energy. For a superconducting metal film, the kinetic inductance is given by [40]

$$L_k = \frac{hR_s}{2\pi^2\Delta}, \tag{2.4}$$

where R_s is the per square resistance of the film (units of $\Omega/\square$) and Δ is the superconducting energy gap determined by the critical temperature of the material. R_s is a function of the material's geometry and resistivity; as the number density of Cooper pairs decrease and the number density of quasiparticles increase, the resistivity increases and thus so does the inductance.

Since both Cooper pairs and quasiparticles act as charge carriers in a superconducting film, one can model the current through the circuit using a two-fluid model such that the total conductivity is given by

$$\sigma = \sigma_1 - i\sigma_2, \tag{2.5}$$

where σ_1 is the conductivity of the quasiparticle path and σ_2 is that of the Cooper pairs. The typical assumption for a superconductor is that $\sigma_2 >> \sigma_1$ (e.g., there is significantly less resistance for the Cooper pairs traversing the material). With this assumption, the surface impedance[7] is then given by [40]

$$Z_s = \frac{1}{\sigma t} \simeq \frac{\sigma_1}{\sigma_2^2 t} + i\omega\left(\frac{1}{\sigma_2 \omega t}\right) = R + i\omega L_k, \tag{2.6}$$

where ω is the circuit resonance frequency and t is the film thickness. However, we do not measure the surface impedance directly when performing readout measurements. What we measure instead is the scattering parameter S_{21} (see §2.4) which is related to the surface impedance by [40]

$$S_{21} = 1 - \frac{1}{1 + 2Z_R/Z_0} \simeq 1 - \frac{Q_r}{Q_c}\frac{1}{1 + 2iQ_r x} \tag{2.7}$$

[7]The surface impedance is a material dependent property and its units are typically reported as $\Omega/\square$. This makes it the preferred impedance reported for thin-film devices such as superconducting detectors.

where Z_R is the impedance of a LEKID capacitively coupled to transmission line, Z_0 is the impedance of the transmission line itself, the Qs are quality factors, and x is the detuning parameter[8]. Z_R depends on the surface impedance of the inductor, the resonator capacitor's impedance, and the coupling capacitor's impedance. The resonator quality factor is given by the capactive quality factor Q_c and the internal quality factor Q_i [56]

$$Q_r^{-1} \equiv Q_c^{-1} + Q_i^{-1}. \tag{2.8}$$

2.3.3 What type of LEKIDs does TolTEC use?

When a photon strikes the superconducting absorber, the minimum energy it must have to break the weakly bound Cooper pair is

$$h\nu_c = 2\Delta, \tag{2.9}$$

where ν_c is the photon frequency and Δ is the superconducing energy gap. From BCS theory, the energy gap for a superconductor is approximately

$$\Delta \approx 1.764 k_B T_C. \tag{2.10}$$

Taken together, this implies that the minimum detectable frequency by a LEKID is

$$\nu_c = \frac{2\Delta}{h} \approx 74\,\mathrm{GHz}\left(\frac{T_C}{1\,\mathrm{K}}\right). \tag{2.11}$$

While T_C is material dependant, there are multiple options for designing LEKIDs for detecting mm-wave photons including aluminum and titanium nitride (TiN) plus

[8]While x is a time dependant quantity related to change in readout voltages I and Q, it can also be related to the readout frequency ω where $x \equiv (\omega - \omega_0)/\omega_0$

titanium (Ti). All of TolTEC's detectors are formed from TiN/Ti/TiN trilayers and are capacitively coupled to their transmission lines.

For a TiN/Ti/TiN trilayer with thicknesses of 4/10/4 nm, as specified for TolTEC's 1.1 mm array, T_C was measured to be 1.4 K resulting in a minimum detectable frequency of $\nu_c \approx 100$ GHz [39, 40]. Titanium has a $T_C = 0.4$ K while TiN has $T_C = 5$ K [63]; by layering the two materials, the device's T_C could be achieved with the proximity effect. For a bilayer of a normal metal and a superconductor, the transition temperature T_C as function of film thickness can be approximated using Usadel theory[9] [65]

$$T_C = T_{C0}\left[\frac{d_s}{d_0}\frac{1}{1.13(1+1/\alpha)}\frac{1}{t}\right]^{\alpha}\frac{1}{d_0} = \frac{\pi}{2}k_B T_{C0}\lambda_f^2 n_s \alpha = \frac{d_n n_n}{d_s n_s} \tag{2.12}$$

where T_{C0} is the transition temperature of the bare superconductor[10], d_n and d_s are the thicknesses of the normal and superconducting films, n_n and n_s are the density of electronic states in the films, λ_f is the Fermi wavelength, and t is the transmission factor. In general, this equation predicts that as the thickness of the superconducting film increases (or the thickness of the normal film decreases), the stack will approach the superconductor's bulk transition temperature. As the thickness decreases, the stack's transition temperature will decrease; in the case of TiN/Ti stacks, T_C can go below that of the Ti film [66].

In order to detect photons down to ν_c, the background thermal noise (due to thermal excitations that may break Cooper pairs) must be minimized by operating the system well below the superconducting transition temperature, T_C, of the array. A focal plane temperature of $T_C/10$ is found to be sufficient to reach this limit

[9]Usadel theory is an expansion of BCS superconductor theory by including the assumption that charge carriers in the superconductor have diffusive motion (as in they move from areas of high concentration to ones with lower concentration) [64].

[10]For this case, since TiN has the higher transition temperature in the stack, it acts as the superconductor while Ti acts as the normal metal despite both being superconductors.

[56]. Thus for TolTEC, the LEKID arrays have a preferred maximum operation temperature of T_{max} ∼140 mK for the lowest possible detector noise. As will be discussed in §4, at the LMT we do operate at about 40 mK hotter than T_{max}.

It is worth noting here that for TolTEC's LEKID arrays, NIST-Boulder noted the need for an additional layer to the TiN/Ti/TiN trilayer absorber. While the standard geometric design (thickness and 2D filling space) was able to accomplish primary goals such as appropriate transition temperature to observe desired photon band, satisfactory polarization efficiency (less than 4% cross-polar leakage), and desired detector responsivity, there was the matter of optimal radiation impedance matching [39]. This last point was accomplished with the addition of a 100 nm thick by 25μm long strips of aluminum (e.g., the aluminum caps seen in Fig 2.7) that acts as a short (aluminum has lower sheet resistance and inductance than the trilayer) to the absorber for the incoming radiation. The addition of a superconductive short to the existing SC layers may reduce the responsivity if the short material has lower gap energy (such as aluminum compared to TiN/Ti/TiN) as quasiparticles will diffuse from the higher gap energy material to the lower, thus lowering the quasiparticle density in the intended absorber material. NIST-Boulder showed that this effect would be negligible for the TolTEC detector sensitivities when testing the 1.1 mm array and, as described in the following chapter, our detectors do meet the desired specifications when measured in the lab [39].

2.3.4 Sources of detector noise

Prior to discussing TolTEC's readout method, it is worth noting that LEKIDs have three primary noise sources intrinsic to the superconductor: two level system (TLS) noise, quasiparticle generation noise, and quasiparticle recombination noise. TLS noise is due to impurities in the films used to make the detectors. These impurities are amorphous oxides which contain multiple two level systems (e.g., two different

energy states) [67]. As such, these systems have a dipole moment that can interact with the resonator, creating a dielectric. As the populations of these systems vary, so does the dielectric and thus the amount of energy dissipated through the coupling of the resonator to these TLSs.

Quasiparticle (QP) generation and recombination noise occur due to fluctuations in the relative populations of the Cooper pairs and quasiparticles [56]. At a given temperature with some background optical power, the number of Cooper pairs and QPs are in dynamic equilibrium. When a Cooper pair is broken, due to thermal fluctuations in the system, two QPs are generated. The QPs can reform into Cooper pairs with other QPs, with some recombination time, releasing energy in the form of a phonon. The QP generation/recombination noise is governed by the random fluctuations in the population numbers of these two charge carriers. If the population of QPs randomly changes, this introduces fluctuations to the inductance, which introduces noise to the measurement.

For typical TiN detector arrays, the intrinsic detector noise has been measured to be $\lesssim 0.4$ aW/$\sqrt{\text{Hz}}$ [38]. At the LMT, we predict the photon noise will be 100 aW/$\sqrt{\text{Hz}}$ at 270 GHz [41]. As such, the detector noise is designed to not be the limiting noise in the system. Combined with detector readout noise on the order of the intrinsic detector noise, the system should be background noise limited (e.g., following the design principles of background limited photometry, or BLIP).

2.4 Detector Readout

In this section, we begin by reviewing the components comprising the readout chain, then describe the procedure to obtain data from the detector arrays. For details of the in-lab performance of TolTEC's detector readout, please refer to §3.5.

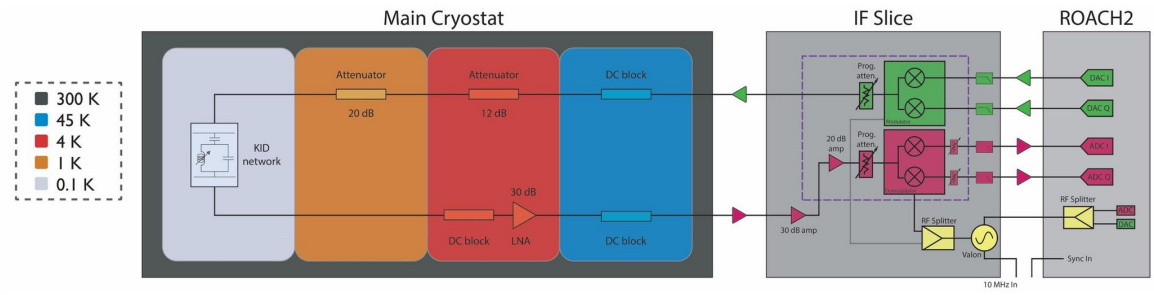

Figure 2.8: A schematic of the radio frequency (RF) signal chain for a single detector network. On one transmission line, there are >500 KIDs coupled for readout.

2.4.1 Design Overview

To readout all of TolTEC's 7716 detectors requires only 13 readout lines. Unlike AzTEC's bolometer arrays, which required a 1:1 detector-readout ratio, TolTEC's LEKID arrays naturally lend themselves to multiplexing through the use of frequency combs generated by the readout electronics to probe resonances on a transmission line. A schematic of a single readout chain is shown in Figure 2.8. Because of the frequencies required to readout the detectors (between $\sim$ 400 and 900 MHz), we perform our readout using radio frequency (RF) hardware.

The detector readout components were developed in collaboration with ASU and another group at UMass. ASU handled the warm electronics including the ROACH2 computers that interface to TolTEC's analysis computers, basing it off of designs for BLAST-TNG [68, 69]. At UMass, Joe Bardin, Mohsen Hosseini, and Wei-Ting Wong developed the cryogenic low noise amplifiers (LNAs) which amplify the signal outgoing from the detector arrays to the warm electronics external to the cryostat [70].

2.4.1.1 Cabling, attenuators, and DC blocks

TolTEC uses two forms of RF transmission lines to carry probe tones and detector signals: (1) stainless steel (SS) semi-flexible cables custom manufactured by ASU; and (2) copper (Cu) hand-formable cables purchased from Mini-Circuits®. Both types

of cables were selected for their low loss ($\lesssim$ 1dB) at the readout frequencies between 400 and 1000 MHz. Additionally, for the attenuators and DC blocks, we selected commercially available parts from Mini-Circuits® and Mouser Electronics®. As will be described in §3.5, fabrication inconsistencies and thermal cycling have lead to issues with lower than expected gain in some of the readout chains.

The SS cables were selected to be used between thermal joints since they have low thermal conductivity. In these locations, the cables will undergo mechanical stress due to thermal contractions. To prevent the cables from experiencing excessive stress, and thus mechanical or electrical failures, we bent the cables into L-shapes and loops (see Fig. 2.9). We found that during the early stages of laboratory testing, a small percentage of the SS cables failed, resulting higher transmission losses. This is not surprising considering the number of SS cables in the system; across the 13 networks, there are 104 SS cables. There was a hypothesis that, due to repeated thermal cycling, the solder between the cable and its connector could weaken and fail. There was evidence of the solder developing cracks over time, but this was only ever at the highest mechanical stress joints, such as between the 1 and 0.1 K stages inside the detector array packages. We have no other evidence that well performing cables would fail with repeated thermal cycling and the failures were likely due to assembly error.

2.4.1.2 Low Noise Amplifiers

TolTEC's cryogenic low noise amplifiers (LNAs) were developed by Joseph Bardin and his group at UMass Amherst[11] . The LNAs were designed to provide 30 dB of gain between 400 and 1200 MHz [70]. The LNAs are two stage rather than single

[11]Dr. Bardin is a faculty member in the Department of Electrical and Computer Engineering. TolTEC's LNAs and their biasing were part of his student Dr. Mohsen Hosseini's thesis (see Chapter 5 of Dr. Hosseini's thesis).

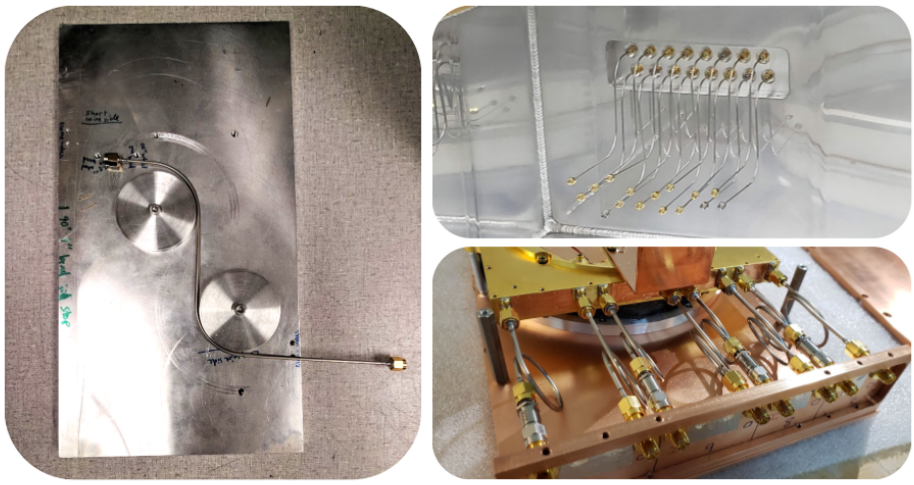

Figure 2.9: *Left*: Stainless steel cable being bent in aluminum bending jig. *Right, top*: Cables with the same wave bend as the left picture installed in the cryostat between the 300 K and 45 K stages. *Right, bottom*: Cables with a loop bend installed in the 1.4 mm detector assembly.

which provides higher control when biasing the amplifiers to adjust the gain provided to the readout chain.

We use a 7 V DC power supply unit (PSU) which is then split into two separate voltage sources for the 1.1 mm array's LNAs and the 1.4 and 2.0 mm arrays' LNAs. There is one LNA per network, so 7 LNAs for the 1.1 mm array and 4 plus 2 LNAs for the 1.4 and 2.0 mm arrays, respectively. The 1.1 mm array has its own bias board while the 1.4 and 2.0 mm arrays share a bias board. Each board has 8 channels, each with two stages, and one can adjust the voltage at three locations per stage (see Fig. 7.7) using the on-board variable resistors. Since there are 16 total bias channels across the two boards, we have spare 3 channels inside the cryostat.

Each bias board connects to their breakout board inside the cryostat with a custom, vacuum-tight Tekdata LTD MDM-100-pin cable. The cable is heat-sunk at the 45 K and 4 K stages with an OFHC Cu mount filled with Stycast-2850 to keep each stage light-tight. After entering the 4 K base, the cable attaches to a 4 K breakout

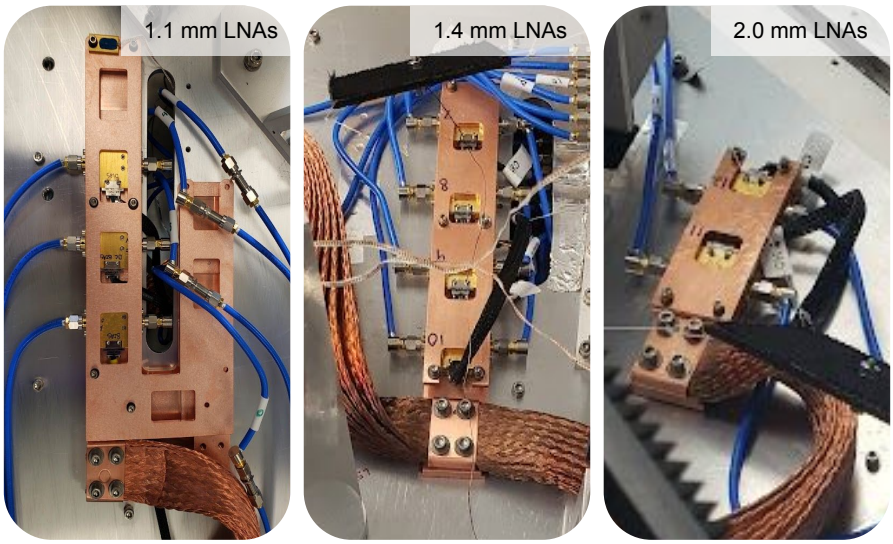

Figure 2.10: The three oxygen-free high-conductivity copper (OFHC Cu) clamps for the low noise amplifiers (LNAs). Each clamp is also connected to a custom copper strap manufactured in the UMass TolTEC laboratory (see Chap. 3 for more details on the copper strap process).

board mounted to the underside of the optics bench using aluminum standoffs. On each breakout board there are again 8 channels that can provide power to an LNA through an MDM-9 to Nano-D9 cable. To minimize chances that the MDM-9 side of the cables will break, they have been potted using Stycast-2850.

All of the LNAs are heat-sunk to the 4 K stage with a custom OFHC Cu stand (plus a thin layer of Apiezon® N Grease) that clamps the LNAs for a single array (see Fig. 2.10). One of the special features of TolTEC's LNAs are that, per LNA, they were designed to dissipate low power, below 7 mW [70]. For 13 LNAs, the total power would be less than 0.1 W which is $\lesssim$5% of the total cooling power offered at the 4 K stage. As discussed in Chapter 3, additional steps to counter the heat load from the LNAs were required to reach TolTEC's designed base temperatures.

2.4.1.3 ROACH2 and IF slices

Located outside of the cryostat are the warm readout electronics. Each of the 13 networks has its own dedicated set of electronics comprised of a ROACH2 computer with an intermediate frequency (IF) slice. The ROACH2 produces the frequency comb which is then modulated by the IF slice to the detector resonance frequency band. The IF slice also adjusts the outgoing and incoming signal's power level using separately programmable attenuators (can be set between 0 to 30 dB). Signals entering the detector are called *drive* signals while those leaving the detector are *sense* signals.

For a more detailed discussion of the componets used for TolTEC's ROACH2 and IF slices, please refer to Gordon+16 which describes a similar system in the context of BLAST-TNG [68].

2.4.2 Reading out a single detector

While TolTEC only operates in this mode for testing, for conceptual clarity it is worth walking through the process to read out a single resonator.

Let us imagine we have a KID resonator with some constant optical loading and, as a result, a resonance frequency of 500 MHz. Knowing the detector's resonance frequency, we first generate a probe tone at 500 MHz on the instrument control computer, or clip, that is then passed to the ROACH2. Onboard the ROACH2 is a 16-bit, 1000 MSample/s digital-to-analog converter (DAC) that produces a time-dependent voltage signal from the tone [68]. This voltage signal is given by the in-phase (I) and quadrature (Q), or I/Q, components

$$I(t) = V_0 \cos(\omega t) \tag{2.13}$$

$$Q(t) = V_0 \sin(\omega t) \tag{2.14}$$

where V_0 is the signal amplitude and ω is the signal's frequency. Note that there are two DACs in a single ROACH2 (one for each I/Q component) and that, at this

stage, we are operating at frequencies between (-240, 240) MHz (also known as the *baseband*). Additionally, the I/Q signals can be related back to the amplitude and phase of the transmission signal $|S_{21}|$, given by

$$|S_{21}| = \sqrt{I(t)^2 + Q(t)^2}, \tag{2.15}$$

$$\phi(t) = \tan^{-1}\left(\frac{Q(t)}{I(t)}\right). \tag{2.16}$$

With this relationship, we can probe a resonator and measure shifts in the resonance due to changing optical power by tracking the amplitude and phase of the transmission signal.

Leaving the DACs in the ROACH2 and moving into the IF slice, the I/Q signal is modulated from the baseband to an RF signal at the resonator frequency using an IQ mixer. This step depends on a user-selected local oscillating (LO) frequency. For instance, if our baseband frequency is -200 MHz and we set our LO frequency to 700 MHz, we obtain the desired 500 MHz probe tone. Mixing this signal creates a pair of upper side band and lower side band frequencies; however, the IF slice has a highpass filter to only permit the upper side band to the next step in the readout chain. The final step before our probe tone exits the IF slice is to set the programmable attenuator value. Typical drive attenuation values range from 10 to 20 dB. Our probe tone signal now leaves the IF slice and enters the cryostat.

Moving through the cryostat to the detector array, we first pass through a SS coax cable from 300 K to 45 K. At the entrance to the 45 K stage is a DC block to reduce conductive power from 300 K. The signal next passes through 45 K SS coax cable that is connected to the 4 K stage with a flexible copper coax cable. At the entrance to the 4 K stage, there is another DC block. From there, we follow the signal through a 1.5 m copper coax cable under the optics bench to a bracket below the detector

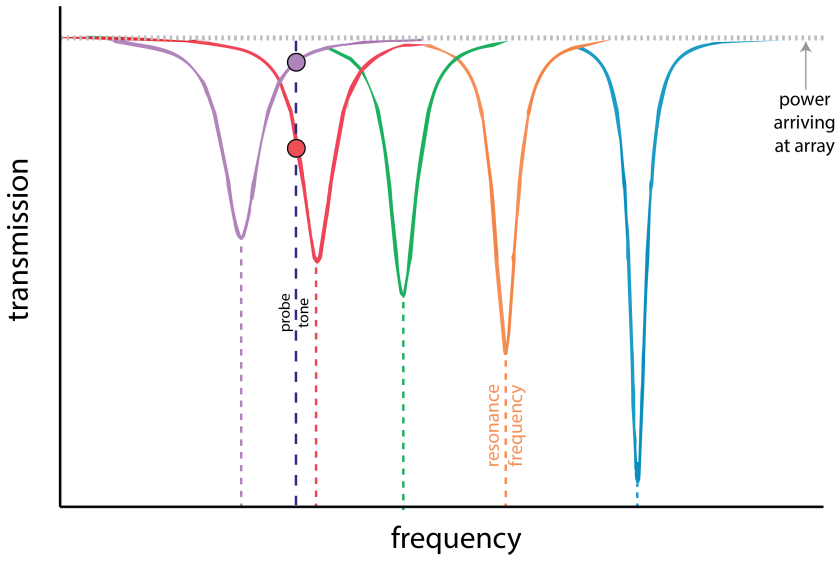

Figure 2.11: A cartoon of how a single detector's transmission (S_{21}) response changes with increasing optical loading. As the optical power incident on the detector increases, the resonance frequency decreases. For a given amount of optical loading, the resonance frequency on the dip is shown by the dashed line pointing to the lowest part of the dip. The amplitude and phase of the resonance dip also changes, which can be traced by measuring the transmission at a probe tone. The dashed line at the top of the figure indicates the readout power that reaches the detector array from the readout electronics after passing through the cold SMA cables, DC blocks, and attenuators (see Fig. 2.8 for details on the layout).

array. At this joint, the signal passes through a 4 K 12 dB attenuator followed by another SS coax cable before entering the detector array package.

Arriving at the detector array package, the probe tone signal's power is reduced again by a 1 K 20 dB attenuator. From the attenuator, the signal passes through one more SS coax cable before reaching the transmission line on the 0.1 K detector array. So, a signal exiting the IF slice with a drive power of -60 dBm will arrive at the array attenuated down to approximately -90 dBm, by design. At the array, if there is a detector with a resonance dip at a similar frequency, our example 500 MHz probe tone signal will lose power depending on where it falls within the dip (see Fig. 2.11). At the deepest point in the dip, this loss will between 2 to 5 dB depending on the detector array. As stated previously, the detector's resonant frequency depends on

the amount of optical loading incident on the device. For this well-known, constant resonance frequency case, our probe tone would be centered at the deepest point in the resonance dip.

Now altered by the detector's transfer function the probe tone signal exits the array and passes through a 1 K SS coax cable, a 4 K SS coax cable, and a 4 K DC block. From the DC block, the signal passes through a flexible copper coax cable to be amplified by the LNAs (about 30 dB in gain) on top of the optics bench. From the LNAs, the signal travels through another copper coax cable, repeats the inverse of its incoming path (4 K copper coax cable, 45 K SS cable, 45 K DC block, and 300 K SS cable), then returns to the IF slice. Once at the IF slice, the signal is amplified by a 30 dB amplifier, then a 20 dB amplifier. The RF signal passes through the programmable sense attenuator before being demodulated back down to I/Q signals in the baseband. Finally the I/Q signals are filtered, then passed to a 12 bit, 550 MSample/s analog-to-digital converter (ADC) in the ROACH2 where the signals associated with that particular tone frequency are output to be collected by the instrument control computers (known as "clips") [68].

2.4.3 Reading out multiple detectors

In the previous section, we read out a single detector with a well-known, constant resonance frequency. When scaling up to reading out multiple detectors the readout path does not change, but the resonance frequencies will vary over time due to changes in the optical loading (not only from a source, but also from the background). Therefore, to read out all the resonators simultaneously first requires a sweep in frequency space to identify where to place the probe tones. Once we identify the frequencies to probe, ideally the center of the resonator prior to observing a source, we can then generate a 'frequency comb' that is a superposition of δ functions in frequency space.

Since the readout method for each network is identical, we will describe the method for a single network.

To perform the readout of a single network, we use a single probe tone for each detector that is first selected by finding resonances when the system does not have loading from the source of interest. As stated before, the probe tones are sent to the detectors as a comb of δ functions with the desired test frequencies. After doing an initial, coarse sweep of the readout frequency space to find detector candidates that respond to the probe tones, we perform a much finer frequency sweep around the candidate tones. These sweeps are respectively known as vector network analyzer (VNA) sweeps and target sweeps. As the optical loading on the detector changes, the resonance frequency shift is estimated with the 'detuning' parameter

$$x = \frac{\delta f}{f} = \frac{f_{probe} - f_r(P_{opt})}{f_r(P_{opt})}, \tag{2.17}$$

where f_r is the value of the resonance frequency, f_{probe} is the frequency at which we measure the transmission, and P_{opt} is the optical loading at the detector [71].

To measure x, we use the S_{21} element of the readout line's scattering matrix S. For a line with a single input and output port, we can use the 2-port model such that S_{21} tells us the transmission from port 1 to port 2. This parameter is defined by an a real, in-phase (I) component and an imaginary, quadrature (Q) component (not to be confused with the resonator quality factor Q_r)

$$S_{21}^* = I + iQ \tag{2.18}$$

where Q exits port 2 with its phase shifted by 90° while I remains unchanged. TolTEC measures I and Q values as a function of time at a user selected sampling rate between 122.07031 Hz and 488.28124 Hz. Ultimately, S_{21} is related to the value of the detuning

factor, x, with factors related to the intrinsic quality of the detectors and the materials used to make them. The equation[12] describing the relationship is [71]

$$S_{21}^{*} = \frac{Q_r}{1 + 2iQ_r x} \tag{2.19}$$

where Q_r is the resonance quality factor and the magnitude of this function is then given by

$$|S_{21}|^2 = S_{21}S_{21}^{*} = \frac{Q_r^2}{1 + (2Q_r x)^2} \tag{2.20}$$

where S_{21}^{*} is the complex conjugate of S_{21}. The previous equation describes a Lorentzian profile centered on the resonance frequency with a FWHM of f_r/Q_r. This allows measurements of the optical loading at the detectors, as a function of time, with changes in the resonance frequency, or equivalently changes in the detuning parameter. To this end, we may calculate $x(t)$ using measured $I(t)$ and $Q(t)$ values

$$x(t) = -\frac{1}{2}\frac{Q}{I^2 + Q^2}. \tag{2.21}$$

The detuning parameter is related to the optical power by a calibration function

$$P_{opt}(t) = \mathcal{P}(x(t)), \tag{2.22}$$

which can be written as

$$\delta P = \frac{x - x_0}{R} = \frac{\delta x}{R} \tag{2.23}$$

where x_0 is the detuning parameter at the background level (e.g., no additional optical power incident on the detectors, resonance frequency is $f_{r,0}$) and the responsivity

[12]The attentive reader will notice that Eqn. 2.19 does not match the previously defined Eqn. 2.7 of presumably the same quantity. For ease of fitting, one can multiply S_{21} by -1 then add 1 such that the function peaks rather than dips at its characteristic frequency ω_0. We also assume that $Q_c = 1$, thus we get Eqn. 2.19 from 2.7.

$R \equiv -\frac{1}{f_{r,0}}\frac{df}{dP}$ [71]. The responsivity is the ratio for a unit change in the detuning parameter given a unit change in optical loading. Note that the optical power incident on the array is linearly dependant on the detuning parameter since the responsivity is constant. This linear response is a significant motivator for utilizing KIDs in astronomy. A description of laboratory responsivity measurements for the 1.1 and 2.0 mm arrays at UMass is provided in Chapter 3.

CHAPTER 3

LABORATORY TESTING

> *"Gideon the Ninth, first flower of my House," she said hoarsely, "you are the greatest cavalier we have ever produced. You are our triumph. The best of all of us. It has been my privilege to be your necromancer."*
>
> Tasmyn Muir, Gideon the Ninth

In Chapter 2, we reviewed the design and layout of the instrument and its subsystems. We now turn to the details of the instrument integration and performance while operating at UMass Amherst. In the following Chapter 4, we will cover the performance during commissioning at the Large Millimeter Telescope.

3.1 Timeline for lab testing at UMass

By May 2021, we had completed 23 runs with all four thermal stages. Between February 2020 and May 2021, we had run the system with its full complement of detectors and readout electronics. The system was completely integrated, tested, and characterized prior to shipping to the LMT. For an overview of major events in TolTEC's hardware development, refer to Figure 3.1.

One of the most critical testing periods was in Summer 2019, TolTEC performed tests using the 1.1 mm array including, but not limited to, microphonics and applied magnetic field testing. Shortly after, in October 2019, we integrated the 2.0 mm array and performed dark testing with two arrays installed. The detector integration was completed with the installation of the 1.4 mm detector array in January 2020. We

began full system testing with plans to finish in lab testing that year; however, the COVID-19 pandemic halted our lab's operation between March and June 2020. One effect of this delay was the discovery of an issue with our dichroic filters' thermal contraction. We concluded our testing at UMass in June 2021, shipping the camera to Mexico in August 2021.

3.2 Cryogenics

The following section has been adapted from DeNigris et. al. (2020) [72].

Here we present the characterization of the system's cryogenic performance. TolTEC's design, and consequentially large size, was driven by its 300 mm diameter window and the area of its 4 K optics bench (1.3 m by 1.0 m), required in order to establish three simultaneously illuminated focal planes. The three focal planes are superconducting detector arrays that must be operated below 200 mK. Therefore, ensuring that the system can consistently reach these base temperatures is one of the first steps in constructing the system.

We begin this section by describing the model we used to design the cryogenic system, then walk through the tests we did to confirm its performance.

3.2.1 Modeling TolTEC cryogenic performance

The TolTEC thermal model was written in Python as a set of object-oriented libraries to be used in the design of a cryogenic system. It considers the four stages' temperatures and physical parameters, such as the materials and geometric properties. The typical work flow of the model is:

1. use material properties and desired stage cold head temperatures to estimate the total heat loading on the system

2. choose a test geometry to use in the model; determine the location and type of joints for test structure

Figure 3.1: A graphic summarizing TolTEC's hardware development and installation at the telescope.

3. use the estimated loading to calculate thermal gradients in the system for given geometries and joints in each stage

4. refine the test geometry until within desired specifications

For the design of TolTEC, there are two main libraries: (1) a `material` library with physical properties of typical cryogenic and construction materials; and (2) a `stage` library to model the four thermal stages of the system. The first library includes materials common to a cryogenic system such as Aluminum-6061 (Al-6061) and oxygen-free high conductivity copper (OFHC Cu); however, it also contains properties of support materials such as fiberglass laminate G10 sheets and carbon fiber cylinders, as well as characteristics of the stainless steel (SS) coax cables in our system. Each class in the materials library allows the user to set the cross-sectional area and length of the part, then calculates its mass, enthalphy, and conductivity. To calculate the conductivities, we used the empirical equations determined by NIST for most materials between 300 and 4 K [73]. Below 4 K, we approximate the conductivity as a linear dependence on temperature when considering either Al-6061 or OFHC Cu.

After generating the materials library, we model each of the four stages using separate Python classes. Within each `stage` we consider the radiative and conductive loading assuming a cold head temperature which, in the case of the reported model values, are the designed stage temperatures 45, 4, 1, 0.1 K. For the radiative loading, we calculate the blackbody emission onto the stage from its warmer surrounding shell. The emissivity selected for this calculation is 10%, which is used as an upper limit for Stages 1 (45 K) and 2's (4 K) polished Al shells. As for the conductive loading, we include the heat from G10 and carbon fiber supports, the conduction through the coaxial cables, LNA wiring and thermometry, and the power dissipated from the readout cabling. Additional sources of loading can easily be added to the stage classes by creating a function for each source of loading. For instance, at Stage 2 we heat sink the low-noise amplifiers (LNAs) used for detector readout; the LNAs generate

$\sim$90 mW of conductive loading on the stage and require a bias current for power, which contributes to both Stage 1 and 2's conductive loading through the wiring to the power supply external to the cryostat [70]. In Table 3.1, the modeled loading from the LNAs is included under the coax cables column for Stage 2.

Stage	Supports	Coax cables	Radiative Loading	Total Load	Cooling Power
45K	2.37 W	0.68 W	15.9 W	19 W	40 W (APTC) + 10 W (DR)
4K	0.16 W	0.03 W	0.01 W	0.2 W	1 W (APTC) + 1 W (DR)
1K	1.25 mW	1.16 mW	0.51 μW	2.1 mW	$\leq$ 50 mW
0.1K	41.1 μW	11.7 μW	0.51 μW	53.8 μW	450 μW

Table 3.1: Table of modeled heat loading and estimated cooling power. For a given thermal stage, we use our thermal model to estimate the total heat load on the system through conduction and radiation. We first consider the loading from mechanical supports (G10 and, for 1 and 0.1 K, G10 + carbon fiber), and conduction from the coax cables. We then estimate the background radiation for each stage from the surrounding stages. The cooling powers from the APTC and/or the DR are shown in the rightmost column. The DR cooling power for each stage was characterized by Oxford Instruments.

Using the model outlined above, we were able to estimate the total radiative and conductive loading for each of TolTEC's four stages. One core assumption when applying the model is that the temperatures used to calculate the background radiation and thermal conductances are the desired stage temperatures. Another key assumption is that the model has three detector arrays installed with all of their readout cabling integrated plus LNAs in use. The loading from having three arrays only becomes a dominant factor when comparing the model to the measured values for Stages 3 and 4. With these assumptions, we were able to estimate the heat loading on the system within a factor of 3 at the coldest stages for the first round of measurements with only one detector array installed.

3.2.2 Utilizing the model to build the 1 and 0.1 K Stages

Having constrained the models to keep the heat loading below 60% of the total cooling power provided by the PTC and the DR, we then calculate thermal gradients

across different geometries of connections. The thermal gradient for heat loading due to conduction is

$$P = \frac{A}{L}\int_{T_{low}}^{T_{high}} k(T)dT$$

where P is the heat loading in Watts, A is the cross sectional area of the busbar, L is the length, and k(T) is the temperature dependent thermal conductivity of the material providing the conduction. At $T < 1K$ the functional form of k(T) can be written as

$$k(T) = \alpha T^2$$

where α is a coefficient dependant on the quality of the material [74]. For OFHC Cu, when annealed, $\alpha = 600$ W m^{-1} K^{-2}; however, when OFHC Cu is not annealed, $\alpha = 180$ W m^{-1} K^{-2}[75]. Integrating and solving for T_{high} in the heat loading equation, we obtain a function to find the hot end temperature across any busbar geometry

$$T_{high} = \sqrt{\frac{PL}{A}\left(\frac{\alpha}{2}\right)^{-1} + T_{low}^2}.$$

For a given T_{low}, we can reduce the thermal gradient $\Delta T = T_{high} - T_{low}$ by increasing the cross-sectional area of the busbar, decreasing its length, or increasing its quality (through α). We were constrained in choosing the central busbar's length by the locations of the detector arrays on the optics bench, having to make the bar at least 1.3 m long in order to reach the 1.1 mm array. The next constraint was a side effect of the length requirement: most companies that offer vacuum annealing of OFHC Cu can only work with pieces less than 0.80 m, thus we were restricted to an $\alpha = 180$ W m^{-1} K^{-2}. With these two limitations, we were then only allowed to optimize the cross-section of the central bar. It is easiest to purchase a bar of OFHC Cu by knowing the bar's desired thickness (e.g., 3.18 mm, 6.35 mm, etc.), so after choosing a width of 38.1 mm for the bar, we ran our model with different thicknesses selected from the available options. Table 3.2 summarizes three central bar thickness simulated using

Stage 3						
Length [m]	Width [mm]	Thickness [mm]	Mass [kg]	$T_{1.1}$ [K]	$T_{2.0}$ [K]	$T_{1.4}$ [K]
1.32	38.1	3.18	1.42	1.10	1.08	1.04
-	-	**6.35**	2.83	1.05	1.04	1.02
-	-	12.7	5.66	1.03	1.02	1.01
Stage 4						
Length [m]	Width [mm]	Thickness [mm]	Mass [kg]	$T_{1.1}$ [K]	$T_{2.0}$ [K]	$T_{1.4}$ [K]
1.32	38.1	3.18	1.42	122	120	110
-	-	**6.35**	2.83	111	110	105
-	-	12.7	5.66	106	105	102

Table 3.2: This table shows the effect of changing the thickness of the central busbar on the temperature along the bar. The reported temperature is at the length along the central busbar where the connection to a band's corresponding peripheral busbar will occur. Therefore, the temperature below the 1.1 mm array will be the hottest since it is located at end furthest from the connection to the DR. The chosen thickness, bolded, strikes a balance between desired thermal parameters and an attempt to minimize the mass of the assembly.

our thermal gradient Python model. While the thickest bar, 12.7 mm, produced the lowest hot end temperature for both busbars, the resulting mass would be doubled or quadrupled for a minimal improvement in thermal gradient. The final geometry of the central busbars was chosen to be 1.32 m long, 0.0381 m wide, and 0.0635 m thick as a compromise between T_{high} and mass.

A similar procedure was used to determine the thermal gradient across the peripheral busbars going to the detector focal planes and magnetic shields (see Figs. 2.3 and 3.2); however, in order to know the low end temperature at the end of the busbar closest to the central busbar, we needed to calculate the gradient across the connection from one to the other. As stated above, we had to consider thermal contractions during cooldown shifting bolted connections out of alignment. All materials have a temperature dependent coefficient of thermal expansion with the relationship typically reported with respect to the initial length at 293 K:

$$\frac{L_T - L_{293K}}{L_{293K}} = \alpha(T)[T - T_{293K}] \tag{3.1}$$

where $\alpha(T)$, not to be confused with the quality factor noted above, is the coefficient of thermal expansion (CTE). While the busbars are all comprised of OFHC Cu, and thus have the same CTE, the longer central bars contract more than the peripheral bars and the bars are orthogonal, resulting in contraction along two axes. By combining polished copper lugs for bolt holes and copper braids for flexibility, we fabricated custom copper straps to have a flexible connection with similar thermal gradients to bulk copper (for more details on our fabrication technique, see §3.2.3.2 or §**??**.

Through testing different heat loads across the straps and measuring the resulting temperature gradients, we found an empirical formula to approximate the thermal gradient given by

$$T_{strap} = \left[\frac{PL}{A}\left(\frac{\alpha}{2}\right)^{-1} + T_{low}^{2.01}\right]^{1/2.01}$$

where A is the cross-sectional area of the braid, L is the length of the braid without the lugs, the conductivity co-efficient $\alpha = 639$ W/m/K$^{2.01}$, and P is the heat loading across the strap. Additionally, since we would be creating a bolted connection between each end of the strap and the central and peripheral busbars, we had to account for the thermal gradient across such a connection. Fortunately, the Super Cryogenic Dark Matter Search (SuperCDMS) experiment group has done extensive work on characterizing the thermal gradients across bolted connections between gold plated copper pieces for temperatures as low as 0.1 K [76, 77]. By adapting their parameters for our design (e.g., #10 bolts for connections, gold plated joints), we developed an estimate in our model for the thermal gradient across our bolted joints. From SuperCDMS' measurements of conductance versus temperature, they find

$$K(T) = 0.1142 T_{low}^{1.1483}$$

where K(T) is the thermal conductance in W K^{-1} [76]. This value is for a joint with a contact area of 1.21e-4 m^2, which is approximately three times smaller than the

majority of our copper strap joints. Since K(T) is directly proportional to area, the correction to K(T) for the area of our straps' copper lugs is given by

$$K(T) = 0.1142\left(\frac{A}{1.21 \times 10^{-4}}\right)T_{low}^{1.1483},$$

where A is the surface area of the bolted joint. To estimate temperature gradient across the joint, we divide the heat loading by the thermal conductance at T_{low}.

With this set of equations, we were able to consider any combination of the thermal joints desired. For instance, to determine the final temperature at the detector arrays, we use the temperatures reported in Table 3.2 for the 6.35 mm thick bars as T_{low} for the respective band. Next, we calculated the gradient across a given copper strap by finding T_{high} after a bolted joint, using that high end temperature as T_{low} for the strap itself, and repeating the same process across the next bolted joint. At this point, we had the temperature at the cold end of the peripheral busbars. We then found the thermal gradient across a busbar using the bulk copper equation from the earlier central busbar analysis. The connection between a peripheral busbar and its respective focal plane was made with a 1.59 mm thick sheet of OFHC Cu, both heavily annealed and gold plated. Using the same method above to find T_{high} at the end of the strip's bolted connection to the detector focal plane, we then take T_{high} to be our final reported value. The same exact analysis was completed for the 1 K stage to find the temperature at the detector shielding.

The remaining connections to design for these two stages were between the DR tailsets and busbars inside the main cryostat. The DR shells contract and bring the assembly vertically upward, as the internal pieces are suspended from a lid, while the components within the main cryostat contract downward (they rest on a series of rings that contract downward). Luckily, lateral motion was limited since the axis running along the length of the connection aligns with the vertical midplane of the main cryostat and contractions along the orthogonal axis will occur symmetrically

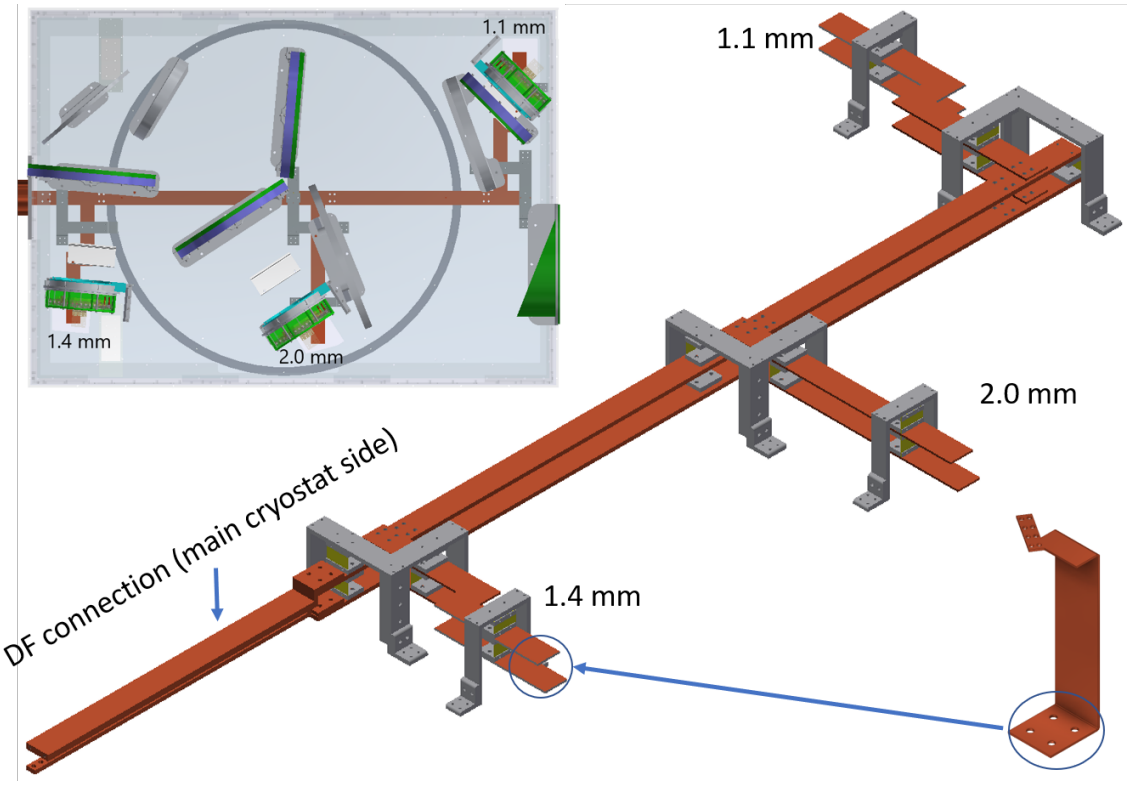

Figure 3.2: CAD model of the 1 and 0.1 K busbars below the optics bench with an example of the copper piece that links the busbars below the optics bench to the detector arrays above. The final copper pieces were gold plated.

around the connection. Thus, the final design had to primarily account for disparate up-down motion as well as contractions along the length of the connections with the largest displacements being on the order of 5 mm. The final design utilized copper straps provided from Oxford Instruments and Technology Applications, Inc. to connect rigid pieces coming from the main cryostat to existing pieces on the DR side. The chosen geometry was modeled using the thermal gradient script described above, resulting in modeled detector temperatures of 120 mK and shield temperatures of 1.1 K, respectively. A CAD assembly of the connections are shown in Figure 3.2.

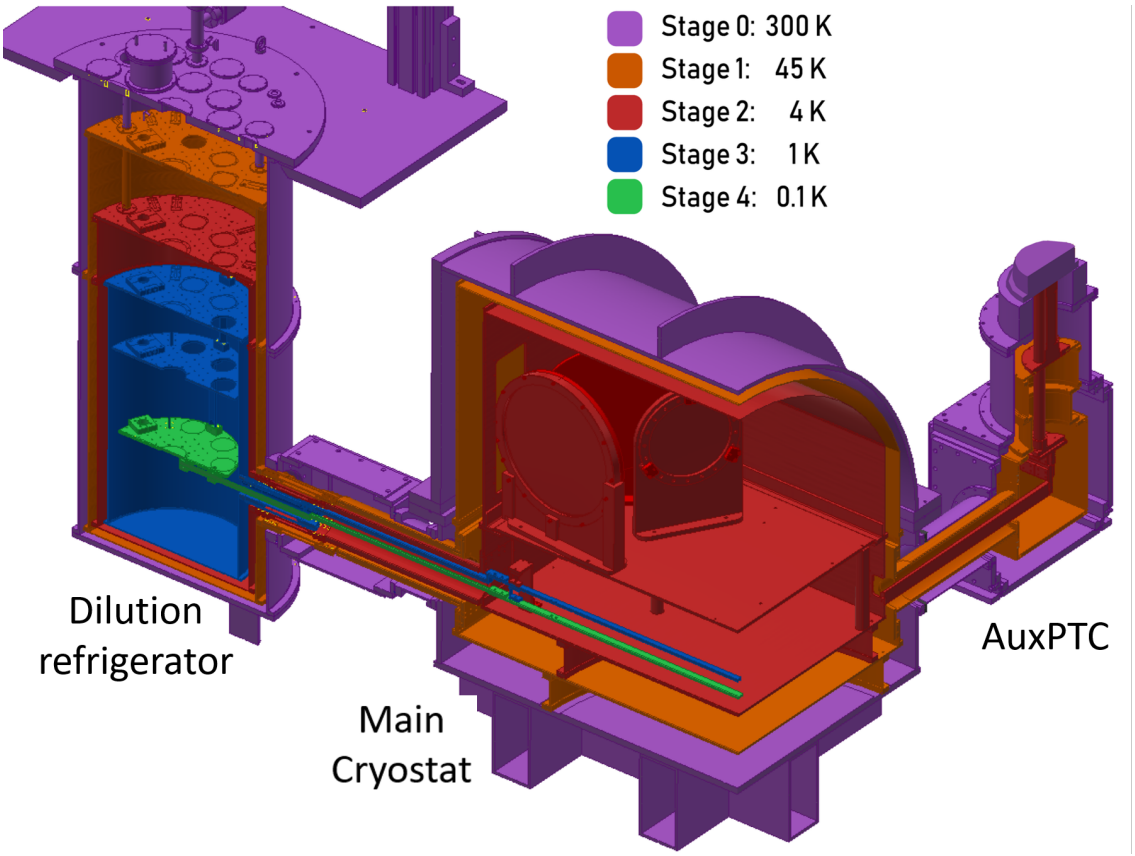

Figure 3.3: 3/4 view of TolTEC CAD model of TolTEC highlighting the four thermal stages interior to the 300K outer vacuum shell. Colors indicate the different thermal stages.

3.2.3 Cryogenic Performance

3.2.3.1 Cryocoolers

TolTEC features two individual cryocoolers. The first is a Cryomech 415 Pulse Tube Cooler, known as the Auxiliary Pulse Tube Cooler (APTC), which is used to cool the 45 and 4 K stages only (also known as Stages 1 and 2). The second is an Oxford Triton 2016 Dilution Refrigerator (DR); the DR alone provides the heat lift for the two coldest stages (also known as Stages 3 and 4). See Figure 3.3 for their relative positions on the cryostat.

To prepare for the full system integration, both cryocoolers were tested in isolation to confirm their designed cooling power (see Table 3.1 for values). We then

attached the cryocoolers to the main cryostat to perform cooling tests without the detectors. The initial performance prior to the installation of the arrays suggested excess loading on the two coldest stages (1 and 0.1 K). Their average temperatures were approximately 1.1 and 0.12 K, respectively. As our system features a unique tailset designed to integrate the main cryostat to the DR, we found it necessary to improve not only the thermal links between these stages but also the radiation shielding between the stages. Due to a mismatch between the design and the fabricated parts, there were gaps and seams that needed aluminum foil coverings and the addition of MLI to ensure no excess optical loading from a warmer stage would leak in to the stage below. Additionally, in some places, the tailset pieces are within 1 cm of each other, requiring careful assembly to ensure no touches occurred during cooldown.

The cryocoolers were ultimately able to reach the average temperatures outlined in Table 3.3. This was within our required range for operating the system. The stability of the temperatures is highlighted by the small standard deviation in the same table. Many of our laboratory cooldowns would last over 10 days with the longest being just over 40 days.

Cooler	Stage	Avg. Temp [K]
APTC	45K	40.081 ± 0.415
	4K	4.576 ± 0.252
DR	45K	48.972 ± 0.917
	4K	3.656 ± 0.379
	1K	0.911 ± 0.0751
	0.1K	0.0922 ± 0.00109

Table 3.3: Table of average base temperatures reached by each cryocoolers' stages. The temperatures reported are measured within the cryocooler, prior to the joint between the respective cryocooler and the main cryostat.

3.2.3.2 Custom Copper Thermal Straps

During our first tests with the 4 K stage, we found there to be a large thermal gradient on the order of a few Kelvin that was unacceptable for the optical volume.

In attempting to establish high stability and consistency across our thermal stages, we found the usage of custom, in-lab developed copper thermal straps to be vital. Our method was developed for use with 2.54 cm diameter OFHC Cu lugs with copper braid purchased from Tranect LTD. The process can be generalized to many other form factors, but the key to minimizing gradients across the strap is a combination of polished lug surfaces and a braising step to attach the braid to the lug. A detailed description of our strap manufacturing process can be found in §**??**.

3.2.3.3 Detector Array Temperatures

Once we installed the arrays, we were able to test the performance of the full thermal link system between the dilution fridge and each array. We had a set of thermometers on the joint between the MC and the bar extending into the main cryostat, a set on each array's 1 and 0.1 K joints, as well as a set on the central busbars and just below the detector arrays under the optics bench. See Table 3.4 for a comparison of the measured temperatures to the modeled temperatures. At the 1 K stage, we found the measured temperatures to be between 9 and 20% higher than the model. The reported measured temperatures are the average of all the measurements between January 2020 and May 2021 as we had completed the majority of our cryogenics modifications before then. We were unfortunately never able to measure the temperature for the 1 K stage at the 1.4 mm array due to a faulty thermometry wire. At the 0.1 K stage, all three detector arrays' measured temperatures were consistently $\sim$ 22% higher than the model's predictions. However, the differences between the measured array temperatures are comparable to those of the model ($\sim 3 - 7$ mK) suggesting a few possibilities for the difference between the prediction and measured values.

One possibility is a higher thermal gradient across the 4 joints between the mixing chamber and the main cryostat busbar. The most likely spots for higher thermal

	Model		Measured	
Band	T_{shield} [K]	T_{det} [mK]	T_{shield} [K]	T_{det} [mK]
1.1 mm	1.09	123	1.31	151
1.4 mm	1.08	116	-	141
2.0 mm	1.07	119	1.17	145

Table 3.4: Modeled versus measured temperatures at the 1 K thermal shielding and 0.1 K array. The modeled geometry aimed to match temperature constraints while allowing flexibility in the final operation of the cryocoolers. While our averaged temperatures are higher than the model, the temperature gradient between the 0.1 K arrays is approximately what we expected. Additionally, while in the lab the 1 K shield temperature for the 1.1 mm array was about 0.1 K higher than desired, as will be described in §4, at the LMT this stage is operates closer to 1.2 K.

gradients are either between the mixing chamber plate and its bar inside the DR or between either one of the sides of the thermal strap bridging the gap between the DR and the main cryostat. The thermal strap we have used since January 2020 was a commercially manufactured part from Technology Applications, Inc. (TAI) that we gold plated. We do not have conductivity measurements of the strap in isolation after the gold plating process, but TAI measured it to be similar to OFHC Cu in their facility. We have seen in the past that the thermal gradient between the mixing chamber plate and bar is sensitive to how well bolted the bar is to the plate. It is difficult to access the top of the plate in order to properly tighten the four bolts holding the bar, thus during disassembly and reassembly of that joint it is possible to have reduced contact between the two surfaces, increasing the final thermal gradient.

Another possibility is that the loading on the arrays could be higher than we anticipated for our model. As described previously, we have minimized the background optical loading as best as possible and assumed a higher value for our model's optical volume (choosing 7 K rather than 4 K). We also only have a rough estimate of the heating due to the electronics, so this is another place that we may have underestimated in our model.

Ultimately, while the measured results do not match the model for both the 1 K and 0.1 K stages, they are near enough to the original maximum desired temperatures of 1.2 K and 150 mK to be satisfactory for operation.

3.3 Detectors

As described in §2.3, TolTEC hosts three superconducting detector arrays, each with their own focal plane. The arrays, designed and fabricated by our collaborators at NIST, are comprised of 7716 Lumped Element Kinetic Inductance Detectors (LEKIDs). LEKIDs are superconducting thin-film microresonators, where the resonator acts as the absorber in the detector [37, 38, 56]. In TolTEC, we use TiN/Ti/TiN thin film resonators patterned on silicon-on-insulator (SOI) wafers [39].

One of the priorities for the testing at UMass was to successfully integrate and test the three detector arrays. We received the arrays in stages starting with the 1.1 mm array at the end of 2018, shortly followed by the 2.0 mm array, and capping off with the 1.4 mm array in 2019. The laboratory characterization included measurements of the detector bandpass, responsivity, efficiency, and noise. As the noise testing was combined into the electronics analysis, I will report the results in §3.5.

3.3.1 Bandpass

The frequency response of the system, or the bandpass, not only depends on the detector sensitivity to a given frequency, but multiple filters at different thermal stages along the optical path to the detector arrays.

To measure the bandpass for each array in TolTEC, we used a blackbody source heated to 200°C coupled into a Fourier Transform Spectrometer (FTS). Our FTS was based on the design of COBE-FIRAS and had been used previously to measure the bandpass of the AzTEC instrument [78, 79]. Refer to Figure 3.4 for a photo of the FTS during testing as well as a simplified diagram of its function.

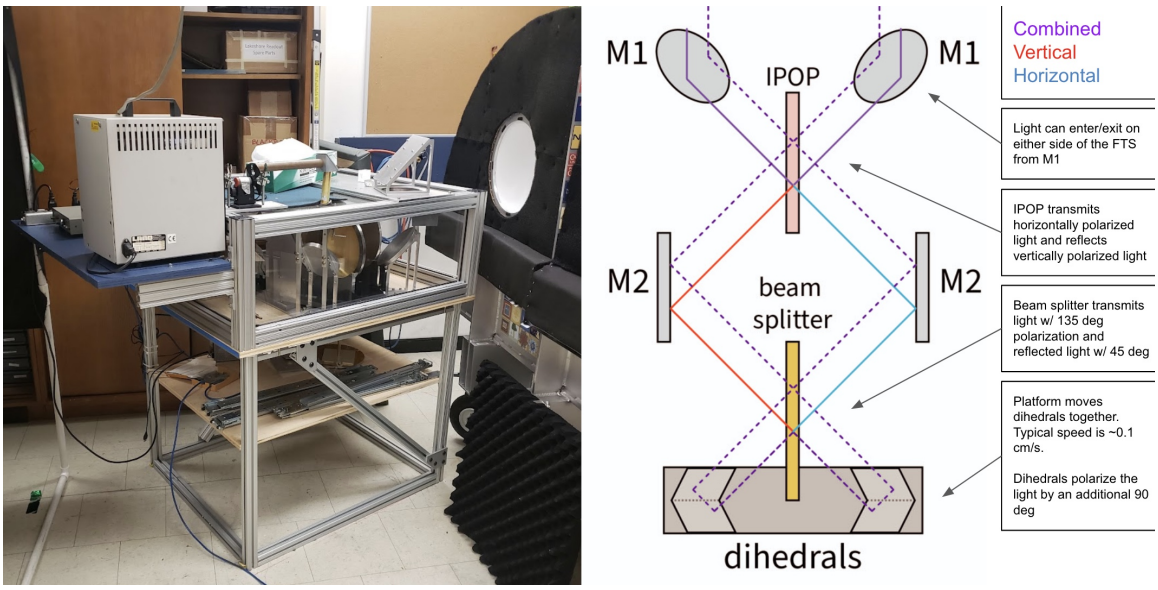

Figure 3.4: *Left*: A photo of the Fourier Transform Spectrometer (FTS) used for bandpass measurements at UMass Amherst. The blackbody source was set to 200°C. The front of TolTEC's aluminum shell was covered with charcoal-imbued cloth in order to reduce the amount of scattered light that could enter the window. *Right*: An illustration showcasing how radiation travels in the FTS. Note that in reality both M2 mirrors are paraboloids rather than flat. The red and blue lines are meant as an example of how incoming light from the lefthand side M1 would be split due to the input-output-polarizer (IPOP).

Following alignment of the FTS with the main cryostat's window, we measured the change in detuning parameter x (see 2.4.3) over time (e.g., 'take timestreams') for between 120-300 s intervals. As the FTS moved its dihedral mirror platform, the path length between the two beams change resulting in wavelength-dependent amounts of constructive and destructive interference. The result is a timestream of interferograms (see Fig. 3.5 for an example) that can be Fourier transformed to obtain the bandpasses. We first calculated the power spectral distribution (PSD) of x, then scaled the Fourier frequencies to the bandpass frequencies using a conversion factor based on the speed of the FTS. Finally, we rescale the spectrum by ν^2 to account for the Rayleigh-Jeans nature of the blackbody source emission. We report our bandpasses after normalizing to the peak value obtained from this method.

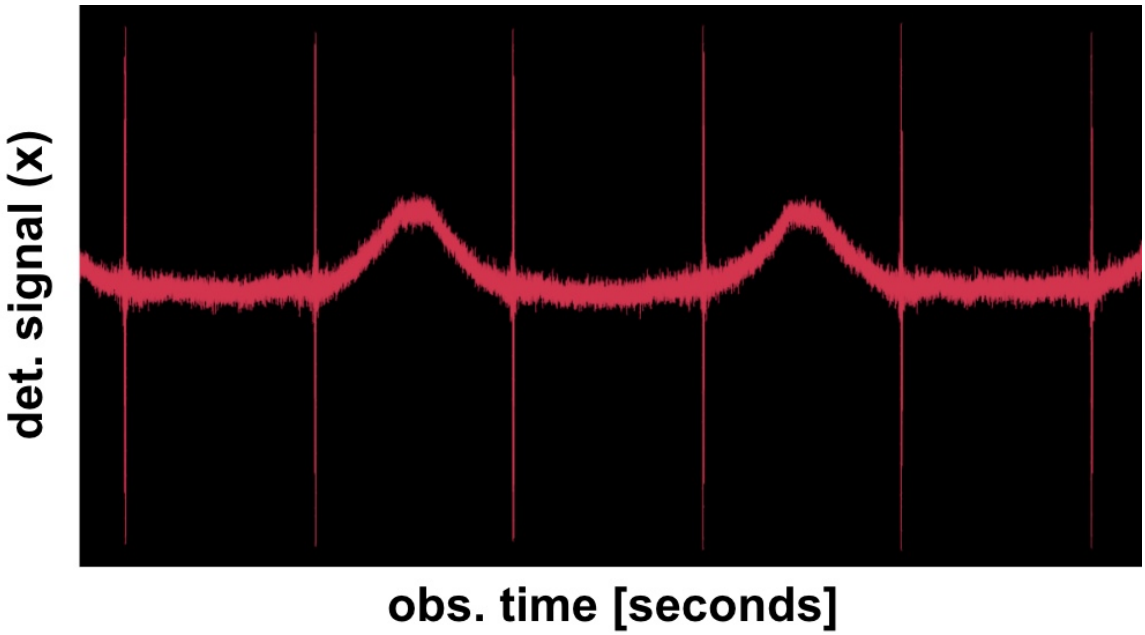

Figure 3.5: An example of a timestream taken using the 1.1 mm array while running the FTS. The sharp, periodic spikes in the timestream are the interference patterns created when the dihedral mirror platform approaches the center of the track. This is known as the "white light fringe" where all the frequencies constructively interfere. At that point, the beam path lengths are identical on both sides, so all light from the source arrives at the window. After taking the Fourier transform of this data, we are able to obtain the bandpasses shown in Figure 3.6.

We performed this test in multiple configurations during the course of laboratory testing. As shown in Fig. 3.6, the 1.1 mm array's bandpass has a cutoff at its low end that does not match the model. We measured the detector array's bandpass with and without the first dichroic filter (DF1) and determined that the filter cuts off at a higher frequency than anticipated. Integrating over the area of the modeled and measured bandpasses using different frequency spectra only resulted in $1-\sigma$ variations on the order of $\lesssim 1\%$.

3.3.2 Responsivity

Responsivity is the fractional shift in signal for a given change in incident power. The responsivity is dependent on detector design choices in geometry and material

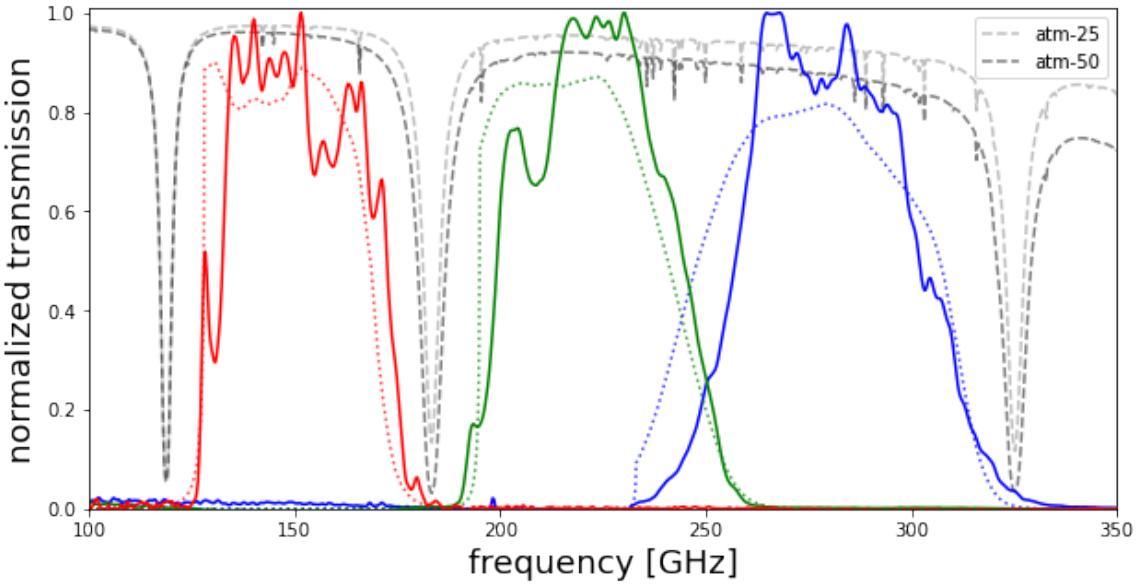

Figure 3.6: TolTEC's bandpasses as measured in the laboratory using a Fourier Transform Spectrometer. The dotted lines are the bandpass models from [41]. There is a low frequency cutoff for the 1.1 mm band that is due to stronger highpass filtering from the first dichroic filter. The shown bandpasses have been normalized to their respective highest value. We also show the relative transmission curves for two static atmospheric models (atm-25 being the 25% quartile atmosphere and atm-50 being the median atmosphere at the LMT).

of the absorber. For TolTEC, the target responsivities were chosen based on the typical variation in optical power seen by the AzTEC camera at the LMT during an observation. While a higher responsivity leads to higher sensitivity, it can also limit the total dynamic range of operation by increasing the rate at which new probe tones need to be generated ("retuning") to stay on resonance.

The equation describing the relationship between change in signal and change in power is given by

$$R = \frac{dx}{dP} = \frac{x - x_0}{P(T) - P(T_0)} \tag{3.2}$$

where x_0 is the detuning parameter measured with no external optical loading on the detectors and P is the optical loading on the detector array due to a source at some temperature T.

We chose to measure responsivities in the laboratory in order to confirm: (1) that they were comparable to NIST's design values; and (2) that they were linear over a broad range of optical powers. The responsivity also provides the calibration function to convert measured changes in detuning parameter x into measured optical power at the detectors. To obtain R, we installed a cryogenic blackbody directly in front of the array to be tested. The blackbody was made from four Ecosorb tiles bolted to an OFHC Cu sheet, offset from an aluminum mounting frame with three G10 standoffs (see Fig. 3.7). On the copper sheet, we Stycasted a ring of five in-series resistors (total resistance about 100Ω) that could be heated by increasing the voltage across them using an external voltage supply. Varying the supply from 0 to 5V, we increased the relative optical loading on the detectors from 0 to 7.5 pW. After heating the blackbody, we would wait two hours for it to thermalize before taking frequency sweep data. For these observations, we used `VNA` sweeps to measure S_{21} between 400 and 900 MHz then fit a Lorentzian to the derivative of the data with respect to frequency (dS_{21}/df) wherever a resonance dip was identified to estimate the resonator frequency f_r (see Fig. 3.8 for an example from observations using the 1.1 mm array) [71].

We used the linear relationship between x and the optical loading dP stated above to estimate the responsivity of a detector as the slope of the relationship. To calculate the loading at a single detector, we use the following equation

$$P_{opt}(T) = A\epsilon \int_0^\infty d\nu f(\nu) \int_{telescope} d\Omega I_\nu \cos\theta p(\Omega) \tag{3.3}$$

where A is the collecting area, ϵ is an absorption efficiency factor (see §3.3.3 for the calculation of ϵ for each array), f(ν) is the bandpass, I_ν is the intensity of the source, and $p(\Omega)$ is the PSF of the detector [79]. The efficiency factor depends on the aperture through which incoming light passes through the arrays. In the lab, we installed a

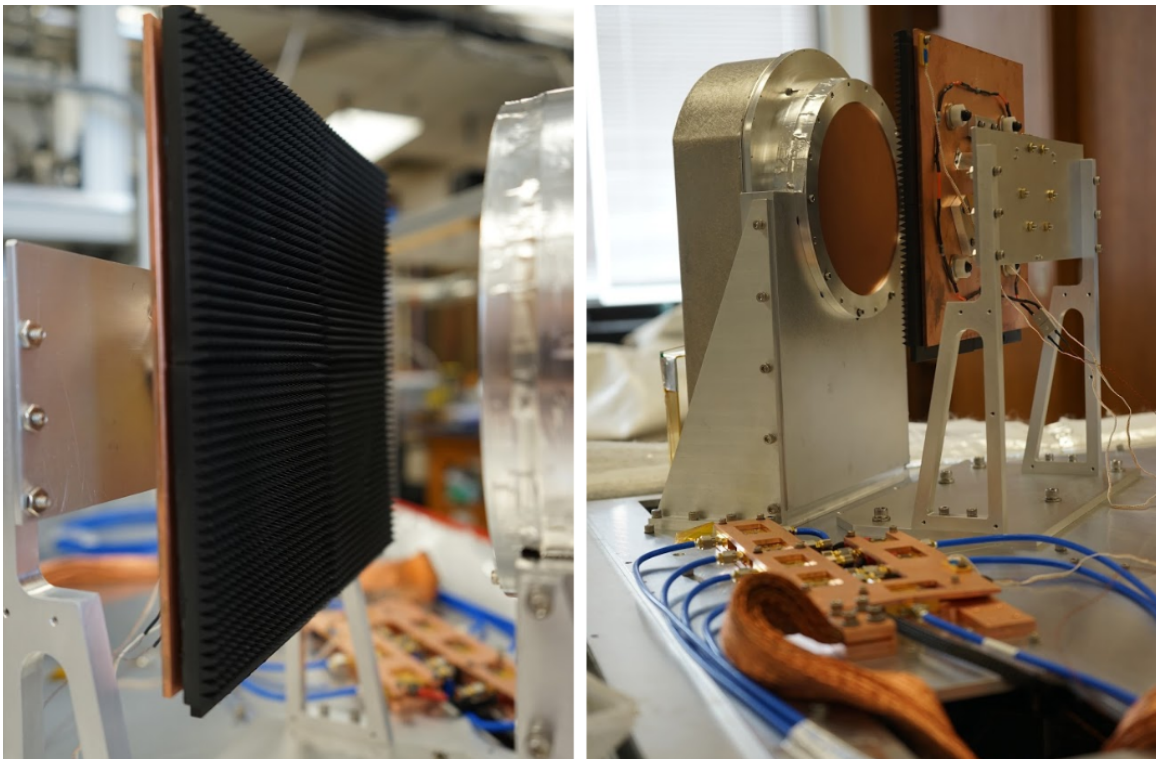

Figure 3.7: The cryogenic blackbody installed on the optics bench in front of the 1.1 mm array prior to closing the cryostat. The blackbody was comprised of four Ecosorb tiles bolted to an OFHC Cu sheet. Since we isolated the blackbody with G10 supports, we could increase the blackbody's temperature independent of the surrounding 4 K volume to provide a desired optical loading at the array. This test was only done for the 1.1 and 2.0 mm arrays. *Image credit*: Y. Ban.

2.54 cm diameter aperture at 4 K over the Lyot stop to simulate the loading expected at the LMT.

The function above can be used to determine the loading from any source at a detector; however, we can simplify this equation with a few assumptions. Firstly, since TolTEC operates in the Rayleigh-Jean limit (low frequency, $h\nu << k_B T$ for T$<$ 10 K) if we observe a blackbody source (say the atmosphere in front of the telescope), we can simplify the equation to

$$P_{opt} = A\Omega\epsilon \int_0^\infty d\nu f(\nu) \frac{\nu^2 k_B T}{c^2} \tag{3.4}$$

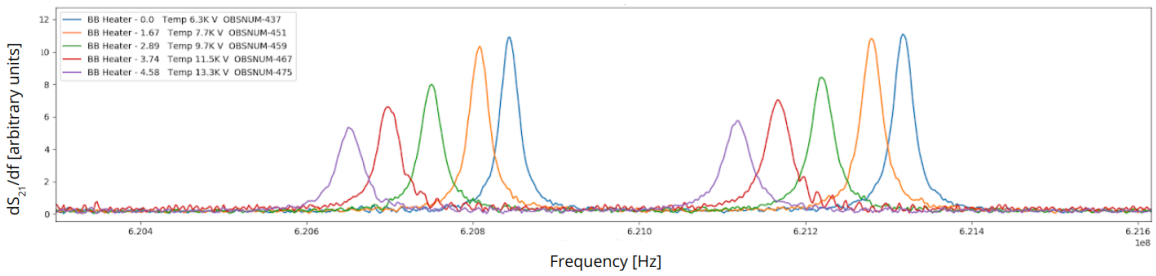

Figure 3.8: An example of derivatives taken of S_{21} with respect to frequency for five temperature settings of the cryogenic blackbody. Pictured here are two optically active detectors' results from the `VNA` sweeps. As the temperature increases, so does the optical loading which drives both the resonator frequency and quality factor lower.

where the product $A\Omega$ is the étendue. Since TolTEC couples to the fundamental Gaussian mode, the étendue is constant throughout the system and is given by λ^2, the wavelength squared. Solving this equation for the expected loading on the arrays from the atmosphere at the LMT suggests that we can expect about 10 pW on the 1.1 mm array, 8 pW on the 1.4 mm array, and 5 pW on the 2.0 mm array [41]. To maintain approximately the same signal response (x) across each band, we must have a responsivity that scales proportional to the power. Thus, if the loading at an array is half as large, such as between the 2.0 mm and 1.1 mm arrays, the responsivity must then be double.

Using Eqn. 3.4 to calculate the power arriving at the detector array for each blackbody temperature, we then turn to our `VNA` sweep data to obtain the change in frequency. As a note, we do not report the change in x rather, for an observation i, we calculate the normalized change in frequency given by

$$dx_i \simeq dS_i = -\frac{f_i - f_0}{f_0} \tag{3.5}$$

where f_i is a candidate tone from the ith fitted VNA sweep and f_0 is a candidate tone from the coldest blackbody measurement. The tones are matched using an assumption that the change in frequency between measurements is less than 50 kHz/K. As all

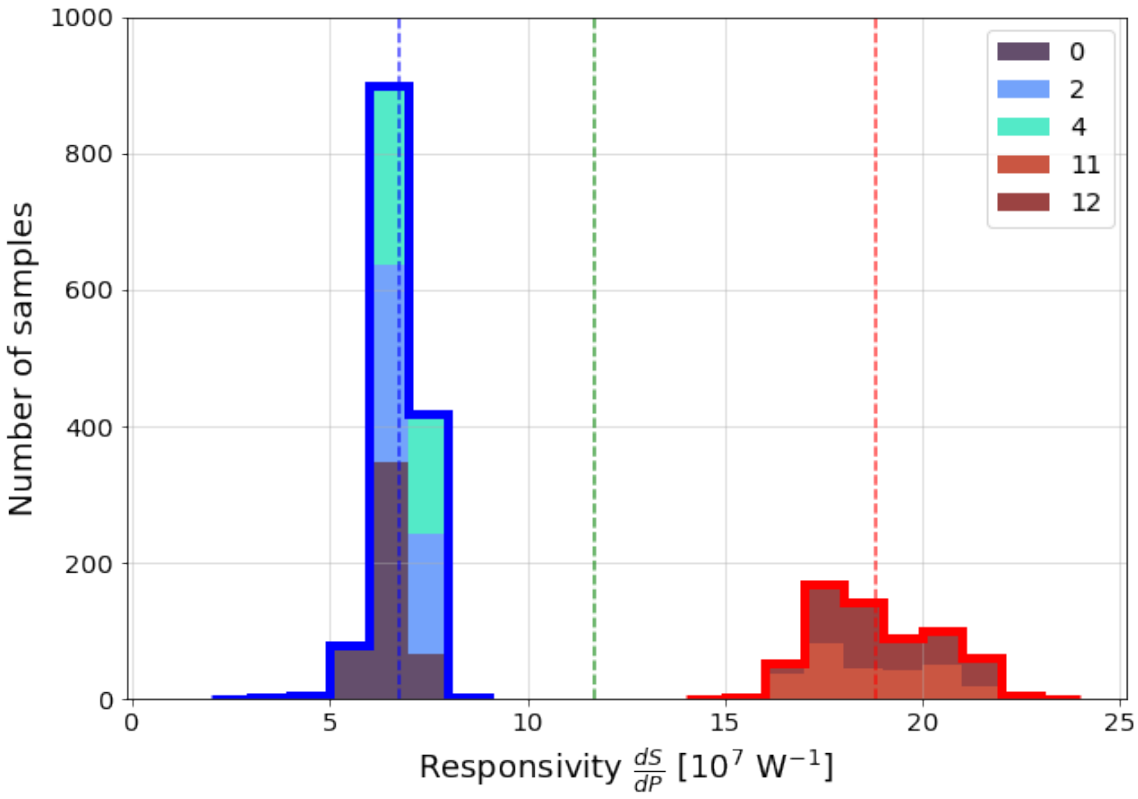

Figure 3.9: Histogram showing the responsivity for the 1.1 and 2.0 mm array detectors. The only networks we measured in the UMass laboratory are indicated by color in the legend. The dashed vertical lines indicate the mean responsivity for the 1.1 mm (blue) and the 2.0 mm (red) arrays. The dashed line between the two indicates the designed 1.4 mm array's responsivity that we use for subsequent calculations.

optically active detectors should ideally shift together and be separated by $\gtrsim 100$ kHz, the chances of false detections is minimal. Dark detectors, ones that have almost no frequency shift between measurements, are excluded from the results below.

Between two separate cooldowns, we were able to calculate the responsivities for networks 0, 2, and 4 on the 1.1 mm array and networks 11 and 12 on the 2.0 mm array. We find that the median responsivity for the 1.1 mm array is about 0.65×10^{-4}/pW, 7% lower than the value measured by NIST. The 2.0 mm array's median responsivity is 1.85×10^{-4}/pW, 68% higher than measured by NIST and 2.7 times higher than the 1.1 mm array. Recall that the 2.0 mm array was designed to have a responsivity

about twice that of the 1.1 mm array in order to equalize their response to the atmosphere at the LMT [39]. While higher than anticipated responsivity can result in an undesired sensitivity to fluctuations in the atmosphere at the observing site, the measured responsivities are not large enough to reduce TolTEC's performance at the LMT.

We chose not to measure the 1.4 mm array's responsivity in the laboratory as it would be costly in time and setup. As will be shown in the following section, we may be overestimating the efficiency for the 1.4 mm array by underestimating its responsivity when using the designed value (1.17×10^{-4}/pW) in our calculations [59].

3.3.3 Efficiency

The efficiency is the fraction of incoming radiation absorbed by the arrays. It can also be used as an indicator of the system's optical performance and can reveal issues in the optical chain. For instance, if we measured low efficiency there could be any number of causes including optical misalignments, poor filter/bandpass definition, AR coating issues, bowed dichroics, and so on. Therefore, measuring the efficiency in the lab is a critical test to show that the system performs as expected.

The total efficiency is a simple product of all efficiency factors along the optical path. For TolTEC, we have

$$\epsilon = \Pi_{i=0}^{n} \epsilon_i = \epsilon_{det} \times \epsilon_{int} \times \epsilon_{ap} \tag{3.6}$$

where ϵ_{det} is the detector coupling efficiency, ϵ_{int} is the internal system aperture efficiency, and ϵ_{ap} is any extra truncation by an aperture, such as the 2.54 cm Lyot stop diameter aperture installed during laboratory testing.

The detector coupling efficiency depends on the detectors' material and geometry, so from the design it was estimated to be approximately 70% [39]. The internal system aperture efficiency was designed to be $\sim 35\%$ [41, 45]. It includes the truncation by

the Lyot stop and feedhorns; however, for the 1.4 and 2.0 mm arrays, we also include an additional factor of 95% to account for scattering loss due to the cold optics. In other words, the theoretical internal system aperture efficiency for the 1.1 mm array is $\epsilon_{int} = 0.35$ while for the 1.4 and 2.0 mm arrays it would be $\epsilon_{int} = 0.332$. Also note that we do assume that the filters, aside from the effect of their bandpasses on the integral in Eqn. 3.4, are otherwise transparent and thus do not provide an additional factor to the internal system aperture efficiency.

It is also important to note that we calculate the aperture efficiency using the ratio of Gaussian beam areas through the window with and without the Lyot stop aperture. Since the incoming radiation is on millimeter scales, we utilize Gaussian beam propagation. We calculate the area of a Gaussian beam using the integral

$$A = 2\pi \int_0^r e^{-r^2/2w^2} r dr \tag{3.7}$$

where $w = 16.442/\sqrt{2}$ cm is the beam radius at the window. Calculating this for the radius of the aperture, 1.27 cm, and of the window, 12.7 cm, we find $\epsilon_{ap} = 0.013$.

In the lab we measured the total efficiency with the following method:

1. With the system at base temperature, get a list of the frequencies of the detectors with the window cover off (loading from the room would be 300 K, but the effective loading would be determined by the Lyot stop aperture cover installed at the time).

2. Place a block of ecosorb in liquid nitrogen in a container large enough to cover the window, then get a list of the detector frequencies with the 77 K loading.

3. Convert the frequency shift between the two measurements into a change in power $\delta P = (f_{300K} - f_{77K})/(R \times f_{300K})$ at the detector array using the array responsivity R from §3.3.2.

4. Use Eqn. 3.4 to estimate $\delta P_{theory}/\epsilon_{theory} = A\Omega \int f(\nu) I_\nu(T)$ by solving twice (once for T = 300 K and once for T = 77 K) and subtracting the results. This is done using the theoretical efficiency for $\epsilon_{theory} = \epsilon_{int} \times 0.7 \times 0.013$ where ϵ_{int} varies by array as discussed above.

5. For each detector, divide the results from 3 and 4 to calculate the observed total efficiency by solving for ϵ in Eqn. 3.4.

Note that this method is highly dependent on the model selected. For instance, if the model underpredicts the loading at the detector arrays by a factor of 2, then the efficiency will be overestimated by that same amount. Additionally, the choice of responsivity has a significant effect on the reported efficiencies. Since each detector has a different value, the choice of the median responsivity does bias the results, however it was not possible to do a 1:1 match between detector and responsivity from the lab measurements.

We repeated this procedure for each cooldown once all three arrays were installed in the main cryostat. We found that the 1.1 array matches the theoretical distribution of efficiencies between 25% and 35%, assuming a range of 70-100% for the expected detector coupling efficiency.

It is important to note that while $25-35\%$ may appear to be an unacceptably small value for an astronomical instrument, this range of values was chosen by design. The primary factor that set the total optical efficiency is the internal aperture efficiency, which has been shown to be on the order of 35%. This value is in turn affected by the design choice to have a larger edge taper at our Lyot stop of -3 dB (as compared to other instruments with edge tapers on order of -10 dB or greater) in order to maximize TolTEC's mapping speed. The mapping speed of an instrument goes as the number of detectors and to increase the number of detectors means decreasing the feedhorn size at the array [41, 80]. Smaller feedhorn apertures increase the size of a detector's beam, which in turn increases the edge taper at the Lyot stop. The

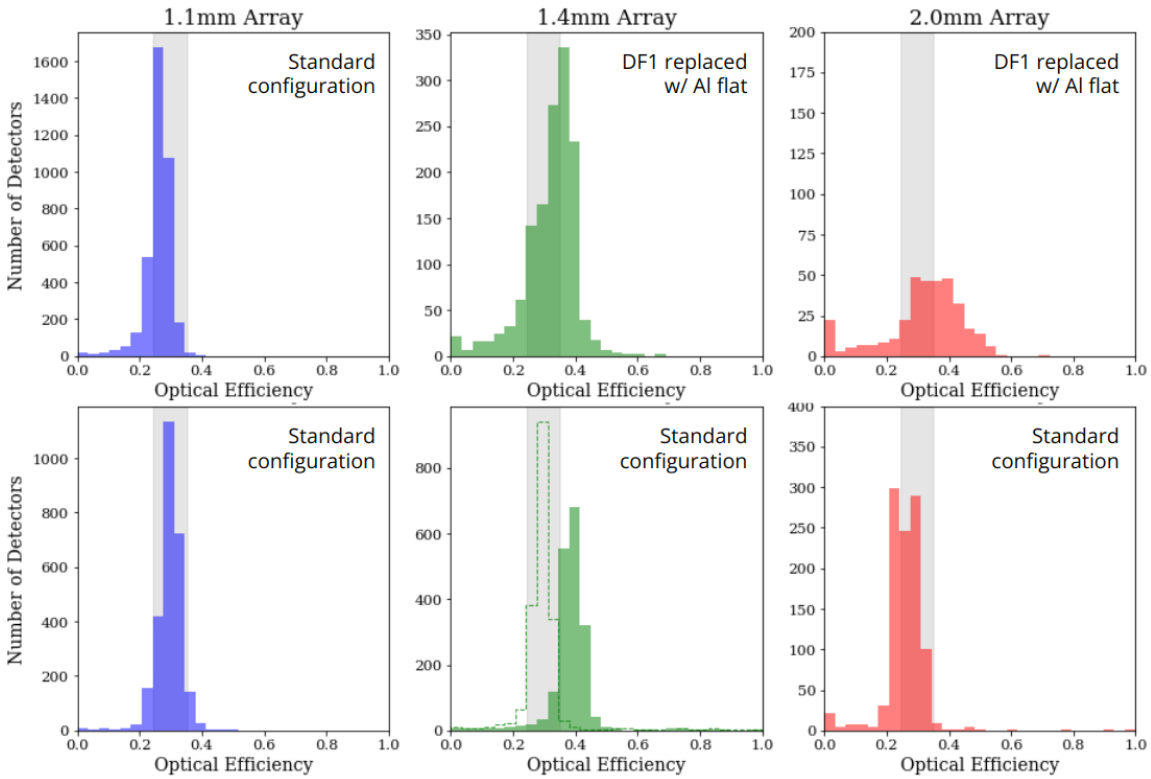

Figure 3.10: Histograms of the TolTEC efficiencies for each detector array. The grey bands show the range of expected optical efficiencies between 25% and 35%. *Top*: The 1.1 mm data was taken in the default testing configuration while the other two datasets were taken with an aluminum flat in place of the first dichroic. The excess efficiency values for the 1.4 mm array suggests that the responsivity may be higher than the design. The excess in the 2.0 mm data may imply a source of excess loading not accounted for in the theoretical power. *Bottom*: Data from the final run in the UMass Amherst laboratory. The dashed green histogram for the 1.4 mm array shows the distribution assuming that we underestimated the array's responsivity by 33%.

mapping speed will only increase with detector number until the loading at the Lyot stop matches that of the telescope; at this point, adding more detectors will not change the mapping speed as those on the edge will not be usable.

Our initial measurements of the 2.0 mm array efficiencies suggested that the detector coupling efficiency suffered due to the bowed dichroic issue described in §3.4.2. There is also a population of detectors with higher than anticipated efficiency which suggests a possible additional source of power unaccounted for in the model for the 2.0 mm array. After repairing the dichroic bowing issue we found that the efficiencies

were more tightly distributed within the desired range. In Figure 3.10 we show an example of the efficiency distribution before and after the dichroic fix.

The 1.4 mm array presented a more unique case in its distribution as its efficiency distribution has its mean about 33% higher than expected. One explanation is that our choice to use the 1.4 mm array's designed responsivity rather than conduct a measurement may be biasing the measured power at the array higher. We know from our measurements of the 2.0 mm array's responsivity that a higher than designed responsivity is possible. If we scale the responsivity from 1.17×10^{-4}/pW by 33%, the new value is 1.56×10^{-4}/pW and the mean of the 1.4 mm array's efficiency matches the expected range. If we scale it by the same amount that the 2.0 mm array's responsivity deviated from its design, 68%, then its responsivity becomes 1.96×10^{-4}/pW. This would be higher than the 2.0 mm array's median responsivity, 1.85×10^{-4}/pW; however, as we have not measured the 1.4 mm array's responsivity directly we can only state that the data implies it to be higher than designed.

3.3.4 Detector Noise

We performed environmental testing to examine the effect of local magnetic fields and vibrations on the detector noise. For the first test, we built a TolTEC-sized Helmholtz coil to surround the main cryostat. While the detectors arrays are each surrounded by a magnetic shield, there are gaps for both cabling and optics. Since superconductors are sensitive to magnetic fields, failing in the presence of ones that exceed their critical field strength, we recorded data for different field strengths up to 765 μT (about 11 times stronger than the largest reported value for Earth's magnetic field intensity). In the second test, we struck the main cryostat with different objects as well as shut off the cryocooler compressors while recording data in order to test microphonics. In both cases we found minimal to no changes in the noise spectra of the data suggesting that the detectors were well isolated.

Another potential source of environmental noise was TolTEC's half-wave plate rotator (HWPR) bolted to the front of the main cryostat around the window. The HWPR modulates incoming polarized light at a 2 Hz frequency allowing TolTEC to perform high resolution polarization studies [81]. Since the HWPR utilizes a magnetic torque motor to rotate the half-wave plate, we also wanted to test the effect of running the HWPR as it produces both a magnetic field and vibrations. As with the other environmental testing, the resulting noise spectra were identical implying that the HWPR would not act as a source of additional noise on the system.

And lastly, while precise measurements of inherent detector noise can only come from isolated, array-only measurements, we were able to perform a test to compare the relative levels of different noise terms in the readout chain. To perform this test we placed a 50Ω terminating load on the input, or drive, port on the main cryostat while leaving the output, or sense, cable connected. During the electronics testing we had independently measured the noise from the cryogenic cabling, LNAs, and warm electronics in order to estimate the detector-only noise. Please refer to §3.5 for further details on the results of these tests.

3.4 Optics

3.4.1 1 K Baffle

During laboratory testing, based on the detector array temperatures and performance, we suspected there was excess loading entering the arrays from the 4 K stage. The thermometry at the Lyot stop measured temperatures of 7 K which, since the edge taper at the Lyot stop is large (-3 dB), would impart extra loading onto the detector arrays. Since we had excess cooling capacity at the 1 K stage, we first tried installing more shielding and baffling at the 1 K stage within the detector assemblies. We additionally blackened the inside of the 4 K magnetic shielding that comprised the outer shell of the detector assemblies. While these steps reduced the loading,

we still found a need to further deaden the 4 K volume. To that end, we designed and fabricated a 1 K baffle to surround the 4 K Lyot stop where the radiation would enter the main cryostat. The baffle, an OFHC-Cu piece blackened using Stycasted charcoal-imbued fabric, absorbs excess in-band loading scattered into the 4 K volume at undesired angles. To account for any other excess loading, we installed a 4 K awning mounted to the top of the 4 K shell using G-10 standoffs. The awning was then thermally coupled to the DR using a flexible copper strap attached between the awning and the panel connecting the 4 K shell and the DR 4 K tailset. See Figure 3.11 for images of the baffle and awning fabrication and installation process.

The baffle was designed to be large enough to avoid intersecting the TolTEC beams entering the Lyot stop while also overlapping the edge of the Lyot stop. Since the baffle would be a different temperature than the surrounding optical volume, it would need to be thermally isolated from the 4 K stage while having a tight coupling to the 1 K stage. To accomplish this, we used 5 carbon fiber tubes to offset the baffle from the 4 K stage and a copper flange to attach the baffle itself to the 1 K busbar through a hole in the optics bench. The baffle itself, due to its large diameter of 43 cm, needed to be fabricated from a rolled copper sheet. We wanted the angle of the baffle to match the Lyot stop to avoid intersecting the beam as well as surrounding optics mounts, so the flat copper sheet was cut with the proper profile prior to rolling. Once rolled in the UMass Astronomy Machine Shop, the sheet was bolted and soldered to close the seam. We also added an additional flange at the flat side of the baffle in order to add more surface area without interrupting the beam, further isolating the Lyot stop from the optical volume and providing more area to capture scattered radiation.

The baffle added 2.26 kg of OFHC Cu to the 1 K stage along with 5 carbon fiber supports to thermally isolate it from the 4 K stage. Comparing the 1 K stage temperatures before and after the installation of the baffle, we find that it added a

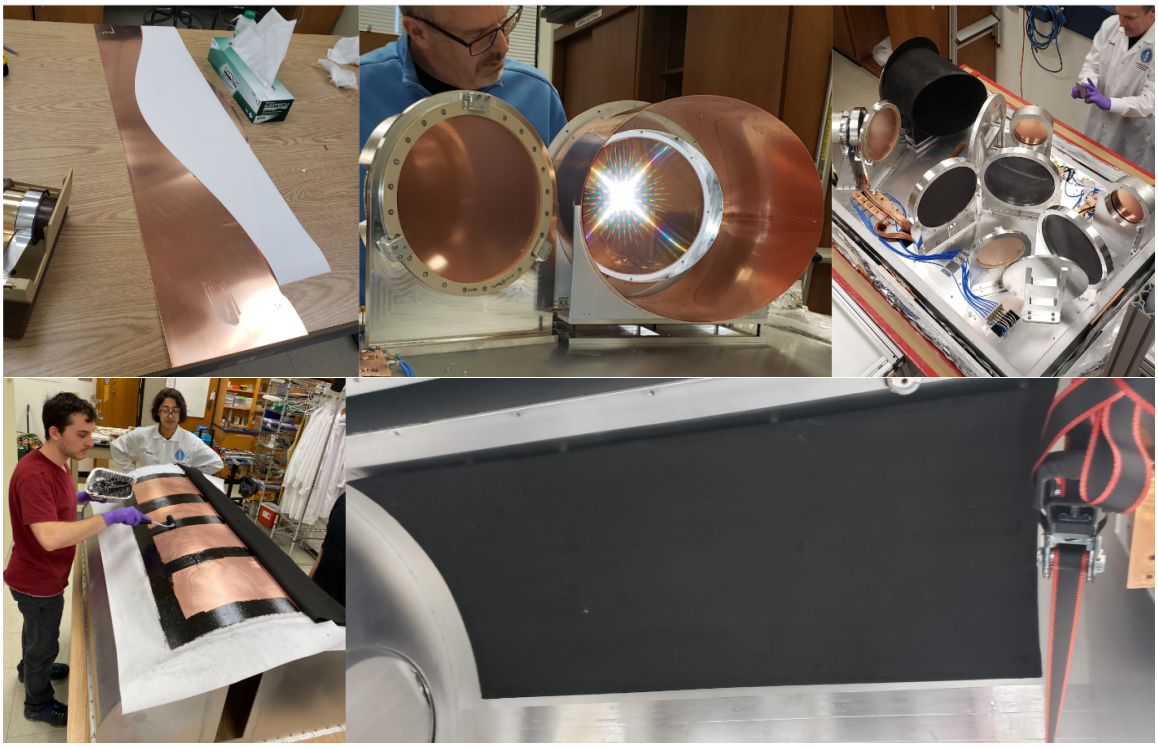

Figure 3.11: 1 K baffle and 4 K awning installed in 4 K optical volume. *Top*: Fabrication steps for the 1 K baffle. The baffle was created from an OFHC Cu sheet cut with a wave in order to match the angle of the Lyot stop once rolled. Once the fit was confirmed, we blackened it using charcoal-imbued cloth glued down with Stycast. *Bottom*: Fabrication for the 4 K awning. Similarly to the 1 K baffle, we attached charcoal-imbued cloth using Stycast. The awning is bolted to the 4 K shell's lid using G10 offsets and directly attached to the dilution refrigerator 4 K connection using an OFHC Cu strap (seen on the right) and a flexible strap below the optics bench (not pictured here).

negligible amount of additional loading on the 1 K stage. Prior to installation, the average 1 K stage temperature at the 1.1 mm array was 1.29 K that then increased to 1.31 K. This was within our desired range for operating the 1 K stage, so no modifications to the baffle were necessary.

3.4.2 Beam Response

We explored the performance of TolTEC's cold optics through the use of beammaps. To perform beammapping with TolTEC in the lab, we used a robot arm (henceforth referred to as Wyatt) that could move in the XY plane parallel to the window (see

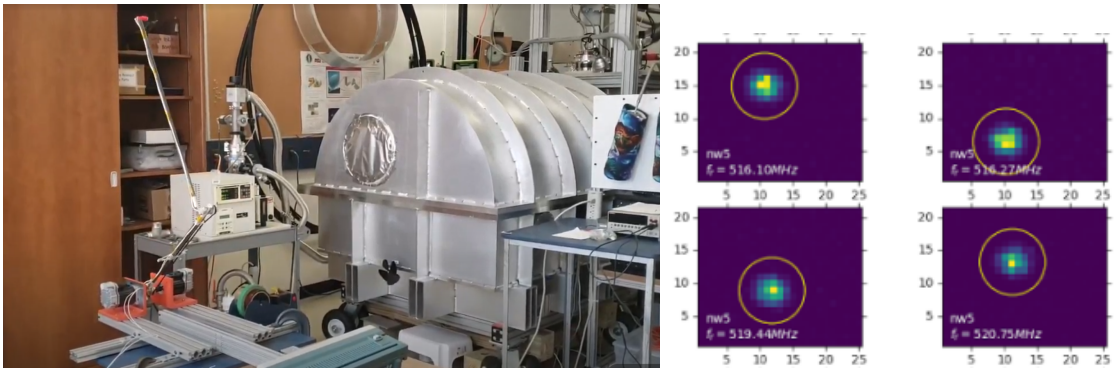

Figure 3.12: *Left*: The XY robot arm Wyatt being tested in the UMass Amherst laboratory prior to a cooldown. The arm would move in the XY plane parallel to the front of the main cryostat while an IR source (red tab at the end of the arm in the photo) was chopped using an oscillating voltage source. *Right*: An example of the beammap observations by a collection of four detectors in network 5. The yellow circle shows where the fitting algorithm identified the source in the map.

Fig. 3.12). Wyatt was designed and fabricated at UMass. The arm was made from two carbon fiber tubes attached to two motors that could actuate the arm to XY positions within a 1.5-m radius to a millimeter-level precision. For the beammap source, we chopped a Hawkeye® IR-75 source at 10 Hz using a 6V amplitude square wave. Using Wyatt we were able to perform automated tests to not only map out the physical locations of the detectors but also to determine if the cold optics were working as designed and if the beams were well aligned between the three arrays.

For completeness, in Figure 3.13, we present an example of two sets of beammaps recorded using Wyatt in order to serve as a point of comparison in the next chapter where we discuss on-sky results obtained at the LMT. For details on the data analysis pipeline to obtain the beammaps and other TolTEC mapping results, please refer to Michael McCrackan's 2022 SPIE paper [82].

In February 2020, just prior to the beginning of the COVID-19 shutdown, our beammap testing revealed that the FoVs for the 1.4 mm and 2.0 mm arrays were compressed compared to the 1.1 mm array [83]. During the quarantine, we developed a set of tests that could determine the cause of the compression. We returned to the

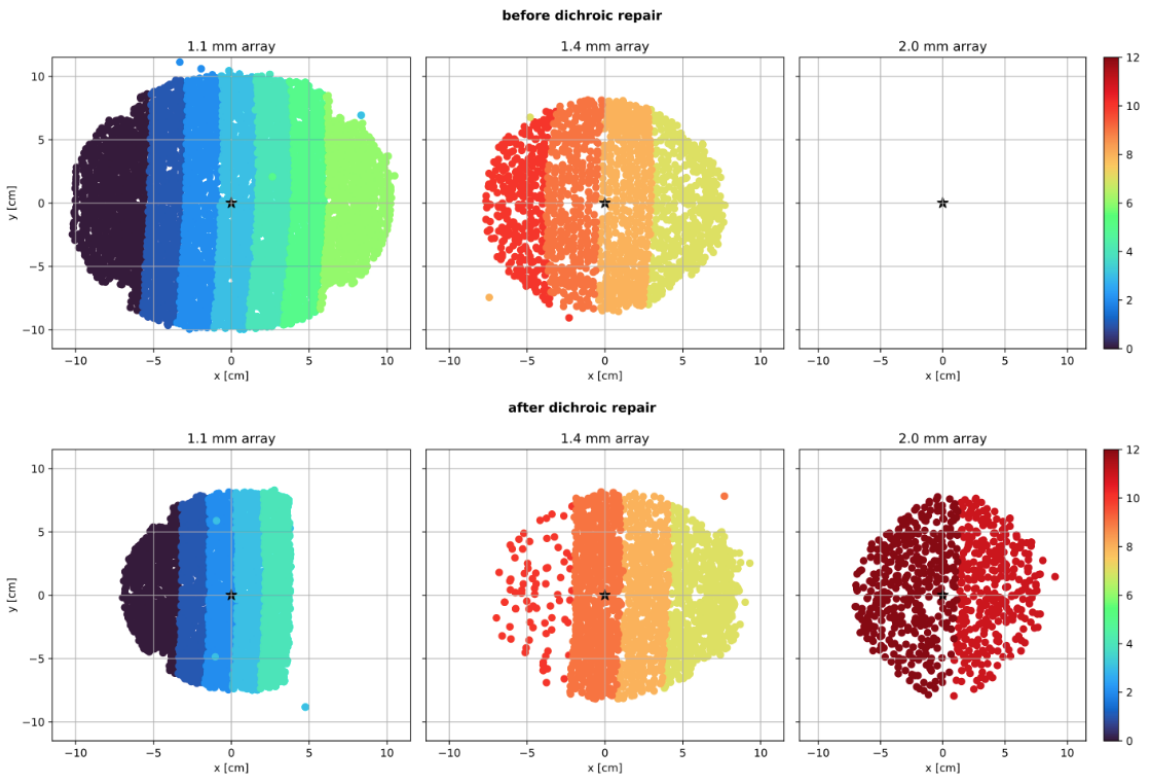

Figure 3.13: Examples of beammaps for taken in 2019 and 2021. The axes are reported in Wyatt's units (centimeters) and the black star indicates (0, 0) on the plots. Colors refer to the network. The change in beammap extent for the 1.1 and 1.4 mm arrays is due to compression of the first dichoric filter in the optics chain. In the 2021 data, we had low gain through network 6 on the 1.1 mm array, so it is not included. Additionally, where networks appear "patchy" it is due to the cut on detectors with a S/N less than 3 rather than detector inactivity. Additionally, for the top panel, we did not have data for the 2.0 mm array.

lab in July 2021 and installed a shiny aluminum flat in the place of the first dichroic. The flat acted as a mirror, reflecting the incoming radiation to the downstream arrays, 1.4 and 2.0 mm, and blocking the 1.1 mm array. During this test, we found that the 1.4 mm array's FoV more closely matched the 1.1 mm array's FoV; however, the 2.0 mm beammaps still showed evidence of compression. This confirmed that the dichroic filters themselves were the source of the smaller than expected FoV. Modeling suggested that a even small contraction of 0.1 mm in the dichroic filter could impart a radius of curvature, or bowing, in the filter on the order of ~ 2.5 m [84].

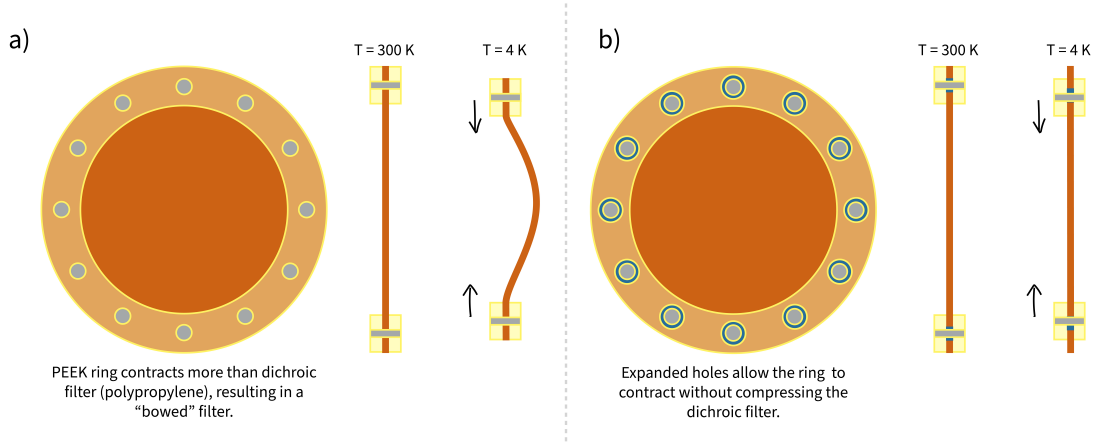

Figure 3.14: Graphic detailing the dichroic filter compression issue. When performing beammaps of the system, we discovered a compression of the field of view for detectors downstream of the 1.1 mm array. We determined this was due to a physical compression of the dichroic filters, also referred to as a "bowing" effect. We fixed this issue by increasing the size of the holes on the filter itself and adding spacers between the filter and the rings. This would allow the PEEK rings to contract to their final size when cold without compressing the PP filter.

The dichroics were designed by Cardiff University with polypropylene (PP) filters bolted between two polyetheretherketone (PEEK) rings. The PEEK rings are held in place by three spring loaded pins attached to an aluminum frame mounted to the 4 K optics bench. By September 2020, we had hypothesized that the bowing might be occurring through the following process:

1. When the cooldown starts, the aluminum frame begins to cool followed by the PEEK rings. The center of the PP filter primarily cools radiatively so it stays warmer than the PEEK rings.

2. If the PEEK ring contracts faster than the PP filter, then the filter will bow. This would differ from the design which was to have the PEEK contract less than the PP so that the filter would be stretched (similar to a drum) throughout the cooldown.

3. At 238 K, the PP filter undergoes a glass transition and becomes locked into its bowed shape.

4. At base temperature, 4 K for the optics, the dichroic is bowed and a compressed beammap will be observed.

Since the PEEK ring needed to contract less than the PP filter, we decided to first try heating the rings while the system cooled to base temperature. On both dichroics, we glued 5 heaters around the PEEK ring facing away from the aluminum frame. To prevent the aluminum from heating as well, we installed three G10 standoffs to isolate the dichroics from their frames. We bolted a thermometer on each dichroic to track the temperature of the PEEK rings; however, we would not be able to measure the PP filter's temperature directly without gluing a thermometer to it. As a solution, we modeled the filter by bolting a thermometer to a new piece of PP Stycasted with charcoal-infused cloth. We thermally isolated this mock-filter, called the HEX bolometer, from the optics bench using four pieces of fishing to hang it.

We were unable to solve the bowing issue with this configuration, so in December 2020 we installed a new set of dichroics from Cardiff that used cast PP (CPP) rather than the previously used biaxially oriented PP. The Cardiff team had observed higher thermal stability and improved flatness with the CPP filters [85]. With the new dichroics installed, we performed the beammaps and again found no improvement. In January 2021, our project manager Steve Kuczarski extracted one of the new dichroics from the cryostat for a test in which he cooled the dichroic in a freezer (255 K or -18°C), then exposed it to room temperature (292 K or 19°C) air. This was an inexpensive way to simulate the situation inside of the cryostat since, being significantly thinner than the PEEK rings, the PP filter would warm faster than the rings when exposed to the room. After cooling in the freezer for four hours, the dichroic was removed and exposed to the room temperature air. Within 30 seconds of exposure to the room temperature air, the PP filter became visibly bowed until

the dichroic fully warmed up. This test confirmed the process that lead to bowing within the cryostat described above.

Once we confirmed the process, we considered the addition of corrective optics in front of L3, L4, and L5[1]. After more deliberation, we determined a simpler solution: the mounting holes on the PP filters were drilled out to be larger than the bolts through the PEEK rings and spacers were added between the rings and the filters. While the rings would still contract more than the filters, these modifications ensured that the filters could not be compressed by this motion (see Figure 3.14). The repair was handled by our collaborators at Cardiff University and the modified dichroics were installed by May 2021. As seen in Figure 3.13, over a year after the discovery of this issue, the 1.4 and 2.0 mm arrays' FoVs following the dichroic fix were no longer compressed and finally matched that of the 1.1 mm array.

3.5 Detector Readout

For a more detailed description of TolTEC's readout electronics design and individual component performance please refer to the following papers [68–70, 86]. Additionally, this thesis does not cover algorithms designed by Zhiyuan Ma to handle the raw data reduction for TolTEC; please refer to Ma et. al. 2020 [71].

The characterization of the detector readout is a continuous process in the lifetime of an instrument. At the beginning of every cooldown, the cold readout chain is examined for "aliveness" to check that we can measure signal from each network. One could also continuously work to lower the system noise, asymptotically approaching the fundamental limit set by the detector noise. In reality, the best we can do is to ensure a low LNA noise temperature and that the warm readout components do not dominate the budget.

[1]A similar solution to the one implemented on the Hubble Space Telescope

In this section, we describe the characterization of the cold loopback gain of the system, the overall readout noise under minimal optical loading, and relative noise contributions from the readout chain elements. In the latter part, we estimate an upper limit for the detector noise in the system.

3.5.1 Cold electronics transmission

At the beginning of each cooldown we measured the forward scattering parameter S_{21} through the cold electronics using a Hewlett-Packard vector network analyzer (HP-VNA). S_{21} describes the loss in signal between the drive (1) and sense (2) ports. We refer to this value as the "loopback gain" for the following tests.

As a note, while we had initially planned to install -12 dB attenuators at the 1 K stage, we found that the ones we selected would superconduct below 2 K. We confirmed this by performing a cold loopback test where we created a 'mock' signal chain that did not pass through an array or LNA only consisting of the SS coax cables, DC blocks, and attenuators. After confirming that the -12 dB attenuators did not work at 1 K, we tested and identified a set of -20 dB attenuators that could work at those temperatures.

With the -20 dB attenuators installed, we expected -38 dB in total loss due to coax cables, DC blocks, and cold attenuators and ~ 30 dB in gain from the low noise amplifiers (LNAs). This would result in an average loopback gain of about -8 dB and, from all of our measurements with the HP-VNA, we found that the median gain at 650 MHz (the middle of our readout band) is approximately -4 dB. The higher loopback gain may be a combination of lower attenuation when cold as well as higher than expected gain from the LNAs.

During testing we occasionally measured loopback gains of -20 dB or lower if a network's stainless steel (SS) coax cables had failed. There were two main modes of failure: (1) the inner conductor pin from the cable would get stuck in its port

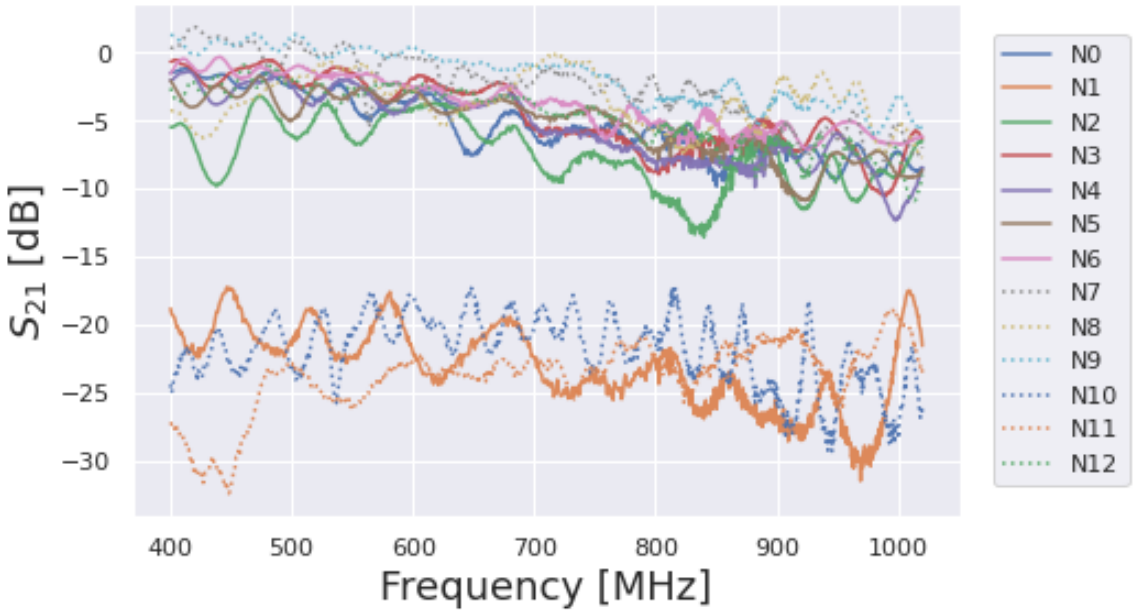

Figure 3.15: The loopback gain through TolTEC's cryostat in the cooldown prior to shipment to the LMT. The median loopback gain for all networks at 650 MHz is approximately -4 dB. Networks 1, 11, and 12 had median loopback gains around -25 dB due to failure of either cryogenic stainless steel coaxial cables or DC blocks. We were able to improve the mean gain for networks 1, 11, and 12 at the LMT by replacing the failed parts.

then be pulled out, or (2) the solder joint connecting the outer conductor to the connector would crack. The 1 K SS cables inside of the 1.4 and 2.0 mm detector arrays experienced the most mechanical stress during cooldowns and had to be replaced twice. We found that increasing the bend radius on these cables reduced the rate of failure.

Another instance in which we observed lower than expected loopback gain was when one or more of a network's DC blocks failed. We identified this failure mode by measuring the loopback gain of the line while the system was open so that we could isolate portions of the signal chain. The DC blocks used in TolTEC[2] are inner only meaning that they have a capacitor placed in the path of the inner conductor only.

[2]Specifically they are BLK-18-S+ DC blocks from Mini-Circuits®.

DC blocks are designed to reduce coupling from DC signals and, more importantly, interrupt the path to 300 K as an uninterrupted inner conductor may be able to carry heat to the array [40]. In TolTEC, we installed DC blocks at the 300-45 K and 45-4 K thermal breaks (e.g., where cables would transition in temperature between the thermal stages) and so there are 4 DC blocks in each network for a total of 52 in the entire system. Over the entire course of laboratory testing, we replaced approximately 10 DC blocks on various networks. Prior to installation at the telescope, we tested each DC block by measuring its transmission before, during, and after being immersed in LN2.

In the case of the LNA gain, we confirmed that they supplied approximately 30 dB while cold. Occasionally we would observe oscillations in loopback measurements that could be removed by adjusting the LNA bias settings. Often this was a result of the current through the collector being accidentally set above its limit (5 mA for the first stage and 3 mA for the second); however, we also found that a poor grounding scheme for the 300 K bias board could induce oscillations that could be observed in the detector timestreams. The grounding scheme we determined best limited this source of readout noise was one such that both the bias boards and their cables' ground lines were connected to the main cryostat chassis.

3.5.2 Noise with minimal optical loading

As described in §2.4, TolTEC records data in three primary ways: (1) `VNA` sweeps, (2) `tunes`, and (3) `timestreams`.

The first, a vector network analyzer (VNA) sweep, is styled after VNA instruments that perform wide bandwidth, high resolution sweeps in frequency. From the `VNA` sweep we obtain a list of candidate frequencies (e.g., tones) that may correspond to a resonator. This list of tones is determined through a fit to the derivative of S_{21} taken with respect to frequency [71].

The second method is called a `tune`. In this method, we perform a 1 MHz sweep with 10 kHz steps centered on each tone selected from the `VNA` sweep. Again, a fit is done, this time in *I/Q* space, to find the deepest point in the resonance and select the frequency at this point as a probe tone. The `tune` script runs the sweep plus fit routine twice in a row with the fit from the first step used to minimize the residuals on the second. This results in a list of frequencies to be used as the probe tones in the next data collection method, `timestreams`.

During a `timestream`, *I(t)* and *Q(t)* data are recorded at the probe tones supplied from the `tune` step. This data can then be reduced to calculate the detuning parameter x, which in turn can be related to loading on the detector using the responsivity R[3]. While x is sensitive to all noise sources, including photon noise, the quadrature parameter r is only sensitive to non-optical noise sources such as the detectors and readout electronics. The quadrature term is defined as

$$r = \frac{1}{2Q_r}, \tag{3.8}$$

where Q_r is the resonance's quality factor. The quadrature is related to the complex transmission coefficient $\tilde{S}_{21}$ through [71, 83]

$$X \equiv \tilde{S}_{21}^{-1} = r + \mathrm{i}x. \tag{3.9}$$

For further details on the transmission coefficient, $\tilde{S}_{21}$, and TolTEC's readout method please refer to §4.4.1.

As stated in §3.3, during laboratory testing we had installed a 2.54 cm diameter aperture over the Lyot stop at the 4 K stage. The goal was to, with the window

[3]It is worth noting that this conversion from x units (ADUs) to physical units (W) was performed in the lab using R. At the telescope, we instead use a flux calibration factor to set determine conversion factor from ADUs to flux units (MJy/sr or mJy/beam). For more information on the flux calibration process at the telescope, see §4.

open and the aperture installed, simulate the loading at the LMT (expected to be ~ 60 K at 1.1 mm when looking through the telescope at the atmosphere). For the following results we operated with even lower loading using a "window closed" mode in which we covered TolTEC's 300 K window with a reflective aluminum bowl. All measurements shown are calculated from 30-120 s `timestreams`.

We report the readout noise as power spectral densities (PSDs) which were calculated using Welch's average periodogram method with Python's `matplotlib.psd` function [87]. Our analysis generates the median PSD value at each frequency element alongside a histogram of the median PSD value for each detector. This can be used to provide an estimate of a "typical" detector channel's noise performance. We also examined deviations from the median spectrum using a histogram of the white noise (frequencies ≥ 10 Hz) for each detector. In Figure 3.16 we show an example of the results from this analysis. From the laboratory testing in the minimal optical loading configuration, we find that the median white noise in the x channel, which contains all noise sources, was 2 times lower than the expected BLIP noise at the LMT.

When performing measurements on-sky, we are most sensitive to signals that lie in the flat white noise portion of the PSD. The lower in frequency the signal falls, the more likely it will be swamped by low frequency noise which, for KIDs, has a strong $1/f$ spectrum. As seen in even in the minimal loading configuration, TolTEC has strong $1/f$ in both the x and r channels. Through a principal component analysis (PCA) of the data, the $1/f$ signal was found to be a common-mode signal in the r channel, which means that all the detectors "observed" the same source of noise [83]. Since all the detectors on a single network are coupled to the same transmission line, this points to a common source: the readout electronics for the network.

Conversely, in the same analysis, it was shown that in the x channel the $1/f$ noise was detector dependent [83]. The x channel includes all sources of noise and thus is

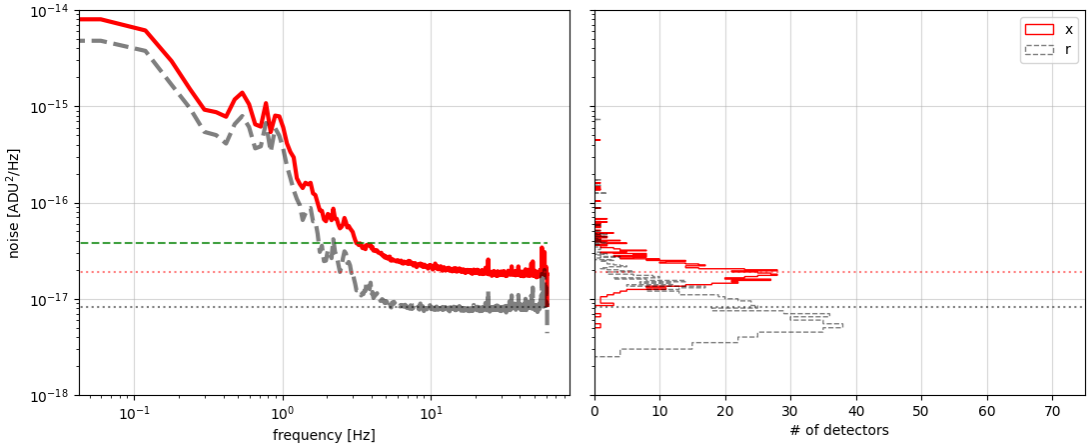

Figure 3.16: An example of a typical PSD for a **single network** under minimal optical loading. Red is the x channel (all noise sources) while black is the r channel (non-optical noise only). The plot on the left is the "typical" detector noise calculated from the median PSD value at each frequency. The green dashed line is the BLIP level for the array plotted. The histogram shows the distribution in overall median values for a detector in both channels. Results such as this show that there is adequate isolation between the x and r channels since their median noise values are on average separated by a factor of 2. Note that the PSD is shown here in the readout units ($\mathrm{ADU}^2/\mathrm{Hz}$) rather than physical units (W^2/Hz).

sensitive to both optical noise[4] and inherent detector noise. KIDs have inherent $1/f$ in their PSDs due to two-level system (TLS) noise; its mitigation remains a major area of research [38, 40, 67]. In TolTEC's case, our results show a similar $1/f$ slope and level as other NIST-Boulder TiN/Ti/TiN KIDs [83]. When we observe at the LMT, atmospheric emission will also contribute $1/f$ noise. Unlike the minimal optical loading case in the lab, atmospheric noise will dominate the x channel and all detectors will see it simultaneously. For common-mode optical signals such as the atmosphere at the LMT, we filter these signals through PCA cleaning and by modulating the signal with TolTEC's half-wave plate rotator (HWPR). While using the HWPR, we will be able to modulate the signal up to a maximum frequency of ~ 8 Hz [81, 83].

[4]Optical noise includes the background limited photon (BLIP) noise which is the quadrature sum of the photon shot noise and wave noise [40].

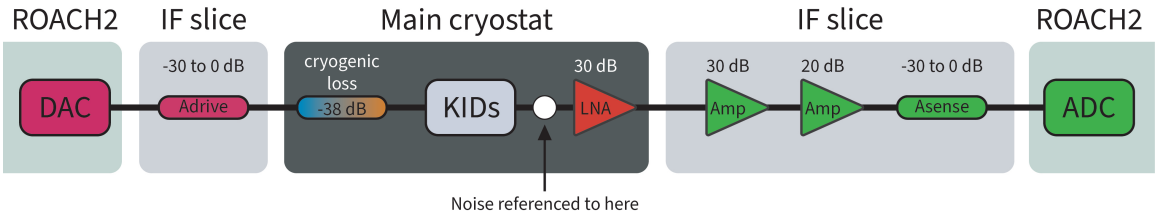

Figure 3.17: Simplified graphic of a single readout network showing the common point used for comparing noise measurements for different elements in the network. *Adrive*, or A_d, and *Asense*, or A_s, refer to the programmable attenuators. The 20 dB amplifier in the IF slice is located on v3 boards along with the programmable attenuators; by this time in the laboratory testing, all IF slices had v3.0 or v3.1 boards installed. For all iterations of the IF slices, the 30 dB amplifier is located off the board. For the tests described in §3.5.3, the drive attenuation A_d was set to 30 dB to minimize the input power to the network.

For more details on TolTEC's atmospheric filtering and the HWPR+HWP, please refer to §4.

Additionally, we found that the separation between our x and r noise was approximately a factor of 2 which suggests the minimum desired separation between the x and r channels. When the channels have less separation in their white noise level, it implies that the readout noise is the dominant source of noise. The readout noise itself was about 5 times less than the BLIP level estimated for the LMT for a nominal observing night. Since r is related to x by adding the photon noise, our laboratory measurements suggested that the instrument's noise under the loading at the LMT should not be dominated by the readout. As will be discussed in §4, our readout noise performance is worse than expected in that we: (1) find a smaller separation between x and r; and (2) the readout noise level is larger than the BLIP. We discuss these results and the planned improvements to the readout chain in §4.

3.5.3 Relative noise contributions

As shown previously, by taking the PSD of the timestream data in the nominal configuration, we can estimate the relative contributions from the detector, readout,

and photon noise. If we instead record this data while different parts of the readout chain are removed or turned off, we can isolate the noise contributions from individual parts of the readout chain. We separate the readout chain into five components: (1) ROACH2 analog-to-digital converter (ADC), (2) intermediate frequency slice input (IF), (3) low noise amplifiers (LNAs), (4) cryogenic loss (drive line), and (5) detectors (KIDs). To perform the measurement for each component we utilized the following configurations:

1. ADC: 50Ω termination on the sense port to the IF slice, 30 dB attenuation on the programmable sense attenuator (A_s)

2. IF + ADC: 50Ω termination on the sense port to the IF slice, $A_s = 0$ dB

3. LNA + IF + ADC: Readout cables attached to cryostat, $A_d = 30$ dB, $A_s = 0$ dB, LNA powered on

4. Drive + IF + ADC: Readout cables attached to cryostat, $A_d = 30$ dB, $A_s = 0$ dB, LNA powered off, LO frequency increased by 100 kHz (moved tones off-resonance)

5. KIDs + drive + LNA + IF + ADC: Readout cables attached to cryostat, A_d varied by network, $A_s = 15$ dB, LNA powered on, readout tones on resonance

The readout tones for the noise testing were selected by performing a `VNA` sweep and `tune` with the window **closed**. We did not re-`tune` (e.g., kept the same tones) between each testing step since we did not change the optical loading. This additionally ensured that the different measurements were comparable. Note that after we did the initial `tune`, we set the programmable drive attenuation (A_d) on the IF slice to 30 dB in order to apply minimal readout power to the input of the system. With this configuration, we should have only measured noise from the output of the component being tested. In subsequent testing at the LMT, we chose to disconnect

the IF slices from the drive port on the main cryostat to avoid applying any amount of input power.

After recording the timestreams, we used the raw I/Q data to calculate the signal magnitude $S = \sqrt{I^2 + Q^2}$. We then calculated the PSD(S) for each measurement,then converted the measured noise to the input of the LNA in order to make a one-to-one comparison. This was done by removing the contribution from attenuators and amplifiers that are used in a measurement (refer to Fig. 3.17 for graphical representation). So, for example, say we have taken a `timestream` of the ADC noise. To convert PSD(S) at the ADC output to noise at the input of the LNA, we calculate

$$\mathrm{PSD(S)_{ADC\,@\,LNA\,in}} = \mathrm{PSD(S)_{ADC}} \times 10^{\mathrm{A_s}/10} \times 10^{-\mathrm{G}/10} \tag{3.10}$$

where A_s is absolute value of the programmable sense attenuation and the gain factor G is given by

$$G = G_{LNA} + G_{IF} = 80\,\mathrm{dB}. \tag{3.11}$$

Applying the same method to each of the other PSD calculations, we have the following conversions to estimate the noise of each component at the input of the LNA:

$$
\begin{aligned}
\mathrm{PSD}_{\mathrm{ADC\,@\,LNA\,in}} &= \mathrm{PSD}_{\mathrm{ADC}} \times 10^{\mathrm{A_s}/10} \times 10^{-\mathrm{G}/10} \\
\mathrm{PSD}_{\mathrm{IF\,@\,LNA\,in}} &= (\mathrm{PSD}_{\mathrm{IF}} - \mathrm{PSD}_{\mathrm{ADC}}) \times 10^{\mathrm{A_s}/10} \times 10^{-\mathrm{G}/10} \\
\mathrm{PSD}_{\mathrm{LNA\,@\,LNA\,in}} &= \Big((\mathrm{PSD}_{\mathrm{LNA}} - \mathrm{PSD}_{\mathrm{ADC}}) \times 10^{\mathrm{A_s}/10} \\
&\qquad - \mathrm{PSD}_{\mathrm{IF\,@\,LNA\,in}} \times 10^{-\mathrm{G_{IF}}/10} \Big) \times 10^{-\mathrm{G}/10} \\
\mathrm{PSD}_{\mathrm{Drive\,@\,LNA\,in}} &= \Big((\mathrm{PSD}_{\mathrm{Drive}} - \mathrm{PSD}_{\mathrm{ADC}}) \times 10^{\mathrm{A_s}/10} \\
&\qquad - \mathrm{PSD}_{\mathrm{IF\,@\,LNA\,in}} \times 10^{-\mathrm{G_{IF}}/10} \Big) \times 10^{-\mathrm{G}/10} \\
&\qquad\qquad - \mathrm{PSD}_{\mathrm{LNA\,@\,LNA\,in}} \\
\mathrm{PSD}_{\mathrm{KIDs\,@\,LNA\,in}} &= \Big((\mathrm{PSD}_{\mathrm{KIDs}} - \mathrm{PSD}_{\mathrm{ADC}}) \times 10^{\mathrm{A_s}/10} \\
&\qquad - \mathrm{PSD}_{\mathrm{IF\,@\,LNA\,in}} \times 10^{-\mathrm{G_{IF}}/10} \Big) \times 10^{-\mathrm{G}/10} \\
&\qquad\qquad - \mathrm{PSD}_{\mathrm{LNA\,@\,LNA\,in}} \\
&\qquad\qquad - \mathrm{PSD}_{\mathrm{Drive\,@\,LNA\,in}}
\end{aligned}
\tag{3.12}
$$

The fundamental noise limit for the system's readout is set by its detectors' inherent noise, such as generation-recombination of the quasiparticles and TLS noise (see §2.3). In practice, the system noise is dominated by its attenuators and low noise amplifier (LNA) [38, 40]. During our testing we confirmed the LNA noise to be the dominant component, accounting for about 50% of the noise budget. The drive noise was the next largest component, followed by the detectors. The warm readout electronics noise was about three orders of magnitude lower than the cold components; this is what we desired for optimal performance as the cold amplifier/attenuators should set the noise floor. At the LMT, following the first phase of commissioning, we found excess warm electronics noise that dominated the readout. In the next chapter, we discuss the discovery and resolution of this excess noise.

CHAPTER 4

COMMISSIONING AT THE LMT

"To love the journey is to accept no such end. I have found...that the most important step a person can take is always the next one."

Brandon Sanderson, Oathbringer

This chapter was written as part of DeNigris et. al. (in prep) with contributions from the TolTEC team (the authors list is provided below). Please refer to the publication for finalized results.

Authors list: Nat S. DeNigris, Peter Ade, Emmaly Aguilar, Itziar Aretxaga, Jason Austermann, Marcial Becerril, Marc Berthoud, Sean Bryan, Luisa Cardona, Daniela Espitia, Daniel Ferrusca, Laura Fissel, Joseph E. Golec, Arturo Gómez, Robert Gutermuth, David Hughes, Stephen Kuczarski, Dennis Lee, Emily Lunde, Zhiyuan Ma, Philip Mauskopf, Michael McCrackan, Jeffrey McMahon, Alfredo Montaña, Giles Novak, Giampaolo Pisano, Alexandra Pope, Iván Rodríguez Montoya, Caleigh Ryan, David Sánchez-Argüelles, Evan Scannapieco, F. Peter Schloerb, Omar Serrano, Sara Simon, Adrian Sinclair, Kamal Souccar, Felix Thiel, Carole Tucker, Eric Van Clepper, Miguel Velazquez, Samantha Walker, Hailin Wang, Eric Weeks, Grant W. Wilson, and Min S. Yun

---

4.1 Introduction

Millimeter/sub-millimeter astronomy offers invaluable insights into the origins of structure in our Universe, ranging from dust-obscured nurseries of young stars all the way out to the search for the oldest, most distant galaxies. In the pursuit of progress in this field, it is crucial to commission new instruments that offer higher spatial resolution, higher sensitivity, and faster mapping speeds. Space-based missions such as *Planck* and *Herschel* have successfully conducted extensive surveys of the mm-wave sky; however, the cost and planning involved in future space missions pose significant limitations both in terms of time and resources. Fortunately, ground-based mm/sub-mm astronomy has made significant strides over the past two decades, enabling high-sensitivity observations with $\leq 1'$ resolutions by integrating large-format cameras with single dish telescopes ([36, 79, 88–91]).

TolTEC is a recently installed facility instrument for the 50-m diameter Large Millimeter Telescope (LMT), situated at an elevation of 4,600 meters (15,000 feet) on the dormant volcano Sierra Negra in Puebla, Mexico. The instrument boasts simultaneous imaging plus polarimetry capabilities at 1.1, 1.4, and 2.0 mm (or 270, 220, and 150 GHz) divided into three individual focal planes. TolTEC's three focal planes consist of 7716 superconducting Lumped Element Kinetic Inductance Detectors (LEKIDs) [39], a recently adopted technology in mm-wave astronomy [37, 38, 40]. The dense arrangement of LEKIDs across each focal plane enables TolTEC to achieve sub-$10''$ beams filling the LMT's $4'$ field of view (FoV), facilitating the creation of high-resolution, large-scale maps of nearby and extra-galactic systems.

In December 2021, the camera was installed at the LMT and began its commissioning observations June 2022. Additional commissioning observations were performed in December 2022 and April 2023. This phase will continue into Fall 2023, ending prior to January 2024. Once commissioning is completed, TolTEC will begin to open its observations to the public. Over its first ten years of operation, TolTEC will

deliver ten 100-hour legacy surveys, addressing topics ranging from local star formation to the evolution of large-scale structures over cosmic time. The results of these surveys will be made available to the public through an open access data archive, including all initial reduction maps. Currently, four of the public legacy surveys have been defined by the public working groups with six remaining open for community input [92].

This paper provides a comprehensive overview of TolTEC's capabilities, performance, and future prospects in anticipation of upcoming observing seasons. §4.2 presents a brief instrument design overview, while §4.3 discusses the installation process at the LMT and compares hardware performance to laboratory measurements. Observing modes available with the LMT are described in §4.4. §4.5 details the map-making pipeline and the data archival structure. TolTEC's calibration is covered in §4.6 and §4.7 presents the performance of the instrument at the site, including specifications on sensitivity and mapping speed. Finally, §4.8 concludes the paper with a discussion of our current performance and the outlook for future observations with TolTEC.

4.2 Instrument overview

Here we briefly describe the key elements of the camera needed to understand its calibration and performance. For the detailed instrument design specifications, please refer to [41]. Additionally, for further information on the layout of the instrument along with TolTEC's laboratory characterization and performance, please refer to [83].

4.2.1 Cryogenics

TolTEC has two separate cryocoolers to establish its four thermal stages at 45, 4, 1, and 0.1 K (see Fig. 4.2). We employ a Cryomech pulse tube cooler (PTC) for the

Figure 4.1: A photo of the TolTEC camera inside the receiver cabin at the Large Millimeter Telescope (LMT). In the foreground are the pumps, cold trap, and electronics rack for TolTEC's dilution refrigerator; in the background is the instrument itself facing the warm coupling optics (see Fig. 4.3). TolTEC was installed in the LMT receiver cabin in December 2021.

primary cooling at the 45 and 4 K stages. An Oxford Instruments dilution refrigerator (DR) cools the 1 and 0.1 K stages and provides additional cooling overhead at the warmer stages. Each cryocoolers rely on Cryomech compressors that both source their cold water in-takes from the same closed air-cooled system. The cryocoolers are both dry and self-contained, able to operate remotely and continuously for months at a time. For additional information on the the cryogenics design and operation, please refer to [72].

The instrument features a nested shell design where each internal stage is thermally isolated from the other through G-10 or carbon fiber supports. The outer vacuum shell (OVS) is a welded aluminum structure with a 1.5 m by 2 m footprint. The 45 K shell is also made from welded aluminum while the 4 K shell is a bolted

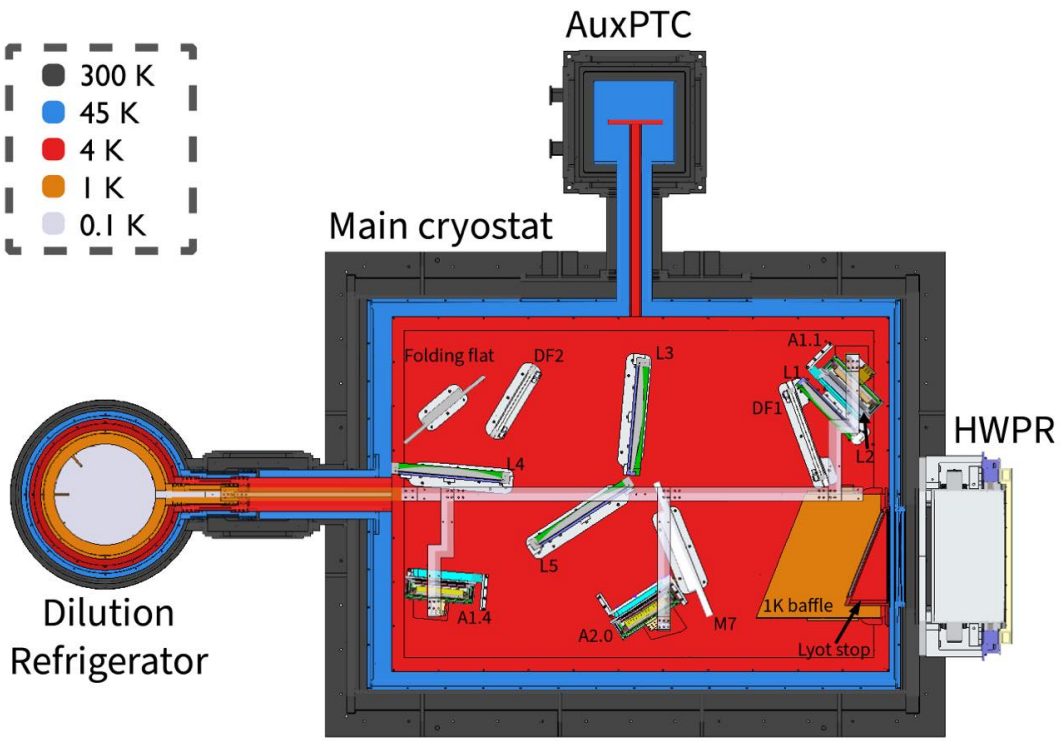

Figure 4.2: A CAD model of a top-down, cross-section view of TolTEC's cryostat. The figure includes both cryocoolers (auxiliary pulse tube cooler and dilution refrigerator), the 300 K half-wave plate rotator (HWPR), and the cold optics. The 1 and 0.1 K bars crossing the main cryostat are located below the optics bench (indicated by their lower opacity in the image). For clarity, neither the warm nor cold readout electronics were included.

aluminum structure. The two coldest stages (1 and 0.1 K) are entirely comprised of annealed, oxygen-free high-conductivity copper (OFHC Cu).

The connections between the stages and their respective cryocooler are formed using OFHC Cu cylindrical shells at 45 and 4 K and busbars at 1 and 0.1 K. At the coldest stage, one of the bars that leads to the main cryostat is directly bolted to the DR's mixing chamber and was found to have a poor thermal contact after installation. For more details on how this affected the instrument's cryogenic performance, see §4.3.3.

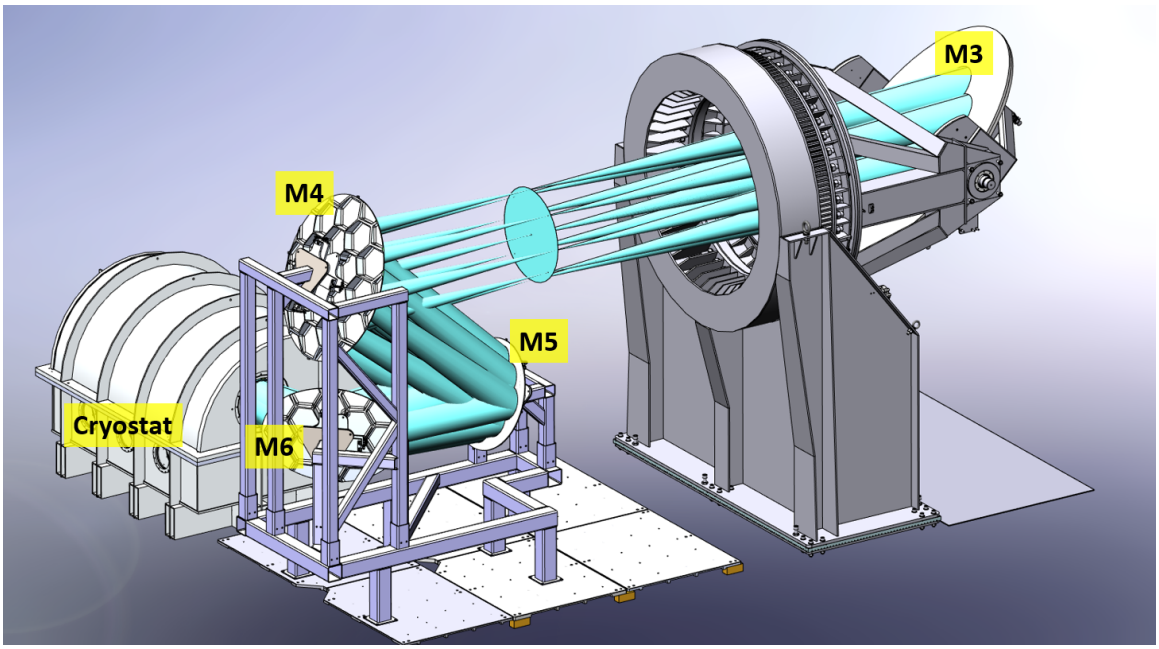

Figure 4.3: A CAD model showing the warm optics (M4, M5, and M6) inside of the receiver cabin. TolTEC's warm optics couple the telescope's tertiary mirror M3 to the TolTEC cryostat. Each of TolTEC's warm optics feature a tip-tilt mechanism to allow for precise adjustments to the alignment.

4.2.2 Optics

The LMT is a Cassegrain telescope consisting of a 50-m ellipsoidal primary dish (M1), comprised of 180 aluminum panels with actuators to correct the dish shape, and a 2-m hyperbolic secondary mirror (M2) [43, 44, 93]. Radiation reflected from the secondary mirror passes to a tertiary mirror (M3) stationed just before the telescope's Cassegrain focus. This mirror then reflects radiation towards TolTEC's warm coupling optics: M4 and M6 are parabolic mirrors while M5 is a flat (see Fig. 4.3). Please refer to [45] for further details on the design and performance of TolTEC's warm coupling optics.

TolTEC's window is a 330 mm diameter anti-reflection (AR) coated Ultra-High Molecular Weight Polyethylene (UHMWP) window based on the design from the SPIDER Project [94]. Immediately internal to the cryostat is a highpass 300 K filter that reflects 95 % of incoming infrared (IR) radiation. Following the 300 K optics,

there is a 45 K filter cassette that acts as a shader, further reflecting IR radiation to prevent it from reaching the 4 K optics volume. The last IR filter and its mount are positioned at an image of the primary mirror, functioning as TolTEC's Lyot stop.

Beyond the Lyot stop is TolTEC's 4 K optical volume where the optics bench is located. The unpolished aluminum cavity has been deadened using a blackened copper sheet mounted to the lid of the 4 K stage, a layer of charcoal-infused cloth to cover the optics bench, and a blackened 1 K baffle surrounding the Lyot stop.

Inside the 4 K volume, incoming radiation reflects off a parabolic aluminum mirror which focuses onto the first dichroic filter (DF) in the optics chain. At the DF, the radiation is split, allowing only 1.1 mm radiation through two silicon lenses that focus it through a lowpass filter onto the 1.1 mm array. The reflected 1.4 and 2.0 mm radiation passes through a silicon lens that focuses it onto the second DF. Here, only 1.4 mm radiation is permitted through, which is then reflected off a folding flat, focused by another silicon lens, and lowpass filtered before arriving at the 1.4 mm array. Lastly, the 2.0 mm radiation is reflected from the second DF to a silicon lens, lowpass filtered, and absorbed onto the 2.0 mm array. Each of the five silicon lenses in the system have a mechanically etched anti-reflection (AR) coating [46, 48].

4.2.3 Half-Wave Plate and Rotator

TolTEC includes an ambient temperature continuously rotating half-wave plate rotator (HWPR) located at the window to the cryostat. Continuous modulation of signal is a commonly used technique to mitigate $1/f$ noise [95]. In the case of TolTEC, this noise can originate in the form of uncorrelated $1/f$ noise from the detectors or in the form of correlated $1/f$ noise from the atmosphere. By modulating the signal at a high enough rate, the astrophysical polarization signal of interest is shifted to frequencies above the low-frequency ranges.

The TolTEC HWPR rotates a half-wave plate at a rate of 2 revolutions per second, modulating the astrophysical signal up to 8 Hz. To reduce the effect of systematics introduced by the HWPR itself, the HWPR utilizes air bearings for steady and stable rotation as well as a high precision optical encoder for precise tracking of the motion [96]. Furthermore, the rotation is driven by a direct drive torque motor. As a result, we eliminate the presence of timing belts or gears that can couple vibrations or other undesired motions to the rest of the system.

Two separate achromatic HWPs will be used to modulate the linear polarization of the incoming signal [97]. While one HWP could theoretically be used across all three TolTEC bands, modeling has shown that there is a tradeoff between the usable bandwidth of the HWP and the extent of the mismatch in the reflectivities and emissivities in the two orthogonal axes. As such, TolTEC includes one HWP optimized for the bands centered on 1.1 mm and 1.4 mm, and another optimized for the bands centered on 1.4 mm and 2.0 mm. Currently, the HWP optimized for the bands centered on 1.1 mm and 1.4 mm is in use.

4.2.4 Detectors and Readout Electronics

Similar to NIKA/NIKA2 and MUSCAT, TolTEC utilizes superconducting kinetic inductance detectors (KIDs) [58, 98]. TolTEC hosts three separate superconducting detector arrays, each with its own focal plane, of TiN/Ti/TiN thin film resonators [39]. Leveraging the inherent multiplexing capability of KIDs, each array is split up into networks with $\geq$ 500 LEKIDs capacitively coupled to a single superconducting transmission line (see Table 4.1 for the breakdown by network). Each network is further divided into pixels, with each pixel consisting of two detectors that offer sensitivity to two linear polarizations at angles of either 0 and 90 degrees or 45 and 135 degrees.

A notable advantage of using KIDs for mm-wave astronomy, compared to other superconducting detectors such as bolometers, is the relative simplicity of the readout electronics chain (see Fig. 2.8). Within the cryostat, we utilize commercially available coax cables, attenuators, and DC blocks; however, our low noise amplifiers (LNAs) were custom-made and are installed at the 4 K stage [70]. External to the cryostat, each network has its own set of warm readout electronics, developed at ASU and based on previous designs for the BLAST-TNG readout [68, 83, 86].

4.3 Installation and Hardware Performance

4.3.1 Overview

TolTEC was installed at the LMT in November 2021 and the first site cooldown occurred on December 21, 2021. After addressing hardware issues that emerged following installation, we began on-sky commissioning in June 2022.

This section describes the procedure to align TolTEC with the telescope using the warm coupling optics, compares the cryogenics performance at the site to the laboratory, and examines the system noise while the window is covered. Additionally, we re-characterized the optical performance by repeating the bandpass and efficiency measurements performed in the laboratory.

4.3.2 Optical Alignment

To align TolTEC with the telescope's tertiary mirror M3, we utilized multiple methods. First, we used a laser theodolite to measure the positions of the mirrors in the receiver cabin to match to the CAD model. We then installed a plate with a laser that had been previously aligned to the 1.1 mm array's center pixel prior to shipment. We found that we had to redo the alignment of the laser since the arrays were in slightly different positions. To realign the laser, we used our robotic XY testing arm Wyatt to perform a beammap on its IR source and identify the new

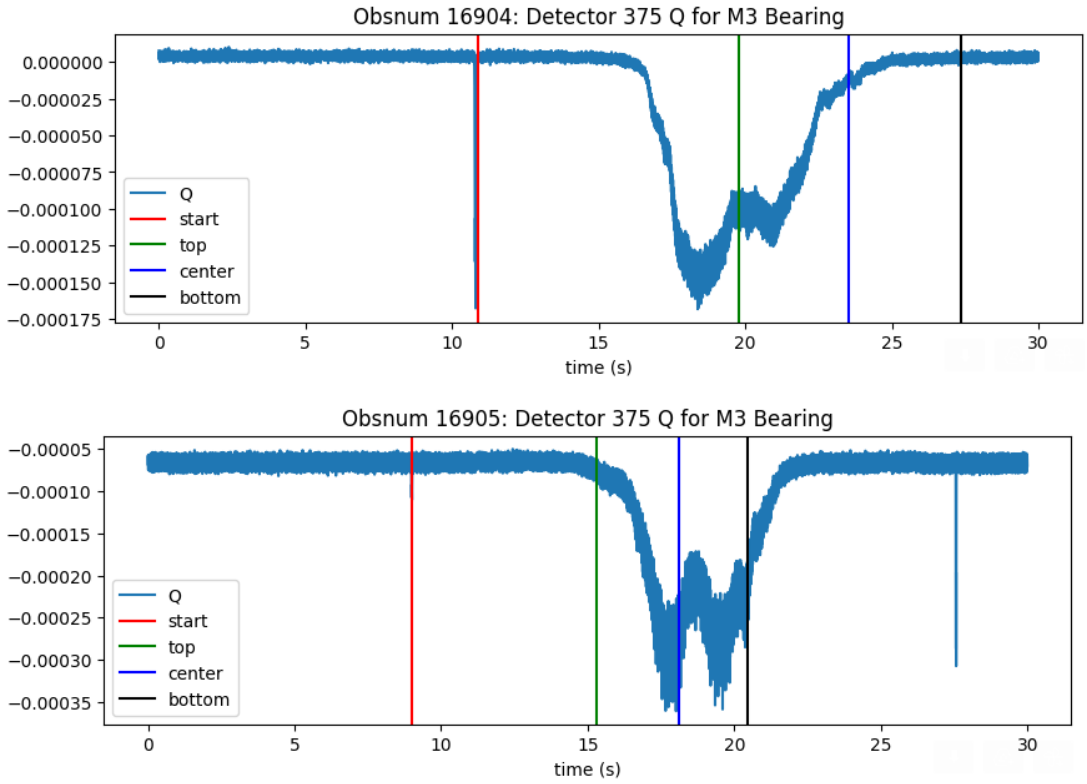

Figure 4.4: Timestreams for one of the central 1.1 mm array detectors. The top plot is before adjusting the mirrors and the bottom is after the adjustments from the blackbody wand tests. The green, blue, and black lines represent the position of the wand during the test, starting from the top of the mirror and moving downward in a straight line. After the adjustment, the center detector now sees the wand at the correct positions during the test.

position of the center pixel. With this set up we were able to center up M6, the warm coupling optic closest to the window; however we found that the laser was too faint and extended by M3 to perform full end-to-end alignment.

For the mirrors leading to M3, we were able to use a secondary method where we dipped blackbody wands in LN2 and slowly moved them to identify the center of the optical beam with respect to the mirror to be adjusted. The top plot of Figure 4.4 shows the offset between the mirror and beam centers. This offset was used to adjust the mirrors resulting in the bottom plot where the mirror and beam centers align. By doing this going from M5 outward, we were able to align the optics to M3.

4.3.3 Cryogenics Performance

For details on the design and laboratory performance of TolTEC's cryogenics, we refer you to [72] and [83].

Following installation at the LMT, we discovered a blockage in the dilution unit and a touch between the 45 and 4 K stages in the DR. Both issues were resolved by May 2022 and since then we have been able to collect thermometry data at the proper base temperatures to compare to TolTEC's laboratory performance.

As we had observed in the laboratory, the system takes approximately 5 days to reach base temperature. Aside from the coldest stage, 0.1 K, the cryogenics have performed as well as during laboratory testing. After installation, the arrays have a base temperature around 185 mK rather than the laboratory measured temperature of $\sim$155 mK (see Figure 4.5). We do not believe the 30 mK increase in array temperature to be due to a higher background loading within the cryostat as the three warmer stages are at their nominal temperature. In the next upgrade to the system, we will confirm this by reinstalling the macroscopic bolometer from our laboratory tests which showed a background loading of approximately 5.8 K.

We note that the loading on the arrays from the window has increased after uninstalling the 2.54 cm diameter aperture we had placed over the Lyot stop for lab testing. Laboratory tests at UMass showed a small change (approximately 5 mK) in array temperature with the aperture removed. As will be discussed in §4.7.2, one of the consequences of a higher loading from the window is that our detectors' quality factors have decreased from on order $\sim$ 20k to $\sim 5-10$k; a higher array temperature does contribute to lower quality factors but it is not the dominant effect.

After these considerations, we suspect that the increase in array temperature is caused by reduced thermal contact between the DR's mixing chamber plate and the OFHC Cu busbar that extends towards the main cryostat. We examined thermometry data from between 2019 to 2022 and found that the temperature at this joint had

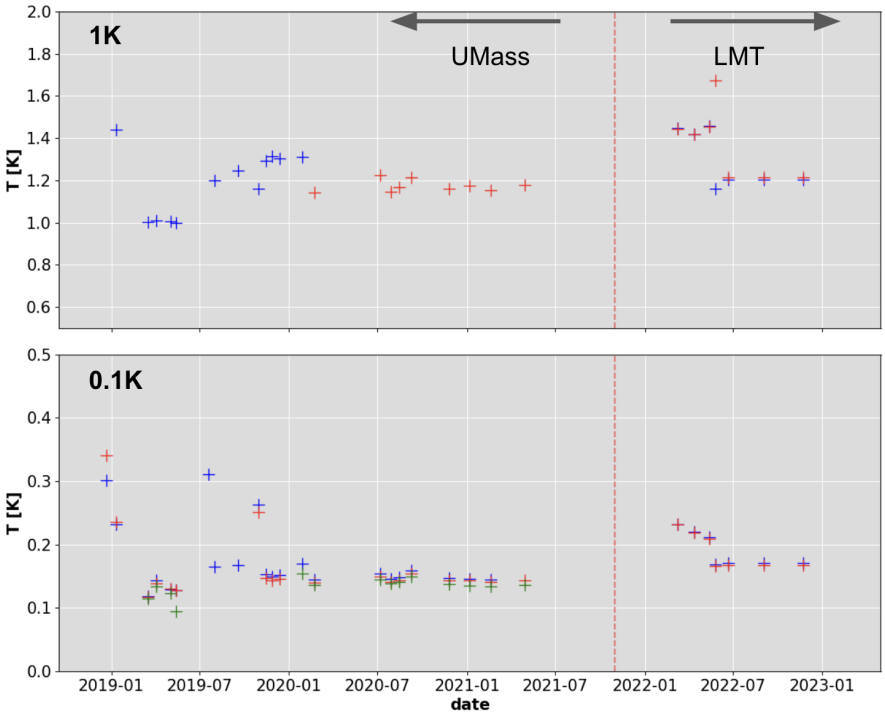

Figure 4.5: TolTEC's array temperatures measured at the warmest point in the 1 and 0.1 K thermal chains (e.g., at the entry of the busbars to the array package). Blue, green, and red points correspond to the 1.1, 1.4, and 2.0 mm arrays, respectively. All data before the vertical dashed red line was taken in the UMass laboratory and after is the data from the LMT cooldowns. As shown here, the 1 K and 0.1 K stages just after arriving at the LMT were operating hotter than seen in the laboratory since we could not reach base temperature due to the hardware issues in the dilution refrigerator. After the repairs, we were able to reach base temperature for the 1 K stage and near base temperature for the 0.1 K stage. The array focal planes at 0.1 K are slightly hotter than before due to worse contact between the mixing chamber and the busbar that connects to the cryostat.

increased by 30 mK. In July 2023, we opened the DR and reinspected the joint. We found that the bolting hardware used had less clamping force than expected. The hardware was reconfigured in order to improve the clamping force when cold and we anticipate a lower thermal gradient in our next cooldown.

4.3.4 Bandpasses

After installation, we decided to remeasure the bandpasses of the instrument to confirm no change in spectral response and to determine the reported bandpasses for

observers. In order to measure the bandpasses of TolTEC's three arrays, we use a Fourier Transform Spectrometer (FTS) that was built at UMass Amherst based on the design of COBE-FIRAS ([78]). We use a 200°C blackbody source as the input to the FTS.

In the laboratory, we were able to directly couple the FTS to the window of the cryostat using a single parabolic mirror. At the LMT, due to the placement of the cryostat and the size of the FTS, the FTS is installed on a scissor lift to couple the parabolic mirror to M3. M3 is coupled to TolTEC's warm optics (see Fig. 4.3) and can pass the FTS signal to the window.

Due to delays and other constraints on operating time at the telescope, we have been yet unable to perform this measurement. Once consistent power is reestablished at the telescope, we plan to cooldown again in January 2024 then perform this measurement. See Fig. 3.6 for TolTEC's spectral response as measured in the laboratory.

4.3.5 Efficiency

As was described in [83], we measured TolTEC's optical efficiency by filling the window with either a 300 K or a 77 K source, then measuring the change in frequency between the two observations. Efficiency measurements such as these provide a quick, but powerful look at the system's overall optical performance. As a note, unlike our in-lab testing configuration, we performed this measurement with the full aperture at the Lyot stop available rather than a 2.54 cm diameter aperture.

For the 300 K source, we opened the window and allowed it to see the warm optics. M3 was rotated away from M4, so TolTEC was observing the back of the M3 mirror mount. This was not a proper 300 K source, so in the future we will cover the window with a layer of charcoal-imbued cloth which will act as a blackbody; the temperature of the receiver cabin is regularly closer to 285 K, so we will also use

this as the warm source temperature. In the case of the cold 77 K source, we filled a Styrofoam container with LN2 and placed a panel of Ecosorb tiles inside as our blackbody source. One issue we found in this test was that the container did not fill the entire window, thus many of the detectors were not usable for this test. Since we were unable to obtain usable observations, we will attempt this test again once the instrument is cold.

4.4 Measurement and Scanning Strategies

4.4.1 Readout Method

The detailed design of the TolTEC's readout electronics, the readout hardware are described in the in-lab characterization paper [83]. The readout procedure and raw KIDs data handling are described both in Wilson et al. [83] and Ma et al. [71]. Since the on-sky commissioning, we have improved the readout procedure and implemented new algorithms to best set the detectors for optimal readout.

4.4.1.1 Detector Identification Sweeps

The detector identification procedure at the site remains the same as that we employed during the lab testing. In brief, we identify the detectors in each network by building a waveform of 1000 equally spaced readout tones, spanning the 500 MHz of readout bandwidth, and then sweeping each network's local oscillator (LO) over a range of 1 MHz in steps of 2 kHz. This fully samples the readout bandwidth with each frequency bin being sampled by two different readout tones at two different times in the sweep. The entire sweep takes 24 s. The detector identification is done by first taking the derivative of the measured readout signal (S21), noted as "D21", which removes the slow-varying baseline, then running an iterative peak find algorithm.

Figure 4.6 shows one of the full network sweep (dubbed as "VNASweep") taken during the 2022 December commissioning. Table 4.1 lists the number of identified

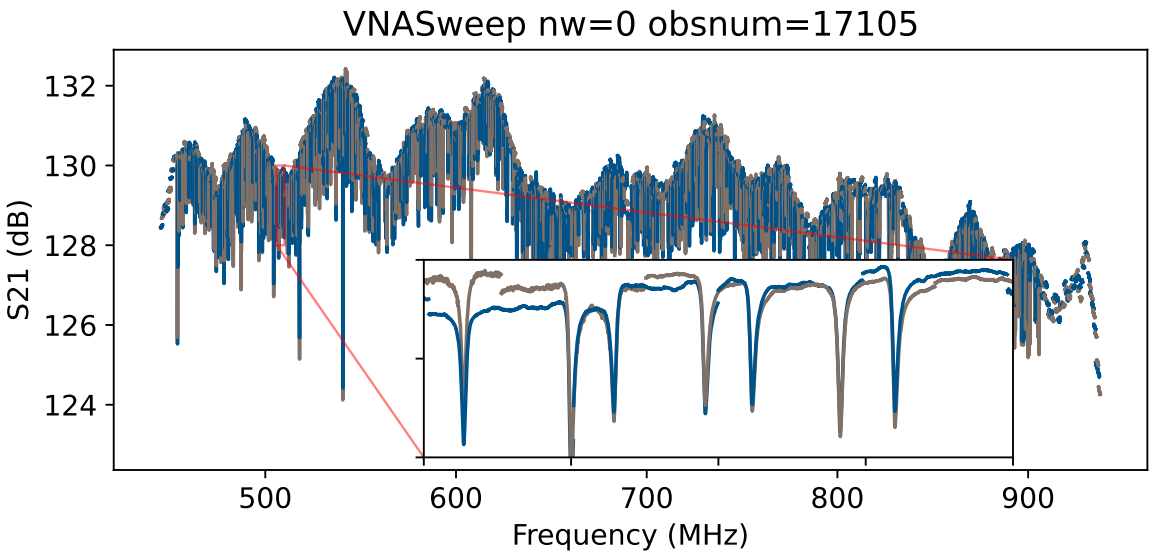

Figure 4.6: The network sweep showing the full 500 MHz bandwidth of the readout of detector network 0. Neighbouring readout channels are plotted in alternating color.

detectors in the 12 networks that were enabled at the time of observation. Note that at site, to account for the varying observing conditions (e.g., background loading), we changed the detector finding algorithm parameters to make it more sensitive, in order to increase the total number of identified detectors, which produced a larger amount of false positives, rendering the numbers higher than the total designed number. The data of false-identified detectors are excluded when making the maps.

4.4.1.2 Tune Procedure

Once detectors are identified in the detector identification sweeps, individual readout tones are placed at the frequency of each resonator as determined by the finding algorithm. There is no electrothermal feedback in a KID readout and so as the optical loading on the detectors change, we must periodically "tune" the readout tones back onto the resonators. We do this with a series of "target" sweeps - one to identify the optimal locations in frequency for the readout tones, and another to verify the choice. Each target sweep is performed by sweeping the LO by ±87.5 kHz in steps of 1 kHz. The I-Q data for each detector from the first target sweep is fit to a generic

Table 4.1: An accounting of the resonators in the three TolTEC arrays by design, automatically identified at lab, and automatically identified at the site. Note that at site, to account for the varying observing conditions (e.g., background loading), we changed the KIDs finding parameters to make it more sensitive to increase the total number of identified detectors, which produced a noticeable amount of false positives, rendering the numbers higher than the total designed number. The data of false-identified detectors are excluded when making the maps. Network 10 is not enabled during the time of observation.

Array	Network	Design	In-lab	At-site
1.1mm	0	684	643	687
	1	522	494	523
	2	558	552	564
	3	564	556	568
	4	556	557	566
	5	510	502	513
	6	618	590	523
1.4mm	7	676	652	595
	8	588	567	515
	9	590	601	602
	10	678	609	–
2.0mm	11	544	526	565
	12	628	588	639

KID resonator model of the form

$$S_{21}(f_p) = \mathcal{G}(\tilde{S}_{21}(f_p; f_r, Q_r)) \,, \tag{4.1}$$

where $\tilde{S}_{21}$ is introduced as the "canonical" form of the transmission coefficient, expressed as

$$\tilde{S}_{21} = \frac{Q_r}{1 + 2\mathrm{i}Q_r \frac{f_p - f_r}{f_r}} \,. \tag{4.2}$$

Introducing

$$r \equiv \frac{1}{2Q_r} \tag{4.3}$$

$$x \equiv \frac{f_p - f_r}{f_r} \tag{4.4}$$

$$X \equiv r + x\mathrm{i} \,, \tag{4.5}$$

Equation 4.2 can be rewritten to a more symmetrical form

$$\tilde{S}_{21} = X^{-1} \,. \tag{4.6}$$

The function $\mathcal{G}$ in Equation 4.1 is related to the complex gain of readout circuit and is parameterized as

$$\mathcal{G}(\tilde{S}_{21}; G, K, M) = G\tilde{S}_{21} + Kf + M \tag{4.7}$$

where G, K and M are complex parameters.

From the fitting, we obtain the best model parameters f_r, Q_r, G, K and M. We use the set of fitted f_r as the refined locations of the tone lookup table, and a second target sweep is made to verify the results. This entire tuning process takes 34s in total.

Figure 4.7 shows a typical model fit in the I-Q plane with the $\tilde{S}_{21}$ (i.e., "normalized" to remove the gain signature) data and model. Following Equation 4.6, we use the fitted parameters from each tuning of the arrays to transform timestream (I, Q) data to timestream (r, x) channels, where x-values are proportional to the optical power variations on the detector and r-values are a quadrature channel sensitive to the readout noise.

We monitor the quality of the tuning of each resonator by measuring the angle, $\phi \equiv \arctan(-x/r) = \arctan(\tilde{Q}/\tilde{I})$. Perfectly in-tune resonators have $\phi = 0$. Our resonator model allows us to predict the readout noise degradation as the resonator goes out of tune and so we monitor the set of θs for the system so that we may run the tuning procedure when needed. The readout noise degradation can be expressed as a function of ϕ, or equivalently the central angle $\theta \equiv 2\phi$, as shown in Figure 4.7.

In Figure 4.8, it shows an example TUNE sweep taken during the 2022 December commissioning. Due to higher background loading, the measured median Q_r values for the 1.1, 1.4, and 2.0mm arrays are 10535, 6510, and 5626, respectively, lower than what we found during the lab testing.

4.4.1.3 DriveFit

Every detector in the system has a *unique* probe tone readout power and frequency. It remains a challenge in fielded KID instruments to select tones for each detector that will yield the best combination of linearity and sensitivity when there are hundreds of resonators on the same feedline. This is further complicated by variations in background loading from the atmosphere which can induce significant shifts in KID resonant frequencies and affect quality factors. When this happens, the network requires a "re-tuning" to address, where the probe tone for each KID is modified to return detectors to optimal operation. For in-lab testing, we developed the "AutoDrive" automated procedure to empirically identify these probe tone powers,

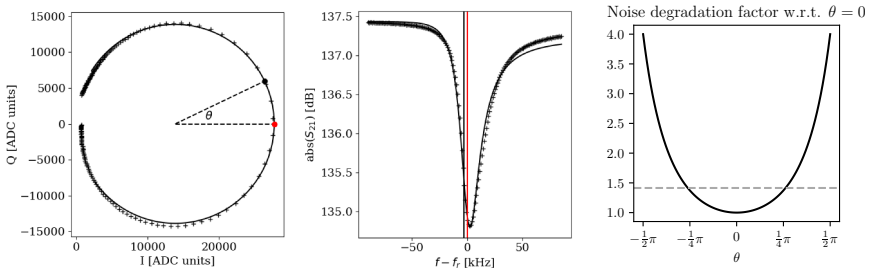

Figure 4.7: *Left*: A typical resonator I-Q plane data and model. The red dot signifies the optimal tone location while the black dot shows the current tone location prior to the tuning. (Middle:) The same data as in the left figure but in the frequency-S_{21} plane. As described in the text, the model is weighted to match the data in the resonance rather than in the wings. The vertical lines show the optimal tone location (red) and current tone location (black). *Right*: The noise degradation as a function of detuning, θ for this detector. The horizontal line marks the angles where the readout noise is $\sqrt{2}$ greater than when the resonance is optimally tuned.

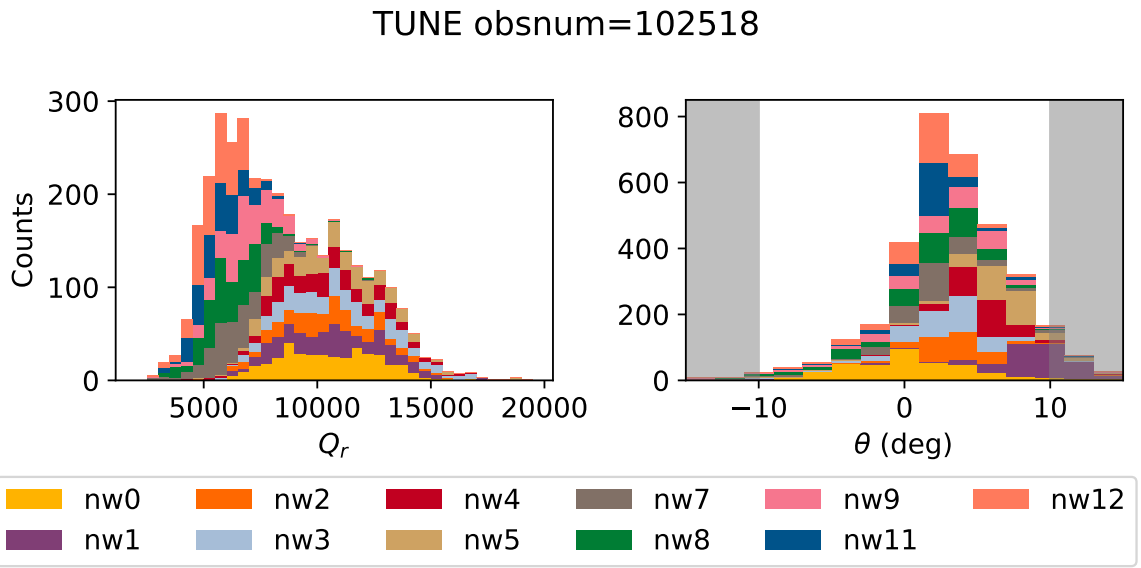

Figure 4.8: *Left*: The histogram of the Q_r values in all good detectors as flagged by the "beammap" reduction routine (see § 4.6.2) during the 2022 December commissioning. The color coding indicates the different detector networks. *Right*: The histogram of the θ values. Detectors fall into the shaded region are "out-of-tune" and will have elevated noise.

or amplitudes, by systematically performing target sweeps from low to high readout powers through reducing the programmable drive attenuation. At high enough readout powers, the nonlinear kinetic inductance of the KIDs will cause the resonator response to enter a bifurcation regime that can be likened to classic Duffing oscillator behavior [38]. MKIDs are usually biased at readout powers before this bifurcation regime to avoid switching between these two states. To optimize sensitivity, it is ideal to drive resonators with large readout powers close to, but before bifurcation as this has been found to overcome amplifier noise and to suppress the effects of two level systems (TLS) noise [67]. From these sweeps, the readout power corresponding to bifurcation of the resonance circle for each KID is determined. A drawback of this procedure is that it takes about 15-30 minutes to finish and has to be done as soon as the list of tones changes, such as due to a change of the weather at the site.

During the on-sky commissioning, we implemented a new, model-based approach called "DriveFit." This new approach involves fitting KIDs with a model [99] for the KID phase that takes into account the kinetic inductance nonlinearity. More details about this new approach can be found in [100]. The kinetic inductance nonlinearity is a purely reactive effect that affects the MKID frequency response. In this method, we find a nonlinearity parameter a [101] for each KID in a network and at each readout power in a target sweep. For this parameter, $a > 4\sqrt{3}/9 \approx 0.77$ corresponds to bifurcation. This method requires fewer target sweeps, about 5, to derive a reasonable estimate of the unique tone frequency, near KID resonance, and tone power for each detector in a network corresponding to a user-defined nonlinearity parameter. We have also found that this method will find an ideal network readout power as set by the drive attenuation. This procedure naturally accounts for varying transmission across the network bandwidth and the varying physical parameters of different detectors.

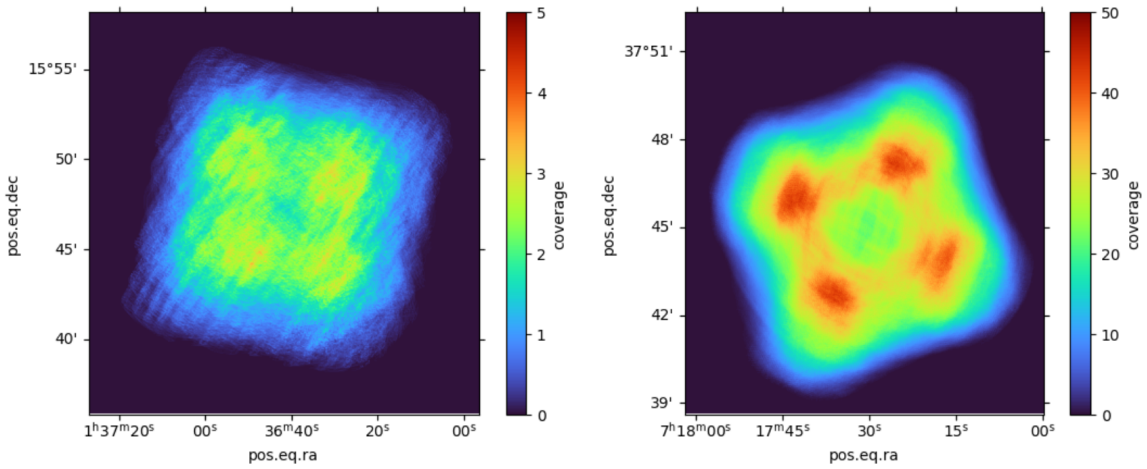

Figure 4.9: Two 270 GHz coverage maps from the December 2022 commissioning run. The left image shows a `raster` scan over M74. The right shows a `lissajous` scan over MACS J0717.5+3745. While the `raster` scan shows fairly uniform coverage, this `lissajous` scan suffered from low coverage over the central region of this map due to sub-optimal selection of parameters; these have been corrected for future observations.

4.4.2 Observing Modes

Currently, TolTEC utilizes two primary scanning patterns for science observations: (1) a `raster` pattern where the telescope is moved along regularly spaced parallel lines and (2) a `lissajous` pattern. We have implemented two additional patterns including the `rastajous` pattern, a combination of the two primary ones, along with a `double lissajous`, a Lissajous that allows for control of both major and minor axes parameters.

All mapping patterns include some overhead time (e.g., time spent off source during the observation) from tunes and pointing observations but, as will be discussed below, some patterns have features that further reduce the scan efficiency. For interactive examples of the TolTEC scanning patterns, please visit the TolTEC Observation Planner site.

4.4.2.1 Raster

In the `raster` scan mode, the telescope is slewed across the source in one direction, steps down by a user-defined amount, then slews in the opposite direction until the entire field is imaged. `Raster` scans are ideal for uniform coverage of large areas of the sky greater than $6'$ in length. Typical maps have speeds of $50''$/s, though scan speeds are limited to no greater than $200''$/s for telescope stability. When performing `raster` scans over the same source, we perform at least two observations using different sky position angles in order to reduce scan-synchronous effects.

The `raster` pattern has an additional overhead factor that comes from the telescope turnaround time at the end of each row. At this location, the telescope acceleration is high and the pointing is not well known meaning this time does not contribute to the final on-source time. The `raster` overhead time can be estimated as the number of rows times an estimated turnaround time per row. The turnaround time depends on the scan speed of the telescope and the step size between rows. The current version of the TolTEC Observation Planner estimates it to be approximately 5 s at each turn.

4.4.2.2 Lissajous

Whereas `raster` scans are preferred for covering large areas, `lissajous` scans are more suited for coverage of areas between ~ 12.5 arcmin^2 to ~ 36 arcmin^2, or on the order of the LMT's field of view. This is currently the smallest available scanning pattern for TolTEC. The pattern is generated by the set of parametric equations for a general Lissajous curve

$$x(t) = x_{len} \sin(\omega_x t + \delta), \tag{4.8}$$

$$y(t) = y_{len} \sin(\omega_y t) \tag{4.9}$$

where the user controls the lengths, speeds, and angular separation for x and y. The equations generate the path that the telescope boresight will follow, but the time it will reach a position on the path is set by the user-defined telescope speed. Since Lissajous patterns are continuous, the scan will continue until the desired exposure time elapses. The proper selection of these parameters is vital for uniform coverage over the map (see Fig. 4.9 for an example of poor central coverage). We found that values of $\omega_x = 5.2\,\mathrm{rad/s}$, $\omega_y = 4\,\mathrm{rad/s}$, $\delta = 45°$ provide sufficient coverage when simulating TolTEC observations. These are now the default parameters when selecting a `lissajous` scan on the TolTEC Observation Planner.

`Lissajous` scans also offer one other benefit over `raster` scans in that they do not experience as high an efficiency loss at turnaround points. During `raster` scans, the telescope must quickly decelerate at the end of each row in order to turn around and scan in the next direction. As stated previously, the data at these locations is not valid and the time adds to the overhead. Conversely, the `lissajous` scan does not have the same level of deceleration when switching directions due to the decreased turn angle (as compared to 180° for a `raster` scan).

4.4.2.3 Additional modes

Given the proper equation for moving the LMT, one can create any scanning pattern desired. As stated previously, we have implemented and tested two additional scanning patterns. The `rastajous` pattern is a superposition of a `lissajous` pattern at each point on a `raster` scan. The main benefit of the `rastajous` scan is the increase in coverage by adding the two patterns together. However, it does suffer the same efficiency loss as the `raster` pattern when the telescope changes scan direction. We recommend only utilizing this pattern for 'medium' scale maps (below 1 deg. sq.) as the time required to complete the scan is much higher than a `raster` map.

The second pattern we have implemented is the `double lissajous` pattern. It is the sum of two independent `lissajous` patterns. This scan pattern can offer coverage for a larger map area than the `lissajous` pattern while minimizing overhead due to telescope motions. It is still limited to areas smaller than the `raster` or `rastajous` maps. We are also exploring additional patterns such as the Lissajous `daisy` pattern implemented at other facilities, such as IRAM-30m and GBT.

Finally, while the HWPR is always installed on the front of the camera, the HWPs can be manually swapped prior to an observation. For all commissioning observations aside from the polarization tests, we opted to not have either HWP installed so as to have access to all three bands (see §4.2.3 for more details).

4.5 Data Reduction and Management

4.5.1 Mapmaking

In order to convert the raw TolTEC Time Ordered Data (TOD) into on-sky maps, we have implemented a standalone, end-to-end data reduction pipeline for TolTEC data, known as `citlali` [82]. In addition, we have integrated existing external mapmaking pipelines, such as the `Minkaki` maximum-likelihood mapmaker [102] and the Time Ordered Astrophysics Scalable Tools (TOAST) software framework [103] into the TolTEC software stack. This approach allows for fast TOD processing and mapmaking of TolTEC data with `citlali`, while also leveraging the more computationally expensive, yet superior astrophysical flux recovery capabilities offered by the maximum likelihood mapmaking pipelines.

4.5.1.1 Citlali

`Citlali` is an open source, C++ software package that reduces both TolTEC science and calibration observations, as well as performs co-addition of multiple observations and post-mapmaking reduction steps, such as map filtering and point source

characterization. The pipeline is optimized to allow for near real-time reductions of most TolTEC raw data products in order to efficiently provide quick-look and calibration observation data products. The core algorithms of `citlali` are built upon those implemented in the data reduction pipeline for the AzTEC camera [104] and have therefore undergone extensive verification through analysis of AzTEC data. Following an initial setup stage which computes map dimensions and aligns the raw TODs and relevant telescope pointing information onto the same time grid at the detector sampling frequency, `citlali` reductions consist of approximately four stages: (1) raw TOD processing, (2) removal of the atmospheric signal, (3) mapmaking, and (4) post-mapmaking analyses which are carried out sequentially.

In the first stage, the raw TODs are subdivided into smaller time-chunks that are processed in parallel and converted from the raw I and Q data into units that are proportional to the incident intensity on the detectors. If an observation is intended to perform polarization measurements, a rotation is applied to each detector's TOD to determine the contribution to each Stokes parameter in the sky reference frame. If one of the continuously rotating half-wave plates (HWPs) are installed, a further rotation by the HWP's position angle is performed. A despiking routine to remove cosmic ray glitches is then applied, followed by low-passing and/or high-passing to remove high-frequency or low-frequency noise respectively. A notch filter is also included to remove narrow-band signatures at high frequencies that are not sufficiently removed by lowpassing. TolTEC's nominal sampling frequency of 488 Hz is higher than required for most observations, so decimation is applied following lowpassing to reduce the computation time and memory footprint during the atmospheric removal stage.

For non-`beammap` observations, flux calibration is performed using a Flux Calibration Factor (FCF) calculated for each detector from a `beammap` observation (see §4.6.2) of a bright flux calibrator. An on-site radiometer provides a measurement of

τ_{225GHz} for each observation [105], which is used to predict the opacity at each of the TolTEC bands from atmospheric models [41, 106, 107]. A polynomial fit of the transmission as a function of elevation is performed for each model and the extinction correction is then applied on a per-sample basis.

`Citlali` utilizes principal component analysis (PCA) to perform atmospheric subtraction. Each time-chunk is mean-subtracted, and its detector correlation matrix is calculated. An eigenvalue decomposition is then carried out and a number of the largest eigenmodes are zeroed out to remove the largest common modes across all the detectors prior to reconstructing the TOD. This technique relies on the fact that the atmospheric signal is the dominant contribution to the total intensity and assumes that its inherent correlations do not vary on timescales smaller than the length of a time-chunk. For bright sources and extended emission, however, a fraction of the astrophysical signal will be removed with this technique; we estimate the extent of this effect by creating and passing a synthetic TOD through the exact same reduction stages, atmospheric subtraction, and reconstruction as the raw TODs, making use of the raw TOD's calculated eigenmodes. This synthetic TOD only includes a 2D Gaussian whose FWHM is derived from the measured FWHMs of each detector in the `beammap` observations, thereby approximating the PSF of each detector.

Two mapmaking algorithms are implemented in `citlali` which are aimed at providing a balance between computation time and the resulting map noise properties. The naive mapmaking algorithm assigns TOD samples to whatever pixel bounds they fall within, producing a simple 2D histogram of the weighted average TOD values. Maps can be weighted using either the inverse of the detector variance or the median sensitivity of each detector calculated in a beammap observation. Detectors with outlier weights greater or less than a user-specified tolerance can be flagged. The flagged detectors can then have their weights set to the median weight of all the detectors within a given array to limit or remove their impact on the final maps.

The second mapmaking algorithm convolves each TOD sample with a truncated Jinc function prior to adding its contribution into the maps. While slower than the naive mapmaker, the truncated Jinc function has no response at spatial scales smaller than those at which the source varies, thereby reducing high frequency noise in the maps [108]. A map of the synthetic point source TOD is also generated using the same algorithm. In order to estimate the noise level of the maps, jackknifed noise realizations are made by multiplying each time-chunk by a random ± 1 to create an arbitrary number of corresponding noise maps.

In the final stage, individual maps are coadded if multiple observations are being reduced and an iterative Wiener filter can be applied in order to improve the map response to point sources. The map filter uses the synthetic point source maps as a filter template in order to restore the flux lost during the removal of the atmospheric signature recovery [109].

`Citlali` outputs its maps and relevant meta information in the FITS file format, which are written to be fully compatible with the `astropy.fits` and `astropy.wcs` python packages. In order to facilitate reductions of TolTEC data with external maximum-likelihood mapmakers, `citlali` can also output partially reduced timestreams after the TODs have been converted from the raw KIDs data units and flux calibrated.

4.5.1.2 Minkasi

`Minkasi` is a maximum likelihood mapmaker that was developed for the MUSTANG2 collaboration ([110, 111]). The formalism that is the foundation for maximum likelihood mapmaking has been described in detail for CMB experiments ([112]). Briefly, this mapmaking method is based on the model that detector timestreams consist of the true sky being operated on by the telescope pointing matrix with the addition of noise. After defining a likelihood for the true sky given the data and maximizing over all sky realizations, the sky map that maximizes the likelihood is a

simple function of the timestreams, telescope pointing, and noise. The timestreams and telescope pointing are given from one's observations, so the difficulty in this mapmaking method is in the estimation of the noise which is not known *a priori* and must be estimated from the data. `Minkasi` handles this estimation in a manner that leverages observations of several thousand detectors over small angular scales in moderate to brief timeframes.

The `Minkasi` mapmaking procedure starts with calibrated timestream outputs from `citlali` where the only actions performed on the timestreams are flux calibrations based off of beammaps and an atmospheric extinction correction. To estimate the noise covariance, timestreams are first rotated into the eigenspace defined by their Singular Value Decomposition (SVD). From there, the rotated timestreams are Fourier transformed from the time domain to the frequency domain and power spectra are taken and smoothed. The noise covariance is therefore defined in Fourier space. Since TolTEC has thousands of detectors and each observations has thousands to tens of thousands of samples, this can be done directly for brief observations but longer timestreams need to be divided up into smaller scans to make the SVD computationally practical.

In a similar vein, the large number of detector samples in a given observation makes the matrix inversion necessary for the direct computation of the maximum likelihood map infeasible. Instead, `Minkasi` solves a linear equation for the map using a Preconditioned Conjugate Gradient (PCG) algorithm. In the implementation of the `Minkasi` mapmaker for TolTEC, the PCG uses the inverse of the counts per map pixel as the preconditioner since this is a satisfactory approximation of the inverse variance and improves convergence. After an initial solution is found by running the PCG for a conservative 80 iterations, the resulting map is reprojected into the timestream space and differenced from the timestream data. These residual timestreams, which should now more accurately resemble the noise in the timestreams, are used to re-estimate the

noise covariance as described above. The PCG is then run again using that estimate of the noise and the previous map solution as a starting point. This procedure is repeated several times to improve the flux recovery in the maps. The resulting maps are free from the bias induced by filtering needed to remove atmospheric correlations present in other mapmakers allowing for better recovery of angular scales larger than the instrument field of view.

4.5.2 Data Archive

The raw TolTEC data are transferred to the data storage service provider Northeast Storage Exchange (NESE) during the daytime. The off-site data processing and analysis are done on the "Unity" cluster, a heterogeneous cluster run by UMass Information Technology that allows groups to "buy-in" by contributing hardware. Members of the Unity cluster have priority access to their own hardware as well as access to all other idle nodes on the cluster. All the data products produced are then packaged and stored back on to the NESE.

As of 2023 August, the data products are still being validated by the science team. Once they are ready, the data products will be made available on the LMT Dataverse, a custom Dataverse instance that runs on the Unity cluster [113]. The end user will be able to search and retrieve the data through the publicly accessible and Virtual Observatory-compliant LMT Data Archive service.

4.6 Calibration

4.6.1 Focus and Astigmatism

Owing to variations in the temperature and weather conditions at the site, the shape of the primary mirror (M1) and position of the secondary mirror (M2) experience both stochastic and systematic fluctuations throughout the course of an observing night. It is therefore necessary to measure and correct for these effects at

several instances throughout the night. These measurements are performed independently through separate focus and astigmatism observations, where a bright point source is mapped using a 30 second, $4' \times 4'$ `lissajous` pattern.

In the focus correction observations, a series of maps (≈ 9 maps) are taken of the same source with the on-axis position of M2 offset within a range of values between -2.0 and 2.0 mm of the nominal position. A similar set of observations (≈ 4 maps) of the same source are taken for astigmatism observations, but instead the primary mirror is deliberately deformed in order to vary the level of astigmatism in the resulting maps. The range of physical deformations explored in the primary mirror are typically between -300 and 300 microns. For both focus and astigmatism observations, the source in the 270 GHz map is fit to a two-dimensional Gaussian and the measured source flux from all observations in the associated focus or astigmatism group are fit to a parabolic equation. The secondary mirror position or primary mirror deformation that corresponds to the maximum value of the source amplitude in the fitted parabola is then utilized as the optimal value. The optimal focus and astigmatism corrections are not constant between different focus and astigmatism observations, with the best secondary mirror vertical position varying between -2.0 and 2.0 mm and the ideal primary mirror deformation at around -75 and 75 mm.

4.6.2 Beammaps

As discussed in Section 4.4.1.1, the number and center frequencies of detectors recovered between different detector identification sweeps can vary. Furthermore, spurious features in the in the frequency sweeps can be falsely identified as actual detectors and be propagated into the raw data products. It is therefore difficult to directly associate a detector's frequency with its physical location on the detector array using the frequency sweep data alone. As the physical location of a detector is a requirement to coadd individual detector timestreams in science and most

calibration maps, we empirically measure individual detector characteristics through a `beammapping` observations of a bright (typically $\geq$ 1 Jy/beam at 270-GHz) point source. In a `beammap` observation, the telescope is slewed over the source in a raster pattern consisting of 300 azimuthal scans at $5'$ in length and $1.5''$ steps in elevation at a rate of $50''/s$. Each `beammap` takes approximately 30 minutes to complete and at least 2 are performed each night, with one near the beginning and one at the end in order to bracket any other observations taken during that night.

During mapmaking, a map is made from the timestream of each tone identified in the detector identification sweep. Each map is then fit to a two-dimensional elliptical Gaussian function in order to measure the peak value, centroid position, and beam shape of that detector's PSF. In addition to being used to identify the detector positions, `beammaps` also serve the purpose of measuring the flux calibration factor (FCF) for each detector. As the atmospheric removal stage of the pipeline can both subtract flux from the source and reduce the measured beamsize in the scan direction, we use an iterative procedure to remove the atmospheric signal and fit the source. In each iteration, the fitted beam is subtracted from the timestream before the atmospheric removal stage and re-added after the atmospheric cleaning has been performed. The source is then fit, and the process is repeated until all the fitted parameters converge to within a given tolerance. The fitted centroid positions are then offset with respect to a reference detector and rotated by the mean source elevation to the horizon.

Falsely identified or noisy detectors are found and flagged to be excluded from future analyses through upper and lower limits on the fitted parameters based on expectations on the on-sky detector footprints, beam shapes, map signal-to-noise, and the median detector sensitivities. An example of the unflagged fitted beam centroids and FWHMs measured from a `beammap` observation of the radio galaxy J1159+292 is illustrated in Figure 11. For our initial commissioning results, we found a need to flag $\sim$ 43% of the tones prior to improvements made to the detector readout hardware.

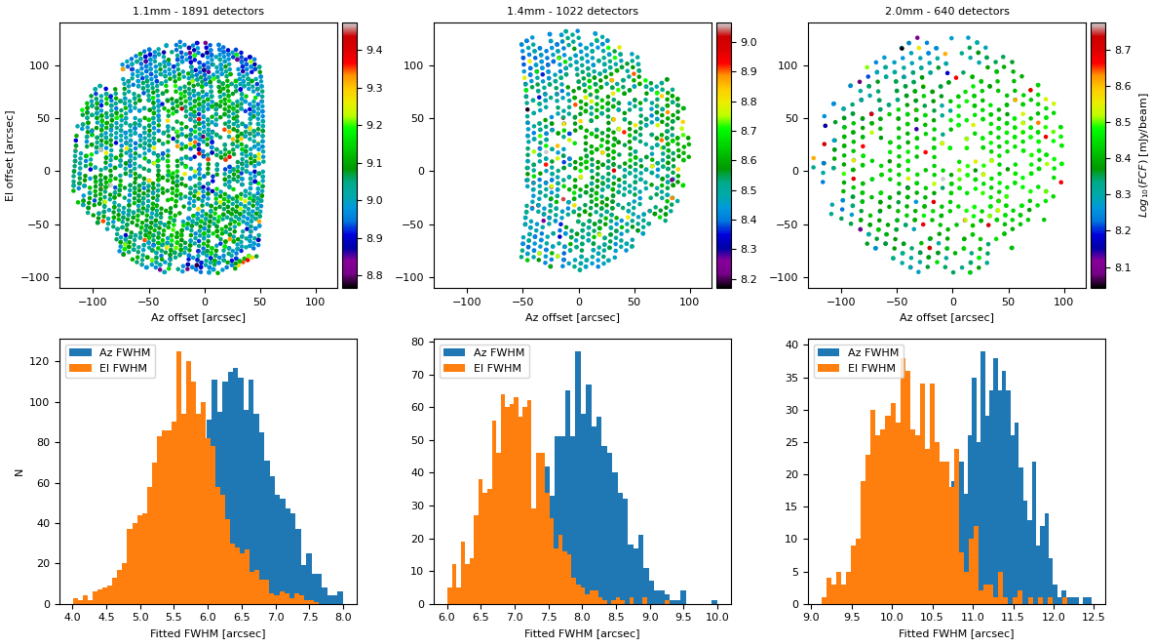

Figure 4.10: Top Row: Fitted detector centroid positions for each of the 3 TolTEC arrays measured from a beammap observation of the radio galaxy J1159+292. The colorscale is the flux-calibration factor for each detector. Falsely identified tones have been excluded. Bottom Row: Histograms of the measured (az, el) beam FWHMs from the same beammap observation for each detector array.

The average measured FWHMs of all unflagged detectors are $6.0 \pm 0.4''$, $7.5 \pm 0.4''$, and $10.7 \pm 0.3''$at 270, 220, and 150-GHz respectively, which are marginally larger than the expected values. Some asymmetries in the beamshapes are also present and are the result of residual errors in the primary mirror shape and telescope focusing.

4.6.3 Flux Calibration

TolTEC's primary flux calibrators include planets Uranus and Neptune as well as asteroids like Ceres. As mentioned above, during `beammap` observations, we estimate the FCF to convert from detector units, $ADUs$, to $mJy/beam$. In Fig. 4.10 we show each detector's flux calibration from a nominal `beammap`. The mean FCF values for each array are $[11.2 \pm 2.40, 3.50 \pm 1.0, 2.60 \pm 0.60] \times 10^8$ mJy/beam for the 1.1, 1.4, and 2.0 mm bands.

4.6.4 Pointing

After the telescope is focused, and immediately before and after a science observation, we perform a `pointing` scan. For our scans, we use a 30 s Lissajous pattern centered on the source. To estimate the pointing correction, we reduce the two pointing maps in alt-az coordinates, generated from all the available detectors. We then fit a 2D Gaussian to the each map to obtain a source offset in alt-az, average the offset value, then propagate the offset for the relevant science observation during the reduction step.

The average pointing offset for all 44 pointing observations made during the December 2022 commissioning phase was $2.01 \pm 5.44''$ in altitude and $-1.02 \pm 6.39''$ in azimuth (see Figure 4.11 for examples of nominal pointing maps). It is important to note that the offset between the three arrays was consistently less than $\sim 1''$, thus for the final utilized offsets for a science observation we average the results from all three arrays and both pointing maps.

Additionally, while we would prefer to utilize bright, well-characterized calibrators as mentioned in the previous section, their availability is limited throughout the year. As a result, we may use pointing observation targets as secondary calibrators. These sources are available year-round and are selected to be within 10° elevation of a science target. Since they are variable on short (e.g., days to weeks) timescales we require external flux measurements from SMA or ALMA close to the same day as the observation. For future runs we will consider submitting proposals for simultaneous observations of the pointing source by either observatory in order to further improve calibration accuracy.

During the fitting step, we obtain the amplitude of the source in raw detector units. We repeat this for each pointing observation during the night, then turn to the SMA Calibrator List or the ALMA Calibrator Source Catalogue to estimate the source flux during the observation. Performing a simultaneous fit between all of the

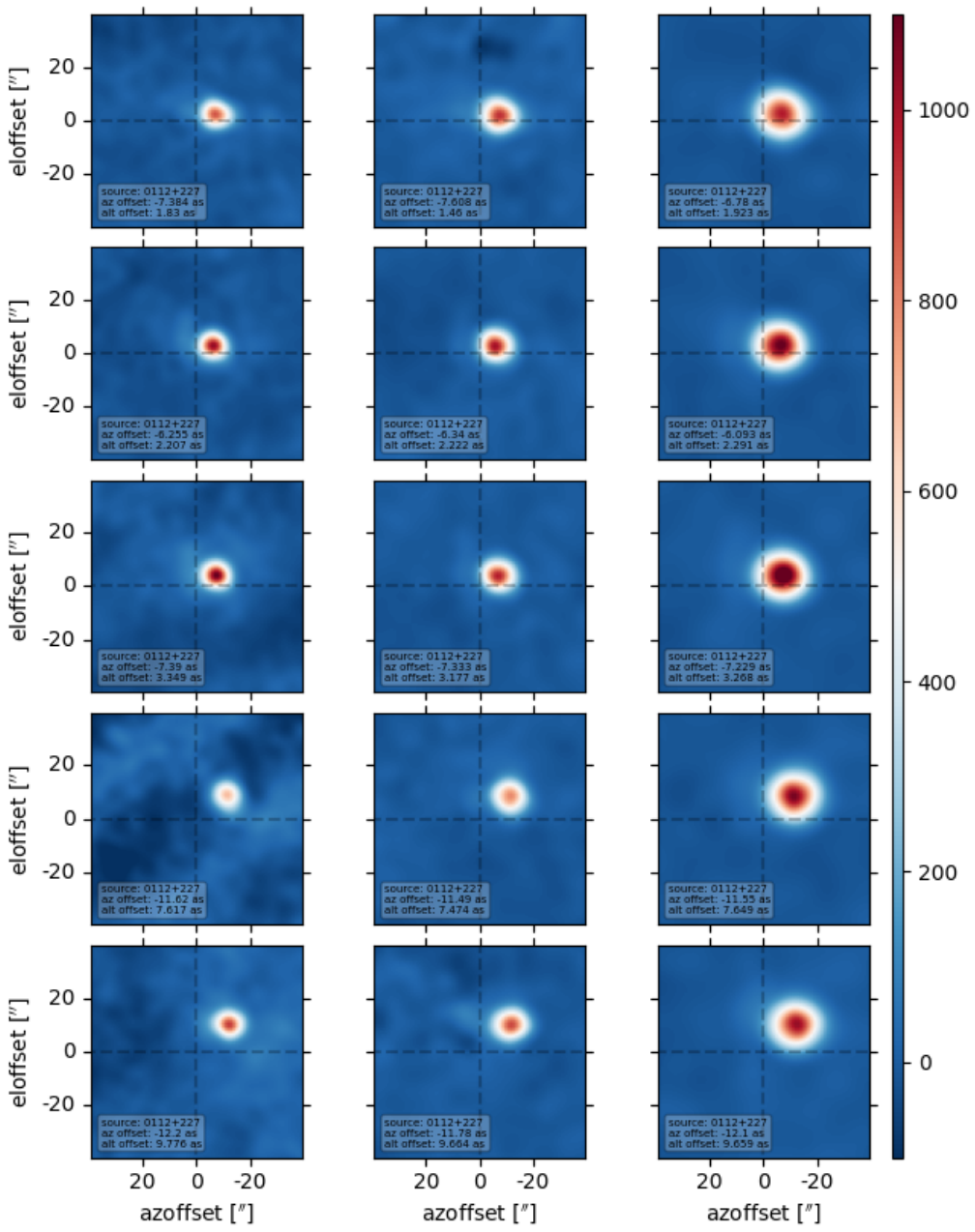

Figure 4.11: Examples of pointing observations for radio galaxy J0112+227. Each map has lines to indicate the location of (0″, 0″) and a label with the fitted alt-az offset values. The maps here have been Wiener filtered with the kernel for display purposes. We confirm that the arrays are well aligned with each other as the offsets for each band are less than 1″with proper focus and astigmatism. The average pointing offset for all 44 pointing observations made while commissioning was $2.01 \pm 5.44''$, $-1.02 \pm 6.39''$.

pointing amplitudes in their raw units and their corresponding external catalog flux, we can estimate the calibration factor for each band. To calculate the calibration factor for each band c_i, where $i \, \epsilon \, [0, 1, 2]$ for bands 2.0, 1.4, and 1.1 mm respectively, using the secondary calibrators we perform the following method:

1. Select the calibrated data given by $A_j \nu_i^{\alpha_j}$ for a source j. This is fit from either ALMA or SMA data with more than one data point in order to estimate α and a measurement near the TolTEC observation date to obtain the amplitude A.

2. For n observation of source j, write a model for the calibrated TolTEC flux given by $c_i \, d_{ijn}$. d_{ijn} is the peak uncalibrated flux in (I, Q) units output from `citlali`.

3. Minimize this equation using `lmfit`: $\Sigma_{jn} \frac{(c_i \, d_{ijn} - A_j \nu_i^{\alpha_j})^2}{\sigma_j^2}$

4. Repeat steps 1-3 for the remaining bands.

As a note, c_i is fit to every pointing observation simultaneously one band i at a time.

From this procedure, we determine calibration coefficients $[10.6 \pm 0.60, 3.41 \pm 0.13, 2.94 \pm 0.12] \times 10^8$ mJy/beam for the 1.1, 1.4, and 2.0 mm bands, respectively. When compared to the beammap-obtained mean FCF values, we find that the results are in good agreement. While this method will not be the primary way to establish the flux calibrations for an observing night, it can be used to confirm the beammap results using a more frequent set of observations.

4.7 Performance

A detailed analysis of TolTEC's extended flux recovery will be the subject of an upcoming paper. In our December 2022 commissioning observations, we were able to obtain successful detections of M1 and MonR2. Here we report initial performance results based on on-sky commissioning results for polarization and readout/detector

Table 4.2: Measured polarization fractions (p) and polarization angles ($\varphi_{\rm sky}$) for 3C 286 in two different configurations with literature values at similar wavelengths. We do not show $\varphi_{\rm sky}$ for observations conducted with the HWP installed as the orientation of the HWP fast axis is not known *a priori*. Measurements made with the HWP installed for the 2.0 mm are not shown as the HWP is optimized for the 1.1 mm and 1.4 mm bands only. Literature measurements at 0.88 mm, 1.3 mm, and 2.0 mm from Hull et al. [114], Nagai et al. [115], and Ritacco et al. [116] respectively.

		1.1 mm	1.4 mm	2.0 mm
No HWP	p	0.188 ± 0.023	0.186 ± 0.031	0.252 ± 0.016
	$\varphi_{\rm sky}$	$37.5^\circ \pm 4.0^\circ$	$42.0^\circ \pm 5.2^\circ$	$37.1^\circ \pm 1.2^\circ$
With HWP	p	0.194 ± 0.028	0.190 ± 0.038	N/A
Literature Values	p	0.157 ± 0.008	0.17 ± 0.02	0.136 ± 0.008
	$\varphi_{\rm sky}$	$37.4^\circ \pm 1.5^\circ$ (~ 0.88 mm)	$38.6^\circ \pm 0.4^\circ$ (~ 1.3 mm)	$28.0^\circ \pm 2.0^\circ$ (~ 2.0 mm)

noise followed by an upper limit for TolTEC's sensitivity and a lower limit for its mapping speeds.

4.7.1 Polarization

Commissioning observations of quasars were used to characterize TolTEC's polarimetric performance. In particular, 3C 286 is a highly polarized source with remarkable stability [117]. Multiple observations of 3C 286 were conducted in various configurations of the half-wave plate during the December 2022 commissioning season.

In Table 4.2, we list the measured polarization fractions (p) and polarization angles ($\varphi_{\rm sky}$) in two different configurations of the HWP along with published values at similar wavelengths [114–116]. The first configuration does not include the HWP in the optical path, while the second includes the HWP at a fixed positon in the optical path. Aside from the inclusion of the HWP, both observations were otherwise identical ~ 5 minute `lissajous` scans. The measurements were computed by splitting the data up into four datasets according to the detector's linear polarization sensitivities (at 0°, 45°, 90°, and 135°) and reducing each dataset separately. The Stokes Q and Stokes U values are then computed by differencing orthogonal components.

Overall, we find agreement with published values shown in Table 4.2 and more recent monitoring observations of 3C 286 from the ALMA Calibrator Source Catalogue and the AMAPOLA program. Furthermore, we see good consistency between observations taken with and without an installed HWP. In the observations conducted with an installed HWP, the HWP is held at fixed, but *a priori* unknown angle. Solving for this based on observations without the HWP, we find that the HWP rotates the polarization angle by $59.4^\circ \pm 5.4^\circ$ and $56.0^\circ \pm 8.2^\circ$ at 1.1 mm and 1.4 mm respectively. From Table 4.2, we see that, despite rotating the polarization angle through this large angle, the polarization fraction remains unchanged by the HWP, demonstrating good HWP performance across a broad range of wavelengths.

4.7.2 Noise

TolTEC's noise performance is an ongoing area of research, especially when it comes to the readout noise. Here we present our initial limits on the readout and detector noise, readout hardware improvements we made in July 2023 based on the commissioning data, and receiver cabin configuration edits to counter vibrational noise.

4.7.2.1 Detector readout noise

While performing observations, we found that the noise measured from timestreams exceeded the laboratory results. We investigated the source of the noise by performing 10 s timestreams and associated frequency sweeps with the window covered for a full range of programmable network attenuation values. We took 2 dB steps in drive and sense attenuation between 0 dB and 30 dB for a total of 256 unique measurements. As the scattering forward transmission S_{21} is recorded by the readout in arbitrary analog-to-digital units (ADUs), we projected from ADUs to physical units of frequency shift or amplitude change to compare with expectations. We found the components of these timestream measurements that correspond to directions tangent

and normal to the resonance circle of each KID. From these components, we calculated the power spectral densities (PSDs) of the frequency direction and amplitude direction noise, respectively. The frequency component usually describes the total system noise while the amplitude direction is related to dissipative components like the low noise amplifier and readout noise sources. More details about this system noise analysis can be found in [100].

From these PSDs, we calculated the median white noise, from 10 Hz to 61 Hz, at each drive attenuation step for each network of the 1.1 mm array. Figure 4.12 shows the median white noise S_{xx} as a function of drive attenuation for a few networks. We find that the frequency and amplitude components are also of similar values and that there is a power law of drive attenuation and white noise S_{xx} as $S_{xx} \sim 1/\text{signal}$, where both axes are on a log scale. This relationship is expected when operating in a readout-dominated regime since amplifier noise and other sources of readout noise decrease with tone power. However, this relation then bottoms out at 15 dB drive attenuation and then greatly increases at lower drive attenuation/higher power. We also calculated the signal power expected at the array for each measurement using a transmission line model which suggested that we were applying excess power to one of the amplifiers in the readout chain. These measurements and modeling suggest that one or more components in the readout are being compressed and this is limiting system sensitivity.

With the cryostat open, we were able to directly measure the P1dB point of the low noise amplifiers. While this result will of course differ from the performance while cold, the warm result does confirm a P1dB of approximately -55 dBm. Since this matches the expected value, we next turned to the warm amplifiers in the IF slices (see Fig. 2.8). The IF slices contain two amplifiers: (1) a 30 dB off-board amplifier and (2) a 20 dB on-board amplifier. When re-evalutating the signal power at each step in the chain, we discovered that the expected power at the 20 dB amplifier

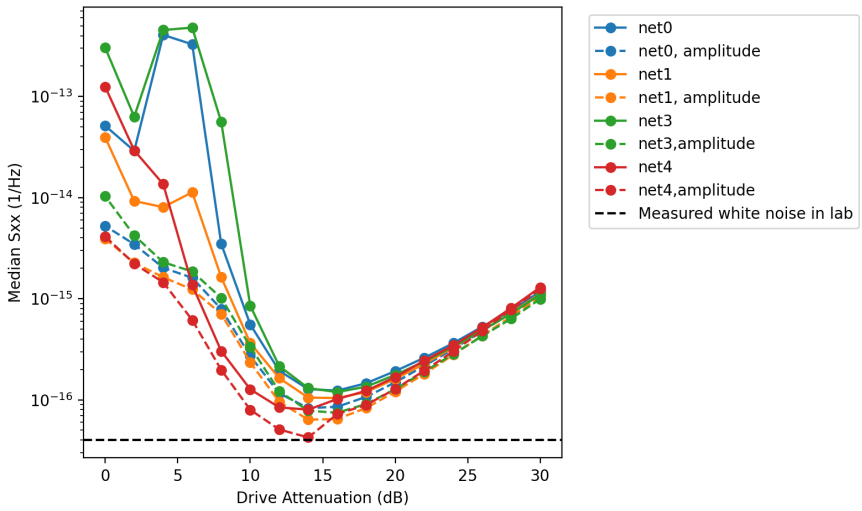

Figure 4.12: Median fractional frequency noise S_{xx} as a function of drive attenuation for several networks. The dots correspond to the median fractional frequency noise in the frequency (solid lines) and amplitude directions (dashed lines) calculated in the white noise regime, from 10 Hz-61 Hz. The black dashed line shows the measured white noise level at NIST.

input was approximately 5 dB higher than its P1dB point. While operating in the laboratory, we utilized signal powers approximately 10 dB lower than we do at the LMT due to the lower optical loading on the arrays thus this issue had not been expected or discovered until installation.

As a solution, we installed 12 dB attenuators on the input to the 20 dB amplifier to provide additional overhead on the signal power entering. The addition of the attenuator reduces the power of the incoming signal down below the amplifier's P1dB point, returning its operation to the linear regime for the tone powers used at the LMT. While this will add additional noise to the readout chain, we expect significant improvement from operating the amplifier in its linear regime.

4.7.2.2 BLIP predictions

We predict the expected background-limited performance (BLIP), where the noise from incident photons is the dominant source of noise in the detector, for the TolTEC 1.1 mm, 1.4 mm, and 2.0 mm arrays. The BLIP sensitivity is calculated as a noise

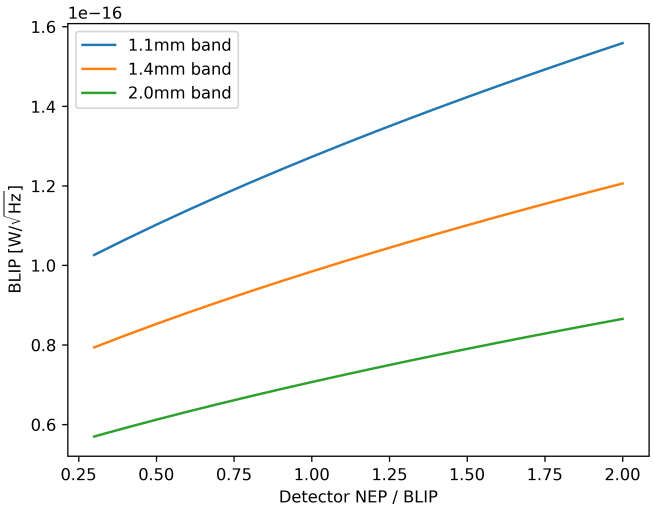

Figure 4.13: Predicted background-limited infrared performance (BLIP) for varying factors of detector noise (detector NEP/BLIP) for the TolTEC 1.1 mm, 1.4 mm, and 2.0 mm arrays for varying factors of detector noise. The BLIP is calculated considering the atmosphere of LMT at 60 degrees elevation and 50% quartile.

equivalent power (NEP) and in units of $\mathrm{W}/\sqrt{\mathrm{Hz}}$. The NEP is the uncertainty in detected power in a bandwidth of 1 Hz or one-half second integration. We implement the method of [41] for these calculations. This includes considering the atmosphere of the LMT at 60 degrees elevation and 50% quartile, the effective telescope and coupling optics, detector optical efficiency (0.7), model passbands, and feedhorn aperture efficiency (0.35). From these calculations, we investigated how different factors of detector noise would affect the BLIP for each passband. Figure 4.13 shows the predicted BLIP for varying factors of detector noise (detector NEP/BLIP) for each array. The BLIP worsens with higher detector noise as expected. We continue to actively work on improving the noise performance of each array and demonstrate background-limited sensitivity.

4.7.2.3 Vibrational noise

In this section, we analyze the impact of the mechanical vibrations of the LMT receiver room on the temporal response of the TolTEC detectors. We have repeatedly observed that the spectra of timestreams in the sky and dark observations present relatively intense lines, some narrow, at particular frequencies. The origin of these lines can be very diverse: intrinsic to the detectors, electromagnetic interference (EMI) coupled to the detectors or the readout lines (coax cables) and devices (mixers, local oscillators, amplifiers, connectors), or even optical disturbances due to mechanical vibrations in the warm mirrors and the camera itself.

Using an MPU6500 accelerometer encapsulated in a plastic casing to adhere to flat surfaces, operating in a range of ± 2g, we measured the magnitude of acceleration in all three axes at the ends of the TolTEC warm mirrors: M4, M5, and M6, as well as in the left front corner of the cryostat, as illustrated in Figure 4.14a. The measurements were made between December 2022 and January 2023, coinciding with the TolTEC commissioning observation period. The mechanical vibrations in the receivers room strongly depend on the operating conditions of the rest of the instruments, mainly their compressors, which despite resting on a foam floor and being located outside the room, generate vibrations that propagate through the floor to the TolTEC camera. On the other hand, the warm TolTEC mirrors are mounted, within the same room, on a platform mechanically isolated from the floor of the receivers room, on which the M3 mirror of the telescope lies (M3 platform hereafter), so that, in principle, they are immune to vibrations from the rest of instruments in the room, except for the Redshift Search Receiver (RSR, [118]) compressor, which is also installed on the platform but at the opposite end. At the time of the measurements, the following were operating: the RSR instrument and its compressor, the MUSCAT continuum camera and its compressor outside the room, and of course, the two TolTEC compressors, also outside the room.

At each point, measurements were made for up to 300 seconds with a sampling frequency of ∼570 Hz, higher than TolTEC's typical sampling frequencies (∼122 or 488 Hz). The entire data was divided into 10-seconds segments, from which the power spectrum was obtained, to average them together finally. Figure 4.14b shows the power spectra obtained at each measurement point.

First, we note that the noise floor in the spectrum of vibrations in the cryostat is a factor of 2 greater than where the mirrors are located, as expected, given the mechanical isolation between them. The M4 mirror has well-defined lines at 29.6 and 41.0 Hz and a forest of narrow, well-defined lines between 53 and 56 Hz (detection threshold of 5 σ). There are a couple of lines at a higher frequency, but given the sampling frequency of TolTEC, we only consider those below 61 Hz for this analysis. The M5 mirror contains fewer lines, but below 61 Hz, two lines stand out at 24.4 and 29.6 Hz. On the other hand, in the M6 mirror, only one line at 41.0 Hz is observable in the TolTEC range. Finally, the cryostat has a forest of lines between 23 and 30 Hz and a high-intensity doublet at 56.9 and 57.4 Hz. To compare with the noise spectra of the detectors, we select those lines observed in at least two different sites: 24.4, 29.6, and 41.0 Hz, as well as the intense doublet observed in the cryostat: 56.9 and 57.4 Hz. Note that this last pair is typical of the vibrations on the floor of the receivers room since it is not observed in other points of the M3 platform (there are some close lines on the M4 mirror, but far enough apart to be considered distinct).

In the arrays, there are some dark detectors (blocked feedhorns) whose spectra can reveal information about the properties of the detectors independently of the characteristics of the incident light. In Figure 4.15, we present the median of the power spectra averaged in 10-second time chunks of the illuminated detectors (solid blue line) classified as "good detectors" and of the dark detectors (solid red line); in some of the networks where the latter have been fully identified. We added the relevant frequencies selected above from the vibration measurements (vertical black

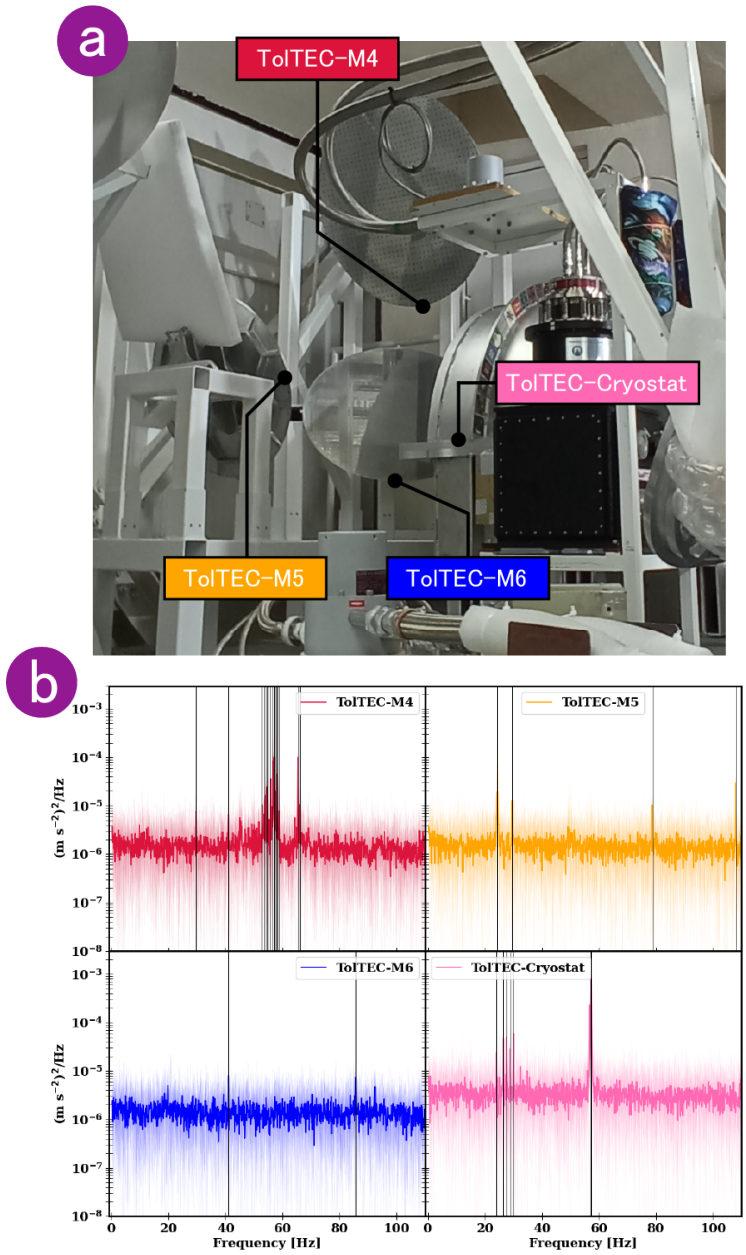

Figure 4.14: a) Vibration measurements on the warm mirrors and the TolTEC cryostat. Each one of the labels indicates the points where the vibration measurements were made using an accelerometer: in one of the front corners of the cryostat, installed on the floor of the receiver cabin, and in the mirrors, M4, M5, and M6, mounted on the M3 platform, mechanically isolated from the room. b) Power spectrum of the magnitude of the acceleration at each measurement point. The lines at the frequencies of: 24.4, 29.6, and 41.0 Hz stand out for being present in multiple places, as well as the double-peak at 56.9-57.4 Hz in the cryostat for its intensity (above 5σ detection).

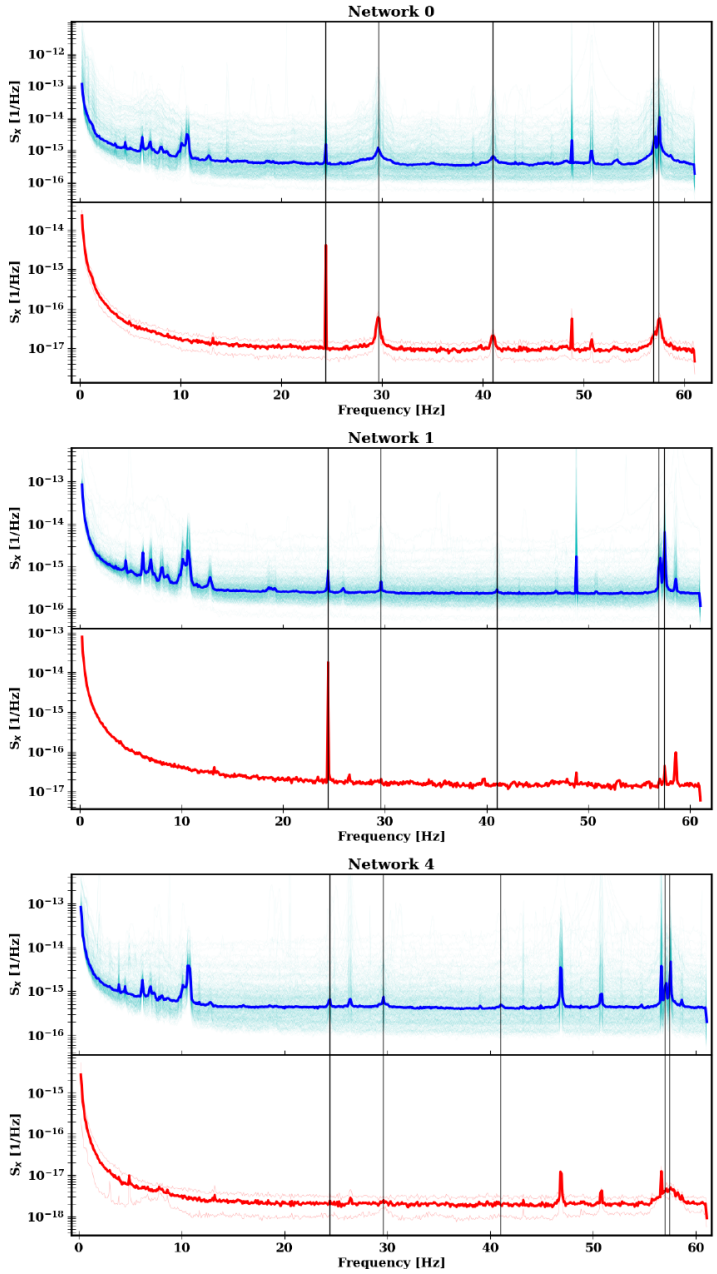

Figure 4.15: Power spectra density of the TolTEC timestreams of a beammap-type observation of those networks where the dark detectors are identified: 0, 1, and 4. For each network, we present the median of the spectra averaged by 10-second chunks of the illuminated detectors labeled 'good' (blue top solid line) and the dark detectors (red bottom solid line). The relevant frequencies related to vibrations in the mirrors and the cryostat of Figure 4.14b are indicated with vertical black lines. Note the coincidence between these lines and some present in the spectra of the timestreams.

lines) to these spectra. The timestreams correspond to a beammap-type observation made on December 19, 2022; the conditions of the receiver cabin are identical to those present during the vibration measurements.

The 24.4 Hz signal is observed with great intensity and narrowness in networks 0 and 1 and is barely perceptible in the illuminated detectors of network 4. The 29.6 Hz signal is distinguishable in the illuminated detectors of the three networks, although the intensity gradually decreases; it is only observed in the dark detectors of network 0. The signal at 41.0 Hz has a similar behavior, present in the three networks but intensifying towards network 0 in the illuminated detectors and only observable in the dark detectors of network 0. The 56.9-57.4 Hz pair is clearly observed in the spectrum of networks 0 and 1 illuminated detectors. In network 4, some structures are observed between 56 and 58 Hz, but they do not match as well as the previous ones.

In general, some mechanical vibrations in the M3 platform (a combination of vibrations in the movement of the telescope and the compressor of the RSR) are transmitted to the warm mirrors of TolTEC, which are appreciated in the timestreams of the detectors, with greater intensity in the detectors illuminated, as expected, except for the 24.4 Hz line whose intensity is similar in both configurations, possibly due to the influence of stray light. Likewise, the intensity of the lines in the detectors increases as we get closer to the edges of the array. On the other hand, the double peak vibration present in the cryostat has been observed in other instruments when the TolTEC and MUSCAT compressors operate together (Becerril M., thesis in preparation). These vibrations are communicated to the detectors in TolTEC by disturbances in the beam from the differential movement between the cryostat and the M3 platform. Rubber vibration isolators have been placed under the frames of the TolTEC and MUSCAT compressors to counteract this effect. The observations in the following commissioning run will allow us to measure if there is a positive effect

on vibration damping in the TolTEC detectors. While for the mirrors, in particular M4, measures are necessary to improve their rigidity, such as installing absorbent rubber between the ends of the mirrors and their supports or mitigating vibrations generated by the RSR compressor.

4.7.3 Sensitivity and Mapping Speed

Sensitivity is one of the key parameters in evaluating the performance of an instrument; it establishes the minimum signal coming from a source that can be recognized above the background noise. More importantly, to evaluate the ability of a camera to perform maps with a defined area and sensitivity in a certain integration time, we resort to the mapping speed. In this section, we present the estimation of the sensitivity in the maps, expressed as the noise equivalent flux density (NEFD), of a set of point sources observations, carried out during the commissioning campaign of December 2022. Consequently, from this result, and considering the properties of the beam in each one of the bands, we calculate the mapping speed in each of them.

The NEFD is the equivalent flux density that produces a unity signal-to-noise ratio in an integration time of 1 second. Given a flux density map M in units of Jy/beam, associated with a coverage map H, in seconds, containing the number of data samples per pixel divided by the sampling frequency, we can estimate the $\mathrm{NEFD_i}$ of a region $\mathrm{A_i}$ that belongs to M, whose area is equivalent to the area of a beam in pixels, in $\mathrm{mJy}\sqrt{\mathrm{s}}$ units as:

$$\mathrm{NEFD_i} = \sigma_i \sqrt{\mathrm{t_{int,i}}} \tag{4.10}$$

where σ_i is the flux density uncertainty within region $\mathrm{A_i}$ and $\mathrm{t_{int,i}}$ is the average integration time of region $\mathrm{A_i}$ measured on the coverage map H.

On the other hand, the mapping speed $\mathrm{M_s}$ is defined as the area of sky A_{sky} that can be mapped at a noise level of 1 mJy in beam-sized map pixels in an hour.

Following the analysis of equation 10 in [41], the mapping speed of the instrument in arcmin^2/mJy^2/hr units is given by:

$$\mathrm{M_s} = \frac{3600\,\eta\,\mathrm{N_{det}}}{\mathrm{N_{beams}}\,\mathrm{NEFD^2}} \tag{4.11}$$

where $\mathrm{N_{det}}$ and η are the total number of detectors and the fraction of valid detectors in the focal plane, respectively. $\mathrm{N_{beams}}$ is the total number of telescope beams in a square arcminute. Considering a Gaussian beam with an FWHM in arcseconds, we can express $\mathrm{N_{beams}}$ as:

$$\mathrm{N_{beams}} = \frac{60^2}{\frac{\pi}{4\ln(2)}\,\mathrm{FWHM}^2}. \tag{4.12}$$

The ratio $\frac{\eta \mathrm{N_{det}}}{\mathrm{N_{beams}}}$ in equation 10 expresses the total area of the sky observed simultaneously by the instrument.

To estimate the sensitivity and mapping speed of the instrument, we have selected 12 point-like source observations made between December 16 and 18, 2022, during the TolTEC commissioning campaign. These observations correspond to small 2' × 2' maps, made using a 60 second `lissajous` scan of bright point-like sources (SNR > 100) where the beam has been previously optimized through the focus/astigmatism procedure.

Given a map, we compute σ_i and $t_{int,i}$ for all possible regions $\mathrm{A_i}$, moving the region across an annular region of map M with an inner radius of 50 pixels, masking the source and secondary lobes features, and an outer radius of 150 pixels to avoid map edges where coverage is poor. For each region, we obtain a point of one color in the graph of integration time (t_{int}) vs. flux density uncertainty (σ) (see Figure 4.16) so that for each map, there is a cloud of points, with a distribution associated with equation 9. Since the individual observations are of short duration, to analyze the behavior at longer integration times, we coadd the 12 observations one by one using inverse variance noise weighting, plotting the cloud of points in the t_{int} vs.

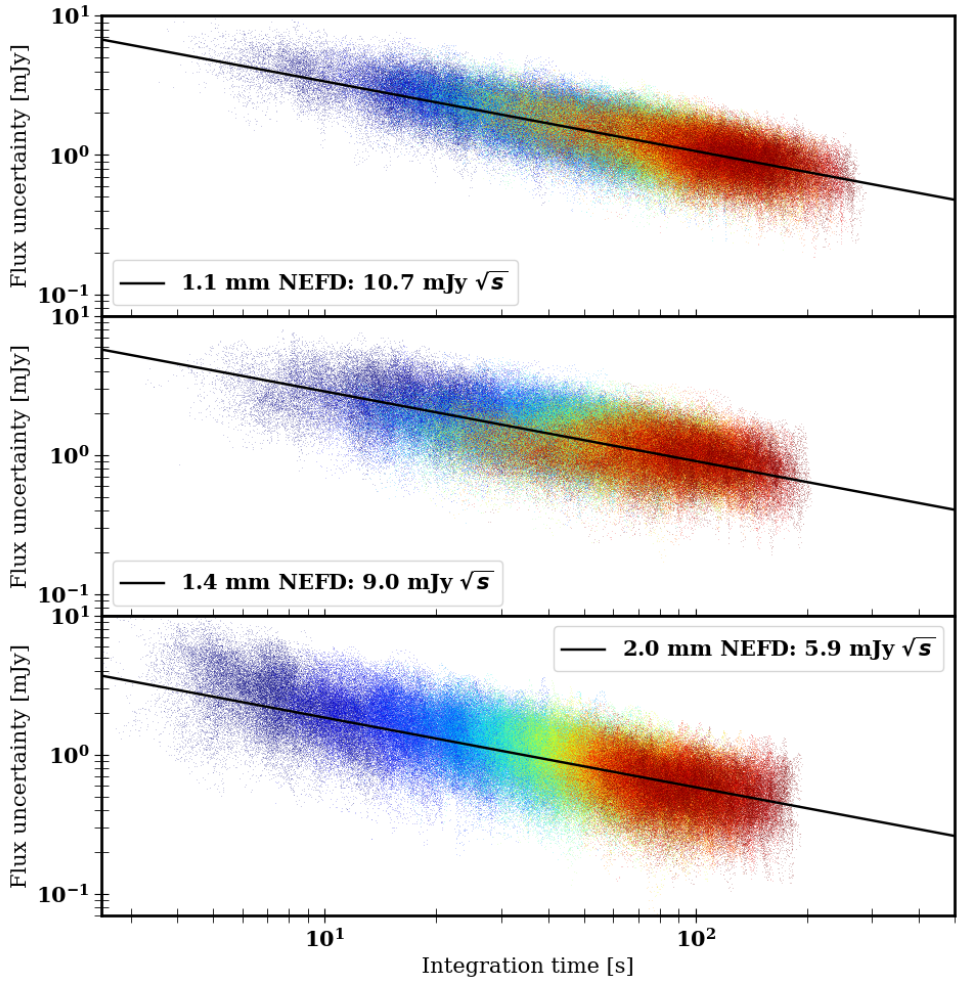

Figure 4.16: Flux density uncertainty vs. integration time of each of the A_i regions for each coadded map in each one of the TolTEC bands. The color of the point cloud indicates the number of images accumulated, dark blue being only one, and red the 12 maps. The solid black line represents the fit of the point clouds with equation 9, which follows a power law with an index of -0.5, as expected. From the fit, we obtain a NEFD of 10.7±1.0, 9.0±1.0, and 5.9±1.0 mJy$\sqrt{s}$ for the 1.1, 1.4, and 2.0 mm bands, respectively.

σ graph for each cumulative map, with a different color as shown in Figure 4.16. We calculate the NEFD by fitting these collections of point clouds to the curve of equation 9, obtaining 10.7±1.0, 9.0±1.0 and 5.9±1.0 mJy$\sqrt{s}$, for the 1.1, 1.4, and 2.0 mm bands, respectively. Because the maps we use in the analysis have been previously corrected for atmospheric extinction (opacity and elevation), the NEFD

Table 4.3: Mean values and uncertainty of NEFD and mapping speed for each TolTEC band at zero opacity and with the telescope observing at the zenith. For the mapping speed, we present the values computed with 100% valid detectors ($\eta = 1$) and the non-flagged fraction employed in the initial commissioning of December 2022.

Band [mm]	1.1	1.4	2.0
NEFD [mJy$\sqrt{\text{s}}$]	10.7	9.0	5.9
rms NEFD [mJy$\sqrt{\text{s}}$]	1.0	1.0	1.0
Mapping speed, $\eta = 1$ [arcmin^2/mJy^2/hr]	1280	1420	3580
rms Mapping speed, $\eta = 1$ [arcmin^2/mJy^2/hr]	240	350	1230
No-flagged detectors fraction, η	0.53	0.57	0.67
Mapping speed, no-flagged [arcmin^2/mJy^2/hr]	680	810	2400
rms Mapping speed, no-flagged [arcmin^2/mJy^2/hr]	160	200	820

we calculate is equivalent to that obtained when the telescope is pointed at the zenith with zero opacity.

The behavior of the noise in the coadded maps is as expected, that is, scales as the square root of the integration time. In the coming commissioning campaigns, coadding more similar observations or with longer exposure times will allow us to confirm whether this behavior is preserved with longer integration times.

Next, using Eqn. 4.11 and considering the beam sizes reported in Section 4.6.2, we obtain the following mapping speeds: 1280, 1420 and 3580 arcmin^2/mJy^2/hr, for 1.1, 1.4 and 2.0 mm, considering $\eta = 1$ in the three bands, and 680, 810 and 2400 arcmin^2/mJy^2/hr using the no-flagged detectors. Table 4.3 summarizes the sensitivity and mapping speed results of the three TolTEC bands. We obtain mapping speed uncertainties by error propagation of beam size and NEFD uncertainties.

4.8 Conclusions

The TolTEC camera was successfully installed at the Large Millimeter Telescope in December 2021. Over the past two years, we have performed engineering and on-sky commissioning tests to characterize the camera's performance at the telescope.

Upon arriving to the LMT, we discovered a series of hardware issues in the cryogenics subsystem that prevented us from nominal operation until May 2022 (see §4.3.3). Following the repairs, we were able to complete on-sky commissioning observations in June 2022, December 2022, and April 2023. In between these periods, the LMT has experienced a number of shutdowns due to hardware (telescope balance, power failure) and environmental concerns (forest fire, volcanic ash, lightning strikes) which has limited TolTEC's on-sky time. However, we continued to iterate on the system's hardware and software during these off-sky periods. This lead to significant improvements for the system, such as the recovery of networks with failed cryogenic readout components and improved detector biasing through implementation of the DriveFit algorithm (see §4.4.1).

During on-sky commissioning, we were able to perform focus and astigmatism corrections, beammaps, and pointing observations. From the beammap and pointing observations, we confirm that the three arrays are well-aligned internal to the cryostat. We do find that the average measured FWHMs are $\lesssim 20\%$ larger than anticipated ($6.0 \pm 0.4''$, $7.5 \pm 0.4''$, and $10.7 \pm 0.3''$at 270, 220, and 150-GHz), but this may be traced back to residual errors in the focusing and astigmatism steps. We are also able to utilize the beammap and pointing observations to independently determine TolTEC's flux calibration factors. Both methods are in good agreement with each other, suggesting that the beammap-derived factors we use for mapmaking are correct.

Through our December 2022 observations, we were able to confirm TolTEC's polarization sensitivity with and without the HWP installed (see §4.7.1. In both cases, our results from observations of 3C 286 are in good agreement with ancillary data from ALMA and NIKA. We also examined TolTEC's on-sky noise performance (§4.7.2). In our observations, we identified vibrations in the receiver cabin as a source of noise on the timestreams. We added vibrational dampening around the cryogenic compressors to reduce this effect; however, we await future observations to confirm

that the noise is no longer present in the data. We also find that TolTEC is not currently operating below the background photon noise limit due to excess readout noise. We identified a source of this noise as the compression of the IF slice amplifiers and installed an attenuator at the input to this amplifier to provide more dynamic range. In Fall 2023, we will be able to confirm if this edit to the system allows us to demonstrate background-limited sensitivity.

Finally, we were able to estimate an upper limit for TolTEC's sensitivity and a lower limit for its mapping speeds using the pointing maps (see Table 4.3 for the results). We find higher than anticipated sensitivities, which in turn lead to lower than expected mapping speeds. From Bryan et. al. [41], we predicted mapping speeds of 1.9-13.4, 3.1-22.0, and 10.5-74.4 $\mathbf{deg}^2/\mathrm{mJy}^2/\mathrm{hr}$ (the lower estimate being scaled by an empirical factor for the atmospheric noise as measured by AzTEC [41]) for the 1.1, 1.4, and 2.0 mm arrays, respectively. Our results are ~ 90 times smaller than anticipated; however, we can attribute part of this to our higher readout noise. We also note that the LMT's primary dish surface will be upgraded over the next year and we expect between a factor of 2 improvement to the sensitivity at 1.1 mm, which would translate to a factor of 4 improvement in mapping speed. Additionally, while our mapping speeds are currently lower than predicted, TolTEC does still demonstrate higher mapping speeds than NIKA2, a comparable ground-based mm-wave instrument that features KIDs [91]. We will be able to confirm any improvements to sensitivity and mapping speed performance by December 2023 following a new series of commissioning observations.

CHAPTER 5

A NOVEL SZ STUDY WITH TOLTEC

"People call me a philosopher or a scientist or an anthropologist. I am none of those things. I am an anamnesiologist. I study what has been forgotten. I divine what has disappeared utterly. I work with absences, with silences, with curious gaps between things. I am really more of a magician than anything else."

Susanna Clarke, Piranesi

A review of the Sunyaev-Zel'dovich Effect is presented in Chapter 1. I first provide an overview of pressure fluctuations in the intracluster medium (ICM) and what physics can be gleaned from their power spectra (§5.1 followed by recent studies of their power spectra (§5.2). Next, in §5.3, I describe the analysis pipeline developed for a future pilot study to examine TolTEC's spatial sensitivity to fluctuations the ICM. After detailing the methodology, I present results from calibrating the pipeline and running it on noiseless simulations of clusters (§5.4). Finally, I conclude with next steps and the outlook for upcoming TolTEC observations (§5.5).

5.1 Pressure Fluctuations in the Intracluster Medium

5.1.1 Physics with Fluctuations

Galaxy clusters are the largest gravitationally bound objects we observe today, having masses between $\sim 10^{14} - 10^{15}\,\mathrm{M}_{\odot}$. The dominant contribution, 90%, to the

cluster's mass is its dark matter (DM) halo while only $\leq 1\%$ is contributed by the hundreds to thousands of member galaxies. The remaining $9-10\%$ of the cluster's mass is comprised of a hot, highly ionized gas known as the intracluster medium (ICM) [119]. The ICM is a diffuse gas, with densities on the order of $n_e \sim 10^{-3}$ cm^{-3} through the center of the cluster, primarily composed of electrons, protons, and ionized heavy elements such as iron. As the Cosmic Microwave Background (CMB) travels through this medium, its photons have a $\sim 1\%$ probability of being Inverse Compton (IC) scattered by the energetic electrons ($T \approx 10^8$ K ≈ 10 keV). The effect of this scattering is a characteristic, redshift-independent distortion of the CMB spectrum known as the Sunyaev-Zel'dovich (SZ) Effect (see Fig. 1.4) [8, 27, 28, 120].

As described in §1, the largest component of the SZ signal from the ICM is the thermal SZ effect (tSZ), which is directly proportional to the integral of the ICM gas temperature and density distribution along the line of sight (LOS). The tSZ can be characterized by a change in CMB intensity given by

$$\Delta I_{tSZ} = I_0\, g(x) y,$$

where $I_0 = 2(k_B T_{CMB})^3/(hc)^2$ (MJy/sr), $x \equiv h\nu/k_B T_{CMB}$ (unitless), and g(x) (unitless) is the spectral shape of the effect given by

$$g(x) = \frac{x^4 e^x}{(e^x-1)^2}\Big(x\frac{e^x+1}{e^x-1} - 4\Big)(1+\delta_{SZE}(x, T_e)),$$

where δ_{SZE} encodes relativistic effects imparted to the spectrum by high energy ICM electrons, and y is the unitless Compton-y parameter is defined as

$$y = \frac{\sigma_T}{m_e c^2}\int_{LOS} n_e k_B T_e dl,$$

which is the integral of the ICM's pressure along the LOS, $P_e = n_e k_B T_e$ [27, 28].

When integrated over the whole cluster, the tSZ can provide a good proxy for the total cluster mass if one assumes hydrostatic equilibrium between the ICM's pressure and the dark mater halo's gravitational potential well. This leads to another common simplifying assumption that the ICM is isothermal, smooth, and spherically symmetric. Taken together, these assumptions drastically simplify the analysis needed to extract the total mass of the cluster.

However, clusters are not truly smooth, idealized matter distributions. In reality, ICMs feature pressure perturbations due to accretion shocks, merger events, and feedback that have been found in both x-ray and mm-wave observations [9, 11, 13, 98, 121–123]. If not removed, deviations from a smooth profile can bias the mass estimate upwards by 10s of %, biasing the inferred cosmological parameters extracted from large cluster surveys [12, 124, 125]. Accurately measuring these pressure fluctuations in distant clusters requires high resolution (sub-arcminute) observations and sensitivity to faint tSZ signals at flux levels less than 1 mJy/beam on scales ranging from $10''$ to several arcminute scales.

High resolution observations of ICM fluctuations would not only improve the use of clusters as cosmological probes. Taken over a large range of redshifts, these observations would also allow us to study cluster evolution through the lens of their thermodynamics. One method we can apply to analyze these observations is calculating the power spectrum of relative pressure fluctuations in the ICM. The peak of this power spectrum is sensitive to the 3D Mach number of gas motions [121, 126]

$$Ma_{3D} \approx 2.4 A_P(k_{peak}), \tag{5.1}$$

where A_P is the characteristic amplitude of the power spectrum and k_{peak} is the spatial frequency at which the spectrum peaks. Assuming the perturbations are adiabatic, the Mach number is given by [121]

$$Ma_{3D} = \sqrt{3} Ma_{1D} = \frac{\sigma_v}{c_s}, \tag{5.2}$$

where σ_v is the turbulent velocity dispersion, c_s is the sound speed[1], and Ma_{1D} is the 1D Mach number. So, with a measurement of the power spectrum peak, we can constrain the amount of turbulence (e.g., large-scale eddies or bulk motions) in the ICM.

Additionally, the slope, or cascade, of the power spectrum is a sensitive probe of the gas conduction [121, 127]. If the ICM has strong conduction, we may observe a dampening of the spectrum's slope between 10 to 1000 kpc (e.g., angular scales from $\sim 2''$ to $150''$ at $z = 0.6$) [127]. The ICM's conductive state is indicative of how well it diffuses/distributes its thermal energy. If the gas has high conduction, and thus distributes its thermal energy efficiently, cold gas that may otherwise accrete onto member galaxies and serve as fuel for future star formation or black hole growth may instead be heated into halo gas [126]. Similarly, strong conduction can remove potential sources of cold gas, such as overdensities formed through turbulence, through thermal expansion. Fully resolving the ICM and its substructure between the cluster core and outskirts is thus vital for probing its thermodynamic state and understanding the role the cluster environment plays in galaxy evolution.

5.1.2 High Resolution Studies of ICM Fluctuations

High resolution studies of ICM fluctuations using tSZ observations began gaining traction with the *Planck* observation of the Coma cluster and its subsequent analysis by Khatri and Gaspari (2016) (henceforth, KG16) [121]. Unfortunately, as a survey instrument *Planck* is limited to studying fluctuations in select, low-redshift clusters due to its large beam size ($\theta_{FWHM} > 5'$). Newer ground-based mm-wave instruments such as MUSTANG/MUSTANG-2 on GBT [36, 88] and NIKA/NIKA2 on

[1]For reference, the Coma cluster has a sound speed of around 1500 km/s [127].

IRAM-30m [35, 57] have proven themselves capable of performing high resolution observations of ICM fluctuations in distant clusters [128]. For instance, a similar study to KG16 was performed on Zwicky 3146 ($z = 0.291$) by conducting a joint analysis with MUSTANG-2 and *XMM-Newton* data [123]. The study concludes with a need for wider, deeper, and higher resolution ($< 10''$) measurements across more wavelengths to detect and fully characterize fluctuations out to higher radii. TolTEC will be uniquely positioned to provide these measurements, through its ability to deeply image cluster scales between the core and the outskirts in three distinct bands.

Below I describe the analysis pipeline I developed for a future pilot study to characterize TolTEC's ability to resolve ICM fluctuations between 50 to 1000 kpc. As stated previously, the importance of this study will be twofold: (1) resolving these fluctuations will improve mass estimates for the clusters which is a vital parameter for cluster-based cosmological studies; and (2) the thermodynamics of clusters is tightly linked to the level of turbulence and conductance in the ICM. Ultimately, the pilot study will serve as a proof of concept before undertaking deeper observations of a larger cluster sample.

5.2 Setting the Stage

5.2.1 The Proposed Cluster Sample

TolTEC was installed at the LMT in December 2021 and, since June 2022, we have been performing commissioning tests to characterize the system (see Chapter 4). The following four clusters have been or will be proposed for 5+ hour observations once TolTEC is available for general purpose observations. The sample is small to start with as we will want to first confirm TolTEC's sensitivity to the tSZ fluctuations; however, it does cover a range of redshifts in order to get a first look at any differences in the power spectra over cosmic time that may be driven by evolution of the universe's large scale structure itself. Additionally, we selected clusters with ancillary data in

Table 5.1: Sample of clusters for proposed pilot study. Redshift, mass, and dynamical state obtained from [129]. POS stands for plane-of-sky while LOS stands for line-of-sight.

ID	z	M_{500}	mm/IR	NIR/optical	x-ray	dynamical state
Abell 1835	0.282	17.1±2.9	Bolocam, Herschel, ACT	HST	Chandra, XMM-Newton	relaxed
MACS 0717.5+3745	0.546	24.9±2.7	Bolocam, Herschel, AzTEC	HST	Chandra, XMM-Newton	LOS-merger
RX J1226.9+3332	0.888	7.8±1.1	Bolocam, Herschel	HST	Chandra, XMM-Newton	POS-merger
RX J1347.5-1145	0.451	21.7±3.0	Bolocam, Herschel, AzTEC	HST	Chandra, XMM-Newton	POS-merger

multiple wavelengths with a priority placed on ones with ACT or Bolocam data. We prioritize these clusters since both ACT and Bolocam overlap with TolTEC bands and their results can provide constraints on the expected flux in TolTEC's maps.

As a note on the scanning patterns for the clusters in the proposed sample, a Lissajous pattern with 6′ sides is large enough to cover a cluster beyond z$\sim$ 0.5 out to R_{200} (see Fig. 5.1). Other groups such as MUSTANG-2 and NIKA2 have had success with similarly sized 'daisy' patterns [91, 122]. It remains an area of research as to which scanning strategy would be preferable for studies with TolTEC at the LMT. As discussed in the next section, preliminary results from two 30 minute observations of MACS J0717 suggest that a Lissajous pattern might not provide enough coverage of the map center when performing SZ observations.

5.2.2 Status of Cluster Observations

As of Summer 2023, TolTEC has attempted to observe only one galaxy cluster, MACS J0717.5+3745. After 1 hour of integration time split between two 30 minute `lissajous` scans, we did not find evidence of tSZ signal in either the 150 or 270 GHz maps. The observation did give us a noise estimate for one hour of integration time across a single beam: 0.50 mJy/beam at 150 GHz and 0.98 mJy/beam at 270 GHz. The decrement, or 150 GHz, signal measured from NIKA after 12 hours was approximately -2 mJy/beam at the center of the cluster where the signal would be strongest [130]. Converting from NIKA's 18″ beam to TolTEC's 9.5″ beam, the maximum decrement measured by TolTEC would be approximately -0.6 mJy/beam. Assuming

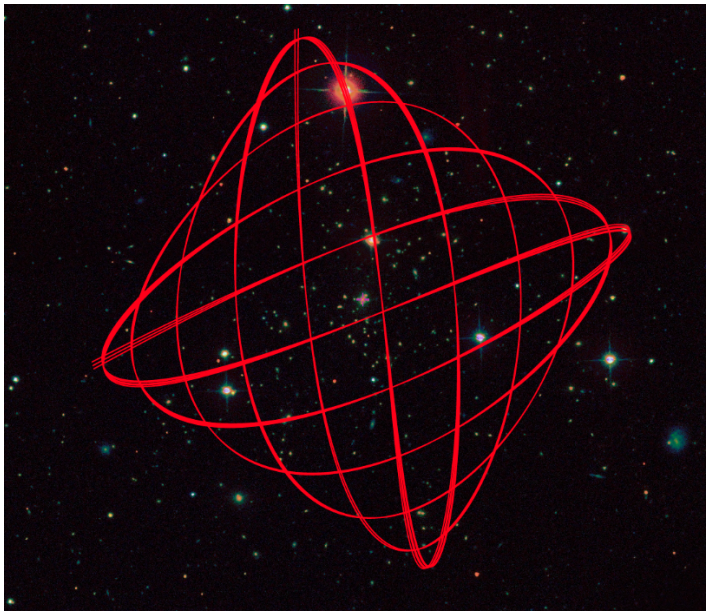

Figure 5.1: An example of a 10 minute TolTEC Lissajous scan over Abell 1835 (background image from the SDSS catalog) generated with the TolTEC Observation Planner. The sides of the Lissajous pattern are 6′ each, but including the 4′ FoV the coverage is closer to 10′ on each side.

the RMS measured scales with $1/\sqrt{t}$, to obtain a S/N=3 detection on the cluster for TolTEC will require about 6 hours of total integration time with its current performance. As discussed in Chapter 4, we do not expect this to be representative of TolTEC's future performance.

5.3 The Analysis Pipeline

5.3.1 Methodology

This pipeline is based off the analysis procedure performed on *Planck* observations of the Coma cluster in KG16 [121]. As such, I use similar approximations in order to estimate the 3D pressure fluctuation power spectrum (P_P) from the 2D Compton-y fluctuation power spectrum (P_y).

The procedure from observation to result uses the following recipe:

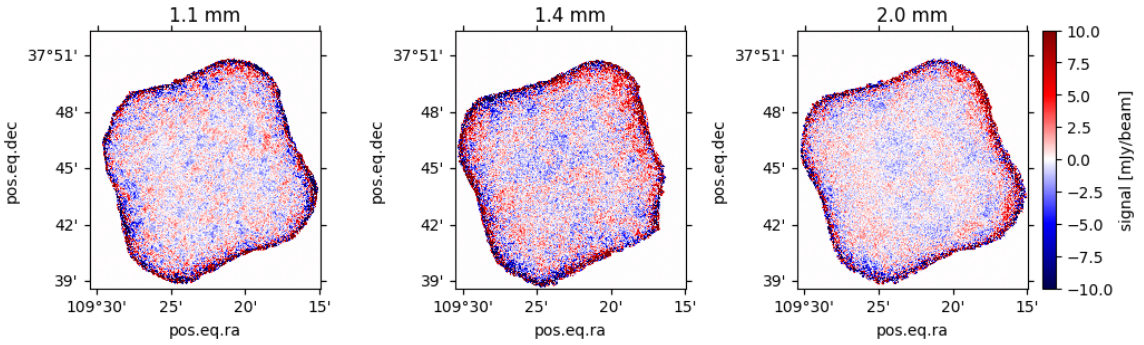

Figure 5.2: Coadded map of the two 30 minute TolTEC observations over MACS J0717.5+3725. The reduction shown here was performed using `citlali`. The observations show no detection in either increment (270 GHz) or decrement (150 GHz) bands.

1. Obtain timestreams through a real or simulated observation, then produce intensity maps in TolTEC's three bands using TolTEC's data reduction software `citlali` (see §4.5.1.1 for more details).

2. Use the hierarchical Bayesian fitting code (`hie_bayes`) to fit Compton-y for each pixel from Eqn. 5.1.1.

3. With the resulting Compton-y map, interpolate the data and estimate the average radial profile of the map, $\bar{y}$. Additionally, fit an isothermal β model y_β to the average profile.

4. Subtract the average radial profile from the data to obtain δy, then divide δy by $\bar{y}$ to obtain the Compton-y fluctuation map $\delta y/\bar{y}$.

5. Using y_β, calculate the integral of the window function (Eqn. 5.5) that will be used to convert between the 2D P_y and the 3D P_P.

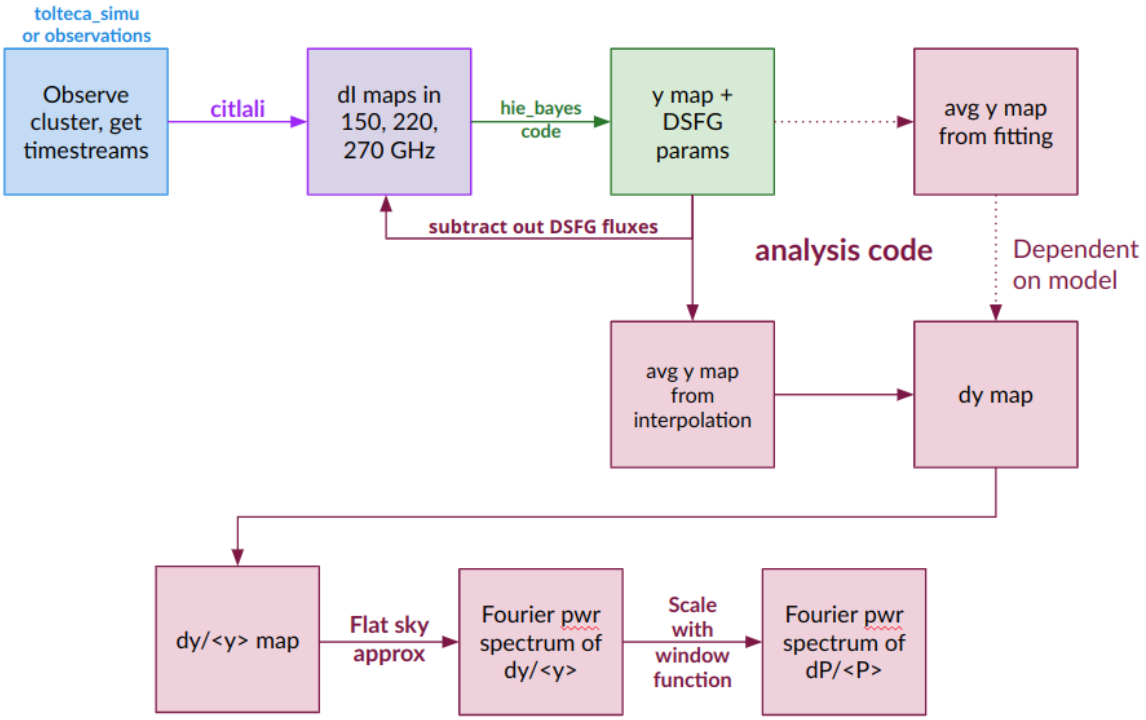

Figure 5.3: A visual showing the analysis pipeline used to calculate the pressure fluctuation power spectrum for a galaxy cluster observed by TolTEC.

6. Mask $\delta y/\bar{y}$ outside user selected radius R and multiply by an apodizing window[2] to reduce ringing on the edges of the Fourier transform (FT).

7. Perform a 2D FT of $\delta y/\bar{y}$. Take the amplitude of the FT P_y and calculate the average value in logarithmically spaced rings from the center out to the mask radius.

8. Divide the result by the integral of the window function to calculate P_y.

See Figure 5.3 for a diagram of the pipeline procedure from beginning to end.

Note that the isothermal β model used for the profile fit is a variation on the equation presented in §1. It is given by [121]

[2]An apodizing window can be any function that smoothly decreases to zero in order to prevent a sharp cutoff at the edge of the mask. When performing a 2D Fourier Transform, sharp cutoffs will introduce ringing effects (which in turn becomes noise in the power spectrum).

$$y_\beta(\theta) = \frac{y_0}{(1 + (\frac{\theta}{\theta_c}))^\beta} \tag{5.3}$$

where θ is the distance from the center of the cluster on the plane of the sky, y_0 is the Compton-y value at $\theta = 0$, and θ_c is the cluster concentration. I fit for the three parameters y_0, θ_c, and β; however, the value for β solved here is technically $(3\beta/2 - 1/2)$ when comparing to the solution presented in §1.

5.3.2 Power spectrum calculation

I use the flat sky approximation throughout this work since our observations will be on angular scales $< 10°$[131, 132]. The flat sky approximation allows us to treat the small portion of the sky we observe in as a plane. This allows us to use Fourier transforms rather than spherical harmonics in the following calculations as well as provides the relationship between the 2D Compton-y and 3D pressure power spectra [121, 132].

With the flat sky approximation, we can write the 2D Compton-y power spectrum as a convolution of the 3D spectrum with a window function [121]

$$P_y(k_\theta) = \int \frac{dk_z}{2\pi} |\tilde{W}(k_z, \theta)|^2 P_P(|\mathbf{k}_\theta + \mathbf{k_z}|), \tag{5.4}$$

where $\mathbf{k}_\theta$ is the Fourier vector in the 2D XY plane of the sky, $\mathbf{k_z}$ is the Fourier vector along the line of sight, and $\tilde{W}(k_z, \theta)$ is the Fourier transform along the line of sight for a weighting function also called the "window function". The window function is given by [121]

$$W(\theta, z) = \frac{\sigma_T}{m_e\, c^2} \frac{\bar{P}(\theta, z)}{\bar{y}(\theta)}, \tag{5.5}$$

where θ is the radial distance from the center of the XY plane and z is the projected distance along the line of sight. In this analysis, I take the same approximation made in KG16 such that $\tilde{W}(k_z, \theta)$ is independent of θ [121]. This is a rough approximation

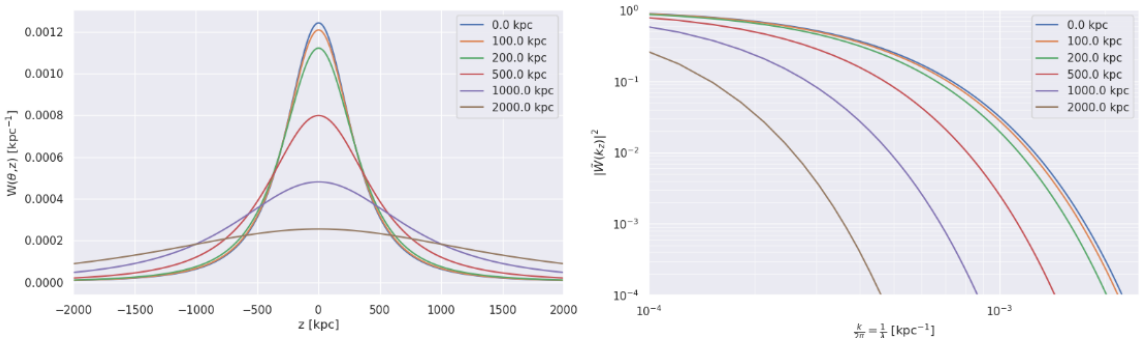

Figure 5.4: *Left*: Reproductions of window functions from [121]. The window function is used to convert from the 2D Compton-y to 3D pressure power spectra using the flat sky approximation. *Right*: The Fourier transform of the window function. The function sharply drops around $k_z/2\pi \geq 5\times10^{-4}$ kpc^{-1}, or $z \leq 2000$ Mpc, for all values of θ. This means the contribution of the Fourier transformed window function to the convolution with the 3D power spectrum is small enough to make this approximation on scales far below the size of an observation.

that holds best within the innermost (R< 1 Mpc) regions of the cluster (see Figure 5.4).

Eqn. 5.4 can be further simplified if we choose to limit the analysis to scales such that $k_z << k_\theta$ (e.g., $z >> \theta$). The Fourier transform of the window function sharply drops around $k_z/2\pi \geq 5 \times 10^{-4}$ kpc^{-1}, or $z \leq 2000$ kpc[3], for all values of θ. This means that the contribution of the Fourier transformed window function to the convolution with the 3D power spectrum is small enough to make this approximation on the scales of a typical observation.

Taking these two assumptions, we can rewrite Eqn. 5.4 as [121]

$$P_y(k_\theta) \simeq P_P(\mathbf{k}_\theta) \int \frac{dk_z}{2\pi} |\tilde{W}(k_z,\theta)|^2 \simeq N(\theta) P_P(\mathbf{k}_\theta), \tag{5.6}$$

[3]Or an angular scale of about 5.5′ at a redshift of 0.5. This is larger than the typical cluster radius R_{500} at $z \sim 0.5$, but on the same scale as R_200.

where $N(\theta)$ is the integral of the Fourier transformed window function. Using the `romberg` integration method in Python, $N(\theta) = [7.4, 7.2, 6.6, 4.6, 2.7, 1.4] \times 10^{-4}$ for $\theta = [0, 100, 200, 500, 1000, 2000]$ kpc.

As was done in similar experiments, I report the results from the analysis pipeline using characteristic amplitudes $A_{2D}(k)$ and $A_{3D}(k)$ [121, 123]. The functions for the characteristic amplitudes are given by

$$A_{2D}(k) = \sqrt{\frac{k^2}{2\pi} P_{2D}(k)}, \tag{5.7}$$

$$A_{3D}(k) = \sqrt{\frac{k^3}{2\pi} P_{3D}(k)} \approx \sqrt{\frac{k^3}{2\pi} \frac{P_{2D}}{N(\theta)}}. \tag{5.8}$$

5.3.3 Caveats

The results presented below do not include the effects of atmospheric noise or contamination from DSFGs. This is to allow for a complete understanding of systematics in the analysis pipeline itself using well-characterized test cases. Since we must eventually deal with both effects in every galaxy cluster observation, I outline the general steps taken for atmospheric and DSFG removal in a general TolTEC observation below. A more detailed overview of these methods can be found in §4.5.1.

Atmospheric noise can be filtered out assuming that over the course of the observation all detectors see approximately the same atmospheric fluctuations in a short time period. TolTEC's data reduction pipeline `citlali` (refer to §4.5.1.1 for more details) uses principle component analysis (PCA) to identify the correlated modes in the detector timestreams and remove the largest ones. This is a powerful method that removes the dominant signal in the intensity maps. However, there is a drawback to this method when applied to sources with extended emission. Astrophysical signals from extended sources will be correlated across a large number of detectors, as compared to a point source, and thus could be removed by the PCA cleaning. The data

reduction pipeline estimates the extent of this effect by running a simulated source through the same process (refer to §4.5.1.1 for more details).

As for DSFGs, there are a few standard methods for removing their contamination from TolTEC observations. First, there is a point source fitter incorporated into `citlali` that can remove well-identified and isolated DSFGs in a post-mapmaking step. This will be implemented to remove the brightest sources that are identified with S/N$>$ 5. This method is currently under investigation by a TolTEC science working group using the December 2022 commissioning observations. The second method is to use external tools on the processed TolTEC maps, such as `PyBDSF` [133], which vary in their extraction methods. The general method is to identify the location of point sources, either by a signal threshold or using a S/N map, then fit a single or multiple 2D Gaussian profiles to best model the shape. There are other methods that can use data from multiple bands to identify the common sources in three maps.

Along those lines, one such method in development that will simultaneously fit SZ and DSFG signals across the entire map simultaneously using Michael McCrackan's hierarchical Bayesian modeling software `hie_bayes`. With TolTEC's simultaneous observations in three bands, it should be possible to disentangle DSFG contamination from the tSZ measurements since they have distinct spectral and spatial shapes. A full examination of this method falls outside the scope of this thesis, but I note here that during initial testing we discovered a positional dependence in the Compton-y maps when resolved DSFGs were not removed from the intensity maps. In a future iteration, `hie_bayes` will include a spatial dependency on the Compton-y distribution in order to remove this degeneracy.

5.4 Results from Simulations

I have tested the pipeline described above using a toy model as well as a simulated smooth, spherically symmetric cluster profile. The toy model was designed to

analytically confirm the amplitude values output by the analysis code. The smooth cluster simulation was selected to examine systematics in the pipeline prior to introducing signals from fluctuations. I conclude this section with a first look at the pipeline output using a Compton-y profile from a hydrodynamical cluster simulation that includes pressure fluctuations [134].

5.4.1 A Toy Model

An important step in any pipeline is to confirm that the procedure is well calibrated and understood analytically. To this end, I utilized a toy model of a 2D $1/f$ spectrum with an arbitrary amplitude. The $1/f$ spectrum, also known as pink noise or fractal noise, is a characteristic feature of not only electronics (see §2.3) but also atmospheric noise while observing. As such, it is a well studied model with a number of methods for generating. Below I describe the method I used to generate a normalized spectrum.

In order to simulate a 2D $1/f$ spectrum, I use the following recipe:

1. Generate an $N \times N$ pixel map using a normal Gaussian distribution with $\mu = 0$ and $\sigma = 1$. This simulates a 2D white noise spectrum.

2. Perform a frequency shift on the white noise map then take the Fast Fourier Transform (FFT). This step ensures that the FFT output $G_w(f_x, f_y)$ is correctly ordered with respect to the input map $g_w(x, y)$ before the next step.

3. Generate the grids of Fourier frequencies $f = \sqrt{f_x^2 + f_y^2}$ for the map centered on (0, 0). To do this, I use the `numpy` FFT frequency function, create a meshgrid for the f_x, f_y values, then calculate f.

4. Approximate the pink noise spectrum by calculating $\frac{1}{f} \times G_w(f)$.

5. Account for `nan` or $\pm\infty$ values and change them to 0. This step could also be accounted for while making the Fourier frequencies by adding a small factor (order of 10^{-9} or smaller) to all values.

6. Perform an inverse frequency shift then take the real values of the inverse FFT. This ensures that the output from the inverse FFT, $g_p(x, y)$ is in the same index order as the input white noise map.

See the first column of Figure 5.5 for three example 2D spectra generated from these steps.

Since the goal of the model is to test the power spectra and resultant amplitude calculations, I skip the averaging steps described in the previous section. The averaging steps will be tested using the smooth profile in the next section. Plugging in the equation for the model $1/f$ spectrum we have

$$P_{model}(k) = \frac{2\pi}{k}, \tag{5.9}$$

where $k \equiv f/2\pi$. I can now use Eqn. 5.7 to calculate the analytic model for the characteristic 2D amplitude to be

$$A_{2D,model} = \sqrt{k}. \tag{5.10}$$

To calculate the amplitudes A_{2D} and A_{3D}, I perform the following procedure after generating the 2D $1/f$ map. Note that this procedure is generalizable to any other spatial map input. The steps are as follows:

1. Perform a Fourier transform on the spatial map to obtain $X(k)$.

2. Calculate the power spectrum for the FT using the relationship $P_k = |X(k)|^2$.

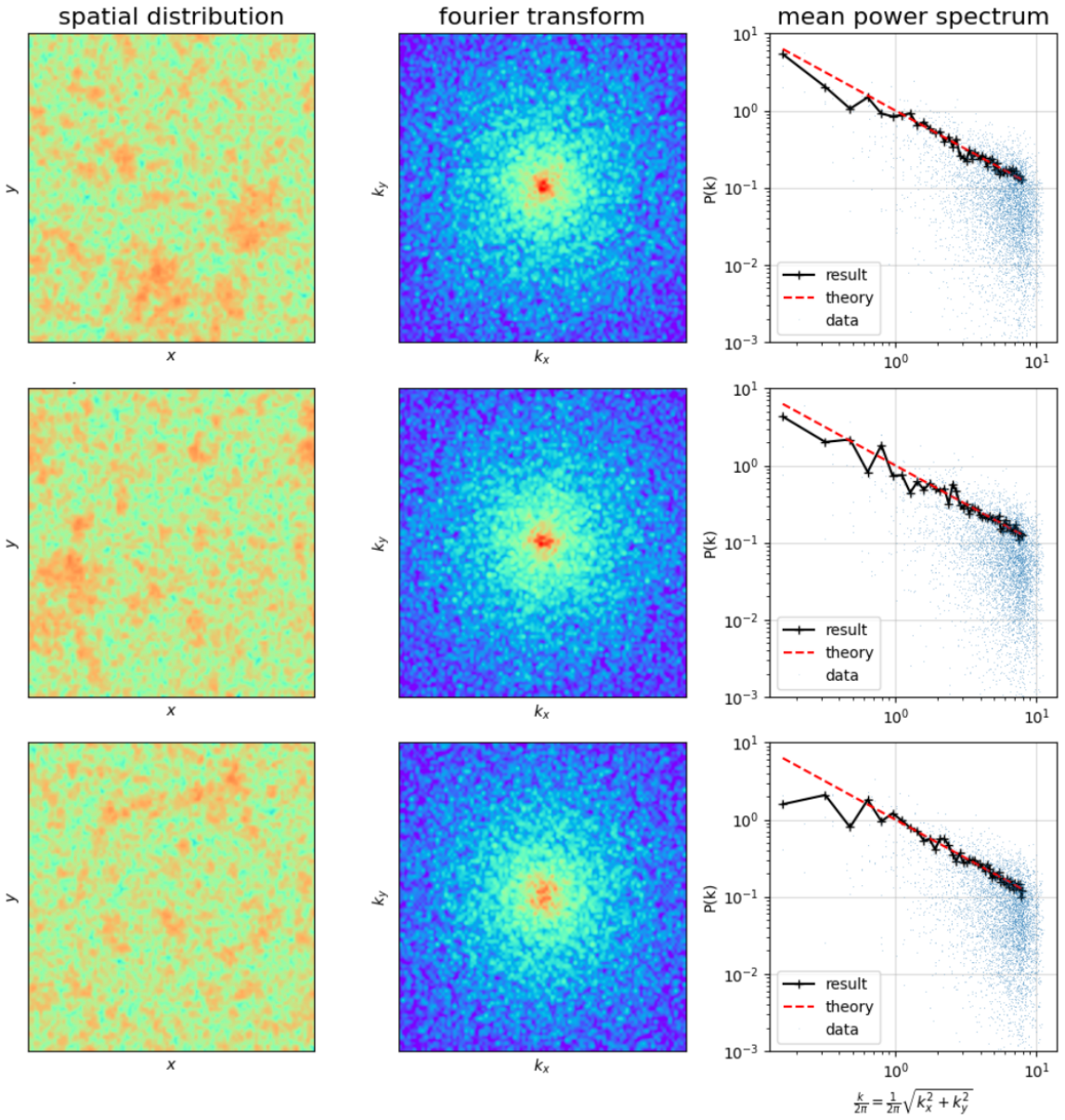

Figure 5.5: Three examples of randomly generated 2D $1/f$ spectra used as a toy model. The left column shows the distributions in spatial coordinates. The center column are the distributions in frequency coordinates after a Fourier transform. The right column are the power spectra calculated from the central column where the dashed line is the expected $1/f$ distribution, the black line is the binned mean of the data, and the scatter plot is the data from the center column. The x-axis on the rightmost plot is in units of pixels^{-1} rather than physical units. This can be easily scaled to inverse kpc using the pixel size in arcseconds along with the redshift of the source.

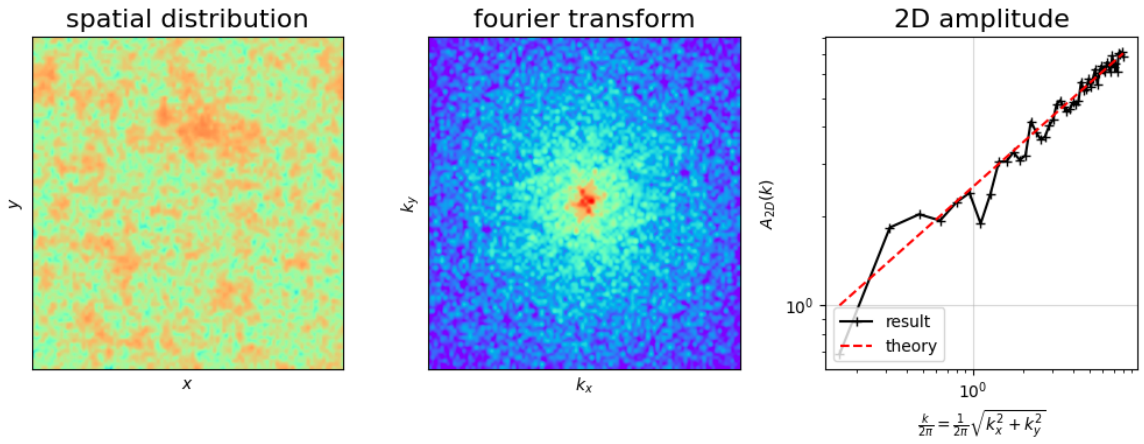

Figure 5.6: An example of a randomly generated 1/f spectrum and the result of continuing the power spectrum analysis shown in Fig. 5.5 to calculate A_{2D}. We show that the averaged profile is well-matched to the analytic form.

3. Take radial bins and average the power spectrum map to obtain a mean profile with respect to k. I use the `stats.binned_statistic` function. Since the average calculated from this method is per bin size, I scale it using the surface area $\pi\delta k^2$. This results in the value P_k, after normalizing by N^2 (the number of pixels).

4. Calculate A_{2D} with the function above.

5. Choose a window function and calculate A_{3D}.

Since the final step, transforming the 2D spectrum into a 3D spectrum, is a simple scaling, I do not show it here. As shown in Figure 5.6, I confirm that the 2D amplitudes match between the theory and a randomly obtained pink noise map. We have confirmed that the Fourier transform procedure works for the toy model. Now, I can repeat the same analysis for any given Compton-y map.

5.4.2 A Spherically Symmetric Cluster

I chose to first work with simulations of smooth, symmetric cluster profiles using the 'universal' pressure profile model outlined in Arnaud et. al. (2010). These models

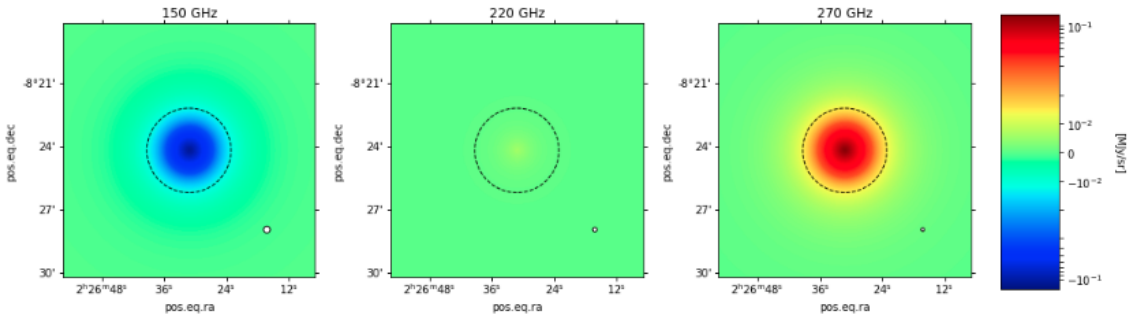

Figure 5.7: Simulated intensity maps in the three TolTEC bands used for the analysis in §5.4.2. The simulation, `cluster_sz`, used to generate the results was developed by Grant Wilson and Zhiyuan Ma. This simulation included only the contribution of SZ signal for purposes of identifying issues in the pipeline. The dashed circle represents TolTEC's $4'$ field of view (FoV) while the smaller white circles in the lower right corners represent a single TolTEC beam.

are well-characterized and would reveal any systematics in the procedure that could not be traced with the toy model; namely, the averaging step.

The software to model these clusters, `cluster_sz` was developed by Grant Wilson and Zhiyuan Ma. To run the simulation, a user selects their cluster's redshift z, cluster mass M_{500}, halo mass M_{200}, cluster concentration c_{500}, and halo concentration c_{200} then chooses which radiation mechanisms to include. Aside from the SZ, options include adding the contribution of CMB anisotropies, cosmic infrared background (CIB) lensing, DSFGs (either randomly placed or using a predetermined sample), and atmospheric noise. I chose to only include the SZ contribution for this initial phase of the study as an idealized case (refer to §5.3.3 for more details). In Figure 5.7 we show the simulated intensity maps in TolTEC's three bands used for the analysis.

After obtaining our simulated intensity maps of the tSZ in each TolTEC band, I ran the maps through the hierarchical Bayesian modeling software `hie_bayes`. The basis of this software is the usage of Bayesian statistics to estimate the distribution of parameters θ that best describe the observed data y. Bayes' theorem is given by

$$P(\theta|y) = \frac{P(y|\theta)P(\theta)}{P(y)}, \tag{5.11}$$

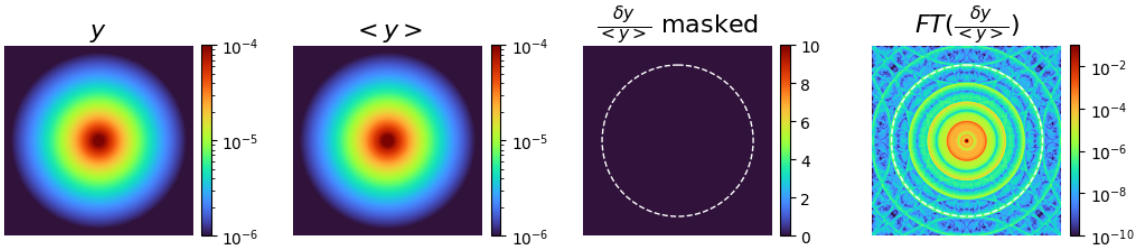

Figure 5.8: Maps from different steps in the analysis procedure. The first map is the median Compton-y map generated from running the `hie_bayes` code on the simulated TolTEC maps shown in Figure 5.7. The second map is the average profile determined from interpolating over the simulated Compton-y map. The third is the difference between the two maps. The final map is the amplitude from the Fourier transform of the Compton-y fluctuation map (e.g., the third map divided by the second). The ringing seen in the center of the amplitude map is due to small scale fluctuations imparted by the averaging technique. The white circle on the final two plots highlight the mask used prior to the Fourier transformation.

where $P(\theta)$ is the prior distribution (the probability of the parameter given our prior knowledge, or the range of allowed parameter space), $P(y|\theta)$ is the posterior distribution (the probability of occurrence y given past occurrence θ is true), or likelihood, and $P(y)$ is the marginal distribution (probability y occurs with no conditions), or evidence. In the process of Bayesian modeling, we calculate the posterior distribution for each parameter used in the model for every pixel in the map. Hierarchical Bayesian modeling provides additional constraints on the prior distributions through the use of hyperparameters and hyperdistributions. We have not yet included hierarchical parameters for the Compton-y fit, so they are not applicable in the following analysis.

Using `hie_bayes`, I can estimate the Compton-y parameter for each pixel using Eqn. 5.1.1 where ΔI is given from the simulated intensity maps. The result is, for each pixel, an array of y values at each step in the fitting code. Given enough steps and high S/N ΔI data, the fit should converge. Convergence for the noiseless, smooth cluster simulation occurred after 200 steps for any pixel. Since I wanted to replicate the pipeline as if it was run on real data, for the results presented here I ran

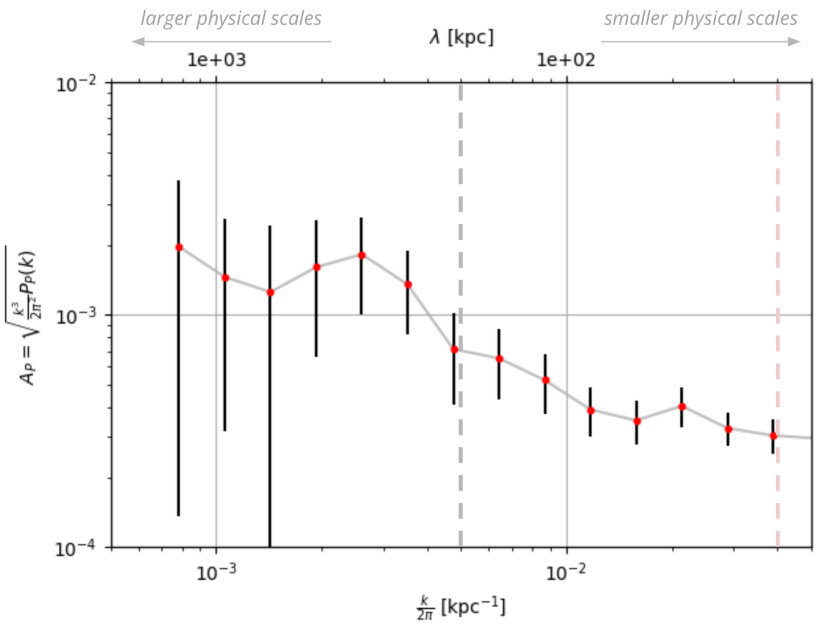

Figure 5.9: The resulting power spectrum for the smooth, symmetric cluster simulation with no contamination from instrument noise, atmospheric noise, or DSFGs. As seen in Fig. 5.8, the power on small scales oscillates due to the ringing at the center of the map. As such, we do not obtain an exact, well-behaved power spectrum back. The top axis converts the spatial frequencies (kpc^{-1}) into a physical units (kpc). With its 5-10″ beams, TolTEC should be able to recover pressure fluctuations from 10s of kpc out to over 1 Mpc, matching the gap between x-ray observations and large-beam observatories such as *Planck*. The dashed pink line indicates the physical size of a 10″ beam at z=0.6 and the dashed grey line indicates the physical size of a 75″ beam at the same redshift.

`hie_bayes` for 2000 steps, dropping the first 100 for the 'burn-in' period. I use the median value for each pixel as the input to the subsequent power spectrum analysis.

The resulting power spectrum for the smooth, symmetric cluster simulation is shown in Figure 5.8. While the fluctuation map $\delta y / < y >$ appears to show a good match between the input and the interpolated average profile, I observe ringing in the center of the power spectrum due to residuals between the two. I tested different binning and interpolation methods with no success in removing the rings entirely. This is an important systematic in the analysis method that requires further optimization.

After obtaining the power spectrum for the fluctuation map, I use the same method laid out in §5.4.1 to calculate the characteristic amplitudes A_{2D} and A_{3D}. I add in an additional step to convert the wavenumber k from inverse pixel units to kpc^{-1}. This is dependant on the pixel size from the mapmaking step, but is typically $1''$ per pixel. It is also dependant on the redshift of the cluster through the angular diameter distance

$$D_A(z) = \frac{c}{1+z}\int_0^z \frac{dz}{H(z)} = \frac{c}{1+z}\int_0^z \frac{dz}{H_0\sqrt{\Omega_M(1+z)^3+\Lambda}}, \tag{5.12}$$

where $H_0 = 2.2e-18$ s^{-1} is the Hubble constant in SI units and we assume a flat universe with $\Omega_M = 0.3$ and $\Lambda = 0.7$. For this test, I assumed a cluster with z=0.6 which results in approximately 0.145 kpc^{-1} per $1''$ pixel. After taking this conversion, I obtain the pressure fluctuation power spectrum shown in Fig. 5.9. As had been observed in the 2D power spectrum map, on small physical scales oscillates due to the ringing at the center of the map. There also appears to be a peak on the scale of the masking radius, which implies that the choice of mask and subsequent apodization step were not sufficient. These will introduce biases when interpreting the energy injection scales on a true observation and so they must be further explored. However, as it stands, this result serves as a proof of concept that we will be able to reduce TolTEC observations of galaxy clusters, obtain their Compton-y map, and extract the 3D pressure power spectrum. Based on the map size used in this example, similar to a ~ 36 arcmin^2 observation, I predict TolTEC will be sensitive to fluctuations on scales between ~ 50 kpc and 1 Mpc.

5.4.3 Extending the Analysis to A Dynamically Active Cluster

As an extension to this study, I ran the pipeline on a simulated galaxy cluster from the Galaxy Cluster Merger Catalog (GCMC). These simulations only include gravitational physics and non-radiative hydrodynamics; however, these two elements

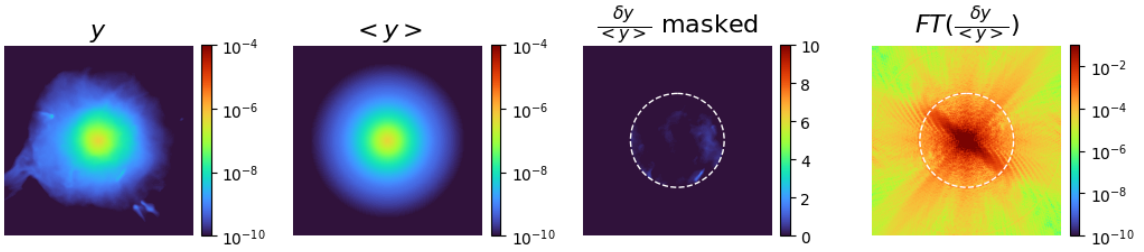

Figure 5.10: An example of a simulated Compton-y map from the Galaxy Cluster Merger Catalog being run through the initial analysis steps. The subtraction of the interpolated average is able to identify the fluctuations in the map and the Fourier transform shows that these fluctuations peak at small spatial scales (or, large k values). The white dashed circle is the same scale as in Fig. 5.8.

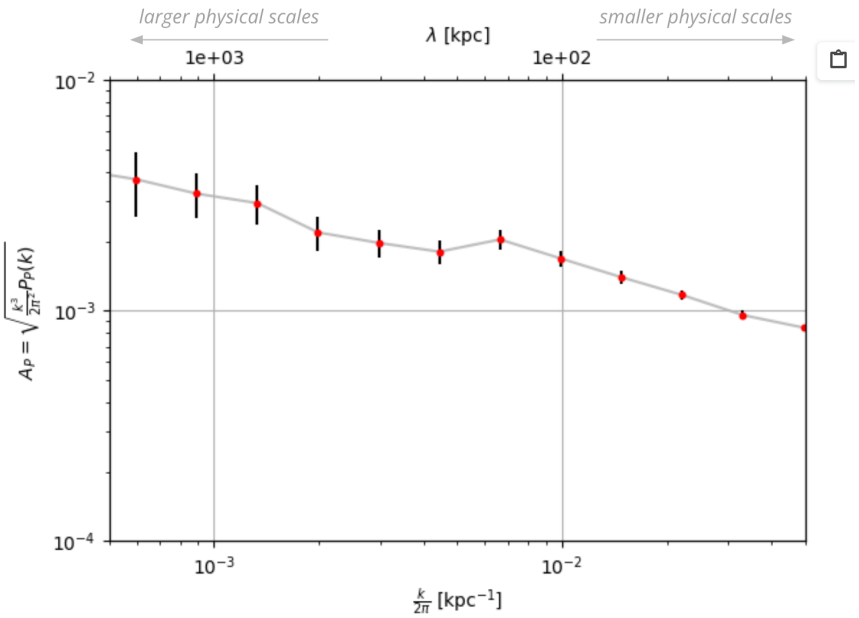

Figure 5.11: An example of the analysis pipeline output for the average pressure fluctuation power spectrum using a simulated Compton-y map from the Galaxy Cluster Merger Catalog. The spectrum recovers a local peak around 500 kpc, which is expected in nearby clusters [121]. The power spectrum continues to increase beyond this peak due to structures near the mask radius ($R_{mask} = 1.5$ Mpc) where the ICM would be accreting gas from the surrounding cosmic web.

generate non-spherically symmetric profiles that simulate clusters in a variety of dynamical states [134]. Testing these is a perfect next step for examining TolTEC's

sensitivity to pressure fluctuations. The GCMC provides FITS files with Compton-y maps that can be fed directly into the analysis pipeline.

I ran the GCMC Compton-y map through the analysis pipeline using the same procedure described in §5.4.2. This initial run on a single simulation with no atmospheric noise shows promise for being able to extract fluctuations from these maps as shown in Figures 5.10 and 5.11. I find a peak in the pressure fluctuation power spectrum on scales ∼500 kpc, which matches the result from Khatri and Gaspari (2016) when observing the nearby Coma cluster [121]. The power spectrum continues to increase beyond this peak due to large scale structures on the eastern side of the map, close to $R_{mask} = 1.5$ Mpc.

Ultimately, this test does not indicate the exact level of fluctuations that TolTEC will be sensitive to; in order to test this, we will need to generate simulated TolTEC observations with `tolteca_simu`. This test does however provide a first look into the relative fluctuation amplitudes and scales the pipeline can identify for a given map. We aggregate all of the next steps for this work in the following section.

5.4.4 Next Steps in Development

The preceding results have shown that the pipeline is ready for tests with realistic TolTEC simulations and observations outside of one major systematic. As stated in §5.4.2, I observe ringing in the power spectrum on the scale of the bins due to residuals between the smooth cluster profile and its interpolated average. The residuals are between 4×10^{-12} and 5×10^{-6} with the largest values closest to the center of the map. Since the Compton-y values are on the order of 10^{-4} at the center, the residuals are higher than desired. This might be handled by introducing a mask to the center of the map; however, we would lose sensitivity to the smallest fluctuation scales. This is a systematic that needs to be further explored and optimized by testing different masks and apodization techniques, interpolation methods, and bin sizes. From a

review of the literature for similar experiments, the optimal bin size has not been systematically determined and remains an open question [121, 123].

In §5.4.3, I apply the pipeline to a dynamic cluster simulation and show that the pipeline is sensitive to fluctuations in the map. I note here that the map of the 2D Fourier transform shows low frequency modes that may introduce bias to the power spectra. This can be tested by highpass filtering the 2D FT map, then performing an inverse Fourier transform to check what was removed in the spatial map. As with the smooth cluster case, the use of different masking and apodizing techniques on the spatial fluctuation map remains another area for testing and optimization.

5.5 Conclusions

Robust studies of pressure enhancements, or fluctuations, in the intracluster medium (ICM) of galaxy clusters are vital to improving our understanding of their formation and evolution. Deviations from a smooth underlying profile can bias mass estimates of clusters which in turn affects their usage as cosmological probes. Thus, the removal of these fluctuations is vital for improving the use of clusters for cosmology. On the other hand, the fluctuations themselves can be used to probe the thermodynamics of the cluster by calculating their power spectrum. The power spectrum amplitude and slope are sensitive to the amount of turbulence and conduction, respectively, in the ICM. To obtain these power spectra requires high resolution, high sensitivity observations of the thermal Sunyaev-Zel'dovich Effect (tSZ) over a wide spatial range. In fact, this type of study is becoming a much wider area of interest thanks to the commissioning of high resolution mm-wave instruments such as MUSTANG-2, NIKA2, and now TolTEC.

In this chapter, I outlined my analysis pipeline to extract the power spectrum of fluctuations from TolTEC observations. I have calibrated the pipeline using a toy model $1/f$ spectrum to confirm it could output the analytically determined amplitude

and slope. In applying the pipeline to simulated cluster distributions, I found new areas for optimization in the pipeline (refer to §5.4.4) but also set a limit on the physical scales TolTEC will be able to recover. From these initial tests, I predict that TolTEC will be sensitive to fluctuations on spatial scales between ~ 50 kpc and 1 Mpc for a cluster at $z = 0.6$.

As stated before, the upcoming analysis of the TolTEC observations will be enhanced by the inclusion of ancillary data. As the redshift increases, TolTEC will become less sensitive to fluctuations below 100 kpc; however, we can then turn to ancillary x-ray observations. For all observations we can utilize results from low resolution survey instruments with similar frequency coverage, such as *Planck* and ACT, to constrain the ICM profile outside of 1 Mpc. Additionally, data from mm/submm instruments outside of TolTEC's bands will be invaluable for disentangling the degeneracy between DSFGs and the tSZ. This will result in lower uncertainty in the Compton-y maps and subsequent power spectra analysis.

In hoping to leverage ancillary data for upcoming TolTEC observations, I provided a sample of four clusters with existing data from HST, Bolocam, *Herschel*, ACT, AzTEC, *XMM-Newton* and/or *Chandra* (see Table 5.1). This small sample could be used as the basis for a pilot study to confirm TolTEC's sensitivity to ICM fluctuations on the scales described above using the pipeline I developed. Following confirmation of TolTEC's exact sensitivities, the pilot study could then be extended into a much larger survey. TolTEC should be able to resolve each sample cluster's profile out to a 1 Mpc radius over a 6×6 arcmin^2 area. Considering the initial mapping speed estimates (see §4.7.3), this should result in a map RMS of 0.1 mJy/beam at 2.0 mm after 1 hour or 45μJy/beam after 5 hours if the map has sufficient coverage. This is equivalent to about a Compton-y value of about 5×10^{-5}; however, fluctuations can be as faint as 5×10^{-6} or lower. To reach these depths within the same time will require the improvements to TolTEC's noise performance discussed in Chapter

4. Once the improvements are made, even with TolTEC's lowest predicted mapping speeds [41], we could expect to recover fluctuations down to 5×10^{-6} within 5 hours of integration time. Overall, TolTEC holds incredible promise for performing novel deep, high resolution observations of the fluctuations in galaxy cluster ICMs.

CHAPTER 6

CONCLUSION

"Why don't we just wait here for a little while, see what happens?"

R.J. MacReady, *The Thing (1984)*

Millimeter wave astronomy offers a unique perspective of both the oldest parts of the Universe as well as the birth places of its newest members. Additionally, there are still many open questions that can be answered using a ground-based high resolution, high sensitivity instrument coupled to a single dish telescope. Specifically, when it comes to the study of galaxy clusters, we can further probe the thermodynamics and formation history by examining pressure fluctuations in the intracluster medium (ICM). To advance our knowledge of the mm-wave universe, we developed the TolTEC camera, a new multi-wavelength imaging polarimeter of the Large Millimeter Telescope (LMT). In this thesis, we described the camera, its design, testing, installation, and initial commissioning. We also outlined a future study that could leverage TolTEC to obtain novel observations of ICM pressure fluctuations out to further redshifts than before.

In Chapter 1, we emphasized that the vast diversity of matter in the Universe, both in scale and type, leads to the natural question of how did this matter organize and on what timescales did it occur[1]. Galaxy clusters serve as a valuable tool when studying this evolution as they are one of the largest gravitationally bound objects

[1]To phrase it another way for the non-astronomer: "How ever did all this stuff get here and when did it start forming?"

seen today. Importantly, these objects likely evolved from the largest random perturbations in the initial density field all the way to massive halos with sizes well over 1 Mpc. Consequentially, cluster number counts, gas mass fractions, and energy densities are highly sensitive to and probes of cosmological parameters such as Ω_M and σ_8. With the proper observational tools we can study these probes out to high redshifts where protoclusters are beginning to form and where the most active moments in accretion/formation are occurring.

The study of the SZ with millimeter wave instruments has matured into a diverse field with studies ranging from high resolution observations of the SZ through galaxy halos to multiple all-sky surveys that identify galaxy clusters out to a redshift of 2. Still, there is a niche yet to be filled with a high resolution camera that can quickly, yet deeply perform follow up observations to these massive surveys. In part to address this need, we developed the TolTEC camera: a new multichroic imaging polarimeter coupled to the 50-m single dish Large Millimeter Telescope. As described throughout this document, TolTEC can probe intermediary scales that ultra-high resolution facilities would need years to cover and that large beam facilities cannot achieve, all to lower map depths than before.

In Chapter 2, we reviewed the design principles for the TolTEC camera, the newest facility instrument for the Large Millimeter Telescope (LMT). The camera is able to simultaneously image in 1.1, 1.4, and 2.0 mm (or 270, 220, and 150 GHz, respectively) with 7716 superconducting Lumped Element Kinetic Inductance Detectors (LEKIDs) across its three focal plane arrays. To date, TolTEC is one of four ground-based mm-wave cameras to feature LEKID arrays making it one of the earliest adopters of this technology.

TolTEC was built, integrated, and tested in the UMass Amherst laboratory between 2017 and 2021. We present key results from laboratory testing in Chapter 3. Prior to shipping TolTEC to the LMT, we fully characterized the system's cryogenic,

detector, optical, and readout performance to confirm the performance matched the design specifications. During testing, we discovered a critical issue in the optics chain due to bowing in the dichroic filters. By performing detailed testing, we were able to identify and correct this issue.

We installed TolTEC at the LMT in late 2021 and began commissioning observations in June 2022, which are presented in Chapter 4. Throughout our first year of on-sky testing, TolTEC has been limited in its amount of observation time due to a combination of hardware issues and unforeseen events[2] including a forest fire, frequent power outages, lightning strikes, snowstorms, and a volcanic eruption.

Despite these intermittent setbacks, TolTEC demonstrates potential in fulfilling the Astro2020 Decadal Survey's request for a fast, powerful mm-wave camera coupled to a single dish telescope. TolTEC hardware performance is comparable to its initial performance in the laboratory with some clear improvements for the readout electronics. Additionally, from the commissioning data in December 2022, we have shown that the optical and detector elements operate as intended. The primary area for improvement lies in the readout electronics and, as of Summer 2023, plans are underway to implement them prior to the Fall 2023 observing season.

As discussed in Chapter 5, even considering the camera's excess readout noise, we should be able us to conduct a pilot SZ study within five hours of integration time per cluster. The analysis pipeline to conduct the study has been built and tested on well-characterized simulations. From the initial results, we anticipate TolTEC will be able to resolve each sample cluster's profile out to a 1 Mpc radius over a 6×6 arcmin^2 area. Though TolTEC has not yet had a successful detection of a cluster after 1 hour of commissioning time, the observations placed an upper limit on TolTEC's current instrument noise level. With the planned upgrades detailed in Ch. 4, the instrument

[2]See definition for "acts of God". While *scientifically* lacking evidence as to its efficacy, the team did consider sending a priest to bless the site.

noise level will fall below the BLIP and allow us to performing deeper observations on the proposed sample, if needed.

TolTEC was designed with a minimum of ten years of full-time operation at the LMT in mind. Considering the commissioning time spent on-sky as of Summer 2023, TolTEC has only observed for 3% of its total lifetime. While the commissioning testing has revealed clear areas for improvement in reducing instrument noise, we also have clear evidence that the camera is well on its way to becoming a linchpin of mm-wave astronomy. To conclude, TolTEC has an exciting future ahead of it, marking a new epoch of mm-wave astronomy.

CHAPTER 7

APPENDIX

Operating Principles of TolTEC's Cryocoolers

Cooling TolTEC to its base operational temperatures represented a major cryogenic challenge in terms of design, fabrication, and assembly. TolTEC uses two liquid-free cooling systems: a Cryomech 415 Pulse Tube Cooler (PTC) henceforth referred to as the Auxiliary Pulse Tube Cooler (APTC) and a dilution refrigerator (DR) from Oxford Instruments.

Both systems operate using similar principles: helium (He) undergoing adiabatic expansion, much like the coolant in a home refrigerator, can be used to absorb heat from an external system. During the compression in a PTC, He is pushed through a heat exchanger, called a regenerator, comprised of a metal mesh with a high heat capacity and surface area. The He gas then enters the pulse tube, which is thermally isolated from its surroundings, where it compresses the gas already in the chamber towards the closed end of the tube. In an adiabatic system, this creates a pressure gradient which then creates a thermal gradient. The lowest pressure, and thus the coolest, end is the open side of the tube. In our system, we have a motor that alternates high/low pressure. When the motor rotates and the pressure decreases (e.g., the volume increases, much like a piston being pulled back), the helium undergoes adiabatic expansion, cooling the gas further. As the helium is allowed to move back into the increased volume, it carries away heat from a heat exchanger connected to TolTEC's main cryostat.

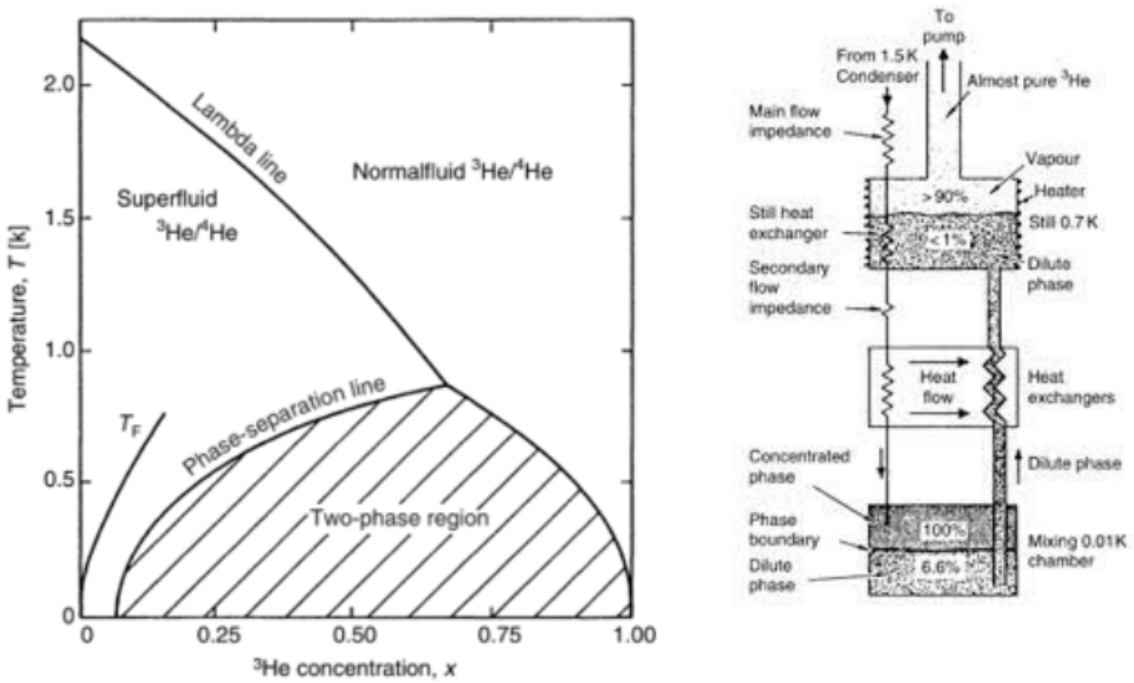

Figure 7.1: Figures from [136]. *Left*: The phase diagram for the helium mixture showing that there is a fundamental non-zero limit for He^3 solubility in the mixture. *Right*: Schematic of a dilution refrigerator showing the separation of the mixture into its concentrated and dilute phases.

Similarly, a DR can use the adiabatic expansion of helium to reach temperatures below 2 mK; however, while PTCs use one isotope of helium to cool the system, a DR uses a mixture of a Fermi liquid He^3 and a superfluid He^4 [135]. As the temperature of the mixture goes to zero, the system undergoes a phase transition and separates into a pure He^3 phase and a dilute He^3 phase. The amount of He^3 suspended in the dilute phase varies with temperature (see Fig. 7.1), however it can never go below 6.7% He^3, 93.3% He^4 [136]. That the solubility of He^3 cannot go to zero is a fundamental property for the operation and design of the dilution refrigerator.

Since the He^4 is a superfluid, the He^3 flows through it due to a pressure gradient between the pure state of He^3 and the dilute state [135]. Transferring the most energetic He^3 atoms from the pure liquid to the dilute state results in an increase in

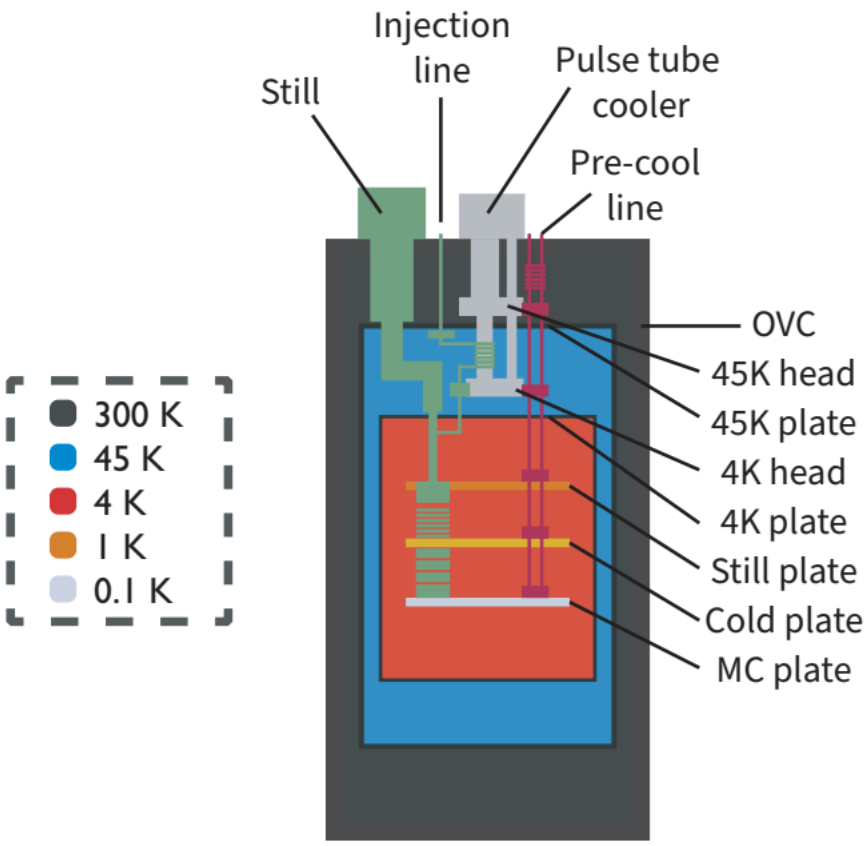

Figure 7.2: Cross sectional view of a dilution refrigerator showing the location of the mixing chamber and approximate temperatures reached in TolTEC. Adapted from a figure in the Oxford Instruments manual for the Triton 2016 dilution refrigerator.

the entropy of the system. The change in entropy provides the cooling power for the coldest stage of the DR in a part called the mixing chamber (MC) (see Figure 7.2).

From Waele's 2011 review of cryocoolers, the cooling power of the MC comes from [135]

$$\dot{Q} = n_3 \frac{\pi^2}{2} R T_M^2 \left(\frac{1}{T_F(x_s)} - \frac{1}{T_F(1)} \right)$$

where n_3 is the He^3 flow rate, R is the ideal gas constant, T_M is temperature of the phase boundary between the concentrated and dilute phases, and T_F is the Fermi temperature of He^3 in the dilute phase, $T_F(x_s)$, and the concentrated phase, $T_F(1)$. The Fermi temperature is given by [135]

$$T_F = \frac{1}{8}\left(\frac{3}{\pi}\right)^2 \frac{h^2}{m_3 k_B}\left[\frac{N_A}{V_m(x)}\right]^{2/3}$$

where h is Planck's constant, m_3 is the effective mass of He^3, k_B is the Boltzmann constant, N_A is Avogadro's number, and V_m is the molar volume of He^3. Once the He^3 enters the dilute phase, it is pulled towards the still, which is at 1 K, through diffusion. As He^3 travels to the still, it cools warm, condensed He^3 entering the MC. He^3 is then preferentially evaporated from the dilute mixture using a room temperature pump and potentially a heater on the still to cycle the He^3 through the system to be condensed and cooled again. Experimentally, one can determine the cooling power of the mixing chamber through applying heat by increasing the electrical current flowing through a resistor, then observing the temperature the chamber settles to for a given heat load.

Custom Copper Strap Procedure

Acronyms/Definitions

- USC = ultra-sonic cleaner
- DIW = deionized water

Copper lug preparation

1. Place lugs in an ultrasonic cleaner with your preferred cleaning agent. We used deionized water mixed with a commercially available surfactant.
2. While wearing nitrile gloves, remove the lugs from the USC and dry using lint-free wipes.
3. Place dried lugs in a kiln for 9 hours at 593degC to anneal.
4. After 9 hours, quench the lugs in a bucket of cold water. Leave to cool overnight.

5. To remove the oxide that forms on the lugs after annealing and quenching, mix the following solution[1] in a glass beaker large enough to hold the lugs:
   (a) 240 mL white distilled vinegar
   (b) 17.06 g uniodized salt
6. Place the glass beaker with the lugs in solution on top of a hotplate set to 90degC.
7. Stir the solution every 10 minutes for the first hour to loosen the oxide better.
8. Cover the beaker with a lid to limit the evaporation of the solution. Leave for at least another hour.
9. If the solution is dark blue but the oxide has not been removed, remake the solution and repeat as needed.
10. When satisfied with the oxide removal, extract lugs from the solution. Rinse the lugs with cool DIW and dry with a lint-free wipe.
11. Next, using a rotary tool sand the lug surface that will mate to the braid(s). We go from 80-grit to 2500-grit to create a polished surface. Make sure to wear a respirator or mask during this step as copper dust is highly toxic.
12. Clean the lugs with acetone, methanol, then 480 seconds in an USC with DIW.
13. Dry the lugs with nitrogen gas. Store any lugs not using in a bag or chamber with nitrogen to limit oxidation.

[1]This is similar to a "jewelers' solution" which removes oxides from metals using a solution with a low molarity of hydrochloric acid that can bind to an oxide (in our case, a copper oxide). The resulting waste is neutral as the output products are water and a copper salt.

14. Place the braid(s) onto the lug mounting surface and perform a quick clamp with a vice to keep the braid in place for the following step. Make sure your clamp does not scuff or mar the lug surface.

15. Place lug in hydraulic press such that no patterns or imprints can left on it (we used flat steel plates).

16. Press the lug with 20 tons for 30 minutes. Rest for 5 minutes.

17. Press again with 20 tons for 80 minutes.

18. Drill your desired bolt hole pattern. Be wary of the copper heating and deforming the pattern during this process.

19. Repeat the press and drill steps with other lugs as desired for your strap geometry.

20. Next, braze the lugs to the braids using a nitrogen backfill. We used an acetylene torch, flux, and solder to do the brazing step. Careful not to add too much solder on the braids as this will lower their conductivity. The braids can also get brittle during this step with too much heating, so be aware of where you apply the heat.

21. Finally, polish the surface either using sandpaper up to 2500 grit or using a milling machine. Clean the piece with acetone and methanol before storing in a bag or chamber filled with nitrogen until ready for use.

22. When installing, clean the joint with acetone and isopropyl alcohol, then apply a thin coat of Apiezon N grease.

Cold Trapping with Pulse Tube Cooler Head

Acronyms/Definitions

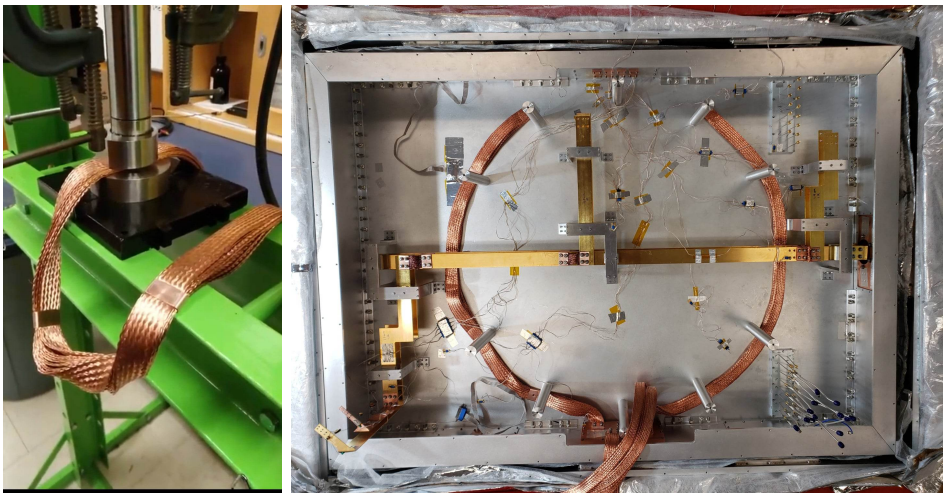

Figure 7.3: *Left*: Copper straps being pressed with OFHC Cu lugs during the fabrication process. *Right*: Same straps installed into the base of the 4 K shell.

- PTC = pulse tube cooler; may refer to cold heads inside of either the dilution refrigerator or auxiliary pulse tube cooler
- Aeroquip = self-sealing fitting commonly used for compressors

Over time, the helium inside the cryocoolers can become contaminated with oil and other impurities. When this occurs, the cryocooler is no longer able to reach base temperature despite no other indicators of excess heat load.

In general, if the system is operated correctly, the following procedure may only be necessary every 5+ years.

This procedure involves working with HIGH PRESSURE gas on the order of 220 PSI. Only attempt if trained to work with these pressures.

Materials

- High purity helium (99.999% or higher)
- Helium manifold plus flexible helium hose
- Mechanical vacuum pump, gauge, and hose

- Turbo vacuum pump
- Cryomech wrenches
- Recharge kit

Preparation

This step will prepares the manifold prior to cleaning the cold head. This can be done at any point prior to the next step, however try to do it as close in time to the cold head cleaning step as possible. It takes about 30-45 minutes to complete the preparation.

1. Position the high purity helium tank and vacuum pump next to the PTC you are planning to use as a cold trap.

   NOTE: DO NOT USE HELIUM GAS OF LOWER PURITY. THIS WILL DEGRADE COLD HEAD PERFORMANCE.

2. Clean the manifold and hose:

   (a) Attach helium flex line hose to the desired helium flex line port on manifold. Leave the other end of the helium flex line hose unattached.

   CAUTION: (1) WHEN CONNECTING OR DISCONNECTING A SELF-SEALING COUPLING, ALWAYS USE TWO WRENCHES. THIS IS TO AVOID LOOSENING THE BODY OF THE COUPLING FROM ITS ADAPTER. (2) ALWAYS CHECK THAT THE FLAT RUBBER GASKET IS IN PLACE BEFORE CONNECTING A SELF-SEALING COUPLING.

   (b) Vent manifold to 50 PSI using the red valve.

   (c) Attach the manifold to a mechanical vacuum pump on the side with the red valve. Attach the helium tank to the manifold side with the black knob using the recharge kit.

(d) Open the black valve to helium line at manifold. Helium tank should be closed.

(e) With the red valve on the manifold closed, turn on the mechanical pump.

(f) When ready, **SLOWLY** open the red valve and pump on the manifold, hose, and helium feedline. Wait until the pressure gauge reads 50 microns or less. This will take between 5 to 10 minutes depending on the size and cleanliness of the line.

(g) Close the red valve to the pump. Set the the helium tank regulator pressure to 50 PSI then **SLOWLY** open the silver valve downstream from the regulator to allow helium into the manifold.

(h) Close the silver valve. Pump the manifold down to 50 microns.

(i) Repeat steps (f)-(h) two more times. Total you will have done 3 pump-purge cycles.

(j) When complete, close the red and black manifold valves.

(k) Close the helium tank, then disconnects the pump and the recharge station.

Cleaning the PTC Head

This step should only be performed when the system is cold. It relies on the system being below 100 K in order to trap impurities in the cold head (they freeze here and are stuck until the system warms up).

This part of the procedure is incredibly time sensitive and dangerous if not followed correctly. DO NOT leave in the middle of the process.

<u>While cold</u>

1. Turn off the compressors.

2. Wait 3-5 minutes for the temperature to do its initial spike.

3. Disconnect the two expansion tank aeroquip fittings (1/4 inch) at the top of the PTC.

4. Disconnect the aeroquip fitting at the top of the head on the PTC to disconnect the cold head from the motor.

5. **IMMEDIATELY** connect the free end of the helium flex hose to the cold head.

6. **IMMEDIATELY** open the red manifold valve to vent helium from the manifold down below 100 PSI. You can purge down to 40 PSI, but keep an eye on the value over the next few days. Never let the pressure go above 300 PSI.

7. Cover the compressor flex hoses with end caps to keep them clean.

After warming to 300K

1. When the system is at 300 K, attach the turbo vacuum pump to the manifold port next to the red valve. Attach the helium line to the black valve port.

2. With the red valve closed, turn on the pump and bring the pressure in the line down to 50 microns.

3. PUMP: Slowly open the red valve to vent the cold head down to 1-2 PSI. Close the valve.

4. PURGE: Add 50 PSI of helium using the tank/black valve.

5. Repeat the pump-purge steps 5 more times.

6. Close the valve to the helium tank. Open the red valve and pump on the cold head overnight.

Recharge helium in cold head

1. After pumping overnight, close the red valve to the vacuum pump.
2. Detach the vacuum pump from the manifold.
3. Slowly pressurize the cold head to match the pressure in the compressor lines (approximately 220 PSI).
4. Close the helium tank. Detach the manifold and hose from the PTC. Detach the helium tank from the manifold. Store manifold and hose in a safe place under pressure. Make sure to label that they are under pressure.
5. Reconnect the hoses at the PTC starting with the two tanks, then the motor.

If after reconnecting everything the pressure at the compressor reads below 220 PSI, use the recharging station and the procedure provided by Cryomech.

TolTEC Start-up and Shut-down

Acronyms/Definitions

- DR = dilution refrigerator; provided by Oxford Instruments, cools 45, 4, 1, and 0.1 K stages.
- APTC = auxiliary pulse tube cooler; provided by Cryomech, cools 45 and 4 K stages.
- PTC = pulse tube cooler; may refer to cold heads inside of either the dilution refrigerator or auxiliary pulse tube cooler
- OVC = outer vacuum chamber
- LN2 = liquid nitrogen
- DU = dilution unit

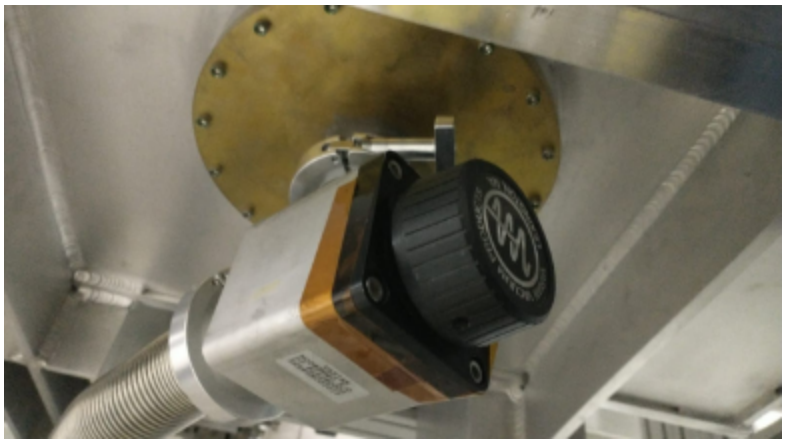

Figure 7.4: TolTEC's main cryostat valve closed with a metal vacuum hose connected to a pump out of frame. Turn the knob to the right to open. It is vital to not torque hard on the valve from a low angle in order to avoid damaging the vacuum seals.

- PC = pre-cool line
- M&C = monitor and control system; a GUI developed by Kamal Souccar for handling both the LMT and its instruments
- KNF = company that manufactures vacuum parts

Start-up from atmospheric pressure

Pump out

1. With the valve to the vacuum port on the main cryostat closed, attach the mechanical pump using at enough vacuum hoses to reach the floor with no tension (this has been typically been just 2 long hoses). Turn on the pump and run with the valve closed for at least one minute.

2. Slowly open the valve to the vacuum port on the main cryostat. Watch the DR OVC pressure on the DR computer with the Oxford Triton Control window. The goal is a decrease of about **400 mbar every 5 minutes** (equivalently, about 1 Torr per second).

   NOTE: Faster than this risks damaging the window and filters!

3. Once the roughing pump out is complete (P$\sim$ 1 mbar, or about an hour of pumping), **fully close the vacuum port valve**. Attach the turbo pump in the same way as the mechanical pump. Cover the turbo pump with a cardboard box and place a space heater near a gap.

   NOTE: This was vital for having the old turbo pump run at full speed, but after the tip-seal replacement we have been okay to run without the heater.

4. Turn on the turbo pump. Run the pump with the valve closed for at least 1 minute to evacuate air from the hose and to get the pump running at full speed.

5. Slowly open the main cryostat valve 1/2 turn. Listen to the pump and adjust the valve to more closed if it seems to be very loud (this implies that the pump is working too hard). Check the OVC pressure on the DR computer to make sure that the pressure is decreasing. Keep opening the valve in 1/2 turn steps, waiting between the steps as needed. It should take about 1 to 2 minutes to fully open the valve.

6. Once the valve is completely open, leave the turbo pump running until the pressure on the DR OVC gauge reads <**3e-2 mbar**. This takes upwards of an hour depending on the turbo pump used and how clean the inside of the cryostat is (i.e., was it left at room pressure for an extended period of time, are there things that need to offgas inside, etc.). You may leave the pump running overnight if confident there will not be a power outage.

7. Once the pressure is correct, you may start the DR and APTC compressors. Follow the instructions below to start the cooldown.

Start the cooldown

Use the checklist below in tandem with the following instructions.

1. Check if the cold trap is full of LN2. If not, have the site crew refill the LN2 during the next steps.

2. Check that the turbo pump is running at full speed and that the main cryostat valve is fully open.

3. Is the thermetry reading out with the nominal resistances? If so, proceed. If not, check the connectors and the excitations.

4. Next, check the cold water to the compressors.

   (a) Check that the heater is off and the fan is turned on for the spot cooler on the 8m level.

   (b) Check that the valve is closed for the bypass on the 29m level.

   (c) Check the flow rate gauges on the 29m level to the left of the compressors. Pull the tab for each and check that each has a flow >4 gpm.

   (d) Check that the compressors say 'Ready to Start' on their electronic front panels. If there are any errors, refer to the Oxford DR manual for guidance on next steps. If the error is due to water, oil, or helium temperatures you can clear the error by physically pressing the OFF button on the front of the compressor. It **cannot** be cleared remotely.

5. Preparing the DR pump rack:

   (a) Make sure that the valves to the DR turbo pump cold water are **closed** if other instruments such as MUSCAT are also starting their cooldowns.
   NOTE: If they are open and other compressors are running, TolTEC's compressors may overheat.

   (b) Check that the fans installed above the DR turbo are powered on and running.

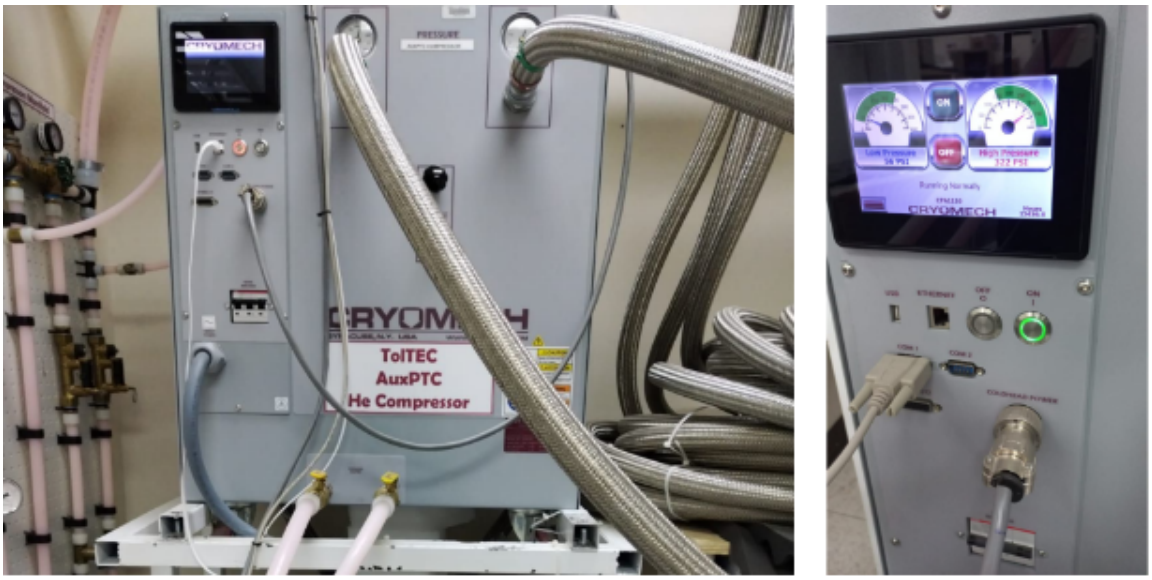

Figure 7.5: TolTEC's Cryomech compressors are located on the 29m level in the receiver cabin. Both of them can be controlled remotely. When they are OFF but ready to start running, the OFF button will glow solid red. When the compressor is RUNNING, the ON button with glow solid green. When in an error state, the OFF button will blink red. As seen in this image, the flow rate gauges to check prior to operation are located to the left of the compressors.

(c) Place a space heater close to the back of the forepump (upper shelf in the pump rack). Turn it on to ensure the forepump starts up in the next step. NOTE: The forepump has shown signs of temperature sensitivity and requires warm air to run. If it does not work, you will not be able to operate the DR safely at base temperature. Please ensure that it is running prior to the next steps.

6. Turn on the compressors:

(a) From the MC software, start a new log for the APTC and thermetry (M&C >Tools >Logging).

(b) On the Oxford computer, start a new log (Triton Control System >logging >Start new log).

(c) Turn on the APTC (use M&C >ToltecCryocmpControl).

(d) Turn on the DR compressor by selecting 'Full cooldown' on the Oxford control software.

NOTE: It can take at least 10 minutes for the pressure at the turbo (P4) and forepump (P5) to drop low enough for the script to start. Keep an eye on it to make sure that it actually starts the script.

7. Monitor the system:

   (a) Keep an eye on the compressor temperatures. If the water or oil looks at risk of overheating (water above 21C, oil over 50C), turn off the APTC compressor until the receiver cabin temps are colder. The room is typically hottest between 21:00-02:00 UTC.

   (b) Check that the temperatures on the cold heads are decreasing using the plotting software on the Oxford computer. If the cold head temperature is static for longer than 10 minutes, check the compressors for errors.

   (c) Watch that the OVC pressure is still decreasing.

Reaching base temperature

1. When the 4 K stage is at 77 K (use the 4 K central busbar stand thermometer), **completely close** the vacuum port valve. Turn off and remove the turbo pump. This is about 3-4 days after starting the cooldown.

   NOTE: If you are not able to remove it before then, it will be okay, but you may begin cryopumping on the turbo. This can introduce oils and other contaminants to the cryostat so please avoid as much as possible.

2. Watch the DR automated scripts. It should switch over to moving mix through the DU rather than the PC. When the pre-cooling script ends, *please open the water valves to the turbo pump in order to allow it to cool.* Make sure that the water pump attached to the side of the DR pump rack is plugged in and that

the filter water level is high enough.

NOTE: When the DU condense cycle starts, V1 may get stuck. Go to View >Enable, right click V1 and select 'close', then right click V1 and select 'open'. This resets the valve state since it usually isn't physically stuck, just an incorrect electronic state.

3. Monitor the system over the next two to three hours. It should reach the base temperatures described in the table below. If not, consider the troubleshooting outlined below.

4. Once the system is in a steady state, you have the option of opening the KNF bypass valve (in the pump rack) and turning off the compressor pump. This operation mode is important for maintaining the compressor pump over TolTEC's lifetime.

Troubleshooting the cooldown

A number of things may go wrong during this process. During commissioning, we dealt with the issues outlined below. In Table 7.1, I note the problem, potential causes, and possible solutions. For more complete troubleshooting tips, please refer to the relevant device manual (electronic copies of most are on the Oxford computer in the receiver cabin).

How to measure DU throughput

1. With the mixture in the tank, all of the DR's pneumatic valves closed, and the pumps off, turn on the forepump and compressor pump.

2. Open V5 and V1. Toggle V9 until the pressure at P2 is:

   (a) 3 bar, if system is at room temperature

   (b) 1 bar, if system is cold

Table 7.1: Table detailing how to troubleshoot the dilution refrigerator's TolTEC specific issues. This table is not all inclusive as Oxford has instructions for common issues in their DR manual.

Symptom	**Cause**	**Solution**
Compressor overheats	Water flow is low	Close valve to turbo pump (if off)
	Water in is too hot	Close valve to turbo pump (if off), check spot cooler temperature and access to cold air
Turbo pump does not reach 820 rpm	Water in is too hot	Open pump rack door and turn on fan pointed at the pump
P3 and P4 in the DR do not decrease	Forepump is too cold, does not reach proper speed	Put a heater at the back of the pump rack pointed at the forepump. Get tip seals replaced if four years since last change
Condense cycle does not start	P2 high, DU blockage	Clean mix, measure throughput at P3 (∼11.6 mbar/min when cold) If P2 does not decrease, collect the mix through V6 and warm up.
	Automation not running correctly	Restart control system; warm Still & MC to about 10K then restart automation; run cycle manually (see details below)

3. Turn off the forepump. Watch the pressure change by hovering over the P3 indicator on the Triton System Control window. You should measure:

   (a) 200 mbar/min, if system is at room temperature

   (b) 11.6 mbar/min, if the system is cold

4. Use the collect mix script to get the helium mix back into the tank. This will leave the turbo pump on and V6, 7, and 8 open after the script completes.

Ending the cooldown

1. If using the KNF bypass valve, close its valve and restart the compressor pump. Remember, the KNF bypass valve is a manual valve inside the pump rack. Otherwise, go to the next step.

2. Select refrigerator >full warm-up from the Triton System Control. This should shut off the DR compressor. On the MC (M&C >ToltecCryocmpControl), turn off the APTC compressor.

3. Make sure that the DR is collecting the mix from the DU. If the heaters do not turn on after 10 minutes, manually set them to 20,000 μW. The warm-up script will continue even after the system has warmed up completely. It will leave V4, 5, 6, 7, 8 open as well as the O, F, and C pumps on.

4. Monitor the system temperatures over the next five days. The PTCs will come to room temperature within 3 days while the rest of the system will take at least 2 more days.

   NOTE: Keep an eye on the dew point as well – if you plan to vent the system, all stages must have their temperature above the dew point to avoid condensation!

5. If you do not plan to open the system, please leave it under vacuum (i.e., do not vent the cryostat). If you need to make internal adjustments, you must vent the system.

Venting the cryostat

1. Once the system is entirely above the dew point, you may vent the system.

2. To perform the venting procedure, first make sure the mix is fully collected, then that the pneumatic valves in the DR are closed on the Triton control system. Make sure all of the DR pumps are turned off.

3. On the main cryostat, on the side closest to the wall, locate the main cryostat vacuum port valve.

4. While watching the OVC pressure gauge on the Triton control system, **SLOWLY** start opening the valve so that the pressure is increasing **less than 10 mbar/min**. **DO NOT open the valve all at once.**

5. Keep slowly opening the valve until you reach atmospheric pressure. When completely vented, close the valve.

6. You may now perform the maintenance work.

Operating the dilution refrigerator manually

ONLY USE THESE INSTRUCTIONS IF YOU HAVE BEEN TRAINED BY AN EXPERIENCED USER.

Once we moved the cryostat to the telescope, there were issues with the automated script to begin the condensation and circulation cycle. This set of instructions reviews how to perform the cycle manually through the remote system.

If there are issues at the site that need to be checked by a person there, use an instant messaging service that is accessible by WiFi. Do not wait if there are obvious issues, this risks damage to the instrument.

I must emphasize again, please only use this set of instructions if you have been trained. Otherwise there can be catastrophic failures in the system that will require a site repair visit.

1. With the still (1 K stage) and the mixing chamber (0.1 K) stage on the DR at 10 K, collect the mix using the automated script.

2. If the mix is not collected automatically, shut off the pumps then shut the open valves.

3. Turn on the compressor pump (C), then open V4.

4. Turn on forepump (F), then open V5.

5. Open V7 and V8 to empty the pre-cool line.

6. Run in this mode until the pressure at P2 is about 0.8 bar. Alternatively, wait until P3 is below 1e-3 mbar.

7. When mix is collected sufficiently (e.g., little to no mix remains in the pre-cool circuit; if too much remains, you will not reach base temperature), close V8, V7, and V4.

8. With V1 **CLOSED** and both compressor and forepump running, toggle V9 until P2 = 2.5 bar. Toggling works by right-clicking the valve and selecting the "toggle" option from the menu that appears.

9. With V6 closed, open V1. The pressure at P2 will immediately drop. If it does not, there might be a blockage. Please refer to the troubleshooting guide for more details.

10. Toggle V9 until P2 = 2.9 bar while V1 is open.

11. Every 10 minutes, check the pressure at P2. Toggle V9 to add more mix and maintain the pressure around 2.5 bar at P2. This process will take at least an hour for the tank to be fully emptied of mix.

12. When the tank pressure (P1) is close to 0.15 bar, you can open V9 rather than toggling it. Keep an eye on P5 and check that the pressure stays below 0.7 bar. If it's close to 0.7 bar, close V9 and wait a few minutes before trying to open the valve again.

13. The pressure at P2 will slowly approach 0.6 bar. Once it is near 0.8 bar, you may start the turbo pump (O). Watch for it to spin up to 820 rpm (speed) with power below 350 W. If the power is around 300 W when it is spinning at full speed, turn the turbo off. There is most likely too much loading on the pump. Check that the water flow to the turbo is adequate (water valves open at the pump rack) and that the fans on the pump rack are turned on.

14. Watch for the pressure at P2 to reach 0.6 bar within the next hour or two. Also watch the thermometry to confirm that the mixing chamber plate is approximately 55-60 mK. If this temperature is reached, this almost guarantees that the system is running correctly, thus it is my first check.

If the temperature is holding steady and there are no warnings, you may leave the system in this state for observing. Be mindful that the compressor pump has a short lifespan, so if there is no observing over the weekend please recollect the mix. When the mix is collected and the stages below the 4 K stage are 10 K or lower, you may repeat this procedure as needed in order to cool the detectors again.

Checklists for dilution refrigerator operation

This procedure assumes that the dilution refrigerator is running at base temperature. If the system is not at base temperature, review the previous instructions.

WEEKLY CHECKLIST

- ❑ Spot cooler water temperature below 70°C.
- ❑ Liquid nitrogen trap last filled on: __/__/__ (refill should happen each Monday).
- ❑ Space heater set up pointed at the forepump.
- ❑ Fans running on the top of the pump rack.

DAILY CHECKLIST

When in charge of running the DR, please use the following checklist twice a day. For the morning, check the system around 9 AM EST. For the evening, check the system around 5 PM EST. Quick checks throughout the day are recommended as well, but you do not have to perform the entire list; merely check the temperatures and the pressures when you do.

- ❑ Compressor is running with no errors.
    - ❑ P_{high} = 20 bar
    - ❑ P_{low} = 5 bar
    - ❑ Water in temp = 9 - 18°C
    - ❑ Water out temp = 20 - 25°C
    - ❑ Oil temp $\leq$ 50.7°C
    - ❑ Helium temp $\leq$ 80°C
- ❑ No warning messages have appeared from the Triton System Control.
- ❑ Compressor pump, forepump, and turbo pump are running.
- ❑ V1 is open, V6 is closed.
- ❑ Pressure values at base temperature
    - ❑ P1 = 5e-4 mbar
    - ❑ P2 = 0.60 - 0.70 bar
    - ❑ P3 = 1.2e-2 mbar
    - ❑ P4 = 4 mbar
    - ❑ P5 = 0.15 mbar

- ❑ Temperature values at base temperature
  - ❑ PT1 Head = 39 K
  - ❑ PT1 Plate = 50 K
  - ❑ PT2 Head = 3.9 K
  - ❑ PT2 Plate = 5 K
  - ❑ Still Plate = 0.9 K
  - ❑ Cold Plate = 0.8 K
  - ❑ Mixing Chamber Plate = 0.055 to 0.060 K
  - ❑ Mixing Chamber Bar = 0.090 to 0.120 K

TolTEC Standard Operation

ONLY USE THESE INSTRUCTIONS WHEN AT BASE TEMPERATURE.

Acronyms/Definitions

- LNA = low noise amplifier; UMass custom-made for operation on the 4K stage
- PSU = power supply unit
- VNA = vector network analyzer; may refer to software method or separate equipment to measure power level across a range of frequencies
- slice = readout electronics; used interchangeably between the IF slice and the ROACH2 plus IF slice

Starting up the electronics

1. Once the system is at base temperature, check that the readout electronic slices' blue coaxial cables are connected to the back of the cryostat. The input signal (drive line) cable will go on the top row while the outgoing signal (sense line)

cable will connect to the bottom row. Each network has its own slice as of this document. Unless otherwise told, please connect the proper number electronic to its matching network.

2. Next, turn on the LNAs. To do this, you will need access to the remote outlet strip. Go to the clipa remote outlet strip page and turn on outlet 5. This controls the power to the LNAs' 7V DC PSU.

Checking connection to the detectors and initial characterization

1. To check if the LNAs are on and if the readout electronics are working properly, the fastest way will be to take a VNA sweep.

   (a) On M&C, find the ToltecRoach panel (M&C ToltecRoach). Select the networks you would like to test using the radio buttons at the top of the panel. The following steps can all be performed simultaneously for all active networks.

   (b) Select the VNA tab. Click VnaLoad, wait for the status to be Done. This step populates the electronics with 1000 tones to use in the next step.

   (c) Click VnaSweep. This will sweep the 1000 tones in 2 MHz channels with 10 samples per frequency step within the channel. The VNA sweep will give us the full S_{21} curve.

   (d) Go to the tolteca page for VNA measurements. If the LNA is off, there will be no obvious indication of detector resonances. Otherwise, you will see structures like those below.

   (e) At this step, you should try to maximize the number of resonances found. This can be done by adjusting the attenuation on the drive and sense lines. Increasing the drive attenuation can reduce the number of resonators driven non-linear by an excess amount of power while decreasing it can

provide more power to underdriven ones. On the other hand, perhaps you need to adjust the amount of power entering the readout electronics. If the signal seems weak/noisy, try decreasing the sense attenuation.

NOTE: This and the following are steps that should only be performed by a TolTEC team member with experience looking at the resonances.

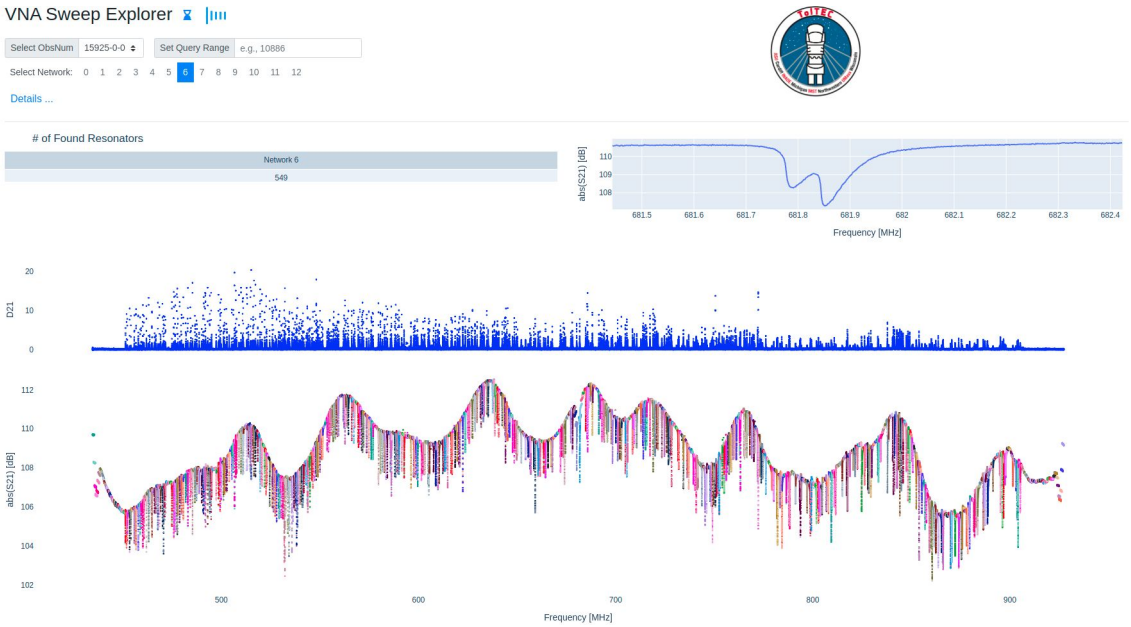

Figure 7.6: Example of a VNA sweep showing that the LNA for the network is on and the readout electronics are performing correctly. Figure is a screenshot from an interactive Dash page created by Grant Wilson and Zhiyuan Ma to examine TolTEC data.

2. After identifying the resonances with a VNA sweep, you may move onto the Tune step (also known as a Target sweep).

   (a) On the same panel, click the Targ tab. Target sweeps take the frequencies identified in the prior step, then performs a high resolution frequency sweep to characterize the resonances.

(b) You may perform these sweeps by clicking the Tune button. Once the sweep is done, head to this page to examine the results.

(c) If the resonances seem asymmetric or broken rather than circular, you might need to increase the drive attenuation. Also, since the power per tone increases when performing a tune, check that the sense attenuation is above 10 dB for each channel.

Starting to observe

This does not cover how to start up/shut down the telescope. The instructions on how to do this are available at the LMT for observers. This section describes the general procedure for getting TolTEC ready for science observations. This procedure assumes that the weather is clear (i.e., no storms, no fog, no ice on the dish, $\tau \leq 0.3$) and the forecast for the next few hours is good.

1. When the system is set up, remove the window cover from the main cryostat. Make sure that the MUSCAT mirror that couples to M3 is stowed and that M3 is pointed towards TolTEC.

2. With the telescope pointed at zenith, have the site crew remove the tarp covering the boresight.

3. With the telescope still pointed at zenith, run a VNA sweep. Confirm that the VNA sweep looks okay using the quick look result. If a warning pops up, check the tolteca page and confirm that the sweeps do not look noisy, have good S/N.

4. Next, run the detector set up scripts to set the tone powers. As of August 2023, these were: 00_toltec_commissioning_startup, 11_toltec_detector_init_manual, 21_toltec_detector_setup_drivefit_manual, and 12_toltec_tune_manual.

5. Make sure the sample rate is set to 122 Hz.

6. Run pointing script. Use this to determine the range and how many steps to include in the focus/astigmatism steps. For ease of observing, choose a source with a flux above 0.5 Jy.

7. Run M2.Z focus and astigmatism steps on a pointing source. If needed, run the M2.X or M2.Y focus scripts as well.

8. Once satisfied with the focus and astigmatism, run the pointing script.

9. Run the beammap script.

10. Run the pointing script again.

11. Once satisfied with beammap result, move on to observations. Observations must start with focus and astigmatism, then a pointing before and after the science observation.

Adjusting the LNAs Biases

NOTE: Wear an electrostatic discharge strap while working on the bias boards or touching the bias cables for the LNAs. They are sensitive to electrostatic discharges and can be easily damaged even when powered off.

1. Attach your ESD strap to the main cryostat chassis.

2. Open the bias board box and remove the MDM100 connector from the board if it is attached.

3. With the 7V bias power supply on and the cables to the bias boards plugged in, use a multimeter to measure the voltages at the test points shown above.

4. Plug in the MDM100 connector to power the LNAs. Once powered up, probe the same test points and compare to the table above.

5. Do not adjust the collector or regulator voltage when the MDM100 connector is plugged in. The base voltage potentiometer is fine to adjust. Clockwise turns increase the resistance, decreasing the voltage.

6. If you believe the collector or regulator voltages to be set incorrectly, unplug the MDM100 connector and the power supply for the board. Measure the resistances at the potentiometers. If probing the top pin to the bottom left or right, unless the channel is shut "off" (see below), the resistance should not be any lower than 2000Ω.

If you would like to adjust the noise level on the LNA (e.g., it is oscillating), try adjusting the base voltage on the second stage first. If you have an external VNA, the process will go quicker if you probe the network while adjusting; however, you can also use TolTEC VNA sweeps if the system is cold.

Additionally, there are cases where a channel is not connected inside the cryostat to an LNA. In this case, the potentiometers have been set such that the regulator and collector voltages output will be about 0.5V. This is lower than the required voltage to run the op amps in the bias board circuit, so this channel should be considered "off". The idea is to reduce the chance of the the op amps hitting their voltage rails and oscillating, thus removing an excess source of noise in the readout.

Laser Alignment Plate (LAP)

When aligning TolTEC to the external warm optics, we first used a laser on an alignment plate. The method was to center Wyatt's IR source after taking a beammap, then install the laser alignment plate (LAP) and align the laser with the IR source. We eventually switched to using timestreams of a cold source over the mirror to be aligned (see §4). The original laser method set-up is included here for completeness.

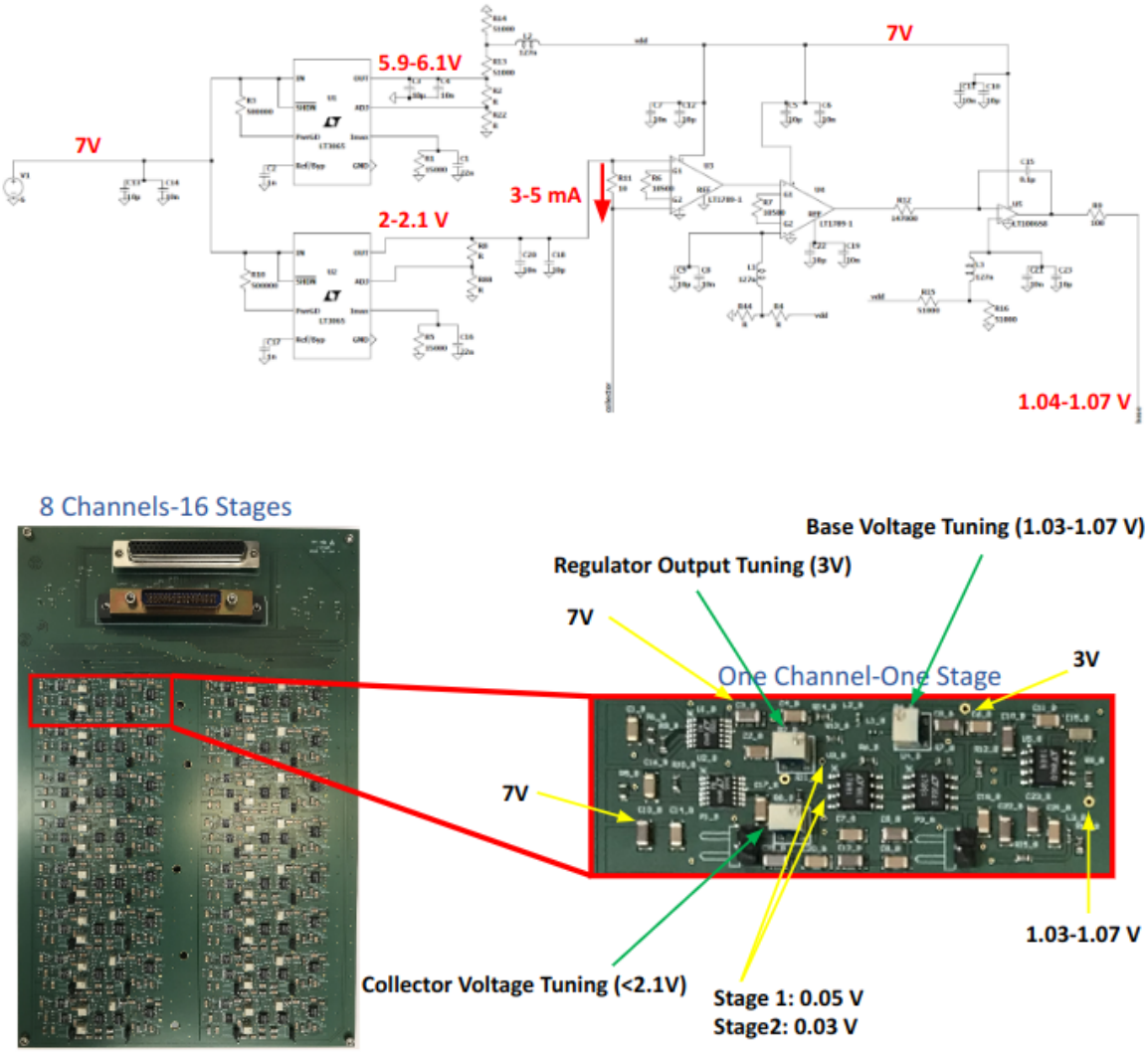

Figure 7.7: *Top*: The circuit diagram schematic for a single channel's stage on one of TolTEC's LNA bias boards. Image credit: M. Hosseini. *Bottom*: One of TolTEC's LNA bias boards with the voltages expected while powered up. The bias boards are identical for each side of the cryostat aside from which of the 8 channels are used. The yellow lines point to probe points on a single channel's stage. Each stage is identical in its layout, but the current through the collector will be lower for Stage 2. Probing between the collector points (the two yellow arrows in the center) probes over a 10Ω resistor, so the current will be between 3-5 mA depending on the stage. Image credit: M. Hosseini.

Mounting onto the cryostat

Tools needed:

- 7/16" wrench
- 6 hex head 1/4-20 bolts
- laser alignment plate
- DPSS-5M green laser
- 3V DC power supply

1. With the TolTEC main cryostat window uncovered, place the laser alignment plate in front of it with the laser pointed outwards.
2. Place two of the 1/4-20 bolts into the bolt holes at the top of the plate to attach it to the cryostat.
3. Lightly pushing up on the plate, install the rest of the bolts until they are finger tight.
4. Working in a star pattern, tighten the bolts with the 7/16" wrench until they are tight. Do not crank on them hard, just make sure they are about 1/4-1/2 of a turn past finger tight while the heads touch the plate. See Figure 7.8 for what the final position should look like.
5. Connect the laser to the connector attached to the twisted wire pair. See Figure 7.8 for how to connect.
6. Attach the wires to the 3V DC power supply. Green goes to +, white goes to -. See Figure 7.8 for how the wires should be connected to the power supply.

7. Since the laser is temperature sensitive, use the laser in 'burst' mode by turning on the power supply, marking the laser location on the mirror, then shutting off.

   NOTE: Do NOT look at the laser directly when operating it. Please wear safety goggles, the laser is powerful enough to damage your eyesight permanently!

8. If needed, find the center position of a beammap by running Wyatt prior to installation of the LAP. Use the turn-screws on the aluminum tube to adjust the laser and align with Wyatt's IR source. Stow Wyatt, then adjust the mirrors.

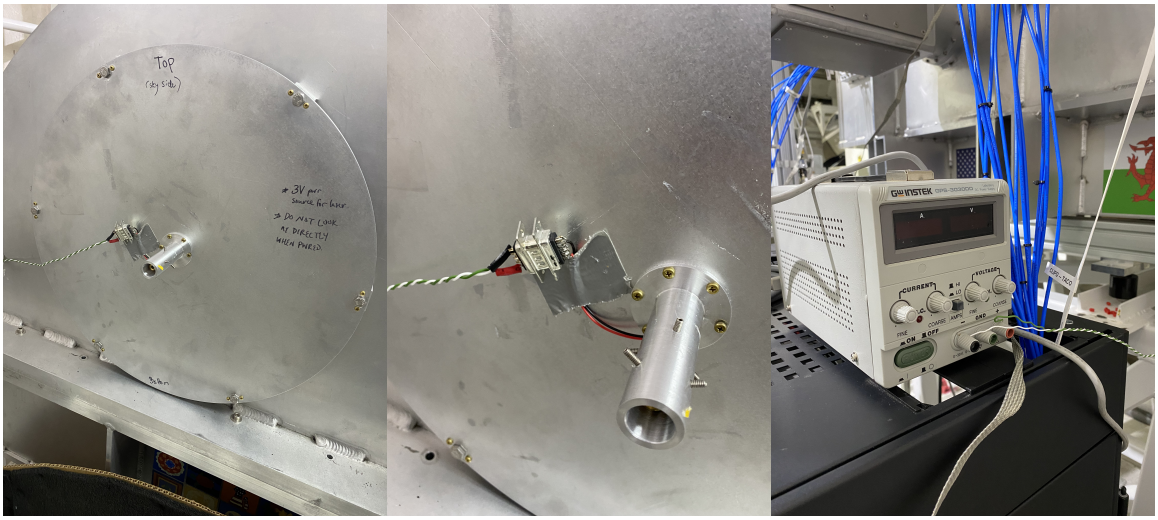

Figure 7.8: *Left*: A photo of the LAP after being mounted on the front of the cryostat. *Middle*: A close-up view of the laser connector needed to go to the power supply. *Right*: The 3V DC power supply used at the telescope. Note the positioning of the wires. Photo credit: G. Wilson.

Dismounting from the cryostat

1. Make sure that the power supply is OFF. Disconnect the wires from the power supply or disconnect the laser connector from the connector going to the wires.

2. To remove the LAP from the main cryostat, first loosen all of the hex head bolts using the 7/16" wrench. Once they are easy to turn by hand, go to the next step.

3. Remove all but two bolts from the plate. Place in the plastic bag that is usually taped to the plate.

4. Supporting the bottom of the plate with one hand, start to remove the remaining two bolts. Gently move the LAP away from the main cryostat window, making sure to avoid touching the window with any part of the plate.

5. Store the LAP with the laser pointing up. Do not touch the alignment bolts around the tube holding the laser.

BIBLIOGRAPHY

[1] Andrea Biviano. From Messier to Abell: 200 years of science with galaxy clusters, 2000. _eprint: astro-ph/0010409.

[2] William Herschel. XII. On the Construction of the Heavens. *Phil. Trans.*, January 1785. doi: https://doi.org/10.1098/rstl.1785.0012. URL `https://royalsocietypublishing.org/doi/10.1098/rstl.1785.0012`. Publisher: Royal Society.

[3] Max Wolf. Die Nebelflecken am Pol der Milchstrasse. *Publikationen des Astrophysikalischen Instituts Koenigstuhl-Heidelberg*, 1:125–176, January 1902.

[4] George O. Abell. *The distribution of rich clusters of galaxies.* PhD Thesis, California Institute of Technology, January 1957.

[5] J. E. Felten, R. J. Gould, W. A. Stein, and N. J. Woolf. X-Rays from the Coma Cluster of Galaxies. *apj*, 146:955–958, December 1966. doi: 10.1086/148972.

[6] R. A. Sunyaev and Ya. B. Zeldovich. The Observations of Relic Radiation as a Test of the Nature of X-Ray Radiation from the Clusters of Galaxies. *Comments on Astrophysics and Space Physics*, 4:173, November 1972.

[7] M. Birkinshaw, S. F. Gull, and H. Hardebeck. The Sunyaev-Zeldovich effect towards three clusters of galaxies. *nat*, 309:34–35, May 1984. doi: 10.1038/309034a0.

[8] T. Mroczkowski, Daisuke Nagai, Kaustuv Basu, Jens Chluba, Jack Sayers, Rémi Adam, Eugene Churazov, Abigail Crites, Luca Di Mascolo, Dominique Eckert, Juan Macias-Perez, Frédéric Mayet, Laurence Perotto, Etienne Pointecouteau, Charles Romero, Florian Ruppin, Evan Scannapieco, and John ZuHone. Astrophysics with the Spatially and Spectrally Resolved Sunyaev-Zeldovich Effects. A Millimetre/Submillimetre Probe of the Warm and Hot Universe. *ßr*, 215:17, February 2019. doi: 10.1007/s11214-019-0581-2. _eprint: 1811.02310.

[9] Elizabeth L. Blanton, T. E. Clarke, Craig L. Sarazin, Scott W. Randall, and Brian R. McNamara. Active galactic nucleus feedback in clusters of galaxies. *Proceedings of the National Academy of Science*, 107:7174–7178, April 2010. doi: 10.1073/pnas.0913904107. _eprint: 1004.0671.

[10] B. R. McNamara and P. E. J. Nulsen. Mechanical feedback from active galactic nuclei in galaxies, groups and clusters. *New Journal of Physics*, 14(5):055023, May 2012. doi: 10.1088/1367-2630/14/5/055023. URL `https://doi.org/10.1088%2F1367-2630%2F14%2F5%2F055023`. Publisher: IOP Publishing.

[11] A. C. Fabian. Observational Evidence of Active Galactic Nuclei Feedback. *araa*, 50:455–489, September 2012. doi: 10.1146/annurev-astro-081811-125521. _eprint: 1204.4114.

[12] N. Battaglia, J. R. Bond, C. Pfrommer, J. L. Sievers, and D. Sijacki. SIMULATIONS OF THE SUNYAEV-ZEL'DOVICH POWER SPECTRUM WITH ACTIVE GALACTIC NUCLEUS FEEDBACK. *The Astrophysical Journal*, 725 (1):91–99, November 2010. ISSN 1538-4357. doi: 10.1088/0004-637x/725/1/91. URL `http://dx.doi.org/10.1088/0004-637X/725/1/91`. Publisher: IOP Publishing.

[13] Shutaro Ueda, Yuto Ichinohe, Sandor M. Molnar, Keiichi Umetsu, and Tetsu Kitayama. Gas Density Perturbations in the Cool Cores of CLASH Galaxy Clusters. *apj*, 892(2):100, April 2020. doi: 10.3847/1538-4357/ab7bdc. _eprint: 1912.07300.

[14] Andrey V. Kravtsov and Gustavo Yepes. On the supernova heating of the intergalactic medium. *mnras*, 318(1):227–238, October 2000. doi: 10.1046/j.1365-8711.2000.03771.x. _eprint: astro-ph/0004333.

[15] Arif Babul, Michael L. Balogh, Geraint F. Lewis, and Gregory B. Poole. Physical implications of the X-ray properties of galaxy groups and clusters. *mnras*, 330(2):329–343, February 2002. doi: 10.1046/j.1365-8711.2002.05044.x. _eprint: astro-ph/0109329.

[16] I. G. McCarthy, J. Schaye, R. G. Bower, T. J. Ponman, C. M. Booth, C. Dalla Vecchia, and V. Springel. Gas expulsion by quasar-driven winds as a solution to the overcooling problem in galaxy groups and clusters. *mnras*, 412(3):1965–1984, April 2011. doi: 10.1111/j.1365-2966.2010.18033.x. _eprint: 1008.4799.

[17] Lei Wang, Xiaohu Yang, Shiyin Shen, H. J. Mo, Frank C. van den Bosch, Wentao Luo, Yu Wang, Erwin T. Lau, Q. D. Wang, Xi Kang, and Ran Li. Measuring the X-ray luminosities of SDSS DR7 clusters from ROSAT All Sky Survey. *mnras*, 439(1):611–622, March 2014. doi: 10.1093/mnras/stt2481. _eprint: 1312.7417.

[18] Michael E. Anderson, Massimo Gaspari, Simon D. M. White, Wenting Wang, and Xinyu Dai. Unifying X-ray scaling relations from galaxies to clusters. *mnras*, 449(4):3806–3826, June 2015. doi: 10.1093/mnras/stv437. _eprint: 1409.6965.

[19] A. Cavaliere and R. Fusco-Femiano. The Distribution of Hot Gas in Clusters of Galaxies. *åp*, 70:677, November 1978.

[20] M. Arnaud. The -model of the intracluster medium - Commentary on: Cavaliere A. and Fusco-Femiano R., 1976, A&A, 49, 137. *Astronomy & Astrophysics*, 500(1):103–104, June 2009. ISSN 0004-6361, 1432-0746. doi: 10.1051/0004-6361/200912150. URL `https://www.aanda.org/articles/aa/abs/2009/22/aa12150-09/aa12150-09.html`.

[21] P. Gorenstein, D. Fabricant, K. Topka, F. R. Harnden, Jr., and W. H. Tucker. Soft X-ray structure of the Perseus cluster of galaxies. *The Astrophysical Journal*, 224:718, September 1978. ISSN 0004-637X, 1538-4357. doi: 10.1086/156421. URL `http://adsabs.harvard.edu/doi/10.1086/156421`.

[22] Andrea Morandi, Ming Sun, William Forman, and Christine Jones. The galaxy cluster outskirts probed by Chandra. *Monthly Notices of the Royal Astronomical Society*, 450(3):2261–2278, May 2015. ISSN 0035-8711. doi: 10.1093/mnras/stv660. URL `https://doi.org/10.1093/mnras/stv660`. _eprint: https://academic.oup.com/mnras/article-pdf/450/3/2261/18754977/stv660.pdf.

[23] X. Barcons, K. Nandra, D. Barret, J. W. den Herder, A. C. Fabian, L. Piro, M. G. Watson, and the Athena Team. Athena: the X-ray observatory to study the hot and energetic Universe. In *Journal of Physics Conference Series*, volume 610 of *Journal of Physics Conference Series*, page 012008, May 2015. doi: 10.1088/1742-6596/610/1/012008.

[24] Jessica A. Gaskin, Douglas A. Swartz, Alexey Vikhlinin, Feryal Özel, Karen E. Gelmis, Jonathan W. Arenberg, Simon R. Bandler, Mark W. Bautz, Marta M. Civitani, Alexandra Dominguez, Megan E. Eckart, Abraham D. Falcone, Enectali Figueroa-Feliciano, Mark D. Freeman, Hans M. Günther, Keith A. Havey, Ralf K. Heilmann, Kiranmayee Kilaru, Ralph P. Kraft, Kevin S. McCarley, Randall L. McEntaffer, Giovanni Pareschi, William Purcell, Paul B. Reid, Mark L. Schattenburg, Daniel A. Schwartz, Eric D. Schwartz, Harvey D. Tananbaum, Grant R. Tremblay, William W. Zhang, and John A. Zuhone. Lynx X-Ray Observatory: an overview. *Journal of Astronomical Telescopes, Instruments, and Systems*, 5:021001, April 2019. doi: 10.1117/1.JATIS.5.2.021001.

[25] The Lynx Team. The Lynx Mission Concept Study Interim Report, 2018. _eprint: 1809.09642.

[26] Stephen Walker, Aurora Simionescu, Daisuke Nagai, Nobuhiro Okabe, Dominique Eckert, Tony Mroczkowski, Hiroki Akamatsu, Stefano Ettori, and Vittorio Ghirardini. The Physics of Galaxy Cluster Outskirts. *Space Science Reviews*, 215(1):7, January 2019. doi: 10.1007/s11214-018-0572-8. _eprint: 1810.00890.

[27] M. Birkinshaw. The Sunyaev-Zel'dovich effect. *physrep*, 310:97–195, March 1999. doi: 10.1016/S0370-1573(98)00080-5. _eprint: astro-ph/9808050.

[28] John E. Carlstrom, Gilbert P. Holder, and Erik D. Reese. Cosmology with the Sunyaev-Zel'dovich Effect. *Annual Review of Astronomy and Astrophysics*, 40(1):643–680, 2002. doi: 10.1146/annurev.astro.40.060401.093803. URL `https://doi.org/10.1146/annurev.astro.40.060401.093803`. _eprint: https://doi.org/10.1146/annurev.astro.40.060401.093803.

[29] P. A. R. Ade, N. Aghanim, M. Arnaud, M. Ashdown, J. Aumont, C. Baccigalupi, A. J. Banday, R. B. Barreiro, R. Barrena, and et al. Planck 2015 results. *Astronomy & Astrophysics*, 594:A27, September 2016. ISSN 1432-0746. doi: 10.1051/0004-6361/201525823. URL `http://dx.doi.org/10.1051/0004-6361/201525823`. Publisher: EDP Sciences.

[30] Seunghwan Lim, Houjun Mo, Huiyuan Wang, and Xiaohu Yang. Detection of missing baryons in galaxy groups with kinetic Sunyaev-Zel'dovich effect, 2017. _eprint: 1712.08619.

[31] Jens Chluba, Daisuke Nagai, Sergey Sazonov, and Kaylea Nelson. A fast and accurate method for computing the Sunyaev-Zeldovich signal of hot galaxy clusters. *Monthly Notices of the Royal Astronomical Society*, 426(1):510–530, October 2012. ISSN 00358711. doi: 10.1111/j.1365-2966.2012.21741.x. URL `http://arxiv.org/abs/1205.5778`. arXiv: 1205.5778.

[32] Jens Chluba, Eric Switzer, Kaylea Nelson, and Daisuke Nagai. Sunyaev–Zeldovich signal processing and temperature–velocity moment method for individual clusters. *Monthly Notices of the Royal Astronomical Society*, 430(4): 3054–3069, February 2013. ISSN 0035-8711. doi: 10.1093/mnras/stt110. URL `http://dx.doi.org/10.1093/mnras/stt110`. Publisher: Oxford University Press (OUP).

[33] M. Hilton, C. Sifón, S. Naess, M. Madhavacheril, M. Oguri, E. Rozo, E. Rykoff, T. M. C. Abbott, S. Adhikari, M. Aguena, S. Aiola, S. Allam, S. Amodeo, A. Amon, J. Annis, B. Ansarinejad, C. Aros-Bunster, J. E. Austermann, S. Avila, D. Bacon, N. Battaglia, J. A. Beall, D. T. Becker, G. M. Bernstein, E. Bertin, T. Bhandarkar, S. Bhargava, J. R. Bond, D. Brooks, D. L. Burke, E. Calabrese, M. Carrasco Kind, J. Carretero, S. K. Choi, A. Choi, C. Conselice, L. N. da Costa, M. Costanzi, D. Crichton, K. T. Crowley, R. Dünner, E. V. Denison, M. J. Devlin, S. R. Dicker, H. T. Diehl, J. P. Dietrich, P. Doel, S. M. Duff, A. J. Duivenvoorden, J. Dunkley, S. Everett, S. Ferraro, I. Ferrero, A. Ferté, B. Flaugher, J. Frieman, P. A. Gallardo, J. García-Bellido, E. Gaztanaga, D. W. Gerdes, P. Giles, J. E. Golec, M. B. Gralla, S. Grandis, D. Gruen, R. A. Gruendl, J. Gschwend, G. Gutierrez, D. Han, W. G. Hartley, M. Hasselfield, J. C. Hill, G. C. Hilton, A. D. Hincks, S. R. Hinton, S. P. P. Ho, K. Honscheid, B. Hoyle, J. Hubmayr, K. M. Huffenberger, J. P. Hughes, A. T. Jaelani, B. Jain, D. J. James, T. Jeltema, S. Kent, K. Knowles, B. J. Koopman, K. Kuehn, O. Lahav, M. Lima, Y. T. Lin, M. Lokken, S. I. Loubser, N. MacCrann, M. A. G. Maia, T. A. Marriage, J. Martin, J. McMahon, P. Melchior, F. Menanteau, R. Miquel, H. Miyatake, K. Moodley, R. Morgan, T. Mroczkowski, F. Nati, L. B. Newburgh, M. D. Niemack, A. J. Nishizawa, R. L. C. Ogando, J. Orlowski-Scherer, L. A. Page, A. Palmese, B. Partridge, F. Paz-Chinchón, P. Phakathi, A. A. Plazas, N. C. Robertson, A. K. Romer, A. Carnero Rosell, M. Salatino, E. Sanchez, E. Schaan, A. Schillaci, N. Sehgal, S. Serrano, T. Shin, S. M. Simon, M. Smith, M. Soares-Santos, D. N. Spergel, S. T. Staggs, E. R. Storer, E. Suchyta, M. E. C. Swanson, G. Tarle, D. Thomas, C. To, H. Trac, J. N. Ullom, L. R. Vale, J. Van Lanen, E. M. Vavagiakis, J. De Vicente, R. D. Wilkinson, E. J. Wollack, Z. Xu, and Y. Zhang. The Atacama Cosmology Telescope: A Catalog of >4000 Sunyaev-Zel'dovich Galaxy Clusters. *apjs*, 253(1):3, March 2021. doi: 10.3847/1538-4365/abd023. _eprint: 2009.11043.

[34] L. E. Bleem, S. Bocquet, B. Stalder, M. D. Gladders, P. A. R. Ade, S. W. Allen, A. J. Anderson, J. Annis, M. L. N. Ashby, J. E. Austermann, S. Avila, J. S. Avva, M. Bayliss, J. A. Beall, K. Bechtol, A. N. Bender, B. A. Benson, E. Bertin, F. Bianchini, C. Blake, M. Brodwin, D. Brooks, E. Buckley-Geer, D. L. Burke, J. E. Carlstrom, A. Carnero Rosell, M. Carrasco Kind, J. Carretero, C. L. Chang, H. C. Chiang, R. Citron, C. Corbett Moran, M. Costanzi, T. M. Crawford, A. T. Crites, L. N. da Costa, T. de Haan, J. De Vicente, S. Desai, H. T. Diehl, J. P. Dietrich, M. A. Dobbs, T. F. Eifler, W. Everett, B. Flaugher, B. Floyd, J. Frieman, J. Gallicchio, J. García-Bellido, E. M. George, D. W. Gerdes, A. Gilbert, D. Gruen, R. A. Gruendl, J. Gschwend, N. Gupta, G. Gutierrez, N. W. Halverson, N. Harrington, J. W. Henning, C. Heymans, G. P. Holder, D. L. Hollowood, W. L. Holzapfel, K. Honscheid, J. D. Hrubes, N. Huang, J. Hubmayr, K. D. Irwin, D. J. James, T. Jeltema, S. Joudaki, G. Khullar, M. Klein, L. Knox, N. Kuropatkin, A. T. Lee, D. Li, C. Lidman, A. Lowitz, N. MacCrann, G. Mahler, M. A. G. Maia, J. L. Marshall, M. McDonald, J. J. McMahon, P. Melchior, F. Menanteau, S. S. Meyer, R. Miquel, L. M. Mocanu, J. J. Mohr, J. Montgomery, A. Nadolski, T. Natoli, J. P. Nibarger, G. Noble, V. Novosad, S. Padin, A. Palmese, D. Parkinson, S. Patil, F. Paz-Chinchón, A. A. Plazas, C. Pryke, N. S. Ramachandra, C. L. Reichardt, J. D. Remolina González, A. K. Romer, A. Roodman, J. E. Ruhl, E. S. Rykoff, B. R. Saliwanchik, E. Sanchez, A. Saro, J. T. Sayre, K. K. Schaffer, T. Schrabback, S. Serrano, K. Sharon, C. Sievers, G. Smecher, M. Smith, M. Soares-Santos, A. A. Stark, K. T. Story, E. Suchyta, G. Tarle, C. Tucker, K. Vanderlinde, T. Veach, J. D. Vieira, G. Wang, J. Weller, N. Whitehorn, W. L. K. Wu, V. Yefremenko, and Y. Zhang. The SPTpol Extended Cluster Survey. *apjs*, 247(1):25, March 2020. doi: 10.3847/1538-4365/ab6993. _eprint: 1910.04121.

[35] R. Adam, A. Adane, P. A. R. Ade, P. André, A. Andrianasolo, H. Aussel, A. Beelen, A. Benoît, A. Bideaud, N. Billot, O. Bourrion, A. Bracco, M. Calvo, A. Catalano, G. Coiffard, B. Comis, M. De Petris, F. X. Désert, S. Doyle, E. F. C. Driessen, R. Evans, J. Goupy, C. Kramer, G. Lagache, S. Leclercq, J. P. Leggeri, J. F. Lestrade, J. F. Macías-Pérez, P. Mauskopf, F. Mayet, A. Maury, A. Monfardini, S. Navarro, E. Pascale, L. Perotto, G. Pisano, N. Ponthieu, V. Revéret, A. Rigby, A. Ritacco, C. Romero, H. Roussel, F. Ruppin, K. Schuster, A. Sievers, S. Triqueneaux, C. Tucker, and R. Zylka. The NIKA2 large-field-of-view millimetre continuum camera for the 30 m IRAM telescope. *åp*, 609: A115, January 2018. doi: 10.1051/0004-6361/201731503. _eprint: 1707.00908.

[36] S. R. Dicker, P. A. R. Ade, J. Aguirre, J. A. Brevik, H. M. Cho, R. Datta, M. J. Devlin, B. Dober, D. Egan, J. Ford, P. Ford, G. Hilton, J. Hubmayr, K. D. Irwin, B. S. Mason, P. Marganian, M. Mello, J. J. McMahon, T. Mroczkowski, C. Romero, S. Stanchfield, C. Tucker, L. Vale, S. White, M. Whitehead, and A. H. Young. MUSTANG2: a large focal plan array for the 100 meter Green Bank Telescope. In Wayne S. Holland and Jonas Zmuidzinas, editors, *Millimeter, Submillimeter, and Far-Infrared Detectors and Instrumentation for Astronomy VII*, volume 9153 of *Society of Photo-Optical Instrumentation Engineers (SPIE) Conference Series*, page 91530J, July 2014. doi: 10.1117/12.2056455.

[37] Peter K. Day, Henry G. Leduc, Benjamin A. Mazin, Anastasios Vayonakis, and Jonas Zmuidzinas. A broadband superconducting detector suitable for use in large arrays. *Nature*, 425:817–821, 2003.

[38] J. Zmuidzinas. Superconducting Microresonators: Physics and Applications. *Annual Review of Condensed Matter Physics*, 3(1):169–214, 2012. doi: 10.1146/annurev-conmatphys-020911-125022. URL `https://doi.org/10.1146/annurev-conmatphys-020911-125022`. _eprint: https://doi.org/10.1146/annurev-conmatphys-020911-125022.

[39] J. E. Austermann, J. A. Beall, S. A. Bryan, B. Dober, J. Gao, G. Hilton, J. Hubmayr, P. Mauskopf, C. M. McKenney, S. M. Simon, and et al. Millimeter-Wave Polarimeters Using Kinetic Inductance Detectors for TolTEC and Beyond. *Journal of Low Temperature Physics*, 193(3-4):120–127, May 2018. ISSN 1573-7357. doi: 10.1007/s10909-018-1949-5. URL `http://dx.doi.org/10.1007/s10909-018-1949-5`. Publisher: Springer Science and Business Media LLC.

[40] P. Mauskopf. Transition edge sensors and kinetic inductance detectors in astronomical instruments. *Publications of the Astronomical Society of the Pacific*, 130(990), January 2018. doi: 10.1088/1538-3873/aabaf0. Publisher: University of Chicago.

[41] Sean A. Bryan, Jason E. Austermann, Philip Mauskopf, Giles Novak, Sara M. Simon, Grant W. Wilson, Jeff McMahon, Daniel Ferrusca, Alfredo Montana, and David Sanchez-Arguelles. Optical design of the TolTEC millimeter-wave camera. In Jonas Zmuidzinas and Jian-RongEditors Gao, editors, *Millimeter, Submillimeter, and Far-Infrared Detectors and Instrumentation for Astronomy IX*, July 2018. doi: 10.1117/12.2314130. URL `http://dx.doi.org/10.1117/12.2314130`. ISBN: 9781510619708 Publisher: SPIE.

[42] Allegra Bothell. Emissivac Polished Surface, June 2018. URL `https://www.atlasuhv.com/emissivac-polished-surface/`.

[43] F. Peter Schloerb. Technical Capabilities of the Large Millimeter Telescope Alfonso Serrano. 2019.

[44] David H. Hughes, F. Peter Schloerb, Itziar Aretxaga, Edgar Castillo-Domínguez, Miguel Chávez Dagostino, Edgar Colín, Neal Erickson, Daniel Ferrusca Rodriguez, David M. Gale, Arturo Gómez-Ruiz, José Luis Hernández Rebollar, Mark Heyer, James Lowenthal, Alfredo Montaña, Marcos Emir Moreno Nolasco, Gopal Narayanan, Alexandra Pope, Iván. Rodríguez-Montoya, David Sánchez-Argüelles, David Smith, Kamal Souccar, Miguel Velázquez de la Rosa Becerra, Grant W. Wilson, and Min S. Yun. The Large Millimeter Telescope (LMT) Alfonso Serrano: current status and telescope performance. In *Society of Photo-Optical Instrumentation Engineers (SPIE) Conference Series*, volume 11445 of *Society of Photo-Optical Instrumentation Engineers (SPIE) Conference Series*, page 1144522, December 2020. doi: 10.1117/12.2561893.

[45] Emily Lunde, Peter Ade, Marc Berthoud, Reid Contente, N. S. DeNigris, Simon Doyle, Daniel Ferrusca, Joey Golec, Stephen Kuczarski, Dennis Lee, Zhiyuan Ma, Philip Mauskopf, Michael McCrackan, Jeffrey McMahon, Giles Novak, Giampaolo Pisano, Sara Simon, Kamal Souccar, Carole Tucker, Matthew Underhill, Eric Van Camp, and Grant Wilson. The optical design and performance of TolTEC: a millimeter-wave imaging polarimeter. In Jonas Zmuidzinas and Jian-Rong Gao, editors, *Millimeter, Submillimeter, and Far-Infrared Detectors and Instrumentation for Astronomy X*, volume 11453, pages 735 – 749. SPIE, 2020. doi: 10.1117/12.2562798. URL `https://doi.org/10.1117/12.2562798`. Backup Publisher: International Society for Optics and Photonics.

[46] Judy Lau, Joseph Fowler, Tobias Marriage, Lyman Page, Jon Leong, Edward Wishnow, Ross Henry, Ed Wollack, Mark Halpern, Danica Marsden, and Gaelen Marsden. Millimeter-wave antireflection coating for cryogenic silicon lenses. *Appl. Opt.*, 45(16):3746–3751, June 2006. doi: 10.1364/AO.45.003746. URL `http://ao.osa.org/abstract.cfm?URI=ao-45-16-3746`. Publisher: OSA.

[47] Karl Young, Qi Wen, Shaul Hanany, Hiroaki Imada, Jürgen Koch, Tomotake Matsumura, Oliver Suttmann, and Viktor Schütz. Broadband millimeter-wave anti-reflection coatings on silicon using pyramidal sub-wavelength structures. *Journal of Applied Physics*, 121(21):213103, June 2017. ISSN 1089-7550. doi: 10.1063/1.4984892. URL `http://dx.doi.org/10.1063/1.4984892`. Publisher: AIP Publishing.

[48] Joseph E. Golec, Jeffrey J. McMahon, Aamire Ali, Grace Chesmore, Leah Cooperrider, Simon Dicker, Nicholas Galitzki, Kathleen Harrington, Rebecca Jackson, Benjamin Westbrook, Edward J. Wollack, Zhilei Xu, and Ningfeng Zhu. Design and fabrication of metamaterial anti-reflection coatings for the Simons Observatory. In Roland Geyl and Ramón Navarro, editors, *Advances in Optical and Mechanical Technologies for Telescopes and Instrumentation IV*. SPIE, December 2020. doi: 10.1117/12.2561720. URL `https://doi.org/10.1117%2F12.2561720`.

[49] Peter Ade, Giampaolo Pisano, Carole Tucker, and Samuel Weaver. A review of metal mesh filters. *Proceedings of SPIE - The International Society for Optical Engineering*, 6275, July 2006. doi: 10.1117/12.673162.

[50] Sara M. Simon, Joseph E. Golec, Aamir Ali, Jason Austermann, James A. Beall, Sarah Marie M. Bruno, Steve K. Choi, Kevin T. Crowley, Simon Dicker, Bradley Dober, Shannon M. Duff, Erin Healy, Charles A. Hill, Shuay-Pwu P. Ho, Johannes Hubmayr, Yaqiong Li, Marius Lungu, Jeff McMahon, John Orlowski-Scherer, Maria Salatino, Suzanne Staggs, Edward J. Wollack, Zhilei Xu, and Ningfeng Zhu. Feedhorn development and scalability for Simons Observatory and beyond. In Jonas Zmuidzinas and Jian-Rong Gao, editors, *Millimeter, Submillimeter, and Far-Infrared Detectors and Instrumentation for Astronomy IX*. SPIE, July 2018. doi: 10.1117/12.2313405. URL `https://doi.org/10.1117%2F12.2313405`.

[51] Jack Ekin. *Experimental Techniques for Low-Temperature Measurements*. October 2006. ISBN 978-0-19-857054-7. doi: 10.1093/acprof:oso/9780198570547.001.0001.

[52] Thomas Middelmann, Alexander Walkov, Guido Bartl, and René Schödel. Thermal expansion coefficient of single-crystal silicon from 7 K to 293 K. *Phys. Rev. B*, 92(17):174113, November 2015. doi: 10.1103/PhysRevB.92.174113. URL `https://link.aps.org/doi/10.1103/PhysRevB.92.174113`. Publisher: American Physical Society.

[53] P. J. B. Clarricoats and A. D. Olver. *Corrugated horns for microwave antennas*. P. Peregrinus on behalf of the Institution of Electrical Engineers London, UK, 1984. ISBN 0-86341-003-0. Type: Book.

[54] Joshua Gundersen and Edward Wollack. Millimeter Wave Corrugated Platelet Feeds. *Journal of Physics Conference Series*, 155:012005, August 2009.

[55] Paul F. Goldsmith. *Quasioptical systems : Gaussian beam quasioptical propagation and applications*. IEEE Press/Chapman & Hall publishers series on microwave technology and RF. IEEE Press New York, New York, 1998. ISBN 0-412-83940-7 978-0-412-83940-5 0-7803-3439-6 978-0-7803-3439-7.

[56] D. Flanigan. *Kinetic inductance detectors for measuring the polarization of the cosmic microwave background*. PhD Thesis, Columbia University, 2018.

[57] A. Monfardini, L. J. Swenson, A. Bideaud, F. X. Désert, S. J. C. Yates, A. Benoit, A. M. Baryshev, J. J. A. Baselmans, S. Doyle, B. Klein, M. Roesch, C. Tucker, P. Ade, M. Calvo, P. Camus, C. Giordano, R. Guesten, C. Hoffmann, S. Leclercq, P. Mauskopf, and K. F. Schuster. NIKA: A millimeter-wave kinetic inductance camera. *åp*, 521:A29, October 2010. doi: 10.1051/0004-6361/201014727. _eprint: 1004.2209.

[58] E. Castillo-Dominguez, P. Ade, P. S. Barry, T. Brien, S. Doyle, D. Ferrusca, V. Gomez-Rivera, P. Hargrave, A. Hornsby, D. Hughes, P. D. Mauskopf, P. Moseley, E. Pascale, A. Perez-Fajardo, G. Pisano, S. Rowe, C. Tucker, and M. Velazquez. Mexico-UK Sub-millimeter Camera for Astronomy. *Journal of Low Temperature Physics*, 193(5-6):1010–1015, July 2018. doi: 10.1007/s10909-018-2018-9. URL `https://doi.org/10.1007%2Fs10909-018-2018-9`. Publisher: Springer Science and Business Media LLC.

[59] Jason E. Austermann and G. W. Wilson. Observations of 2mm array, November 2019.

[60] X. Liu, W. Guo, Y. Wang, M. Dai, L. F. Wei, B. Dober, C. McKenney, G. C. Hilton, J. Hubmayr, J. E. Austermann, J. N. Ullom, J. Gao, and M. R. Vissers. Superconducting micro-resonator arrays with ideal frequency spacing and extremely low frequency collision rate, 2017. _eprint: 1711.07914.

[61] J. Bardeen, L. N. Cooper, and J. R. Schrieffer. Theory of Superconductivity. *Phys. Rev.*, 108(5):1175–1204, December 1957. doi: 10.1103/PhysRev.108.1175. URL `https://link.aps.org/doi/10.1103/PhysRev.108.1175`. Publisher: American Physical Society.

[62] B. Mazin, P.K. Day, H.G. LeDuc, A. Vayonakis, and J. Zmuidzinas. Superconducting Kinetic Inductance Photon Detectors. *Proc. SPIE*, 4849, 2002.

[63] Michael R. Vissers, Jiansong Gao, Martin Sandberg, Shannon M. Duff, David S. Wisbey, Kent D. Irwin, and David P. Pappas. Proximity-coupled Ti/TiN multilayers for use in kinetic inductance detectors. *Applied Physics Letters*, 102 (23), June 2013. doi: 10.1063/1.4804286. URL `https://doi.org/10.1063%2F1.4804286`. Publisher: AIP Publishing.

[64] F Altomare and A.M Chang. Superconductivity: Basics and Formulation. In *One-Dimensional Superconductivity in Nanowires*, pages 1–29. John Wiley & Sons, Ltd, 2013. ISBN 978-3-527-64904-4. doi: https://doi.org/10.1002/9783527649044.ch1. URL `https://onlinelibrary.wiley.com/doi/abs/10.1002/9783527649044.ch1`. Section: 1 _eprint: https://onlinelibrary.wiley.com/doi/pdf/10.1002/9783527649044.ch1.

[65] John M. Martinis, G. C. Hilton, Kent D. Irwin, and David A. Wollman. Calculation of Tc in a Normal-Superconductor Bilayer Using the Microscopic-Based Usadel Theory. *Nuclear Instruments & Methods in Physics Research Section A-accelerators Spectrometers Detectors and Associated Equipment*, 444:23–27, 2000.

[66] M. Faverzani, E. Ferri, A. Giachero, C. Giordano, B. Margesin, R. Mezzena, A. Nucciotti, and A. Puiu. Characterization of the low temperature behavior of thin Titanium/Titanium Nitride multilayer films. *Superconductor Science Technology*, 33(4):045009, April 2020. doi: 10.1088/1361-6668/ab7435.

[67] J. Gao. *The Physics of Superconducting Microwave Resonators*. PhD Thesis, California Institute of Technology, 2008.

[68] Samuel Gordon, Brad Dober, Adrian Sinclair, Samuel Rowe, Sean Bryan, Philip Mauskopf, Jason Austermann, Mark Devlin, Simon Dicker, Jiansong Gao, and et al. An Open Source, FPGA-Based LeKID Readout for BLAST-TNG: Pre-Flight Results. *Journal of Astronomical Instrumentation*, 05(04):1641003, December 2016. ISSN 2251-1725. doi: 10.1142/s2251171716410038. URL `http://dx.doi.org/10.1142/S2251171716410038`. Publisher: World Scientific Pub Co Pte Lt.

[69] A. K. Sinclair, E. Schroeder, D. Zhu, M. Colangelo, J. Glasby, P. D. Mauskopf, H. Mani, and K. K. Berggren. Demonstration of Microwave Multiplexed Readout of DC-Biased Superconducting Nanowire Detectors. *IEEE Transactions on Applied Superconductivity*, 29(5), August 2019. doi: 10.1109/TASC.2019.2899329. _eprint: 1905.06880.

[70] M. Hosseini, W. T. Wong, and J. Bardin. A 0.4–1.2 GHz SiGe Cryogenic LNA for Readout of MKID Arrays. *2019 IEEE/MTT-S International Microwave Symposium*, January 2019. URL `http://par.nsf.gov/biblio/10112748`.

[71] Zhiyuan Ma, Michael McCrackan, N. S. DeNigris, Kamal Souccar, Grant W. Wilson, Paul Horton, Dennis Lee, Philip Mauskopf, Giles Novak, Iván Rodríguez-Montoya, and Javier Zaragoza-Cardiel. The TolTEC data analysis pipeline and software stack. In Juan C. Guzman and Jorge Ibsen, editors, *Software and Cyberinfrastructure for Astronomy VI*, volume 11452, page 114522O. SPIE, 2020. doi: 10.1117/12.2560735. URL `https://doi.org/10.1117/12.2560735`. Backup Publisher: International Society for Optics and Photonics.

[72] N.S. DeNigris, G.W. Wilson, M.E. Eiben, E. Lunde, P. Mauskopf, and R. Contente. Developing a Large-Scale Cryogenic System for the Simultaneous Operation of Three Detector Focal Planes in TolTEC, A New Multichroic Imaging Polarimeter. January 2020.

[73] E. Marquardt, J. Le, and R. Radebaugh. Cryogenic Material Properties Database. pages 681–687. January 2002. doi: 10.1007/0-306-47112-4_84.

[74] J. Nicol and T.P. Tseng. Thermal Conductivity of Copper between 0.25 K and 4.2 K. *Phys. Rev.*, 92, 1953.

[75] N.J Simon, R.P. Reed, and E.S. Drexler. *Oxygen Free High Conductivity Copper: Thermal Properties*. 1992. Publication Title: Properties of Copper and Copper Alloys at Cryogenic Temperatures Section: 7.

[76] R. L. Schmitt. Thermal conductance measurements of bolted copper joints for SuperCDMS. *Cryogenics*, 70, 2015.

[77] R. C. Dhuley. Thermal conductance modeling and characterization of the SuperCDMS SNOLAB sub- Kelvin cryogenic system. *IOP Conf. Ser.: Mater. Sci. Eng.*, 278, 2017.

[78] John C. Mather, Dale J. Fixsen, and Richard A. Shafer. Design for the COBE far-infrared absolute spectrophotometer (FIRAS). In Marija S. Scholl, editor, *Infrared Spaceborne Remote Sensing*, volume 2019 of *Society of Photo-Optical Instrumentation Engineers (SPIE) Conference Series*, pages 168–179, October 1993. doi: 10.1117/12.157823.

[79] G. W. Wilson, J. E. Austermann, T. A. Perera, K. S. Scott, P. A. R. Ade, J. J. Bock, J. Glenn, S. R. Golwala, S. Kim, Y. Kang, D. Lydon, P. D. Mauskopf, C. R. Predmore, C. M. Roberts, K. Souccar, and M. S. Yun. The AzTEC mm-wavelength camera. *mnras*, 386(2):807–818, May 2008. doi: 10.1111/j.1365-2966.2008.12980.x. _eprint: 0801.2783.

[80] Philip Mauskopf, August 2023.

[81] Dennis Lee, Giles Novak, Marc Berthoud, John Bussan, Robert Golenia, Eric Van Clepper, Grant Wilson, N. S. DeNigris, Zhiyuan Ma, Michael McCrackan, Kamal Souccar, Laura Fissel, Akanksha Bij, Felix Thiel, Itziar Aretxaga, Daniel Ferrusca Sr, Philip Mauskopf, Emily Lunde, Peter Ade, Carole Tucker, Giampaolo Pisano, Erin Guilfoil Cox, Laurence Sabin, Carlos Carrasco-Gonzalez, Alice Pasetto, Arturo Gómez-Ruiz Sr, Chat Hull, Jason Austermann, James Beall, Jiansong Gao, and Michael Vissers. The TolTEC camera: polarimetric commissioning and performance of the continuously rotating half-wave plate. In Jonas Zmuidzinas and Jian-Rong Gao, editors, *Millimeter, Submillimeter, and Far-Infrared Detectors and Instrumentation for Astronomy XI*, volume 12190, page 121901O. SPIE, 2022. doi: 10.1117/12.2627725. URL `https://doi.org/10.1117/12.2627725`. Backup Publisher: International Society for Optics and Photonics.

[82] Michael McCrackan, Zhiyuan Ma, Nat S. DeNigris, Caleigh Ryan, Kamal Souccar, Grant W. Wilson, Itziar Aretxaga, Akanksha Bij, Laura Fissel, Joseph E. Golec, Robert Gutermuth, Dennis Lee, Giles Novak, Felix Thiel, Samantha Walker, and Javier Zaragoza-Cardiel. The TolTEC camera: the citlali data reduction pipeline engine. In Jorge Ibsen and Gianluca Chiozzi, editors, *Software and Cyberinfrastructure for Astronomy VII*, volume 12189, page 121891H. SPIE, 2022. doi: 10.1117/12.2629095. URL `https://doi.org/10.1117/12.2629095`. Backup Publisher: International Society for Optics and Photonics.

[83] Grant Wilson, Sophia Abi-saad, Peter Ade, Itziar Aretxaga, Jason Austermann, Yvonne Ban, Joseph Bardin, J. Beall, Marc Berthoud, Sean Bryan, John Bussan, Edgar Castillo-Domínguez, Miguel Chavez Dagostino, Reid Contente, Natalie DeNigris, Bradley Dober, Miranda Eiben, Daniel Ferrusca, Laura Fissel, and Min Yun. The TolTEC camera: an overview of the instrument and in-lab testing results. page 1, December 2020. doi: 10.1117/12.2562331.

[84] G. W. Wilson, Stephen Kuczarski, and Phil Mauskopf, April 2020.

[85] Carole Tucker. Re: [Toltec-team] Results from Beammaping, August 2020.

[86] Sam Gordon, Adrian Sinclair, Philip Mauskopf, Gabriele Coppi, Mark Devlin, Bradley Dober, Laura Fissel, Nicholas Galitzki, Jiansong Gao, Johannes Hubmayr, Nathan Lourie, Ian Lowe, Christopher McKenney, Federico Nati, and Javier Romualdez. Preflight Detector Characterization of BLAST-TNG. *Journal of Low Temperature Physics*, 200(5-6):400–406, April 2020. doi: 10.1007/s10909-020-02459-6.

[87] P. Welch. The use of fast Fourier transform for the estimation of power spectra: A method based on time averaging over short, modified periodograms. *IEEE Transactions on Audio and Electroacoustics*, 15(2):70–73, 1967. doi: 10.1109/TAU.1967.1161901.

[88] S. R. Dicker, P. M. Korngut, B. S. Mason, P. A. R. Ade, J. Aguirre, T. J. Ames, D. J. Benford, T. C. Chen, J. A. Chervenak, W. D. Cotton, M. J. Devlin, E. Figueroa-Feliciano, K. D. Irwin, S. Maher, M. Mello, S. H. Moseley, D. J. Tally, C. Tucker, and S. D. White. MUSTANG: 90 GHz science with the Green Bank Telescope. In William D. Duncan, Wayne S. Holland, Stafford Withington, and Jonas Zmuidzinas, editors, *SPIE Proceedings*. SPIE, August 2008. doi: 10.1117/12.788361. URL `https://doi.org/10.1117%2F12.788361`.

[89] A. Catalano, M. Calvo, N. Ponthieu, R. Adam, A. Adane, P. Ade, P. André, A. Beelen, B. Belier, A. Benoît, A. Bideaud, N. Billot, N. Boudou, O. Bourrion, G. Coiffard, B. Comis, A. D'Addabbo, F. X. Désert, S. Doyle, J. Goupy, C. Kramer, S. Leclercq, J. F. Macías-Pérez, J. Martino, P. Mauskopf, F. Mayet, A. Monfardini, F. Pajot, E. Pascale, L. Perotto, V. Revéret, L. Rodriguez, G. Savini, K. Schuster, A. Sievers, C. Tucker, and R. Zylka. Performance and calibration of the NIKA camera at the IRAM 30 m telescope. *åp*, 569:A9, September 2014. doi: 10.1051/0004-6361/201423557. _eprint: 1402.0260.

[90] J. A. Sobrin, P. A. R. Ade, Z. Ahmed, A. J. Anderson, J. S. Avva, R. Basu Thakur, A. N. Bender, B. A. Benson, J. E. Carlstrom, F. W. Carter, T. W. Cecil, C. L. Chang, J. F. Cliche, A. Cukierman, T. de Haan, J. Ding, M. A. Dobbs, D. Dutcher, W. Everett, A. Foster, J. Gallichio, A. Gilbert, J. C. Groh, S. T. Guns, N. W. Halverson, A. H. Harke-Hosemann, N. L. Harrington, J. W. Henning, W. L. Holzapfel, N. Huang, K. D. Irwin, O. B. Jeong, M. Jonas, T. S. Khaire, A. M. Kofman, M. Korman, D. L. Kubik, S. Kuhlmann, C. L. Kuo, A. T. Lee, A. E. Lowitz, S. S. Meyer, D. Michalik, J. Montgomery, A. Nadolski, T. Natoli, H. Nguyen, G. I. Noble, V. Novosad, S. Padin, Z. Pan, J. Pearson, C. M. Posada, W. Quan, A. Rahlin, J. E. Ruhl, J. T. Sayre, E. Shirokoff, G. Smecher, A. A. Stark, K. T. Story, A. Suzuki, K. L. Thompson, C. Tucker, K. Vanderlinde, J. D. Vieira, G. Wang, N. Whitehorn, V. Yefremenko, K. W. Yoon, and M. Young. Design and characterization of the SPT-3G receiver. In Jonas Zmuidzinas and Jian-Rong Gao, editors, *Millimeter, Submillimeter, and Far-Infrared Detectors and Instrumentation for Astronomy IX*, volume 10708 of *Society of Photo-Optical Instrumentation Engineers (SPIE) Conference Series*, page 107081H, July 2018. doi: 10.1117/12.2314366. _eprint: 1809.00032.

[91] L. Perotto, N. Ponthieu, J. F. Macías-Pérez, R. Adam, P. Ade, P. André, A. Andrianasolo, H. Aussel, A. Beelen, A. Benoît, and et al. Calibration and performance of the NIKA2 camera at the IRAM 30-m Telescope. *Astronomy & Astrophysics*, 637:A71, May 2020. ISSN 1432-0746. doi: 10.1051/0004-6361/201936220. URL `http://dx.doi.org/10.1051/0004-6361/201936220`. Publisher: EDP Sciences.

[92] A. Montaña, M. Chávez Dagostino, I. Aretxaga, G. Novak, A. Pope, G. Wilson, and TolTEC Team. TolTEC: unveiling the hidden universe. *Memorie della Societa Astronomica Italiana*, 90:632, January 2019.

[93] A. S. Pérez-Grovas. The Large Millimeter Telescope (LMT). In E. Falco, J. A. Fernandez, and R. F. Ferrero, editors, *Revista Mexicana de Astronomia y Astrofisica Conference Series*, volume 4 of *Revista Mexicana de Astronomia y Astrofisica Conference Series*, pages 67–73, November 1996.

[94] A. S. Rahlin, P. A. R. Ade, M. Amiri, S. J. Benton, J. J. Bock, J. R. Bond, S. A. Bryan, Hsin C. Chiang, C. R. Contaldi, B. P. Crill, O. Doré, M. Farhang, J. P. Filippini, L. M. Fissel, A. A. Fraisse, A. E. Gambrel, N. N. Gand ilo, S. Golwala, Jon E. Gudmundsson, M. Halpern, M. F. Hasselfield, G. Hilton, W. A. Holmes, V. V. Hristov, K. D. Irwin, William C. Jones, Zigmund D. Kermish, C. L. Kuo, C. J. MacTavish, P. V. Mason, K. Megerian, L. Moncelsi, T. A. Morford, J. M. Nagy, C. B. Netterfield, R. O'Brient, C. Reintsema, J. E. Ruhl, M. C. Runyan, J. A. Shariff, J. D. Soler, A. Trangsrud, C. Tucker, R. S. Tucker, A. D. Turner, A. C. Weber, D. V. Wiebe, and E. Y. Young. Pre-flight integration and characterization of the SPIDER balloon-borne telescope. In Wayne S. Holland and Jonas Zmuidzinas, editors, *Millimeter, Submillimeter, and Far-Infrared Detectors and Instrumentation for Astronomy VII*, volume 9153 of *Society of Photo-Optical Instrumentation Engineers (SPIE) Conference Series*, page 915313, July 2014. doi: 10.1117/12.2055683. _eprint: 1407.2906.

[95] Satoru Takakura, Mario Aguilar, Yoshiki Akiba, Kam Arnold, Carlo Baccigalupi, Darcy Barron, Shawn Beckman, David Boettger, Julian Borrill, Scott Chapman, Yuji Chinone, Ari Cukierman, Anne Ducout, Tucker Elleflot, Josquin Errard, Giulio Fabbian, Takuro Fujino, Nicholas Galitzki, Neil Goeckner-Wald, Nils W. Halverson, Masaya Hasegawa, Kaori Hattori, Masashi Hazumi, Charles Hill, Logan Howe, Yuki Inoue, Andrew H. Jaffe, Oliver Jeong, Daisuke Kaneko, Nobuhiko Katayama, Brian Keating, Reijo Keskitalo, Theodore Kisner, Nicoletta Krachmalnicoff, Akito Kusaka, Adrian T. Lee, David Leon, Lindsay Lowry, Frederick Matsuda, Tomotake Matsumura, Martin Navaroli, Haruki Nishino, Hans Paar, Julien Peloton, Davide Poletti, Giuseppe Puglisi, Christian L. Reichardt, Colin Ross, Praween Siritanasak, Aritoki Suzuki, Osamu Tajima, Sayuri Takatori, and Grant Teply. Performance of a continuously rotating half-wave plate on the POLARBEAR telescope. *Journal of Cosmology and Astroparticle Physics*, 2017(05):008–008, May 2017. ISSN 1475-7516. doi: 10.1088/1475-7516/2017/05/008. URL `https://iopscience.iop.org/article/10.1088/1475-7516/2017/05/008`.

[96] T. Essinger-Hileman, A. Kusaka, J. W. Appel, S. K. Choi, K. Crowley, S. P. Ho, N. Jarosik, L. A. Page, L. P. Parker, S. Raghunathan, S. M. Simon, S. T. Staggs, and K. Visnjic. Systematic effects from an ambient-temperature, continuously rotating half-wave plate. *Review of Scientific Instruments*, 87(9): 094503, September 2016. ISSN 0034-6748, 1089-7623. doi: 10.1063/1.4962023. URL `https://pubs.aip.org/aip/rsi/article/365808`.

[97] L. Moncelsi, P. A. R. Ade, F. E. Angilè, S. J. Benton, M. J. Devlin, L. M. Fissel, N. N. Gandilo, J. O. Gundersen, T. G. Matthews, C. B. Netterfield, G. Novak, D. Nutter, E. Pascale, F. Poidevin, G. Savini, D. Scott, J. D. Soler, L. D. Spencer, M. D. P. Truch, G. S. Tucker, and J. Zhang. Empirical modelling of the BLASTPol achromatic half-wave plate for precision submillimetre polarimetry. *mnras*, 437:2772–2789, January 2014. doi: 10.1093/mnras/stt2090. _eprint: 1208.4866.

[98] F. Ruppin, F. Mayet, G. W. Pratt, R. Adam, P. Ade, P. André, M. Arnaud, H. Aussel, I. Bartalucci, A. Beelen, A. Benoît, A. Bideaud, O. Bourrion, M. Calvo, A. Catalano, B. Comis, M. De Petris, F. X. Désert, S. Doyle, E. F. C. Driessen, J. Goupy, C. Kramer, G. Lagache, S. Leclercq, J. F. Lestrade, J. F. Macías-Pérez, P. Mauskopf, A. Monfardini, L. Perotto, G. Pisano, E. Pointecouteau, N. Ponthieu, V. Revéret, A. Ritacco, C. Romero, H. Roussel, K. Schuster, A. Sievers, C. Tucker, and R. Zylka. First Sunyaev-Zel'dovich mapping with the NIKA2 camera: Implication of cluster substructures for the pressure profile and mass estimate. *åp*, 615:A112, July 2018. doi: 10.1051/0004-6361/201732558. _eprint: 1712.09587.

[99] Yue Dai, Kunpeng Jia, Guanghao Zhu, Hui Li, Yue Fei, Yuqing Guo, Hang Yuan, Hao Wang, Xiaoqing Jia, Qingyuan Zhao, Lin Kang, Jian Chen, Shining Zhu, Peiheng Wu, Zhenda Xie, and Labao Zhang. All-fiber device for single-photon detection. *PhotoniX*, 4(1):7, February 2023. ISSN 2662-1991. doi: 10.1186/s43074-023-00085-5. URL `https://doi.org/10.1186/s43074-023-00085-5`.

[100] Samantha Walker. *Development of Superconducting Detectors for Millimeter-Wave Astronomy and Cosmology*. PhD Thesis, University of Colorado Boulder, 2023.

[101] L. J. Swenson, P. K. Day, B. H. Eom, H. G. Leduc, N. Llombart, C. M. McKenney, O. Noroozian, and J. Zmuidzinas. Operation of a titanium nitride superconducting microresonator detector in the nonlinear regime. *Journal of Applied Physics*, 113(10), March 2013. ISSN 0021-8979. doi: 10.1063/1.4794808. URL `https://doi.org/10.1063/1.4794808`. _eprint: https://pubs.aip.org/aip/jap/article-pdf/doi/10.1063/1.4794808/15108284/104501_1_online.pdf.

[102] Rolando Dünner, Matthew Hasselfield, Tobias A. Marriage, Jon Sievers, Viviana Acquaviva, Graeme E. Addison, Peter A. R. Ade, Paula Aguirre, Mandana Amiri, John William Appel, L. Felipe Barrientos, Elia S. Battistelli, J. Richard Bond, Ben Brown, Bryce Burger, Erminia Calabrese, Jay Chervenak, Sudeep Das, Mark J. Devlin, Simon R. Dicker, W. Bertrand Doriese, Joanna Dunkley, Thomas Essinger-Hileman, Ryan P. Fisher, Megan B. Gralla, Joseph W. Fowler, Amir Hajian, Mark Halpern, Carlos Hernández-Monteagudo, Gene C. Hilton, Matt Hilton, Adam D. Hincks, Renée Hlozek, Kevin M. Huffenberger, David H. Hughes, John P. Hughes, Leopoldo Infante, Kent D. Irwin, Jean Baptiste Juin, Madhuri Kaul, Jeff Klein, Arthur Kosowsky, Judy M. Lau, Michele Limon, Yen-Ting Lin, Thibaut Louis, Robert H. Lupton, Danica Marsden, Krista Martocci, Phil Mauskopf, Felipe Menanteau, Kavilan Moodley, Harvey Moseley, Calvin B. Netterfield, Michael D. Niemack, Michael R. Nolta, Lyman A. Page, Lucas Parker, Bruce Partridge, Hernan Quintana, Beth Reid, Neelima Sehgal, Blake D. Sherwin, David N. Spergel, Suzanne T. Staggs, Daniel S. Swetz, Eric R. Switzer, Robert Thornton, Hy Trac, Carole Tucker, Ryan Warne, Grant Wilson, Ed Wollack, and Yue Zhao. THE ATACAMA COSMOLOGY TELESCOPE: DATA CHARACTERIZATION AND MAPMAKING. *The Astrophysical Journal*, 762(1):10, January 2013. ISSN 0004-637X, 1538-4357. doi: 10.1088/0004-637X/762/1/10. URL `https://iopscience.iop.org/article/10.1088/0004-637X/762/1/10`.

[103] Theodore Kisner, Reijo Keskitalo, Andrea Zonca, Jonathan R. Madsen, Jean Savarit, Maurizio Tomasi, Kolen Cheung, Giuseppe Puglisi, David Liu, and Matthew Hasselfield. hpc4cmb/toast: Update Pybind11. *Zenodo*, October 2021. doi: 10.5281/zenodo.5559597. URL `https://doi.org/10.5281/zenodo.5559597`. Version Number: 2.3.14.

[104] K. S. Scott, J. E. Austermann, T. A. Perera, G. W. Wilson, I. Aretxaga, J. J. Bock, D. H. Hughes, Y. Kang, S. Kim, P. D. Mauskopf, D. B. Sanders, N. Scoville, and M. S. Yun. AzTEC millimetre survey of the COSMOS field - I. Data reduction and source catalogue. *mnras*, 385:2225–2238, April 2008. doi: 10.1111/j.1365-2966.2008.12989.x. _eprint: arXiv:0801.2779.

[105] D. Ferrusca and J. Contreras R. Weather monitor station and 225 GHz radiometer system installed at Sierra Negra: the Large Millimeter Telescope site. In Suzanne K. Ramsay, Ian S. McLean, and Hideki Takami, editors, *Ground-based and Airborne Instrumentation for Astronomy V*, volume 9147 of *Society of Photo-Optical Instrumentation Engineers (SPIE) Conference Series*, page 914730, July 2014. doi: 10.1117/12.2055005.

[106] M. Zeballos, D. Ferrusca, J. Contreras R., and D. H. Hughes. Reporting the first 3 years of 225-GHz opacity measurements at the site of the Large Millimeter Telescope Alfonso Serrano. In Helen J. Hall, Roberto Gilmozzi, and Heather K. Marshall, editors, *Ground-based and Airborne Telescopes VI*, volume 9906 of *Society of Photo-Optical Instrumentation Engineers (SPIE) Conference Series*, page 99064U, July 2016. doi: 10.1117/12.2232168.

[107] Scott Paine. The am atmospheric model. July 2022. doi: 10.5281/zenodo.6774376. URL `https://zenodo.org/record/6774376`.

[108] J. G. Mangum, D. T. Emerson, and E. W. Greisen. The On The Fly imaging technique. *Astronomy & Astrophysics*, 474(2):679–687, November 2007. ISSN 0004-6361, 1432-0746. doi: 10.1051/0004-6361:20077811. URL `http://www.aanda.org/10.1051/0004-6361:20077811`.

[109] T. A. Perera, G. W. Wilson, K. S. Scott, J. E. Austermann, J. R. Schaar, and A. Mancera. An Efficient and Optimal Filter for Identifying Point Sources in Millimeter/Submillimeter Wavelength Sky Maps. *Publications of the Astronomical Society of the Pacific*, 125:838–848, July 2013. doi: 10.1086/671756. _eprint: 1304.0413.

[110] Jonathan Sievers. minkasi. *sievers/minkasi*, 2023. URL `https://github.com/sievers/minkasi`.

[111] Charles E. Romero, Jonathan Sievers, Vittorio Ghirardini, Simon Dicker, Simona Giacintucci, Tony Mroczkowski, Brian S. Mason, Craig Sarazin, Mark Devlin, Massimo Gaspari, Nicholas Battaglia, Matthew Hilton, Esra Bulbul, Ian Lowe, and Sara Stanchfield. Pressure Profiles and Mass Estimates Using High-resolution Sunyaev-Zel'dovich Effect Observations of Zwicky 3146 with MUSTANG-2. *apj*, 891(1):90, March 2020. doi: 10.3847/1538-4357/ab6d70. _eprint: 1908.09200.

[112] C. M. Cantalupo, J. D. Borrill, A. H. Jaffe, T. S. Kisner, and R. Stompor. MADmap: A MASSIVELY PARALLEL MAXIMUM LIKELIHOOD COSMIC MICROWAVE BACKGROUND MAP-MAKER. *The Astrophysical Journal Supplement Series*, 187(1):212–227, March 2010. doi: 10.1088/0067-0049/187/1/212. URL `https://doi.org/10.1088%2F0067-0049%2F187%2F1%2F212`. Publisher: American Astronomical Society.

[113] Gary King. An Introduction to the Dataverse Network as an Infrastructure for Data Sharing. *Sociological Methods \& Research*, 36(2):173–199, November 2007. doi: 10.1177/0049124107306660. URL `https://gking.harvard.edu/files/dvn.pdf`.

[114] Charles L. H. Hull, Josep M. Girart, and Qizhou Zhang. 880 m SMA Polarization Observations of the Quasar 3C 286. *The Astrophysical Journal*, 830: 124, October 2016. ISSN 0004-637X. doi: 10.3847/0004-637X/830/2/124. URL https://ui.adsabs.harvard.edu/abs/2016ApJ...830..124H. ADS Bibcode: 2016ApJ...830..124H.

[115] H. Nagai, K. Nakanishi, R. Paladino, C. L. H. Hull, P. Cortes, G. Moellenbrock, E. Fomalont, K. Asada, and K. Hada. ALMA Science Verification Data: Millimeter Continuum Polarimetry of the Bright Radio Quasar 3C 286. *The Astrophysical Journal*, 824:132, June 2016. ISSN 0004-637X. doi: 10.3847/0004-637X/824/2/132. URL https://ui.adsabs.harvard.edu/abs/2016ApJ...824..132N. ADS Bibcode: 2016ApJ...824..132N.

[116] A. Ritacco, N. Ponthieu, A. Catalano, R. Adam, P. Ade, P. André, A. Beelen, A. Benoît, A. Bideaud, N. Billot, O. Bourrion, M. Calvo, G. Coiffard, B. Comis, F. X. Désert, S. Doyle, J. Goupy, C. Kramer, S. Leclercq, J. F. Macías-Pérez, P. Mauskopf, A. Maury, F. Mayet, A. Monfardini, F. Pajot, E. Pascale, L. Perotto, G. Pisano, M. Rebolo-Iglesias, V. Revéret, L. Rodriguez, C. Romero, F. Ruppin, G. Savini, K. Schuster, A. Sievers, C. Thum, S. Triqueneaux, C. Tucker, and R. Zylka. Polarimetry at millimeter wavelengths with the NIKA camera: calibration and performance. *Astronomy and Astrophysics*, 599:A34, March 2017. ISSN 0004-6361. doi: 10.1051/0004-6361/201629666. URL https://ui.adsabs.harvard.edu/abs/2017A&A...599A..34R. ADS Bibcode: 2017A&A...599A..34R.

[117] R. A. Perley and B. J. Butler. Integrated Polarization Properties of 3C48, 3C138, 3C147, and 3C286. *The Astrophysical Journal Supplement Series*, 206:16, June 2013. ISSN 0067-0049. doi: 10.1088/0067-0049/206/2/16. URL https://ui.adsabs.harvard.edu/abs/2013ApJS..206...16P. ADS Bibcode: 2013ApJS..206...16P.

[118] N. Erickson, G. Narayanan, R. Goeller, and R. Grosslein. An Ultra-Wideband Receiver and Spectrometer for 74–110 GHz. In A. J. Baker, J. Glenn, A. I. Harris, J. G. Mangum, and M. S. Yun, editors, *From Z-Machines to ALMA: (Sub)Millimeter Spectroscopy of Galaxies*, volume 375 of *Astronomical Society of the Pacific Conference Series*, page 71, October 2007.

[119] Simon D. M. White, Julio F. Navarro, August E. Evrard, and Carlos S. Frenk. The baryon content of galaxy clusters: a challenge to cosmological orthodoxy. *Nature*, 366(6454):429–433, December 1993. ISSN 1476-4687. doi: 10.1038/366429a0. URL https://doi.org/10.1038/366429a0.

[120] Y. B. Zeldovich and R. A. Sunyaev. The Interaction of Matter and Radiation in a Hot-Model Universe. *apss*, 4:301–316, July 1969. doi: 10.1007/BF00661821.

[121] Rishi Khatri and Massimo Gaspari. Thermal SZ fluctuations in the ICM: probing turbulence and thermodynamics in Coma cluster with ${\it Planck}$. *Monthly Notices of the Royal Astronomical Society*, 463(1):655–669, November 2016. ISSN 0035-8711, 1365-2966. doi: 10.1093/mnras/stw2027. URL http://arxiv.org/abs/1604.03106. arXiv: 1604.03106.

[122] Simon R. Dicker, Charles E. Romero, Luca Di Mascolo, Tony Mroczkowski, Jonathan Sievers, Emily Moravec, Tanay Bhandarkar, Mark Brodwin, Thomas Connor, Bandon Decker, Mark Devlin, Anthony H. Gonzalez, Ian Lowe, Brian S. Mason, Craig Sarazin, Spencer A. Stanford, Daniel Stern, Khunanon Thongkham, Dominika Wylezalek, and Fernando Zago. The Massive and Distant Clusters of WISE Survey X: Results from a Sunyaev-Zeldovich Effect Pilot Study of Massive Galaxy Clusters at z>1 using the GBT + MUSTANG2. 2020. _eprint: 2006.06703.

[123] Charles E. Romero, Massimo Gaspari, Gerrit Schellenberger, Tanay Bhandarkar, Mark Devlin, Simon R. Dicker, William Forman, Rishi Khatri, Ralph Kraft, Luca Di Mascolo, Brian S. Mason, Emily Moravec, Tony Mroczkowski, Paul Nulsen, John Orlowski-Scherer, Karen Perez Sarmiento, Craig Sarazin, Jonathan Sievers, and Yuanyuan Su. Inferences from surface brightness fluctuations of Zwicky 3146 via the Sunyaev-Zeldovich effect and X-ray observations. *arXiv e-prints*, page arXiv:2305.05790, May 2023. doi: 10.48550/arXiv.2305.05790. _eprint: 2305.05790.

[124] N. Battaglia, J. R. Bond, C. Pfrommer, and J. L. Sievers. On the Cluster Physics of Sunyaev-Zel'dovich and X-Ray Surveys. II. Deconstructing the Thermal SZ Power Spectrum. *apj*, 758(2):75, October 2012. doi: 10.1088/0004-637X/758/2/75. _eprint: 1109.3711.

[125] Camille Avestruz, Daisuke Nagai, and Erwin T. Lau. STIRRED, NOT CLUMPED: EVOLUTION OF TEMPERATURE PROFILES IN THE OUTSKIRTS OF GALAXY CLUSTERS. *The Astrophysical Journal*, 833(2):227, December 2016. ISSN 1538-4357. doi: 10.3847/1538-4357/833/2/227. URL http://dx.doi.org/10.3847/1538-4357/833/2/227. Publisher: American Astronomical Society.

[126] M. Gaspari and E. Churazov. Constraining turbulence and conduction in the hot ICM through density perturbations. *åp*, 559:A78, November 2013. doi: 10.1051/0004-6361/201322295. _eprint: 1307.4397.

[127] M. Gaspari, E. Churazov, D. Nagai, E. T. Lau, and I. Zhuravleva. The relation between gas density and velocity power spectra in galaxy clusters: High-resolution hydrodynamic simulations and the role of conduction. *Astronomy & Astrophysics*, 569:A67, September 2014. ISSN 0004-6361, 1432-0746. doi: 10.1051/0004-6361/201424043. URL http://www.aanda.org/10.1051/0004-6361/201424043.

[128] F. Ruppin, R. Adam, P. Ade, H. Ajeddig, P. André, E. Artis, H. Aussel, A. Beelen, A. Benoît, S. Berta, L. Bing, O. Bourrion, M. Brodwin, M. Calvo, A. Catalano, B. Decker, M. De Petris, F. X. Désert, S. Doyle, E. F. C. Driessen, P. R. M. Eisenhardt, A. Gomez, A. H. Gonzalez, J. Goupy, F. Kéruzoré, C. Kramer, B. Ladjelate, G. Lagache, S. Leclercq, J. F. Lestrade, J. F. Macías-Pérez, A. Maury, P. Mauskopf, F. Mayet, M. McDonald, A. Monfardini, E. Moravec, M. Muñoz-Echeverría, L. Perotto, G. Pisano, N. Ponthieu, V. Revéret, A. J. Rigby, A. Ritacco, C. Romero, H. Roussel, K. Schuster, S. Shu, A. Sievers, S. A. Stanford, D. Stern, C. Tucker, and R. Zylka. Mapping the intracluster medium temperature in the era of NIKA2 and MUSTANG-2. In *mm Universe @ NIKA2 - Observing the mm Universe with the NIKA2 Camera*, volume 257 of *European Physical Journal Web of Conferences*, page 00043, July 2022. doi: 10.1051/epjconf/202225700043. _eprint: 2111.01446.

[129] Jack Sayers, Alfredo Montaña, Tony Mroczkowski, Grant W. Wilson, Michael Zemcov, Adi Zitrin, Nathália Cibirka, Sunil Golwala, David Hughes, Daisuke Nagai, Erik D. Reese, David Sánchez, and John Zuhone. Imaging the Thermal and Kinematic Sunyaev-Zel'dovich Effect Signals in a Sample of Ten Massive Galaxy Clusters: Constraints on Internal Velocity Structures and Bulk Velocities. *arXiv e-prints*, page arXiv:1812.06926, December 2018. _eprint: 1812.06926.

[130] R. Adam, I. Bartalucci, G. W. Pratt, P. Ade, P. André, M. Arnaud, A. Beelen, A. Benoît, A. Bideaud, N. Billot, H. Bourdin, O. Bourrion, M. Calvo, A. Catalano, G. Coiffard, B. Comis, A. D'Addabbo, M. De Petris, J. Démoclès, F.-X. Désert, S. Doyle, E. Egami, C. Ferrari, J. Goupy, C. Kramer, G. Lagache, S. Leclercq, J.-F. Macías-Pérez, S. Maurogordato, P. Mauskopf, F. Mayet, A. Monfardini, T. Mroczkowski, F. Pajot, E. Pascale, L. Perotto, G. Pisano, E. Pointecouteau, N. Ponthieu, V. Revéret, A. Ritacco, L. Rodriguez, C. Romero, F. Ruppin, K. Schuster, A. Sievers, S. Triqueneaux, C. Tucker, M. Zemcov, and R. Zylka. Mapping the kinetic Sunyaev-Zel'dovich effect toward MACS J0717.5\mathplus3745 with NIKA. *Astronomy &amp\mathsemicolon Astrophysics*, 598:A115, February 2017. doi: 10.1051/0004-6361/201629182. URL `https://doi.org/10.1051%2F0004-6361%2F201629182`. Publisher: EDP Sciences.

[131] Andrew H. Jaffe and Marc Kamionkowski. Calculation of the Ostriker-Vishniac effect in cold dark matter models. *prd*, 58(4):043001, August 1998. doi: 10.1103/PhysRevD.58.043001. _eprint: astro-ph/9801022.

[132] G. W. Wilson. *An Instrument and Technique for Measuring the Anisotropy in the Cosmic Microwave Background Radiation*. PhD thesis, Brown University, 1998.

[133] David Rafferty and Niruj Mohan. Python Blob Detector and Source Finder (PyBDSF). URL `https://github.com/lofar-astron/PyBDSF/tree/master`.

[134] Kaylea Nelson, Erwin T. Lau, Daisuke Nagai, Douglas H. Rudd, and Liang Yu. Weighing Galaxy Clusters with Gas. II. On the Origin of Hydrostatic Mass Bias in \ensuremath\LambdaCDM Galaxy Clusters. *apj*, 782(2):107, February 2014. doi: 10.1088/0004-637X/782/2/107. _eprint: 1308.6589.

[135] A. T. A. M. de Waele. Basic Operation of Cryocoolers and Related Thermal Machines. *J. Low Temp. Phys.*, 2011.

[136] Frank Pobell. *Matter and Methods at Low Temperatures*. Springer Berlin, Heidelberg, 1992. ISBN 978-3-662-08578-3.